

QUANTIFYING NON-FICKIAN TRANSPORT  
IN POROUS AND FRACTURED MEDIA USING FRACTIONAL-CALCULUS BASED  
STOCHASTIC MODELS

by

BINGQING LU

YONG ZHANG, COMMITTEE CHAIR  
GEOFFREY R. TICK  
YUEHAN LU  
CHARLES O'NEILL  
CHRISTOPHER T. GREEN

A DISSERTATION

Submitted in partial fulfillment of the requirements for the  
degree of Doctor of Philosophy in the Department of  
Geological Sciences in the Graduate School of  
The University of Alabama

TUSCALOOSA, ALABAMA

2019



## ABSTRACT

Non-Fickian or “anomalous” transport, where the target’s spatial variance grows nonlinearly in time, describes the pollutant dynamics widely observed in heterogeneous geological media deviating significantly from that described by the classical advection dispersion equation (ADE). The ADE describes the Fickian-type of transport, with symmetric snapshots like the Gaussian distribution in space (Berkowitz et al., 2006). Non-Fickian transport can be observed at all scales. Non-Fickian transport is typically characterized by apparent (as heavy as power-law) early arrivals and late time tailing behaviors in the tracer breakthrough curves (BTCs). Non-Fickian transport is well known to be affected by medium heterogeneity. Heterogeneity can refer to variations in the distribution of geometrical properties, as well as variations in the biogeochemical properties of the medium, which cannot be mapped exhaustively at all relevant scales. Complex geometric structures and intrinsic heterogeneity in geological formations affect predictions of tracer transport and further challenge remediation analyses. Hence, efficient quantification of non-Fickian transport requires parsimonious models such as the fractional engine based physical models.

In this dissertation, I first compared three types of time non-local transport models, which include the multi-rate mass transfer (MRMT) model, the continuous time random walk (CTRW) framework, and the tempered time fractional advection dispersion equation (tt-fADE) model. I then found that tt-fADE can model the rate-limited diffusion and sorption-desorption of Arsenic in soil. Additionally, non-Fickian dynamics for pollutant transport in field-scale discrete fracture networks (DFNs) were explored. Monte Carlo simulations of water flow were then conducted

through field-scale DFNs to identify non-Darcian flow and non-Fickian pressure propagation. Finally, to address non-Fickian transport for reactive pollutants, I proposed a time fractional derivative model with the reaction term.

Findings of this dissertation improve our understanding of the nature of water flow and pollutant transport in porous and fractured media at different scales. The correlated parameters and relationships between media properties and parameters can enhance the applicability of fractional partial differential equations that can be parameterized using the measurable media characteristics. This provides one of the most likely ways to improve the model predictability, which remained the most challenge for stochastic hydrologic models.

## DEDICATION

To my parents, and to Boyi.

## LIST OF ABBREVIATIONS AND SYMBOLS

ADE	advection-dispersion equation
REV	representative elementary volume
CTRW	continuous time random walk
MRMT	multi-rate mass transfer
FDE	fractional differential equation
PDF	probability density function
fpDE	fractional-order partial differential equation
tt-fADE	tempered time fractional advection-dispersion equation
SRMT	single-rate mass transfer
BTC	breakthrough curve
DFN	discrete fracture network
$C_m$	aqueous concentration in the mobile zone
$C_{im,j}$	aqueous concentration in the $j$ -th immobile zone
$\beta_j$	capacity coefficient
$v$	velocity vector

$D$	dispersion coefficient tensor
$n$	number of distinct immobile phases
$\alpha_j$	first-order mass transfer rate
*	convolution
$g(t)$	memory function
$\Gamma(\cdot)$	Gamma function
$C_{im}$	overall concentration in immobile domains
$\sim$	Laplace transform
BBF	Brilliant Blue FCF
$Q$	flow rate
$L$	travel distance
$R$	retardation coefficient
$\theta$	porosity
RMSE	root mean square error
$M$	initial mass injected into the column
$A$	cross-section area
$D_a$	apparent diffusion coefficient
$k$	slope of the late-time tail

$\gamma$	time index
$\lambda$	truncation parameter
As	arsenic
i.d.	inner diameter
$\alpha_L$	longitudinal dispersivity
$R^2$	coefficient of determination
$\beta_{tot}$	total capacity coefficient
$q$	fluid flux
$K$	hydraulic conductivity tensor
$k_r$	relative permeability of the medium
$z$	elevation head
$\overline{\nabla}$	two-dimensional gradient operator
$S_{sf}$	specific storage coefficient in fractures
$K_f$	saturated hydraulic conductivity in fractures
$C_f$	concentration in fractures
$\lambda_f$	first-order decay constant in fractures
$S_{BTC}$	slope of the BTC recession limb
SDE	standard dispersion equation
HGS	HydroGeoSphere
$erf(\cdot)$	error function
$J$	hydraulic gradient
fADRE	fractional advection-dispersion-reaction equation
ADRE	advection-dispersion-reaction equation

MIM	mobile-immobile
$\delta(\cdot)$	Dirac delta function
RMSLE	root mean squared logarithmic error

## ACKNOWLEDGMENTS

I would like to thank everyone that contributed to this research, directly and indirectly. Specially, I would like to thank my academic advisor Dr. Yong Zhang for giving me the opportunity to work with him in the University of Alabama. I am very thankful for his massive help and guidance throughout the completion of this dissertation. I also want to thank my research group members for their extensive help in my research. I also thank the useful comments and inputs from all my dissertation committee members, Dr. Geoffrey R. Tick, Dr. Yuehan Lu, Dr. Charles O'Neill, and Dr. Christopher T. Green. I am very grateful to the Department of Geological Sciences for providing me the opportunity to develop my research skills and the graduate council fellowship, the teaching assistantship funding, the research assistantship funding, and the Lindahl Ph.D. scholarship.

The research conducted to develop this dissertation was partially funded by the National Science Foundation of the US, the National Natural Science Foundation of China, the University of Alabama Graduate School Research and Travel Support Fund, and the UA Department of Geological Sciences A.S. Johnson Travel Fund.

## CONTENTS

ABSTRACT .....	ii
DEDICATION .....	iv
LIST OF ABBREVIATIONS AND SYMBOLS .....	v
ACKNOWLEDGMENTS .....	ix
LIST OF TABLES .....	xvi
LIST OF FIGURES .....	xix
CHAPTER 1: INTRODUCTION .....	1
CHAPTER 2: COMPARISON OF TIME NONLOCAL TRANSPORT MODELS FOR CHARACTERIZING NON-FICKIAN TRANSPORT: FROM MATHEMATICAL INTERPRETATION TO LABORATORY APPLICATION.....	8
2.1 Abstract .....	8
2.2 Introduction.....	9
2.3 Review and evaluation of time nonlocal transport models.....	12
2.3.1 Multi-Rate Mass Transfer model .....	12
2.3.2 Tempered Time Fractional Advection-Dispersion Equation model.....	14
2.3.3 Continuous Time Random Walk framework.....	16
2.4 Applications: Capturing non-Fickian transport in multidimensional porous media.....	19
2.5 Model fit and comparison .....	22
2.5.1 The ADE model with equilibrium sorption .....	22
2.5.2 The MRMT model .....	25

2.5.2.1 MRMT model 1 with a single mass-transfer rate .....	26
2.5.2.2 MRMT model 2 with a single diffusion rate .....	29
2.5.2.3 MRMT model 3 with two mass-exchange rates .....	30
2.5.2.4 MRMT model 4 with power-law distributed rate coefficients .....	31
2.5.3 The tt-fADE model (2-8) .....	34
2.5.4 The CTRW model.....	39
2.6 Discussion.....	40
2.6.1 Comparison of transport models.....	40
2.6.2 Parameter sensitivity .....	44
2.6.3 Application to field transport.....	47
2.7 Conclusion .....	50
2.8 Supplementary Materials .....	53
2.9 Acknowledgments.....	62
2.10 References.....	63
<b>CHAPTER 3: QUANTIFYING TRANSPORT OF ARSENIC IN BOTH NATURAL SOILS AND RELATIVELY HOMOGENEOUS POROUS MEDIA USING STOCHASTIC MODELS .....</b>	<b>67</b>
3.1 Abstract.....	67
3.2 Introduction.....	68
3.3 Review of previous numerical modeling of arsenic transport in soils.....	69
3.4 Stochastic models to simulate arsenic mobility in saturated soils .....	72
3.5 Laboratory experiments and model applications .....	76
3.5.1 Case 1: Leaching experiments through heterogeneous soils .....	76

3.5.2 Case 2: Flushing experiment: As (V) transport through laboratory columns packed with ideal homogeneous glass beads .....	81
3.5.2.1 MRMT model .....	84
3.5.2.2 fADE model .....	86
3.5.2.3 SRMT model.....	90
3.6 Discussion.....	91
3.6.1 Model comparison .....	91
3.6.2 Leaching versus flushing experiments.....	94
3.6.3 Extension of arsenic transport in large-scale soils.....	96
3.7 Conclusion .....	96
3.8 Acknowledgments.....	99
3.9 References.....	99
 <b>CHAPTER 4: APPLICATION OF TEMPERED-STABLE TIME FRACTIONAL-DERIVATIVE MODEL TO UPSCALE SUBDIFFUSION FOR POLLUTANT TRANSPORT IN FIELD-SCALE DISCRETE FRACTURE NETWORKS .....</b>	 <b>106</b>
4.1 Abstract.....	106
4.2 Introduction.....	107
4.3 Monte Carlo Simulations and the Fractional Advection-Dispersion Equation .....	109
4.3.1 Generating the Random Discrete Fracture Networks .....	110
4.3.2 Modeling Groundwater Flow and Pollutant Transport through the DFNs.....	112
4.3.3 Applying the Fractional Advection-Dispersion Equations to Quantify Transport .....	117
4.4 Results of Monte Carlo Simulations.....	118
4.5 Discussion.....	120
4.5.1 Impact of Fracture Density on Non-Fickian Transport.....	120

4.5.2 Impact of Fracture Orientation on Non-Fickian Transport.....	121
4.5.3 Impact of Matrix Permeability on Late-Time BTC .....	123
4.5.4 How to Approximate the Time Index $\gamma$ Given the Limited Late-Time BTC?.....	124
4.5.5 Subdiffusive Transport Shown by Plume Snapshots .....	125
4.6 Conclusions.....	127
4.7 Acknowledgments: .....	129
4.8 References.....	129
<b>CHAPTER 5: IDENTIFYING NON-DARCIAN FLOW AND NON-FICKIAN PRESSURE PROPAGATION IN FIELD-SCALE DISCRETE FRACTURE NETWORKS.....</b>	<b>135</b>
5.1 Abstract.....	135
5.2 Introduction.....	135
5.3 Monte Carlo Simulation and Standard-Dispersion Equation.....	137
5.3.1 Random Discrete Fracture Network Generation.....	138
5.3.2 Modeling Groundwater Flow and Pressure Propagation in DFNs .....	138
5.3.3 Standard-Dispersion Equation to Quantify Pressure Propagation .....	139
5.4 Results of Monte Carlo Simulations .....	139
5.5 Discussion.....	142
5.5.1 Fracture Density and Hydraulic Gradient Affect Non-Darcian Flow.....	142
5.5.2 Impact of Fracture Density on Non-Fickian Pressure Propagation .....	144
5.5.3 Impact of Matrix Permeability on Transient Flow .....	146
5.5.4 Non-Darcian Flow versus Non-Fickian Pressure Propagation .....	146
5.6 Conclusion .....	147
5.7 Acknowledgements.....	148

5.8 References.....	148
CHAPTER 6: QUANTIFYING FATE AND TRANSPORT OF NITRATE IN SATURATED SOIL SYSTEMS USING FRACTIONAL-DERIVATIVE MODEL .....	150
6.1 Abstract.....	150
6.2 Introduction.....	151
6.3 Nitrate dynamics revealed by laboratory experiments documented in literature .....	155
6.3.1 Review of laboratory experiment 1: saturated soil from a test site in Beijing, China .....	155
6.3.2 Review of laboratory experiment 2: nitrate leaching in aridisols and entisols .....	157
6.4 Methodology development .....	158
6.4.1 Stochastic model to simulate nitrate reaction and transport in saturated soils .....	158
6.4.2 Numerical solver and validation .....	160
6.5 Applications .....	164
6.5.1 Results of model application for laboratory experiment 1.....	164
6.5.2 Results of model application for laboratory experiment 2.....	165
6.6 Discussion.....	168
6.6.1 Variation of model parameters among experiments .....	168
6.6.1.1 Model parameters for laboratory experiment 1 .....	169
6.6.1.2 Model parameters for laboratory experiment 2 .....	170
6.6.2 Impacts of reaction on nitrate dynamics .....	171
6.6.3 Model generalization: bacteria transport .....	173
6.7 Conclusion .....	178
6.8 Acknowledgments.....	180
6.9 References.....	180

CHAPTER 7: CONCLUSIONS .....	186
Reference .....	194

## LIST OF TABLES

Table 2-1. Measured and fitted parameters (using the ADE model with equilibrium sorption) for BBF transport through the Leca beads at different flow rates and travel distances and field tests .....	21
Table 2-2. The fitted parameters for the single mass-transfer rate mobile-immobile model (i.e., equations (2-27), (2-28)) at different flow rates and travel distances.....	28
Table 2-3. The fitted parameters for the single diffusion rate MRMT model at different flow rates and travel distances .....	30
Table 2-4. The fitted parameters for the two-set MRMT model at different flow rates and travel distances.....	31
Table 2-5. The best-fit parameters for the power-law MRMT model 4 at different flow rates and travel distances .....	32
Table 2-6. The best-fit parameters for the tt-fADE model (2-8) at different flow rates and travel distances.....	35
Table 2-7. The best-fit parameters for the CTRW model.....	40
Table 3-1. Leaching experiment: Parameters for the time fADE model (3-3).....	77
Table 3-2. Leaching experiment: Parameters for the MRMT model.....	80
Table 3-3. Case 2 - Fitted parameters for the MRMT model .....	85
Table 3-4. Case 2 - Fitted parameters for the time fADE model for the two glass-bead column experiments.....	86
Table 3-5. Case 2 - Fitted parameters for the single rate, double porosity, first order mass transfer (SRMT) model.....	90

Table 3-6. Case 2 - The root mean square error (RMSE) for the time fADE, SRMT, and MRMT model. ....	93
Table 3-7. Case 2 - The Akaike information criterion (AIC) value for the time fADE, SRMT, and MRMT model.....	93
Table 4-1. Model parameters, initial and boundary conditions used in the simulations .....	114
Table 4-2. Best-fit parameters for the tt-fADE model (4-9) for DFNs with different fracture densities and orientation scenarios.....	120
Table 6-1. Experiment 1: Best-fit parameters for the advection–dispersion–reaction equation (ADRE) and the fADRE model (6-1) for nitrate transport in the soil columns (Zheng et al., 2012).....	165
Table 6-2. Experiment 2: Best-fit parameters of the fADRE model (6-1) for nitrate transport through four soil columns from a high input cropping system.....	168
Table 6-3. The best-fit parameters of the fADRE model (6-1) for two bacteria ( <i>E. coli</i> and <i>Klebsiella</i> sp.) through three saturated soil columns (1-3) .....	176
Table 6-4. The RMSLE of the BTCs fitted by the MIM (6-10) and fADRE model (6-1) for two bacteria ( <i>E. coli</i> and <i>Klebsiella</i> sp.) moving through three saturated soil columns (1-3) (Figure 6-5). ....	176

## LIST OF FIGURES

Figure 2-1. Experimental setup.....	20
Figure 2-2. Laboratory tracer test: Comparison between the measured (symbols) and the modeled (lines) breakthrough curves using the ADE, the tt-fADE (red thick lines), the CTRW (green dashed lines), and the MRMT model with the water flow rate $Q = 1.4$ mL/s.....	22
Figure 2-3. The best-fit dispersivity in the ADE model (2-25) versus the travel distance. ....	24
Figure 2-4. The best-fit dispersivity in the ADE model versus the water flow rate. ....	25
Figure 2-5. Dispersivity in the tt-fADE model changes with the travel distance and flow rate. ..	36
Figure 2-6. The tt-fADE model parameters change with the travel distance and flow rate. ....	37
Figure 2-7. Sensitivity analysis for coefficients in the tt-fADE model. ....	45
Figure 2-8. Study site map.....	48
Figure 2-9. Field tracer test: comparison between the measured field data (symbols) and the modeled (lines) breakthrough curves using the ADE, the tt-fADE (red thick lines), the CTRW (green dashed lines), and the MRMT models.....	50
Figure 2-S1. Comparison between the measured (symbols) and modeled (lines) breakthrough curves using the ADE model (black line), the tt-fADE model (red line) and the CTRW model (green line) with the experimental water flow rate $Q = 0.4$ mL/s.....	53
Figure 2-S2. Comparison between the measured (symbols) and modeled (lines) breakthrough curves using the ADE model (black line), the tt-fADE model (red line) and the CTRW model (green line) with the experimental water flow rate $Q = 0.6$ mL/s.....	54

Figure 2-S3. Comparison between the measured (symbols) and modeled (lines) breakthrough curves using the ADE model (black line), the tt-fADE model (red line) and the CTRW model (green line) with the experimental water flow rate  $Q = 0.8$  mL/s..... 55

Figure 2-S4. Comparison between the measured (symbols) and modeled (lines) breakthrough curves using the ADE model (black line), the tt-fADE model (red line) and the CTRW model (green line) with the experimental water flow rate  $Q = 1.0$  mL/s..... 56

Figure 2-S5. Comparison between the measured (symbols) and modeled (lines) breakthrough curves using the ADE model (black line), the tt-fADE model (red line) and the CTRW model (green line) with the experimental water flow rate  $Q = 1.2$  mL/s..... 57

Figure 2-S6. Comparison between the measured (symbols) and the modeled (lines) breakthrough curves using the ADE, the tt-fADE, the MRMT, and the CTRW models with the water flow rate  $Q = 0.4$  mL/s. .... 58

Figure 2-S7. Comparison between the measured (symbols) and the modeled (lines) breakthrough curves using the ADE, the tt-fADE, the MRMT, and the CTRW models with the water flow rate  $Q = 0.6$  mL/s. .... 59

Figure 2-S8. Comparison between the measured (symbols) and the modeled (lines) breakthrough curves using the ADE, the tt-fADE, the MRMT, and the CTRW models with the water flow rate  $Q = 0.8$  mL/s. .... 60

Figure 2-S9. Comparison between the measured (symbols) and the modeled (lines) breakthrough curves using the ADE, the tt-fADE, the MRMT, and the CTRW models with the water flow rate  $Q = 1.0$  mL/s. .... 61

Figure 2-S10. Comparison between the measured (symbols) and the modeled (lines) breakthrough curves using the ADE, the tt-fADE, the MRMT, and the CTRW models with the water flow rate  $Q = 1.2$  mL/s. .... 62

Figure 3-1. Leaching experiment: Comparison between measured (circles) and modeled (lines) arsenic breakthrough curves for four arsenic-contaminated soils (a) BH, (b) FW, (c) JA, (d) PA using the two-site model (red line), the MRMT model with two rates (green line), and the time fADE model (black line)..... 77

Figure 3-2. Leaching experiment: Comparison between the measured (circles) and modeled (lines) As breakthrough curves using the SRMT model..... 79

Figure 3-3. Case 2 (Flushing experiment): Schematic diagram showing the setup of the column transport flushing experiments (i.e., glass bead packings). ..... 81

Figure 3-4. Case 2 (Flushing experiments): Comparison between the measured (circles) and modeled (lines) As BTCs using the time fADE model (black line), the SRMT model (red line) and the MRMT model (green line) with three different experimental water flow rates  $Q = 4$  mL/min, 2 mL/min, and 0.5 mL/min through the first column (40 cm ( $L$ )  $\times$  5.5 cm ( $i.d.$ )) ..... 83

Figure 3-5. Case 2 (Flushing experiments): Comparison between the measured (circles) and modeled (lines) As BTCs using the time fADE model (black line), the SRMT model (red line) and the MRMT model (green line) with three different experimental water flow rates  $Q = 2.5$  mL/min, 0.5 mL/min, and 0.2 mL/min through the second column (20 cm ( $L$ )  $\times$  2.6 cm ( $i.d.$ )). 84

Figure 4-1. Map of the fractured domain, showing flow geometry and boundary conditions ... 114

Figure 4-2. BTCs at the control plane  $x=50$  m for three different fracture densities (a), (b) and (c); (b) and (d) have the same fracture density with different orientations ..... 119

Figure 4-3. BTCs at the control plane  $x=50$  m for three different fracture densities (a), (b) and (c) with matrix permeability of  $1.1 \times 10^{-13}$  m<sup>2</sup> (red lines and circles) and  $5.5 \times 10^{-15}$  m<sup>2</sup> (green lines and crosses) ..... 124

Figure 4-4. One realization of plume snapshots for the first time step ( $t = 1$  day) for the three different fracture densities: (a) the DFNs with 20 fractures, (b) 60 fractures, and (c) 80 fractures; the 13<sup>th</sup> time step ( $t = 2000$  years) for the three different fracture densities: (d) 20 fractures, (e) 60 fractures, and (f) 80 fractures. .... 126

Figure 4-5. Monte Carlo results of plume snapshots for the first time step ( $t = 1$  day) for the three different fracture densities: (a) the DFNs with 20 fractures, (b) 60 fractures and (c) 80 fractures; the 13<sup>th</sup> time step ( $t = 2000$  years) for the three different fracture densities: (d) 20 fractures, (e) 60 fractures and (f) 80 fractures. .... 127

Figure 5-1. Ensemble average flux at the outlet boundary for the three DFN scenarios with a different number of fractures: 20 (a), 60 (b), and 100 (c)..... 140

Figure 5-2. The normalized, ensemble average of transient flux for DFNs with the number of fractures being 20 (a), 60 (b) and 100 (c) ..... 141

Figure 5-3. The same as Fig. 5-2, except that the hydraulic conductivity for the rock matrix is  $K = 1 \times 10^{-8}$  m/s..... 143

Figure 5-4. One realization of the hydraulic head distribution with the matrix hydraulic conductivity  $K = 1 \times 10^{-7}$  m/s and hydraulic gradient  $J = 0.1$  at an early time ( $t = 1 \times 10^4$  s) for the DFN with 20 (a), 60 (b), and 100 fractures (c) ..... 144

Figure 5-5. Histogram of the flux of 100 realizations for each node at the outlet boundary for the DFN with 20 (a), 60 (b), and 100 fractures (c) ..... 146

Figure 6-1. Distribution of numerical error in space with different numbers of time ..... 164

Figure 6-2. Experiment 1: Comparison between the measured (symbols) and modeled (lines) breakthrough curves (BTCs) using the ADRE (black line) and the fADRE (6-1) (red line) ..... 165

Figure 6-3. Experiment 2: The measured (symbols) and modeled (lines) BTCs for nitrate using the ADE (black line) (Mahmood-UI-Hassan et al., 2010), the MIM model (6-10) (red line) (Mahmood-UI-Hassan et al., 2010) and the fADRE model (6-1) (green line) ..... 167

Figure 6-4. Sensitivity analysis for the reaction rate coefficient  $K$  in the fADRE model (6-1) . 173

Figure 6-5. Comparison between the measured (symbols) and modeled (lines) BTCs for the two bacteria (*E. coli* and *Klebsiella* sp.) through three different soil columns (column 1, 2, 3) using the MIM model (black line) (Bai et al., 2016) and the fADRE model (red line) in log-log plots to show the early and late time tails. .... 175

## CHAPTER 1: INTRODUCTION

Groundwater provides the drinking water for 2 billion people, but it is facing an unprecedented risk of contamination worldwide, due to various contaminants released from agriculture, industry, and human activities. Given the enormous amount of contamination, groundwater remediation actions allow of no delay. The resources available for investigation and clean-up are extremely limited compared to the scope and the depth of the current situation in groundwater contamination. Over the past quarter century, the United States (U.S.) has placed a high priority on cleaning up sites where contaminants have leaked, spilled, or been disposed of in soil and groundwater. Anywhere from 300,000 to 400,000 contaminated sites in the U.S. are scheduled for cleanup in the coming decades, at an estimated total cost as high as \$500 billion to \$1 trillion (Council, 1997, 1994; Russell et al., 1991). Reasonable managements, protection, and remediation of groundwater require adequate understanding and accurate prediction of water flow and pollutant transport dynamics in real-world aquifers (which are heterogeneous porous and fractured media), motivating this dissertation study.

Tracer breakthrough experiments, starting from the 1950 s – 1960 s, provided the basic datasets for quantifying contaminant transport in porous media. Most attempts at quantifying contaminant transport have relied on the solution of some form of a classical, well-known governing equation called the advection-dispersion equation (ADE), which was derived by applying the mass-balance equation expressed by the gradient of the pollutant's advective and

dispersive mass flux (Anderson, 1984). The ADE is a macroscopic and continuum equation, where the parameters must be measured in a representative elementary volume (REV). The REV can be defined as the minimum volume of a complex heterogeneous medium (e.g., soil) where the spatial variation of the given parameter reaches stable with the medium size (Bear and Bachmat, 1990). Measured properties of the media are assumed to represent an average of the parameter within the REV (such as hydraulic conductivity and effective porosity). In addition, the dispersive flux is described by Fick's second law of diffusion, leading to the mass balance equation  $\frac{\partial c}{\partial t} = D \frac{\partial^2 c}{\partial x^2}$  for pure diffusion. The ADE model can quantify Fickian-type of transport, commonly assumed for homogeneous systems. However, there are two problems if we use the ADE to evaluate dispersion in the groundwater systems: 1) the real-world dispersive flux does not follow Fick's law, and 2) dispersivity cannot be defined by a physically measurable parameter (dispersivity  $\alpha$  [L] was usually assumed to be the characteristic length of the pores inside the REV, and the dispersion coefficient is defined as  $D = \alpha \cdot v$ ). Historically, dispersion has been represented by the Fickian process since 1922 (Taylor, 1922). This assumption has been applied to porous media since then, but it has been questioned by various researchers. For example, Fried (1975) found that the ADE solution did not fit the laboratory experimental results. This Fickian diffusion assumption is only valid after the dispersion process has been fully developed after a certain amount of time. For the heterogeneous system, this asymptotic process requires substantial transport from the pollutants after released from the source. Furthermore, for some certain hydrogeologic settings such as large-scale alluvial aquifers, dispersion may take extremely long time to reach Fickian (Anderson, 1984a). Deviations between the ADE model and experimental results necessitate consideration of more sophisticated

transport theories, such as the continuous time random walk (CTRW) framework (Berkowitz et al., 2006), the multi-rate mass transfer (MRMT) approach (Haggerty et al., 2000; Haggerty and Gorelick, 1995), and the fractional differential equations (FDEs) (Meerschaert et al., 2008). To account for the impacts of a broad distribution of media's properties on pollutant particle transport, a probabilistic approach/stochastic model with a probability density function (PDF) describing key characteristics of solute transport is considered. In addition, the poor parameter predictability and vague physical meaning of parameters hinder further applications of the stochastic models for real-world heterogeneous systems. These historical challenges may be solved by the fractional calculus, where an integer-order derivation is replaced with a fractional-order derivative. Fractional-order partial differential equations (fPDEs) are promising tools, since they are naturally related to systems with memory and fractals. They have been increasingly used to build models in fluid flow, finance, and physical and biological processes and systems (Debnath and Bhatta, 2004; Luchko and Gorenflo, 1999; Podlubny, 2001; Turut and Güzel, 2013). For example, Ahmed and Elgazzar (2007) used the fPDEs to model nonlocal epidemics. Electrochemistry has also benefited a lot from the fractional calculus (Oldham, 2010). fPDEs have been used to model various hydrological processes for 15 years, see the review in Zhang et al. (2017). In the fPDE models, the complex variation of mass, momentum, and energy in the heterogeneous system can be efficiently upscaled to capture spatial/temporal nonlocality without the need to map the detailed system heterogeneity. Better understanding of this ubiquitous non-Fickian transport dynamics, parameter definition, and further model selection are the primary motivations for studying numerical simulation of flow and transport in the porous and fractured media. The overarching goal of this dissertation is to connect the media's properties with fractional calculus model parameters, qualitatively and quantitatively. The dissertation consists

of seven chapters, an introduction chapter (Chapter 1), four published journal articles (Chapter 2-5) and one in revision (Chapter 6), and an overall conclusion (Chapter 7).

Chapter 2, entitled “*Comparison of time nonlocal transport models for characterizing non-Fickian transport: From mathematical interpretation to laboratory application*”, coauthored by Yong Zhang, Chunmiao Zheng, Christopher T. Green, Charles O’Neill, HongGuang Sun, and Jiazhong Qian, was published in *Water*. This chapter focuses on the first ever systematic evaluation of the promising time nonlocal transport models. I compared three popular time nonlocal transport models, including the MRMT model, the CTRW framework, and the tempered time fractional ADE (tt-fADE), by focusing on their physical interpretation and feasibility in capturing non-Fickian transport. Laboratory column transport experiments and field tracer tests were conducted to provide abundant datasets for model evaluation.

Chapter 3, entitled “*Quantifying transport of arsenic in both natural soils and relatively homogeneous porous media using stochastic models*”, coauthored by Jia Song, Shiyin Li, Geoffrey R. Tick, Wei Wei, Jianting Zhu, Chunmiao Zheng, and Yong Zhang, was published in *Soil Science Society of America Journal*. This study proposes a tempered time fractional ADE to model the rate-limited diffusion and sorption-desorption of Arsenic (As (V)) in soil. Processes of As (V) leaching from natural soils contain multiple stages of sorption-desorption. The relationship between model parameters and soil properties (including the clay content and pH condition) is also revealed. Leaching and flushing experiments of As (V) are compared to evaluate the impact of different experimental conditions on As (V) transport dynamics. The time fADE, single-rate mass transfer (SRMT), and MRMT models are compared to improve the understanding of As (V) transport processes in complex soil systems.

Chapter 4, entitled “*Application of tempered-stable time fractional-derivative model to upscale subdiffusion for pollutant transport in field-scale discrete fracture networks*”, coauthored by Yong Zhang, Donald M. Reeves, HongGuang Sun, and Chunmiao Zheng, was published in *Mathematics*. This study explores non-Fickian dynamics for pollutant transport in field-scale discrete fracture networks (DFNs), by investigating how fracture and rock matrix properties influence the leading and tailing edges of pollutant BTCs. Fractured reservoirs exhibit erratic internal structures and multi-scale heterogeneity, resulting in complex non-Fickian dynamics. A Monte Carlo approach is used to simulate pollutant transport through DFNs with a systematic variation of medium properties, and the resultant non-Fickian transport is upscaled using a tempered-stable fractional in time ADE. Numerical results serve as a basis for determining both the qualitative and quantitative relationships between BTC characteristics and model parameters, in addition to the impacts of fracture density, orientation, and rock matrix permeability on non-Fickian dynamics of pollutants. The observed impacts of medium heterogeneity on tracer transport especially at late time can enhance the application of the fPDEs, since the models can now be parameterized using the measurable fracture–matrix characteristics.

Chapter 5, entitled “*Identifying non-Darcian flow and non-Fickian pressure propagation in field-scale discrete fracture networks*”, coauthored by Yong Zhang, Yuan Xia, Donald M. Reeves, HongGuang Sun, Dongbao Zhou, and Chunmiao Zheng, was published in *Journal of Geoscience and Environment Protection*. This study explores the non-Darcian flow and its driven factors in field-scale DFNs. I conducted Monte Carlo simulations of water flow through DFNs to identify non-Darcian flow and non-Fickian pressure propagation in field-scale DFNs, by adjusting fracture density, matrix hydraulic conductivity, and the general hydraulic gradient imposed in the media. Numerical simulations and analyses showed that interactions of the

fracture architecture with the hydraulic gradient affect non-Darcian flow in DFNs, by generating and adjusting complex pathways for water. The fracture density affects significantly the propagation of hydraulic head/pressure in the DFN, likely due to fracture connectivity and flow channeling. The non-Darcian flow pattern does not correlate to the non-Fickian pressure propagation process directly in the regional-scale DFNs, because they refer to different states of water flow with different controlling factors. Findings of this study improve our understanding of the nature of water flow and pressure transfer in the DFNs which has been widely used to study pollutant transport in fractured aquifers.

Chapter 6, entitled “*Quantifying fate and transport of nitrate in saturated soil systems using fractional-derivative model*”, coauthored by Xiaoting Liu, Peiyao Dong, Geoffrey R. Tick, Chunmiao Zheng, Yong Zhang, Muhammad Mahmood-UI-Hassan, Hongjuan Bai and Edvina Lamy, is currently under review in *Applied Mathematical Modeling*. The works mentioned above (Chapter 2-5) reveal the nature of non-Fickian transport for conservative tracers, while most real-world pollutants involve chemical reactions. Hence, this study aims to develop and validate a novel fractional-derivative, advection-dispersion-reaction equation (fADRE) with first order decay to quantify nitrate contaminants transport in various soil systems. Applications show that the fADRE model can consider both hydrological and biogeochemical processes describing the fate and transport of nitrate in saturated soil. The model is tested and validated using the results from three independent studies including: 1) nitrate transport in natural soil columns collected from the North China Plain agricultural pollution zone, 2) nitrate leaching from aridisols and entisols soil columns, and 3) two bacteria (*Escherichia coli* and *Klebsiella* sp.) transport through saturated soil columns. The qualitative relationship between model parameters and the target

system properties (including soil physical properties, experimental conditions, and nitrate/bacteria physical and chemical properties) is also explored in detail, as well as the impact of chemical reactions on nitrate transport and fate dynamics. Results show that the fADRE can be a reliable mathematical model to quantify non-Fickian and reactive transport of chemicals in various soil systems, and it can also be used to describe other biological degradation and decay processes in soil and groundwater.

In Chapter 7, conclusions from each chapter are summarized, specifically focusing on the improved understanding of the major mechanisms for non-Fickian transport in the porous and fractured media which are gained through comparison, validation, fitting processes and application with the real world experimental data.

## CHAPTER 2:

### COMPARISON OF TIME NONLOCAL TRANSPORT MODELS FOR CHARACTERIZING NON-FICKIAN TRANSPORT: FROM MATHEMATICAL INTERPRETATION TO LABORATORY APPLICATION

#### 2.1 Abstract

Non-Fickian diffusion has been increasingly documented in hydrology and modeled by promising time nonlocal transport models. While previous studies showed that most of the time nonlocal models are identical with correlated parameters, fundamental challenges remain in real-world applications regarding to model selection and parameter definition. This study compared three popular time nonlocal transport models, including the multi-rate mass transfer (MRMT) model, the continuous time random walk (CTRW) framework, and the tempered time fractional advection-dispersion equation (tt-fADE), by focusing on their physical interpretation and feasibility in capturing non-Fickian transport. Mathematical comparison showed that these models have both related parameters defining the memory function and other basic-transport parameters (i.e., velocity  $v$  and dispersion coefficient  $D$ ) with different hydrogeologic interpretation. Laboratory column transport experiments and field tracer tests were then conducted, providing data for model applicability evaluation. Applications confirmed the well-known conclusion that the tt-fADE and CTRW models performed better than the traditional ADE in characterizing non-Fickian dynamics. The best-fit velocity and dispersion coefficient,

however, differ significantly between the tt-fADE and CTRW. Fitting exercises further revealed that the observed late-time breakthrough curves were heavier than the MRMT solutions with no more than two mass-exchange rates and lighter than the MRMT solutions with power-law distributed mass-exchange rates. Therefore, the time nonlocal models, where some parameters are correlated and exchangeable and the others have different values, differ mainly in their quantification of pre-asymptotic transport dynamics. In all models tested above, the tt-fADE model is attractive, considering its small fitting error and the reasonable velocity close to the measured flow rate.

## 2.2 Introduction

Non-Fickian or anomalous transport, where the plume variance grows nonlinearly in time, has been well-documented for solute transport in heterogeneous aquifers (Anderson 1984; Zheng and Gorelick 2003; Zheng et al. 2010; Bakshevskaia and Pozdniakov 2016; Chang and Yeh 2016; Cvetkovic et al. 2016), soils (Bromly and Hinz, 2004; Huber et al., 2012; Aviv Naftaly et al., 2016), and rivers (Nordin and Troutman, 1980; Zaramella et al., 2016). Non-Fickian transport for dissolved contaminants can occur at all scales, varying from field scale (Bianchi and Zheng, 2016) to micro- and nano-scale media (Ziemys et al. 2012; Karadimitriou et al. 2016). Non-Fickian diffusion, which is characterized by slow diffusion (sometimes further classified as sub-diffusion), has been long believed to be related to sorption/desorption between mobile and immobile domains under an equilibrium assumption (van Genuchten and Wierenga, 1976) or kinetic conditions (Sardin et al. 1991; Cvetkovic and Dagan 1994), or mass exchange between flow regions with relatively high and low velocities (Haggerty et al., 2000). Note here the term “diffusion” contains both molecular diffusion and mechanical dispersion (representing

the local variation of advection from the mean velocity), and hence “non-Fickian diffusion” is used interchangeable with “non-Fickian transport” in this study.

To capture non-Fickian transport induced by solute retention, various transport models have been developed, starting from the standard advection-dispersion equation (ADE) with either equilibrium or kinetic sorption (Valocchi 1985; Jury and Horton 2004) and the two-domain or two-site models proposed originally in chemical engineering (Coats et al., 1964). Time nonlocal transport models were then developed to capture solute retention in natural geologic media with intrinsic physical and chemical heterogeneity. There are at least three popular time nonlocal transport models, which are the multi-rate mass transfer (MRMT) model (Haggerty and Gorelick 1995; Haggerty et al. 2000), the hydrologic version of the continuous time random walk (CTRW) developed by Berkowitz and colleagues (see the extensive review in Berkowitz et al. (2006) and the mathematical version of CTRW in Meerschaert and Scheffler (2001)), and the tempered time fractional advection-dispersion equation (tt-fADE) model (Meerschaert et al., 2008). Some of these models have been compared theoretically. For example, mathematical similarity between the CTRW framework, the tt-fADE, and the MRMT model was explored by Dentz and Berkowitz (2003) and Berkowitz et al. (2006) (whose major conclusion will be repeated below for clarification), and the numerical approximation of the MRMT model using CTRW schemes was developed by Benson and Meerschaert (2009).

While previous studies showed that most of the time nonlocal models are identical with correlated parameters, fundamental challenges remain in real-world applications regarding to model selection and parameter definition. Various stochastic models have been developed for three decades in hydrology, but they have not become a routinely modeling tool, due to many reasons (Cirpka and Valocchi 2016; Sanchez-Vila and Fernàndez-Garcia 2016). For example,

given well-controlled laboratory transport experiments using heterogeneous sand columns and conservative tracers (which have been widely used to understand real-world diffusion and the resultant transport dynamics are known to be non-Fickian), a newcomer however faces the challenge of model selection: which time nonlocal model should be used to capture the observed non-Fickian dynamics under specific flow/transport conditions, such as conservative tracer transport in saturated, heterogeneous columns repacked in the lab with a stable, relatively high water flow rate? To my best knowledge, there is, unfortunately, no literature providing such an answer for this simple question. The above time nonlocal transport models were originally built upon different physical theories and contain different (number of) parameters. A better understanding of the potential benefits and limitations of different time nonlocal transport models as applied to non-Fickian dynamics, therefore, is required before they can be reliably applied for real-world applications and attract new users with limited knowledge in stochasticity.

This study will systematically evaluate the above (MRMT, CTRW, and tt-fADE) theoretical treatments of non-Fickian transport of conservative solutes, with respect to their parameters and ability to represent non-Fickian dispersion, especially the late-time tailing behavior, which is typical for hydrological processes in heterogeneous geological media. Late-time dynamics of contaminant transport is also a major concern of many environmental issues, such as groundwater contamination remediation and aquifer vulnerability assessment. I then applied all the modeling methods for laboratory column transport experiments and field tracer tests. I emphasize here that the application of a time nonlocal transport model to capture non-Fickian transport is not new at all. What's new in this study is the quantitative, practical comparison of non-local transport models given real-world data.

The rest of the work is organized as follows. In Section 2.3, I review the above time nonlocal transport models. In Section 2.4, the time nonlocal transport models are applied to model non-Fickian transport in multidimensional heterogeneous porous media. The applicability of those time nonlocal models is checked using laboratory experiments and field tests. My laboratory experiments, where a conservative tracer moving through heterogeneous Leca beads, exhibit typical non-Fickian diffusive behavior with elongated late-time tails. The field tracer tests also exhibit apparent tailing behaviors. Section 2.5 checks and compares all the time nonlocal models for characterizing the observed non-Fickian dynamics. Further analyses are shown in Section 2.6, where I group the transport models and briefly discuss parameter uncertainty. Conclusions are finally drawn in Section 2.7.

### 2.3 Review and evaluation of time nonlocal transport models

The core of the time nonlocal models is the appropriate definition of the memory function, which controls the distribution of waiting times for contaminants trapped by immobile zones. In this section, I focus on the theoretical background, especially the memory function, for each model and explore potential correlation of critical parameters in different models. For example, previous studies emphasized that the tt-fADE is a specific form of the CTRW framework since the tt-fADE assumes a truncated power-law memory function, which is one of the memory functions previously assumed by the CTRW framework (Berkowitz et al., 2006). Identical functionality was also pointed out for the MRMT and the CTRW framework; see section 2.2.

#### 2.3.1 Multi-Rate Mass Transfer model

The MRMT model describes mass transfer between a mobile domain and any number of immobile domains with varying properties. The linear, multi-rate, first-order solute transport equations in the absence of sources/sinks can be written as (Haggerty and Gorelick, 1995):

$$\frac{\partial C_m}{\partial t} + \sum_{j=1}^n \beta_j \frac{\partial C_{im,j}}{\partial t} = -\nabla \cdot [v C_m - D \nabla C_m] \quad (2-1a)$$

$$\frac{\partial C_{im,j}}{\partial t} = \alpha_j [C_m - C_{im,j}], \quad j = 1, 2, \dots, n \quad (2-1b)$$

where  $C_m$  and  $C_{im,j}$  [ $ML^{-3}$ ] represent the aqueous concentrations in the mobile zone and the  $j$ -th immobile zone, respectively;  $\beta_j$  [dimensionless] is the capacity coefficient usually defined as the ratio of porosities of the  $j$ -th immobile and the mobile phases;  $v$  [ $LT^{-1}$ ] is the velocity vector;  $D$  [ $L^2T^{-1}$ ] is the dispersion coefficient tensor;  $n$  [dimensionless] is the number of distinct immobile phases; and  $\alpha_j$  [ $T^{-1}$ ] is the first-order mass transfer rate (also called the rate coefficient) associated with the  $j$ -th immobile zone. When  $n = 1$ , Eq. (2-1) reduces to the single-rate mass transfer (SRMT) model.

The summation term in the left hand side of (2-1a) can be expressed as a convolution, leading to the time-nonlocal form (Haggerty et al. 2000; Schumer et al. 2003a):

$$\frac{\partial C_m}{\partial t} + g(t) * \frac{\partial C_{im,j}}{\partial t} = -\nabla \cdot [v C_m - D \nabla C_m] \quad (2-2)$$

where the symbol “\*” denotes convolution, and  $g(t)$  [ $T^{-1}$ ] is a memory function defined by the weighted sum of the exponential decay from individual immobile zones (Haggerty et al., 2000):

$$g(t) = \int_0^\infty \alpha b(\alpha) \exp(-\alpha t) d\alpha \quad (2-3)$$

where  $b(\alpha)$  [ $T$ ] is a density function of first-order rate coefficients.

In terms of similarities with the other nonlocal methods discussed below, the MRMT model captures the time nonlocality caused by the diffusion-limited transport of solutes in immobile zones. A practical advantage of this approach is that the memory function has explicit hydrogeological meaning and thus it may be calculated, fitted, or even predicted (Zhang et al., 2007). Finally, the parameters  $v$ ,  $D$  and  $g(t)$  can be spatially variable, so the MRMT method can capture the local variation of solute transport speed caused by nonstationary heterogeneity.

### 2.3.2 Tempered Time Fractional Advection-Dispersion Equation model

The tt-fADE is one analytic technique that accounts for the time nonlocality of the medium, and simultaneously accounts for convergence of a stochastic solute particle motion process (i.e., a CTRW) to a limit distribution. In particular, if the distribution of trapping times between the movement of solute particles has an infinite mean, then the overall transport equation has one fractional-order derivative representing “dispersion” in time, leading to the standard time fractional advection-dispersion equation (t-fADE) model. Assuming a power-law memory function to describe random waiting times in the immobile zones (Schumer et al., 2003):

$$g(t) = \frac{t^{-\gamma}}{\Gamma(1-\gamma)}, \quad (2-4)$$

where  $\Gamma(\cdot)$  is the Gamma function, and the exponent  $0 < \gamma \leq 1$ . Then by definition,

$$\frac{\partial C_m(x,t)}{\partial t} * g(t) = \frac{\partial C_m(x,t)}{\partial t} * \frac{t^{-\gamma}}{\Gamma(1-\gamma)} = \frac{\partial^\gamma C_m(x,t)}{\partial t^\gamma} \quad (2-5)$$

is a Caputo fractional derivative of order  $\gamma$ . Inserting (2-5) into the MRMT model (2-1) and assuming that the solute is initially placed in the mobile zone only, one obtains the following standard t-fADE describing the mobile and immobile solute transport:

$$\frac{\partial C_m}{\partial t} + \beta \frac{\partial^\gamma C_m}{\partial t^\gamma} = -\nabla \cdot [v C_m - D \nabla C_m] - \beta C_m(x, t=0) \frac{t^{-\gamma}}{\Gamma(1-\gamma)} \quad , \quad (2-6a)$$

$$\frac{\partial C_{im}}{\partial t} + \beta \frac{\partial^\gamma C_{im}}{\partial t^\gamma} = -\nabla \cdot [v C_{im} - D \nabla C_{im}] + C_m(x, t=0) \frac{t^{-\gamma}}{\Gamma(1-\gamma)} \quad . \quad (2-6b)$$

where  $C_{im}$  denotes the overall chemical concentration in all immobile domains.

Meerschaert et al. (2008) generalized the t-fADE (2-6) by introducing an exponentially truncated power-law function, which is an incomplete Gamma function, as the memory function:

$$g(t) = \int_t^\infty e^{-\lambda s} \frac{\gamma s^{-\gamma-1}}{\Gamma(1-\gamma)} ds \quad , \quad (2-7)$$

where  $\lambda > 0 [T^{-1}]$  is the truncation parameter in time. This modification leads to the tt-fADE:

$$\frac{\partial C_m}{\partial t} + \beta e^{-\lambda t} \frac{\partial^\gamma}{\partial t^\gamma} [e^{\lambda t} C_m] - \beta \lambda^\gamma C_m = -\nabla \cdot [v C_m - D \nabla C_m] - \beta C_m^0 \int_t^\infty e^{-\lambda \tau} \frac{\tau^{-\gamma-1}}{\Gamma(1-\gamma)} d\tau \quad (2-8a)$$

$$\frac{\partial C_{im}}{\partial t} + \beta e^{-\lambda t} \frac{\partial^\gamma}{\partial t^\gamma} [e^{\lambda t} C_{im}] - \beta \lambda^\gamma C_{im} = -\nabla \cdot [v C_{im} - D \nabla C_{im}] + C_m^0 \int_t^\infty e^{-\lambda \tau} \frac{\tau^{-\gamma-1}}{\Gamma(1-\gamma)} d\tau \quad (2-8b)$$

where  $C_m^0 = C_m(x, t=0)$  denotes the initial source located only in the mobile phase. At a time

$$t \ll 1/\lambda \quad , \quad (2-9)$$

the tail of the mobile-phase breakthrough curve (BTC) declines as a power law function:

$$C_m(x, t) \propto t^{-1-\gamma} \quad . \quad (2-10)$$

while at a much later time  $t \gg 1/\lambda$ , the slope of the mobile-phase BTC reaches infinity (i.e., the late-time BTC tail declines exponentially). Therefore, the value of  $\lambda$  controls the transition of the BTC late-time tail from a power-law function to exponential function (Zhang et al., 2014).

The use of the tt-fADE (2-8) to model mobile/immobile anomalous solute transport is motivated by four factors: 1) the equation governs the limits of known stochastic processes; 2) it describes a combination of first-order mass transfer models and reduces to known

mobile/immobile equations in the integer order case; 3) the equation has tractable solutions that model the significant features of solute plume evolution in time and space; and 4) the equation is parsimonious, with no more parameters than the standard MRMT model (2-1) with multiple pairs of rate and capacity coefficients. To summarize, the tt-fADE has one major limitation compared to the MRMT model (2-1) and the CTRW model discussed below: the memory function embedded in the tt-fADE is a specific form (2-7), while the memory function used in the MRMT and the CTRW model can have different forms.

### 2.3.3 Continuous Time Random Walk framework

Derivation of the CTRW model in hydrologic sciences (Berkowitz et al., 2006) starts from the generalized master equation with the kernel  $\Phi$  defined as (in Laplace space ( $t \mapsto s$ )) (Klafter and Silbey, 1980):

$$\tilde{\Phi}(x, s) = \frac{s \tilde{\Psi}(x, s)}{1 - \tilde{\phi}(s)}, \quad (2-11)$$

where the tilde “ $\sim$ ” denotes the Laplace transform,  $\tilde{\Psi}(x, s)$  is the Laplace transform of the joint density of jump length and duration, and  $\tilde{\phi}(s)$  is the Laplace transform of the transition time or duration density  $\phi(t) = \int_{-\infty}^{+\infty} \Psi(x, t) dx$  used in the master equation (Montroll and Weiss, 1965)

$$\hat{p}(k, s) = \frac{1 - \tilde{\phi}(s)}{s} \frac{1}{1 - \tilde{\phi}(s) \hat{f}(k)}, \quad (2-12)$$

where the right-hand side term is valid for independent jump size and transition time, and  $\hat{f}(k)$  denotes the jump size density.

Berkowitz et al. (2006) defined a memory function  $M$  to replace  $\tilde{\phi}(s)$  in (2-12)

$$\tilde{M}(s) = \frac{t_1 s \tilde{\phi}(s)}{1 - \tilde{\phi}(s)} , \quad (2-13)$$

where  $t_1 [T]$  denotes a “*typical median transition time*” for particles. Inserting (2-13) into (2-12), and taking the Laplace and Fourier inverse transform, the following well-known CTRW framework was obtained for the hydrologic community (Berkowitz et al., 2006):

$$\frac{\partial p(x,t)}{\partial t} = \int_0^t M(t-\tau) \left[ -v_\psi \frac{\partial}{\partial x} + D_\psi \frac{\partial^2}{\partial x^2} \right] p(x,\tau) d\tau , \quad (2-14)$$

where  $v_\psi$  denotes the average velocity, and  $D_\psi$  is the dispersion coefficient. When deriving the CTRW (2-14) from the master equation (2-12), the jump size density  $\tilde{f}(k)$  in (2-12) needs to be expanded as

$$\hat{f}(k) \approx 1 - \mu i k + \frac{\alpha^2}{2} (i k)^2 , \quad (2-15)$$

resulting in the spatially-averaged velocity  $v_\psi$  and dispersion coefficient  $D_\psi$  in (2-14):

$$v_\psi = \frac{\mu}{t_1} , \quad (2-16a)$$

$$D_\psi = \frac{\sigma^2}{2t_1} . \quad (2-16b)$$

Therefore, here the “*typical median transition time*”  $t_1$  is actually the mean waiting time:

$$t_1 = \int_0^{+\infty} t \phi(t) dt . \quad (2-17)$$

The CTRW memory function  $M$  defined by (2-13) has various forms, to capture various BTCs. One popular form is the exponentially truncated power-law, defined by the transition time  $\phi$  (see equation (2-16) in Dentz et al. (2004)):

$$\phi(t) = B \frac{\exp(-t/t_2)}{(1+t/t_1)^{1+\xi}} . \quad (2-18)$$

where the factor  $B = \{t_1 \tau_2^{-\xi} \exp(\tau_2^{-1}) \Gamma^*(-\xi, \tau_2^{-1})\}^{-1}$  (with  $\tau_2 = t_2 / t_1$ .) keeps the integral of  $\phi(t)$  to be 1. For simplicity and direct comparison between models, I constrain the exponent  $\xi$  to be  $0 < \xi < 1$  in this study. The Laplace transform of (2-18) is (see equation (2-17) in Dentz et al. (2004))

$$\tilde{\phi}(s) = \frac{\Gamma^*(-\xi, \tau_2^{-1} + t_1 s)}{\Gamma^*(-\xi, \tau_2^{-1})} (1 + \tau_2 s t_1)^\xi \exp(t_1 s) . \quad (2-19)$$

A simple manipulation shows the relationship between the MRMT memory function  $g(t)$  and the CTRW memory function  $M(t)$  in Laplace space:

$$\tilde{M}(s) = \frac{1}{\theta_M + \theta_I \tilde{g}(s)} . \quad (2-20)$$

where  $\theta_M$  [dimensionless] and  $\theta_I$  [dimensionless] are the porosity in the mobile and (total) immobile domains, respectively. Inserting (2-13) and (2-19) into (2-20), I obtain:

$$\begin{aligned} \tilde{g}(s) &= \frac{1 - \tilde{\phi}(s)}{\theta_I t_1 s \tilde{\phi}(s)} - \frac{\theta_M}{\theta_I} \\ &= \frac{1}{\theta_I t_1 s} \frac{\Gamma^*(-\xi, \tau_2^{-1})}{\Gamma^*(-\xi, \tau_2^{-1} + t_1 s) (1 + \tau_2 s t_1)^\xi \exp(t_1 s)} - \frac{1}{\theta_I s t_1} - \frac{\theta_M}{\theta_I} . \end{aligned} \quad (2-21)$$

There is no analytical solution for  $g$  in real time  $t$ , except for the following asymptote at late time  $t \gg t_1 \tau_2$ :

$$g(t) \propto \exp\left(-\frac{t}{t_1 \tau_2}\right) = \exp\left(-\frac{t}{t_2}\right) . \quad (2-22)$$

Based on (2-22), I obtain the late-time growth rate for  $p$

$$p(t_{late}) \propto -\frac{\partial g(t)}{\partial t} \propto \exp\left(-\frac{t}{t_2}\right) . \quad (2-23)$$

Therefore, for time  $t \gg t_2$ , the non-Fickian transport transitions to Fickian diffusion. The cutoff time scale  $t_2$  in (2-18), as explained by Dentz et al. (2004), “*corresponds to the largest heterogeneity length scale*”. In another numerical study by Willmann et al. (2008),  $t_2$  was also called “*the late cutoff time*”. The above analysis shows that  $t_2$  is functionally equivalent to the inverse of the truncation parameter  $\lambda$  used in the tt-fADE model (2-8).

For the intermediate time  $t_1 \ll t \ll t_2$ , one can obtain the memory function  $g$  by solving (2-21) numerically (e.g., using the numerical inverse Laplace transform). This was done by Dentz et al. (2004), who found that the transition probability scales as a power-law function

$$p(t) \propto t^{-\xi-1}, \text{ where } t_1 \ll t \ll t_2. \quad (2-24)$$

Comparing (2-24) and (2-10), I find that the power-law exponent  $\xi$  in the CTRW framework is functionally equivalent to the scale index  $\gamma$  in the tt-fADE model (2-8).

Hence, the parameters in the CTRW framework (2-14) (e.g.,  $\xi$  and  $t_2$ ) are related to the parameters in the tt-fADE model (2-8) ( $\gamma$  and  $\lambda$ ), except for  $t_1$  in (2-14), which may be estimated by the mean diffusive time. Parameters predicted by one model (such as the tt-fADE) may also help to improve the estimated parameters of the other (i.e., the CTRW framework).

## 2.4 Applications: Capturing non-Fickian transport in multidimensional porous media

Here I apply the above time nonlocal transport models to capture non-Fickian transport observed in multidimensional, heterogeneous porous media. Well-controlled laboratory experiments of sand column transport were conducted, to provide data to evaluate the three nonlocal transport models reviewed above. I used a cylindrical organic glass tube filled with non-uniform “lightweight expanded clay aggregate” (Leca) beads to monitor solute transport in

saturated porous media. Leca beads were selected since they contain high intra-granular porosity, which can lead to retention for solution transport likely occurring in the field. The length of the Leca column was 100 cm with an internal diameter of 4 cm. The experimental apparatus was composed of water flumes, a model body, piezometer tubes, and a detection device (Fig. 2-1). The diameter of the Leca beads varied from 1.0 to 2.0 mm. A pulse of Brilliant Blue FCF (BBF), which is a conservative organic compound typically used as colorant for foods, with the volume of 5 mL was injected into the column (from the bottom of the glass tube set vertically) at a concentration of 0.1 g/L, representing an instantaneous point source. An ultraviolet visible light spectrophotometer was used to measure the absorbance of solute, and the absorbance was then converted to concentration. Continuous sampling provided tracer BTCs used to check the applicability of the nonlocal transport models.

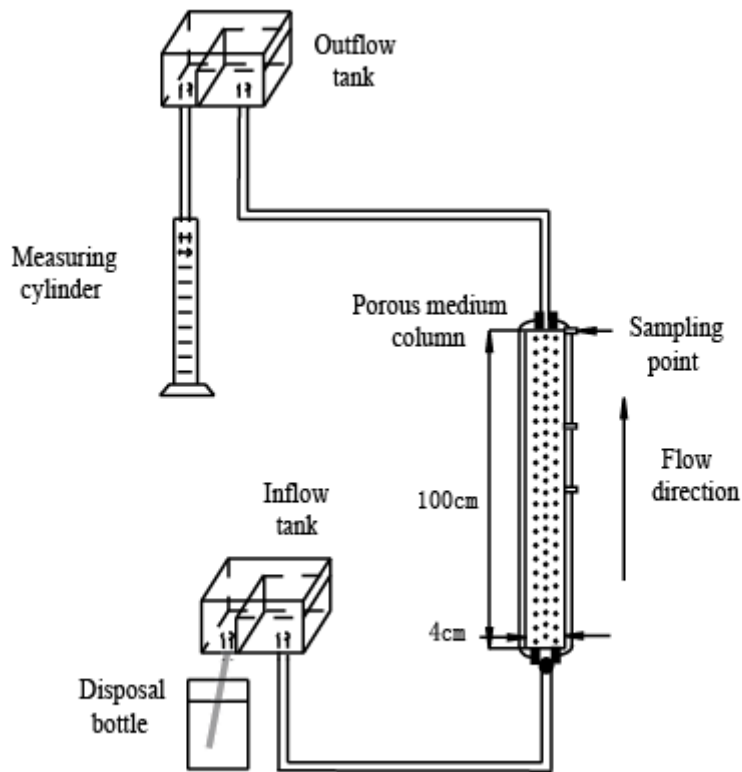


Figure 2-1. Experimental setup.

Six flow rates (increasing from 0.4, 0.6, 0.8, 1.0, 1.2, to 1.4 mL/s; see Table 2-1) were carried out in the experiment. For each flow rate, three experimental runs were conducted where the BBF BTCs were collected at three sections of the sand column, varying from 50, 70, to 100 cm. During each run with the similar flow rate, the hydraulic gradient between the inlet and outlet was kept constant in time, and therefore the flow velocity for the three experimental runs should be close to each other.

Experiment	$Q$ (mL/s)	$L$ (cm)	$v^*$ (mm/s)	$D^*$ (mm <sup>2</sup> /s)	$\theta$	$RMSE$
	Measured	Measured	Fitted	Fitted	Measured	Calculated
Lab	0.4	50	1.2	5	0.391	2.746
		70	1.12	7	0.391	1.518
		100	1.066	5.3	0.391	2.3
	0.6	50	1.449	6.8	0.391	2.159
		70	1.55	15	0.391	0.776
		100	1.63	9.2	0.391	1.995
	0.8	50	2.23	15.5	0.391	1.57
		70	2.2	22	0.391	0.974
		100	2.07	14	0.391	1.546
	1	50	2.67	20	0.391	1.851
		70	2.85	24	0.391	1.426
		100	2.9	16	0.391	2.923
	1.2	50	3.25	23	0.391	2.796
		70	3.22	28	0.391	1.533
		100	3.04	19	0.391	2.397
	1.4	50	3.48	40	0.391	1.088
		70	3.85	50	0.391	0.902
		100	3.7	38	0.391	1.328
Field	83.33	200	0.003	0.694	0.3	n/a
		400	0.004	0.984	0.3	n/a
		600	0.004	0.926	0.3	n/a

Table 2-1. Measured and fitted parameters (using the ADE model with equilibrium sorption) for BBF transport through the Leca beads at different flow rates and travel distances and field tests. In the legend,  $Q$  represents the flow rate;  $L$  denotes the travel distance (i.e., the length of the column);  $v^*$  ( $=v/R$ ) is the average flow velocity divided by the retardation coefficient;  $D^*$  ( $=D/R$ ) is the dispersion coefficient divided by the retardation coefficient;  $\theta$  is the porosity; and  $RMSE$  stands for root mean square error between observed values and predicted values.

The measured BTCs all exhibit late-time tailing behavior (see Fig. 2-2 and Figs. 2-S1 - 2-5), which is one of the major characteristics of non-Fickian transport.

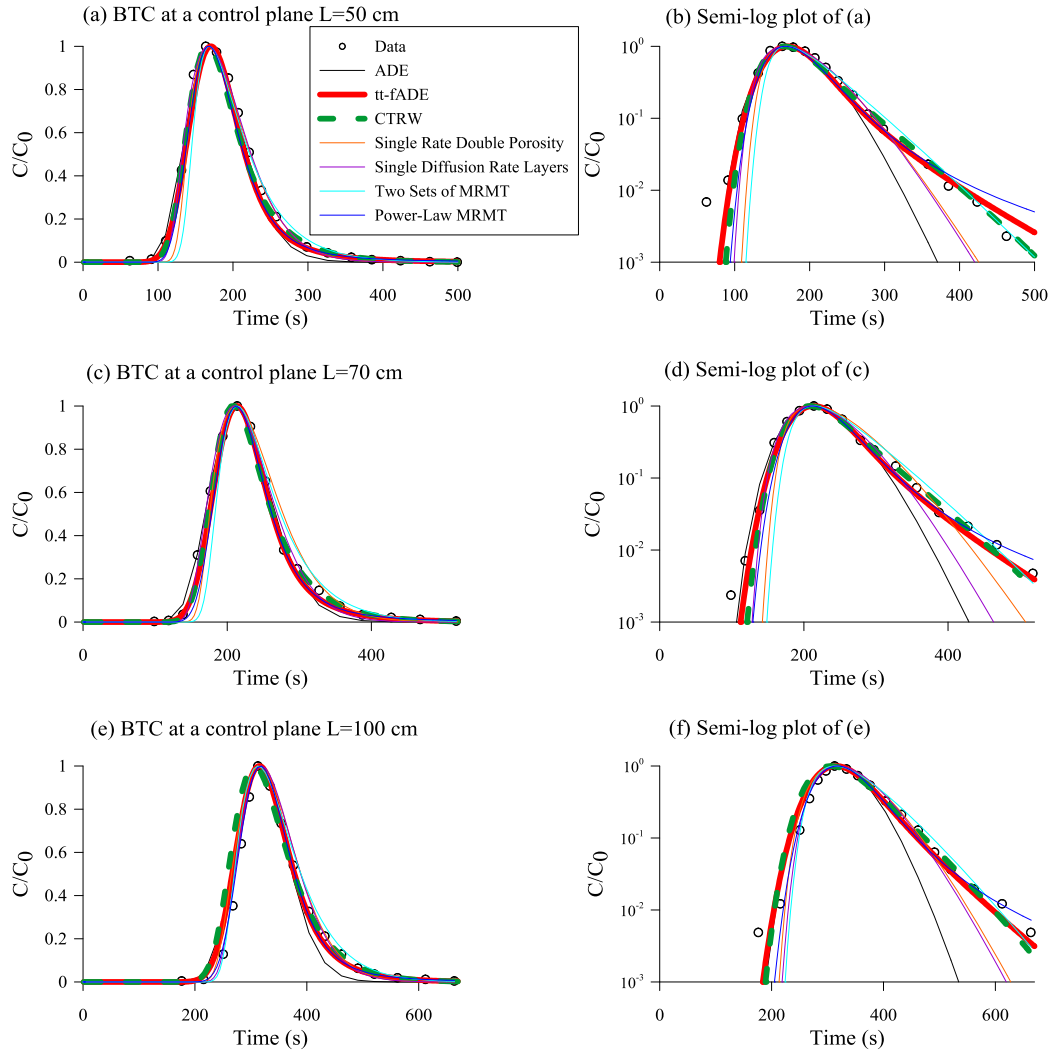


Figure 2-2. Laboratory tracer test: Comparison between the measured (symbols) and the modeled (lines) breakthrough curves using the ADE, the tt-fADE (red thick lines), the CTRW (green dashed lines), and the MRMT model with the water flow rate  $Q = 1.4$  mL/s.

## 2.5 Model fit and comparison

Comparisons of the measured and best-fit BTCs using the above three time-nonlocal transport models and the classical ADE are shown in Fig. 2-2 and Figs. 2-S6 - 2-10. In this section, I briefly introduce the model fitting process, and then compare the model results.

### 2.5.1 The ADE model with equilibrium sorption

For comparison, I first use the classic ADE with equilibrium sorption to quantify the measured BTCs. The governing equation for one-dimensional chemical transport in groundwater with advection, dispersion, and retardation is (van Genuchten and Alves, 1982):

$$R \frac{\partial C}{\partial t} = D \frac{\partial^2 C}{\partial x^2} - v \frac{\partial C}{\partial x} \quad , \quad (2-25)$$

which has the following solution with an instantaneous point source at the origin:

$$C(x,t) = \frac{M}{2A\sqrt{\pi D^* t}} \exp\left[-\frac{(x-v^* t)^2}{4D^* t}\right] \quad , \quad (2-26)$$

where  $M$  [M] represents the initial mass injected into the column;  $A$  [ $L^2$ ] is the cross-section area; and  $R$  [dimensionless] is the retardation coefficient. From a mathematical perspective,  $R$  acts as a rescaling factor in time. Hence, I reduce the three parameters  $v$ ,  $D$ , and  $R$  in the ADE model to two parameters  $v^*$  ( $=v/R$ ) and  $D^*$  ( $=D/R$ ). The best fit values for parameters  $v^*$  and  $D^*$  are listed in Table 2-1. These two parameters were calibrated manually based on visual inspection.

In my Leca-column transport experiments, the relatively large flow velocity led to a large Peclet number ( $P_e \gg 1$ ) and the dispersion coefficient  $D$  relates to  $v$  via  $D = \alpha v$ , where  $\alpha$  [ $L$ ] denotes the dispersivity. The relationship between dispersivity  $\alpha$  and the travel distance in the laboratory experiments is shown in Fig. 2-3. For a fixed flow rate,  $\alpha$  fluctuates with the travel distance without any fixed trend, due likely to the relatively short travel distance and the fast flow rate, where solute dispersion cannot stabilize.

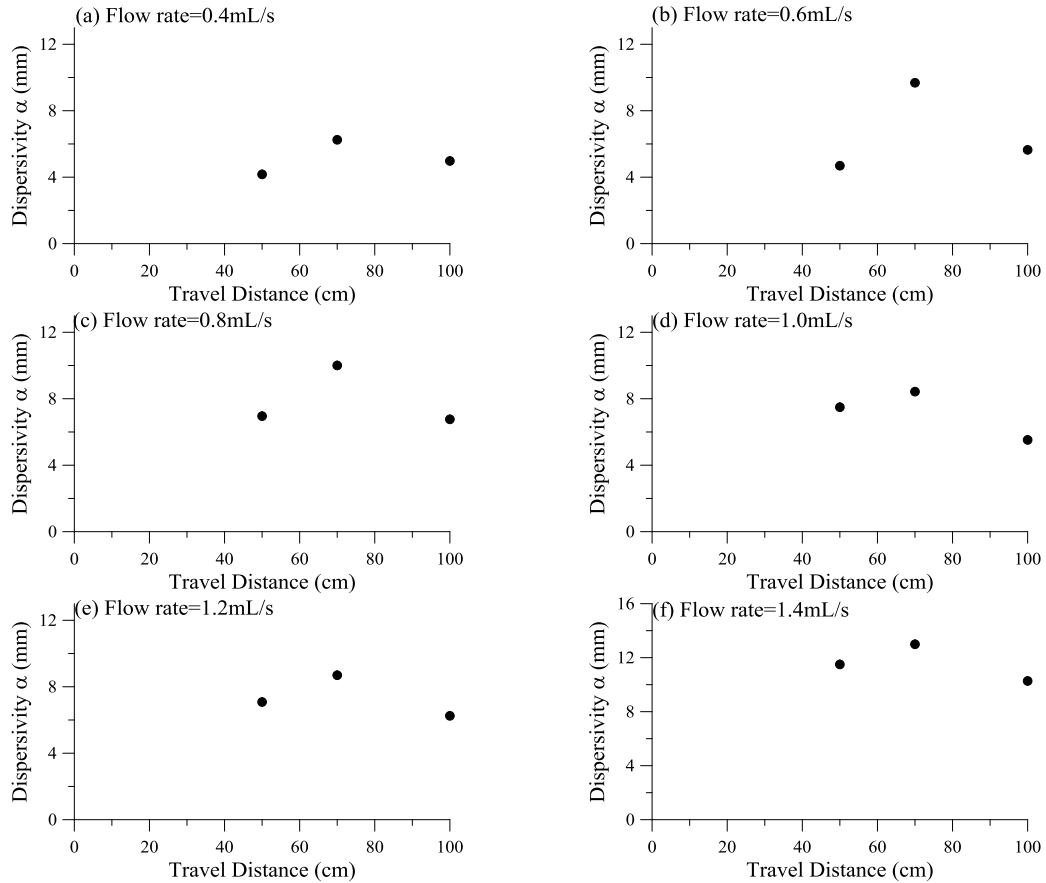


Figure 2-3. The best-fit dispersivity in the ADE model (2-25) versus the travel distance.

The relationship between dispersivity and flow rate in the laboratory experiments is shown in Fig. 2-4. Although the best-fit dispersivity fluctuates with the flow rate, it generally increases with an increasing flow velocity. A larger flow velocity causes a wider spatial distribution of contaminant plume, requiring a larger dispersivity in the ADE model, which was well-known and used here to double check whether the ADE model is used correctly.

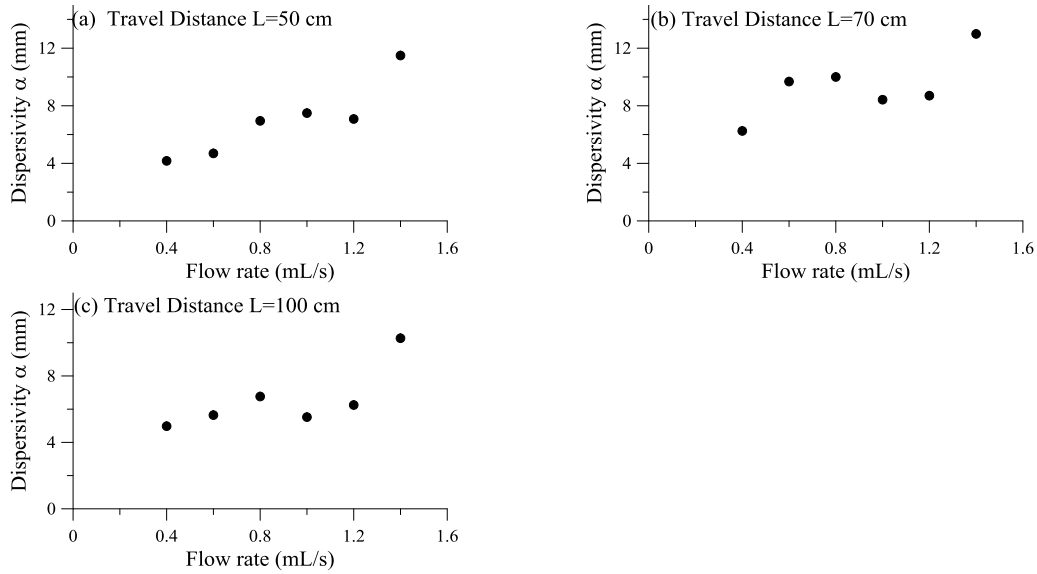


Figure 2-4. The best-fit dispersivity in the ADE model versus the water flow rate.

In the BTCs measured at three travel distances with six different flow rates in the laboratory experiments and field tracer tests (Figs. 2-2, 2-9), the ADE model (2-25) captures the rapid increase of early-time BTCs, but overestimates the decline of the late-time BTC tails although the delay of transport due to retardation was considered in the ADE (2-25). This implies that the delayed transport observed in my laboratory experiments and field tests is more complex than equilibrium adsorption described in (2-25), where the sorbed or immobile concentration is a simple linear function of the dissolved concentration.

### 2.5.2 The MRMT model

The MRMT model (2-1) has various specific forms, which might be useful for applications and therefore require further evaluation. For example, the immobile domain can be characterized as multiple layers with a distribution of diffusion rate coefficients or first-order mass-transfer rates, or be simplified as a layer with a single diffusion rate which can be attractive in applications due to its simplicity in manipulation. There is, however, no solid physical justification for the selection of any of these forms, given simply the limited information for a

sand column like the one used in my laboratory. For systematic analyses of all potential mass transfer models, I selected the following four MRMT subsets with different mass-transfer formulations:

1) MRMT model 1 (single mass-transfer rate): the immobile zones can be simplified by a single first-order mass-transfer rate (which is also the single-rate double-porosity model);

2) MRMT model 2 (single diffusion rate): the immobile zones have a single diffusion rate for all layers;

3) MRMT model 3 (two mass-transfer rates): the immobile zones have two sets of rate coefficients;

4) MRMT model 4 (multiple mass-transfer rates): the immobile zones have a power-law distribution of (first-order mass-transfer) rate coefficients.

I use the STAMMT-L version 3.0 code (Haggerty, 2009) to solve the above four MRMT models. Best-fit results, which were calibrated manually, are shown in Figs. 2-2, 2-9 and Figs. 2-S6 - 2-10 and discussed below.

### 2.5.2.1 MRMT model 1 with a single mass-transfer rate

The general mobile-immobile (MIM) model with diffusion in the immobile zone can be written as (Haggerty and Gorelick, 1995):

$$\frac{\partial C_{m,t}}{\partial t} + T(x,t) = -v \nabla C_{m,t} + D \nabla^2 C_{m,t}, \quad (2-27a)$$

$$\frac{\partial C_{im,t}}{\partial t} = \frac{D_a}{r^{n-1}} \nabla \left[ r^{n-1} \nabla C_{im,t} \right], \quad (2-27b)$$

where  $T(x,t)$  [ $ML^{-3}T^{-1}$ ] is a transient term accounting for rate-limited mass transfer between the mobile and immobile domains, and  $D_a$  is the apparent diffusion coefficient (equals to the

effective pore diffusion divided by the immobile zone retardation factor). Here  $n$  denotes the dimensionality of the problem, and  $n = 1, 2, 3$  denotes diffusion into layers, cylinders, and spheres, respectively. For a single rate first-order mass-transfer approximation,  $T(x,t)$  can be expressed as (Haggerty, 2009):

$$T(x,t) = \beta \frac{\partial C_{im,t}}{\partial t}, \quad (2-28a)$$

$$\frac{\partial C_{im,t}}{\partial t} = \alpha [C_{m,t} - C_{im,t}], \quad (2-28b)$$

which is the single rate version of the MRMT model (2-1).

The best-fit parameters using the single-rate MIM model (2-27)-(2-28) are listed in Table 2-2. The fitting exercise showed the sensitivity of model parameters to the travel distance and water flow rate in the laboratory experiments. First, the dispersivity  $\alpha$  does not change with the travel distance (Table 2-2), since the plume expansion with time is captured by the mass transfer term in the model. This is different from the standard ADE model, where the dispersivity must increase with the travel distance to capture scale-dependent dispersion.

Experiment	$Q$ (mL/s)	$L$ (cm)	$\alpha_L$ (mm)	$v$ (mm/s)	$\beta_{tot}$	$\alpha$ (s <sup>-1</sup> )
	Measured	Measured	Fitted	Fitted	Fitted	Fitted
Lab	0.4	50	1.5	1.4	0.5	0.05
		70	1.5	1.35	0.5	0.04
		100	1.5	1.35	0.5	0.04
	0.6	50	1.5	1.68	0.5	0.05
		70	1.5	1.71	0.4	0.04
		100	1.5	1.68	0.31	0.03
	0.8	50	1.5	2.38	0.45	0.06
		70	1.5	2.32	0.4	0.04
		100	1.5	2.15	0.33	0.05
	1	50	1.5	2.75	0.45	0.06
		70	1.5	2.93	0.43	0.06
		100	1.5	2.93	0.35	0.07
	1.2	50	1.5	3.15	0.3	0.06
		70	1.5	3.15	0.3	0.06
		100	1.5	3.13	0.28	0.06
	1.4	50	1.5	3.52	0.35	0.06
		70	1.5	3.95	0.35	0.06
		100	1.5	3.98	0.35	0.06
Field	83.33	200	210	0.004	0.5	0.135
		400	230	0.004	0.5	0.1
		600	230	0.004	0.5	0.03

Table 2-2. The fitted parameters for the single mass-transfer rate mobile-immobile model (i.e., equations (2-27), (2-28)) at different flow rates and travel distances. In the legend,  $L$  denotes the travel distance (i.e., the length of the column);  $\alpha_L$  is the dispersivity;  $v$  is the flow velocity;  $\beta_{tot}$  is the total capacity coefficient; and  $\alpha$  stands for the mass transfer rate.

Second, the average velocity used in the model is slightly larger than the measured BTC peak velocity and the ADE velocity (note that the ADE velocity is also larger than the real BTC peak velocity), probably due to the assumption that there might be an immobile domain interacting with the mobile domain. The parameter  $v$  (or  $D$ ) in the MRMT and ADE models has different meanings and hence may not have the same value. Parameters  $v$  and  $D$  in the MRMT model refer to the mobile domain (Fiori et al. 2015), and therefore the velocity in the MRMT model is generally larger than the ADE velocity, while the opposite is expected for the dispersion coefficient  $D$ . This holds true for all the MRMT formulations.

Third, the capacity coefficient  $\beta$  either remains constant or decreases very slightly with the travel distance, implying that the medium heterogeneity might not significantly change with the medium's length.

Fourth, the rate coefficient  $\alpha$  increases slightly and the capacity coefficient  $\beta$  decreases slightly with an increasing flow rate at each control plane. This subtle change is likely due to the assumption that the faster water flows correspond to less volumetric proportion of immobile domains. A faster flow may decompose immobile domains and enhance the mass exchange between mobile and immobile domains, resulting in a larger mass exchange rate  $\alpha$ .

#### 2.5.2.2 MRMT model 2 with a single diffusion rate

The layered diffusion model is a specific case of the MRMT model (Haggerty and Gorelick, 1995) with the following rate and capacity coefficients:

$$\alpha_j = \frac{(2j-1)^2 \pi^2 D_a}{4 a^2}, \quad j = 1, 2, \dots, N_{im}, \quad (2-29a)$$

$$\beta_j = \frac{8}{(2j-1)^2 \pi^2} \beta, \quad j = 1, 2, \dots, N_{im}, \quad (2-29b)$$

The best-fit parameters for model (2-29) are listed in Table 2-3. There is no apparent correlation between the mass transfer rate and the travel distance or water flow velocity. The same conclusion is found for the capacity coefficient.

Experiment	$Q$ (mL/s)	$L$ (cm)	$\alpha_L$ (mm)	$v$ (mm/s)	$\beta_{tot}$	$\alpha_d$ (s <sup>-1</sup> )
	Measured	Measured	Fitted	Fitted	Fitted	Fitted
Lab	0.4	50	1.5	1.55	0.6	0.02
		70	1.5	1.48	0.6	0.02
		100	1.5	1.43	0.6	0.02
	0.6	50	1.5	1.73	0.5	0.03
		70	1.5	2.22	0.8	0.02
		100	1.5	2.12	0.61	0.02
	0.8	50	1.5	2.69	0.61	0.03
		70	1.5	2.85	0.7	0.02
		100	1.5	2.55	0.55	0.03
	1	50	1.5	3	0.55	0.03
		70	1.5	3.3	0.55	0.02
		100	1.5	3.25	0.48	0.05
	1.2	50	1.5	3.73	0.48	0.04
		70	1.5	3.69	0.48	0.03
		100	1.5	3.25	0.31	0.03
1.4	50	1.5	4.25	0.6	0.03	
	70	1.5	4.9	0.6	0.03	
	100	1.5	4.1	0.4	0.02	
Field	83.33	200	210	0.004	0.5	0.05
		400	210	0.004	0.5	0.04
		600	210	0.005	0.5	0.03

Table 2-3. The fitted parameters for the single diffusion rate MRMT model at different flow rates and travel distances. In the legend,  $\alpha_d$  is the diffusion rate coefficient ( $\alpha_d = D_d/a^2$ , where  $D_d$  is the apparent diffusion coefficient and  $a$  is the layer half-thickness).

### 2.5.2.3 MRMT model 3 with two mass-exchange rates

MRMT model 3 contains two pairs of coefficients: two rate coefficients ( $\alpha_1$  and  $\alpha_2$ ) and two capacity coefficients ( $\beta_1$  and  $\beta_2$ ) corresponding to the first and the second immobile domains, respectively. The best-fit parameters are listed in Table 2-4. The dispersivity  $\alpha_L$  remains constant, since solute plume expansion (due likely to solute retention) is mainly captured by mass exchange between mobile and the two immobile zones. Or in other words, the two pairs of parameters,  $\alpha_j$  ( $j=1, 2$ ) and  $\beta_j$  ( $j=1, 2$ ), control the mass exchange. Their values fluctuate (without predictable trends) with the travel distance and flow rate in the laboratory experiments, although  $\alpha_2$  decreases with increasing  $\alpha_1$  for the same flow rate. There is no efficient way to directly measure the rate coefficient or capacity coefficient, which creates a challenge for the

application of the MRMT model with multiple pairs of rate and capacity coefficients for more complicated problems in more heterogeneous media.

Experiment	$Q$ (mL/s)	$L$ (cm)	$\alpha_L$ (mm)	$v$ (mm/s)	$\alpha_1$ (s <sup>-1</sup> )	$\beta_1$	$\alpha_2$ (s <sup>-1</sup> )	$\beta_2$
	Measured	Measured	Fitted	Fitted	Fitted	Fitted	Fitted	Fitted
Lab	0.4	50	1.5	1.12	0.08	0.08	0.015	0.15
		70	1.5	1.1	0.08	0.09	0.015	0.15
		100	1.5	1.025	0.1	0.09	0.008	0.1
	0.6	50	1.5	1.31	0.08	0.07	0.02	0.13
		70	1.5	1.54	0.15	0.08	0.02	0.25
		100	1.5	1.55	0.15	0.08	0.015	0.15
	0.8	50	1.5	1.96	0.05	0.15	0.03	0.08
		70	1.5	2.08	0.05	0.2	0.015	0.1
		100	1.5	1.88	0.065	0.1	0.018	0.1
	1	50	1.5	2.3	0.05	0.12	0.03	0.15
		70	1.5	2.5	0.07	0.13	0.025	0.13
		100	1.5	2.57	0.2	0.11	0.02	0.11
	1.2	50	1.5	2.85	0.07	0.12	0.02	0.13
		70	1.5	2.87	0.06	0.11	0.027	0.13
		100	1.5	2.87	0.07	0.1	0.025	0.011
	1.4	50	1.5	3.33	0.08	0.17	0.03	0.17
		70	1.5	3.8	0.09	0.17	0.03	0.17
		100	1.5	3.75	0.08	0.15	0.03	0.16
Field	83.33	200	210	0.004	0.4	0.2	0.1	0.2
		400	210	0.004	0.4	0.2	0.1	0.2
		600	210	0.004	0.4	0.1	0.1	0.1

Table 2-4. The fitted parameters for the two-set MRMT model at different flow rates and travel distances. In the legend,  $\alpha_1$  and  $\beta_1$  represent the mass transfer rate and capacity coefficient of the first immobile domain, respectively; and  $\alpha_2$  and  $\beta_2$  are the mass transfer rate and capacity coefficient of the second immobile domain, respectively.

#### 2.5.2.4 MRMT model 4 with power-law distributed rate coefficients

The density of rate coefficient for MRMT model 4 can be defined as (Haggerty et al., 2000):

$$b(\alpha) = b(\alpha_{\min}, \alpha_{\max}, k) = \begin{cases} \beta_{\text{tot}} \frac{(k-2)\alpha^{k-3}}{\alpha_{\max}^{k-2} - \alpha_{\min}^{k-2}} & k \neq 2 \\ \beta_{\text{tot}} \frac{1}{\ln(\alpha_{\max}/\alpha_{\min})\alpha} & k = 2 \end{cases}, \text{ for } \alpha_{\min} \leq \alpha \leq \alpha_{\max} \quad (2-30)$$

where  $\alpha_{\min}$  [ $T^{-1}$ ] denotes the minimum rate coefficient,  $\alpha_{\max}$  [ $T^{-1}$ ] is the upper bound of the rate coefficient, and  $k$  is the exponent.

In the fitting parameters shown in Table 2-5, the dispersivity  $\alpha_L$  remains stable for the same reason mentioned above for the other MRMT models. Flow velocity used in this model can be approximated by the peak velocity for the measured BTC. The total capacity coefficient ( $\beta_{tot}$ ) does not significantly change with the travel distance. The exponent  $k$  controls the slope of the late-time BTC in a log-log plot, and hence a larger  $k$  denotes faster decline of the late-time BTC. The best-fit  $k$  slightly increases with an increasing flow rate, due likely to the relatively faster decline of the late-time solute concentration under a larger water flow rate.

Experiment	$Q$ (mL/s)	$L$ (cm)	$\alpha_L$ (mm)	$v$ (mm/s)	$\beta_{tot}$	$k$	$\alpha_{min}$ (s <sup>-1</sup> )	$\alpha_{max}$ (s <sup>-1</sup> )	
	Measured	Measured	Fitted	Fitted	Fitted	Fitted	Fitted	Fitted	
Lab	0.4	50	1.6	1.4	0.5	2.25	0.01	0.6	
		70	1.6	1.35	0.5	2.25	0.01	0.6	
		100	1.6	1.35	0.5	2.25	0.01	0.6	
	0.6	50	1.6	1.69	0.5	2.292	0.011	0.6	
		70	1.6	1.85	0.6	2.292	0.012	0.6	
		100	1.6	2.1	0.6	2.292	0.012	0.6	
	0.8	50	1.6	2.83	0.7	2.29	0.013	0.6	
		70	1.6	2.95	0.8	2.29	0.012	0.6	
		100	1.6	3.05	0.8	2.29	0.013	0.6	
	1	50	1.6	3.59	0.8	2.3	0.013	0.6	
		70	1.6	4.05	0.85	2.3	0.013	0.6	
		100	1.6	4.16	0.8	2.3	0.014	0.6	
	1.2	50	1.6	4.63	0.8	2.335	0.014	0.6	
		70	1.6	4.63	0.8	2.335	0.014	0.6	
		100	1.6	4.44	0.75	2.335	0.014	0.6	
	1.4	50	1.6	4.95	0.85	2.358	0.014	0.6	
		70	1.6	5.48	0.8	2.358	0.015	0.6	
		100	1.6	5.5	0.8	2.358	0.015	0.6	
	Field	83.33	200	210	0.004	0.5	2.25	0.01	0.6
			400	210	0.004	0.5	2.25	0.01	0.6
			600	210	0.005	0.5	2.25	0.01	0.6

Table 2-5. The best-fit parameters for the power-law MRMT model 4 at different flow rates and travel distances. In the legend,  $k$  stands for the slope of the late-time tail, and  $\alpha_{min}$  and  $\alpha_{max}$  stand for the lower and upper boundary of the mass transfer rates, respectively.

It is also noteworthy that, on one hand, the minimum mass transfer rate ( $\alpha_{min}$ ) in (2-30) controls the maximum waiting time for solute particles, which is functionally equivalent to the inverse of the cutoff time scale  $t_2$  in the CTRW framework and the truncation parameter  $\lambda$  in the

tt-fADE model. In general,  $\alpha_{\min}$  increases with an increasing flow rate (Table 2-5). A relatively fast flow may accelerate the mass exchange between mobile and immobile domains, and generate a shorter mean residence time for solute particles in the immobile domain, leading to a larger mass transfer rate. On the other hand, the maximum mass transfer rate ( $\alpha_{\max}$ ) in (2-30) defines the shortest waiting time (for solute particles between two displacements), whose impact on the late-time transport dynamics can be overwhelmed by the other smaller rates. Numerical results also show that  $\alpha_{\max}$  apparently does not change with the travel distance and flow rate. Hence,  $\alpha_{\max}$  can be kept constant for all cases (Table 2-5).

As shown in Figs. 2-2, 2-9 and Figs. 2-S6 - 2-10, the MRMT model 4 captures the BTC late-time tail much better than the other mass-transfer formations with fewer rate coefficients. However, compared with the tt-fADE model, the simulated tail of the MRMT model 4 tends to be slightly heavier at the end of the modeling time. In other words, it slightly underestimates the mass transfer rate at the late time. Note that the memory function in the tt-fADE is not exactly the same as that in the MRMT model 4. The tt-fADE has exponentially-truncated power-law rate coefficients, while the MRMT model 4 simply deletes any rate coefficient larger than  $\alpha_{\max}$  and smaller than  $\alpha_{\min}$ . This subtle difference in memory functions between the tt-fADE and MRMT model 4 might be the reason for the difference observed here. In addition, the MRMT model 4 (with six model parameters) requires one more parameter than the tt-fADE model.

As shown in Figs. 2-2, 2-9 and Figs. 2-S6 - 2-10, both the MRMT model 1 and model 2 can capture most characteristics of the observed BTCs, except for the late-time tailing. Therefore, I need more than one mass-transfer rate to fit the solute transport in the one-dimensional heterogeneous sand column and field tracer tests. Increasing the number of

immobile domains improves the model's performance at late times, but more immobile domains complicate the model application.

### 2.5.3 The tt-fADE model (2-8)

The failure of the standard ADE model and the SRMT model in capturing the late-time BTC tailing motivates the application of the other time non-local transport models such as the tt-fADE model (2-8). A numerical solver of (2-8) can be found in Zhang et al. (2015). The best-fit results using this model are shown in Figs. 2-2, 2-9 and Figs. 2-S1 - 2-5, where both the peak and the late time tailing can be captured simultaneously.

The best-fit parameters are shown in Table 2-6, where the best-fit velocity  $v$  is slightly larger than the measured peak velocity  $v_{peak}$ , due to the fractional-order capacity coefficient  $\beta$  in the left-hand side of the tt-fADE equation (2-8) when  $\gamma \rightarrow 1$ :

$$v = (1 + \beta) v_{peak} \quad . \quad (2-31)$$

Experiment	$Q$ (mL/s)	$L$ (cm)	$v$ (mm/s)	$D$ (mm <sup>2</sup> /s)	$\alpha$ (mm)	$\gamma$	$\beta$ (s <sup><math>\gamma</math>-1</sup> )	$\lambda$ (s <sup>-1</sup> )	$RMSE$
	Measured	Measured	Fitted	Fitted	$\alpha = D / v$	Fitted	Fitted	Fitted	Calculated
Lab	0.4	50	1.1	0.2	0.18	0.25	0.011	0.01	0.379
		70	1.05	0.2	0.19	0.25	0.011	0.01	0.171
		100	1	0.2	0.2	0.25	0.011	0.01	0.343
	0.6	50	1.3	0.2	0.15	0.292	0.013	0.011	0.461
		70	1.4	0.4	0.29	0.292	0.013	0.012	0.296
		100	1.49	0.4	0.27	0.292	0.013	0.012	0.489
	0.8	50	1.91	0.5	0.26	0.29	0.018	0.013	0.577
		70	1.95	0.6	0.31	0.29	0.018	0.012	0.398
		100	1.84	0.6	0.33	0.29	0.018	0.013	0.443
	1	50	2.25	1.8	0.8	0.3	0.014	0.013	0.529
		70	2.4	1.8	0.75	0.3	0.014	0.013	0.218
		100	2.4	1.8	0.75	0.3	0.014	0.014	0.326
	1.2	50	2.86	1	0.35	0.335	0.019	0.014	0.405
		70	2.84	1	0.35	0.335	0.019	0.014	0.19
		100	2.81	1	0.36	0.335	0.019	0.014	0.26
	1.4	50	3.18	3	0.94	0.358	0.026	0.014	0.636
		70	3.55	3	0.85	0.358	0.026	0.015	0.38
		100	3.45	3	0.87	0.358	0.026	0.015	0.329
Field	83.33	200	0.004	0.69	198	0.358	0.17	0.01	n/a
		400	0.005	0.69	148	0.358	0.17	0.01	n/a
		600	0.005	0.69	148	0.358	0.17	0.01	n/a

Table 2-6. The best-fit parameters for the tt-fADE model (2-8) at different flow rates and travel distances. In the legend,  $\alpha$  is the dispersivity;  $\gamma$  is the time/scale index;  $\beta$  is the fractional-order capacity coefficient; and  $\lambda$  is the truncation parameter.

Figs. 2-5 - 2-6 show the best fit parameters versus the flow rate and travel distance in the laboratory experiments. The best-fit dispersivity  $\alpha$  does not change significantly with the travel distance (Fig. 2-5), which is different from the scale-dependent dispersion observed by other studies (Pickens and Grisak, 1981).

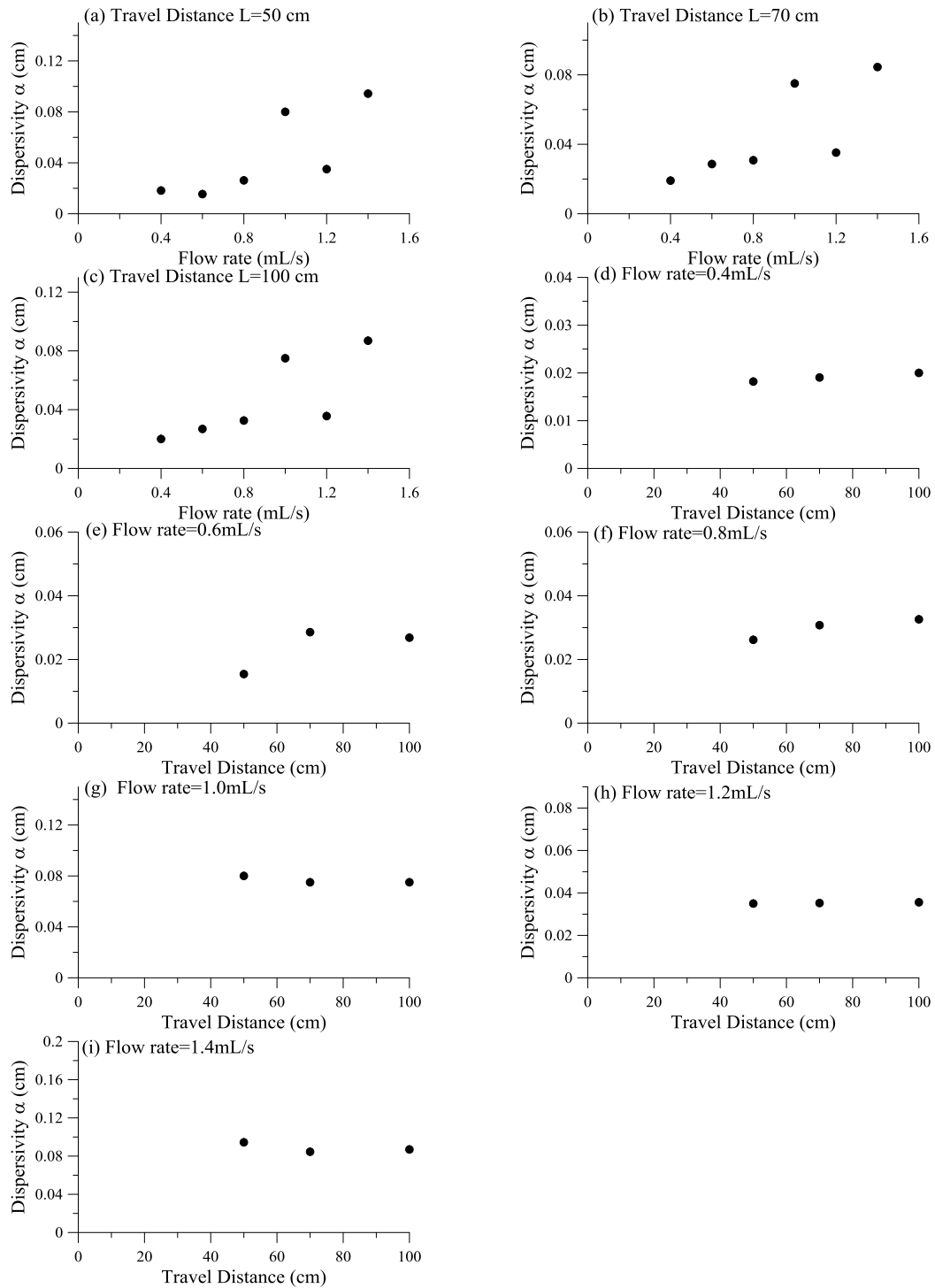


Figure 2-5. Dispersivity in the tt-fADE model changes with the travel distance and flow rate.

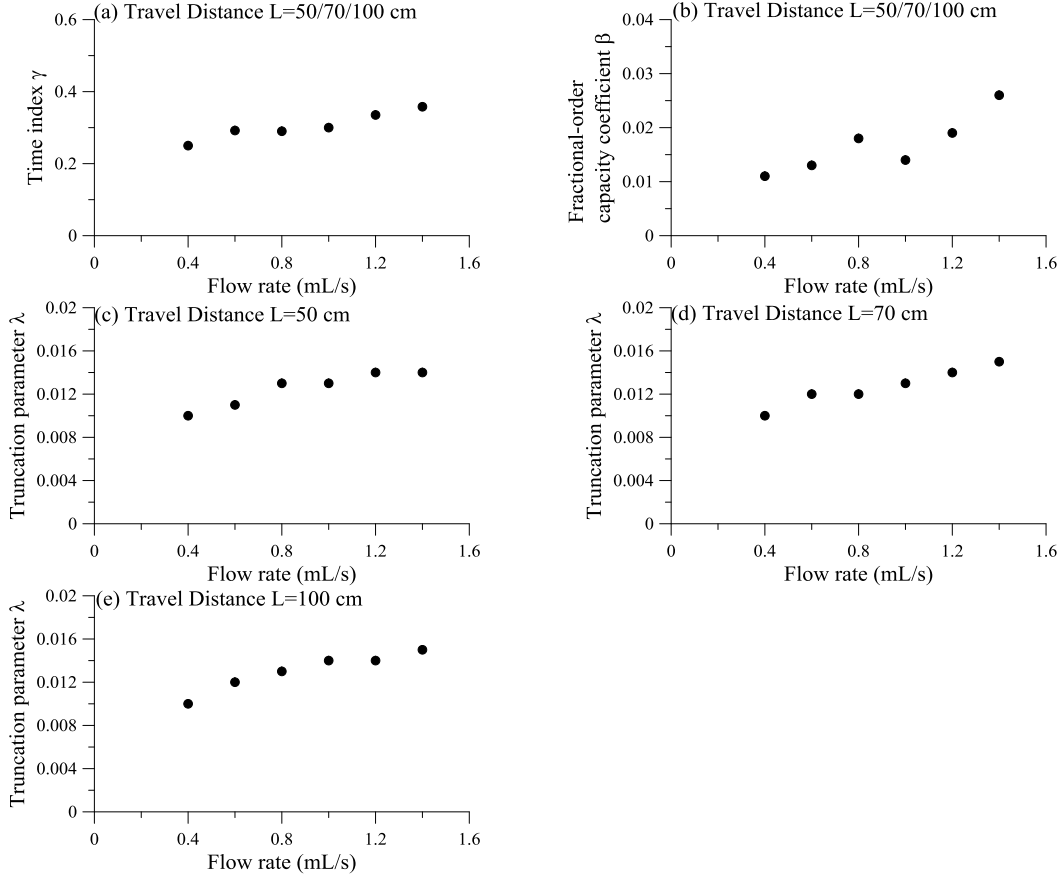


Figure 2-6. The tt-fADE model parameters change with the travel distance and flow rate.

This discrepancy might be due to the following reasons: 1) the travel distance is too short to observe any stable trend of dispersion (tracer injection at the inlet may cause a boundary effect on transport and random deviation from the local mean velocity), and 2) the system is advection dominated (as a typical laboratory sand-column transport experiment) and therefore the estimates of  $D$  might be too uncertain to clearly show a subtle trend. In addition, the best-fit dispersivity increases with an increasing flow rate. The faster the water flows, the wider the plume becomes, requiring a larger dispersivity. This is consistent with the fitting results of the other models mentioned above.

The other model parameters, including the time index  $\gamma$ , capacity coefficient  $\beta$ , and the truncation parameter  $\lambda$ , vary with the flow rate (Fig. 2-6). First, the time index  $\gamma$  increases with

an increasing flow rate, since a larger  $\gamma$  represents a shorter mean residence time for solute particles in the immobile domain (here I assume that the mean residence time in the immobile domain decreases with an increasing flow velocity). Second, the capacity coefficient  $\beta$  also increases with the flow rate, showing that the variation of the time index might overshadow the variation of the capacity coefficient. Third, the truncation parameter  $\lambda$  increases with the flow rate, implying that the non-Fickian transport converges to its Fickian asymptote more quickly if the flow rate is larger. This trend might be due to the decreased immobile portion with a higher flow rate in the short sand column. In addition, the truncation parameter  $\lambda$  is relatively small, in order to capture the relatively heavy late-time tails.

The above three parameters ( $\gamma$ ,  $\beta$ , and  $\lambda$ ), however, generally remain constant at different travel distances if the flow rate remains unchanged (Table 2-6). The packing procedure for the sand column was designed to yield a macroscopically homogeneous texture, and, indeed, the results imply that the statistics of medium properties (such as the sand size distribution, specific surface area, effective porosity, and/or internal structure) are spatially uniform. For example, a uniform fractional capacity coefficient  $\beta$  suggests that the ratio of mobile to immobile volume is constant in space. This phenomenon holds true for the field tracer tests. The spatial uniformity of these parameters simplifies the fitting procedure. For each flow rate with different sample distances, the time index and the capacity coefficient can be calibrated a single time for one sampling distance, and then kept constant for the other sampling distances.

Therefore, when using the tt-fADE model (2-8), I only need to fit three parameters: velocity, dispersion coefficient, and truncation parameter. Fitting is further simplified by using the observed BTC peak velocity as a lower bound when predicting the velocity in the tt-fADE model.

#### 2.5.4 The CTRW model

For comparison purposes, I use the CTRW model (2-14) to fit the BTCs. The best-fit results using this model are shown in Figs. 2-2, 2-9 and Figs. 2-S1 - 2-5, where both the peak and the late time tailing can be captured simultaneously. I used the CTRW MATLAB Toolbox Version 3.1 developed by Cortis and Berkowitz (2005). The CTRW framework with the truncated power-law transition time  $\phi(t)$  (2-18) was used, as suggested by Berkowitz et al. (2006), since it can efficiently capture the transition from non-Fickian to Fickian transport (Dentz et al., 2004).

This popular CTRW model contains five unknown parameters, which are  $\zeta$ ,  $t_1$ ,  $t_2$ ,  $v_\psi$  and  $D_\psi$ . The time  $t_1$  expressed by formula (2-17) represents the approximated mean transition time. The power law behavior in the BTC begins from  $t_1$  and ends at  $t_2$ . Knowledge of parameters gained in the fitting exercise of the tt-fADE model in Section 2.5.3 improves the predictability of the CTRW model. In particular, I set the power-law exponent  $\zeta$  in the CTRW model equal to the time index  $\gamma$  in the tt-fADE model (2-8), and approximate the cutoff time scale  $t_2$  in the CTRW framework using the inverse of the truncation parameter  $\lambda$  in the tt-fADE. Here a smaller  $\zeta$  represents more disorder of the host system. The remaining three parameters, including the velocity  $v_\psi$ , the dispersion coefficient  $D_\psi$ , and the mean waiting time  $t_1$  in (2-14), can be fitted using the observed BTCs. The best-fit parameters using the CTRW model are listed in Table 2-7.

Experiment	$Q$ (mL/s)	$L$ (cm)	$v_\psi$ (mm/s)	$D_\psi$ (mm <sup>2</sup> /s)	$\zeta$	$\log_{10}t_1$ (s)	$\log_{10}t_2$ (s)	$RMSE$
	Measured	Measured	Fitted	Fitted	Fixed	Fitted	Fixed	Calculated
Lab	0.4	50	0.465	0.375	0.25	1.7	2	0.239
		70	0.637	0.686	0.25	1.7	2	0.447
		100	0.9	14	0.25	1.7	2	0.862
	0.6	50	0.505	0.5	0.292	1.7	1.94	0.932
		70	0.735	1.47	0.292	1.7	1.93	0.859
		100	1.13	2	0.292	1.7	1.93	1.201
	0.8	50	0.575	0.75	0.29	1.8	1.9	1.317
		70	0.84	3.43	0.29	1.8	1.92	0.491
		100	1.15	4	0.29	1.8	1.9	0.976
	1	50	0.66	1	0.3	1.8	1.9	2.039
		70	0.994	2.94	0.3	1.81	1.89	0.78
		100	1.41	4	0.3	1.81	1.86	0.265
	1.2	50	0.76	1.75	0.335	1.81	1.84	0.972
		70	1.05	3.43	0.335	1.81	1.84	0.457
		100	1.5	4	0.335	1.81	1.84	0.913
	1.4	50	0.82	2.75	0.358	1.8	1.84	1.237
		70	1.288	5.88	0.358	1.8	1.83	0.713
		100	1.8	12	0.358	1.8	1.815	0.439
Field	83.33	200	0.3	0.03	0.358	1	2	n/a
		400	0.18	0.009	0.358	1	2	n/a
		600	0.12	0.0025	0.358	1	2	n/a

Table 2-7. The best-fit parameters for the CTRW model. In the legend,  $v_\psi$  is the CTRW transport velocity, which can be different from the average pore velocity  $v$ ;  $D_\psi$  is the dispersion coefficient with the subscript  $\psi$  indicating CTRW interpretation;  $\zeta$  is the power-law exponent;  $t_1$  is the mean transition time; and  $t_2$  is the truncation time scale.  $\zeta$  is converted from  $\gamma$  in the tt-fADE model (2-8), and  $t_2$  is converted from  $\lambda$  in the tt-fADE model.

## 2.6 Discussion

### 2.6.1 Comparison of transport models

Two groups: The transport models discussed in Section 2.5 can be classified into two main groups. The first group includes the ADE with equilibrium adsorption, the single mass-transfer rate MIM model, and the single diffusion rate MRMT model, which capture the observed early-time BTC and its peak, but underestimate the persistent late-time tail of each BTC. The second group includes the MRMT model with two or a power-law distributed rate coefficients, the tt-fADE, and the CTRW model with a truncated power-law memory function, which can capture the overall trend and positive skewness of the BTC. The two rate coefficients

in the MRMT model, however, might not be adequate to capture heavy late-time tailing for solute transport observed in the field. There is no efficient way to predict the capacity coefficient and the mass transfer rate in the MRMT model, especially when there are multiple sets of mass transfer rates due to various retention capabilities in natural soils with spatial variable hydraulic properties. In contrast, the tt-fADE and the CTRW model are applicable for a wider range of non-Fickian transport.

MRMT model: As articulated by Dentz and Berkowitz (2003), the MRMT model relates closely to the CTRW framework in capturing solute retention times. Particularly, the mean transition time  $t_1$  in the CTRW framework is related to the inverse of the mean rate coefficient in the MRMT model with power-law distributed rate coefficients. My fitting exercise in Section 2.5.2.4 shows that the BTC is not sensitive to  $\alpha_{\max}$ . The mean transition time  $t_1$  in the CTRW framework and the maximum boundary  $\alpha_{\max}$  used in the MRMT model might not be needed when capturing the late-time tailing of solute transport (note that the cutoff time  $t_2$  in the CTRW model or the minimum rate coefficient  $\alpha_{\min}$  in the MRMT model play a more important role than  $t_1$  or  $\alpha_{\max}$  in affecting the late-time BTC), and therefore they may be removed from the fitting parameters to simplify the model applications. Note that the tt-fADE model does not need the lower-bound of retention times. In addition, the MRMT model with power-law distributed rate coefficients tends to slightly overestimate the late-time tailing in BTCs (Figs. 2-2, 2-9 and Figs. 2-S6 - 2-10), implying that the actual mass transfer rates may decline faster than a power-law function at late times.

CTRW model: The CTRW framework has a complex relationship to the tt-fADE model. On one hand, as discussed in Section 2.3.3 and checked in Section 2.5.4, the power-law exponent

$\zeta$  in the CTRW framework is functionally equivalent to the scale index  $\gamma$  in the tt-fADE, and the cutoff time scale  $t_2$  in CTRW is equivalent to the inverse of the truncation parameter  $\lambda$  in the tt-fADE. On the other hand, the velocity and dispersion coefficient in the CTRW framework significantly differ from those in the tt-fADE model. Similarly, they are not directly related to the solution of the traditional ADE. Applications in Section 2.5.4 show that the average CTRW transport velocity  $v_\psi$  (1.303 mm/s) is ~59% less than the average real peak velocity (3.18 mm/s) of the observed BTC and ~62% less than the average best-fit velocity (3.39 mm/s) in the tt-fADE model at the flow rate  $Q=1.4$  mL/s. For the field tracer tests, the CTRW transport velocity  $v_\psi$  (0.3 mm/s) is two orders of magnitude larger than the real peak velocity (0.003 mm/s) of the observed BTC, which is similar with the best-fit velocity (0.004 mm/s) in the tt-fADE model. The velocity used in the tt-fADE model can be calculated by using equation (2-31), instead of fitting. This procedure further eliminates the number of parameters in the tt-fADE model and makes the fitting more convenient. In addition, the dispersion coefficient in the CTRW framework  $D_\psi$  cannot be kept constant under the same flow rate for different travel distances like the dispersion coefficient in the tt-fADE model for both laboratory experiments and field tracer tests.

Therefore, the spatially averaged velocity defined by formula (2-16a) for the CTRW framework may differ from the actual pore-scale velocity. In the CTRW model, different from the traditional ADE, the advective, dispersive, and diffusive transport mechanisms are combined in the random walk formalism. The advective component and the dispersive component are calculated by spatial moments of the same joint PDF for particle transitions and hence cannot be disconnected (Berkowitz et al., 2006). In particular, according to equation (2-16a), velocity in the CTRW model can be estimated by determining the characteristic time and mean distance, which is the first moment of the PDF of transition displacement. It is, however, difficult to predict the

effective velocity  $v_{\psi}$  without detailed knowledge of the porous medium. It is also noteworthy that the generalized master equation (2-17) does not separate the effects of the spatially varying velocity field on solute particle displacement into an advective part and a dispersive part. The concept of CTRW therefore does not build an explicit relationship between real velocity and model velocity, and the same is true for the dispersion coefficient. In addition, the power-law exponent  $\zeta$  can also affect the overall magnitude of solute plume expansion, an effect that intermingles with the dispersion coefficient  $D_{\psi}$  and the effective velocity  $v_{\psi}$ . The above analysis is consistent with the result in Fiori et al. (2015), who found that many parameters, particularly  $v_{\psi}$  and  $\zeta$ , in the CTRW model are correlated with each other. Their fitting exercises showed that different parameter combinations can lead to the same mean Eulerian velocity predicted by the model, implying that the estimated model parameters were not unique.

*tt-fADE model:* In the tt-fADE model, the best-fit velocity  $v$  can be larger than the plume peak's velocity  $v_{\text{peak}}$  because the effective velocity used in the tt-fADE is adjusted by the elapsed time for solutes spent in retention, as represented by the fractional-order capacity coefficient  $\beta$  on the right-hand side of equation (2-31). In this study, laboratory experiments with six flow rates and field tracer tests show that the best-fit velocity in the tt-fADE model is close to the measured BTC's peak velocity, since the capacity coefficient shown in equation (2-31) is relatively small. Because the transport velocity used in the tt-fADE model (2-8) is not significantly different from the BTC's peak velocity, the tt-fADE model uses an independent parameter, the time index  $\gamma$ , to control the power-law distribution of the late-time BTC. This parameterization of the tailing is relatively simple as compared to the CTRW model, with three parameters,  $v_{\psi}$ ,  $D_{\psi}$  and  $\zeta$ , that contribute to time-nonlocal non-Fickian dispersion. I calculate

the root mean square error (RMSE) for the laboratory experiments. Comparison of the RMSE (see Table 2-1, 2-6, 2-7) of the two models and the ADE model demonstrates that they both perform better than the standard ADE, especially in describing tailing behavior in a heterogeneous medium. When the formula (2-31) is used, the tt-fADE model is more convenient to apply in practice than the CTRW framework, since the former contains fewer parameters.

Why the fitted four-parameter tt-fADE model can provide the best performance? There are two reasons. First, according to the physical derivation of the tt-fADE in section 2.3.2, the tt-fADE separates motion in the mobile zone (using the basic transport parameters  $v$  and  $D$  to define advection and Gaussian diffusive displacement) and retention in the immobile domains. When the tracer particle moves in the mobile domain, its average speed is  $v$ , with a finite time required to finish the jump. This physical separation might be reasonable in hydrogeological media. In the CTRW framework, the memory function defines the random waiting time between two subsequent jumps, while the motion can finish instantaneously (in other words, no physical time is required for the tracer particle to move). This physical discrepancy may also cause the discrepancy of the two basic transport parameters  $v$  and  $D$  between the two models, in addition to the spatial average parameters required by the CTRW framework. Second, the tt-fADE does not specify the lower-bound of the waiting time (using an additional parameter such as the lower-limit  $t_1$  in the CTRW framework), since the slow advection can also affect the late-time BTC tail. Mass exchange can apparently affect the late-time BTC tail only when the diffusive time scale is much longer than the advective time scale, as pointed out by Haggerty et al. (2000). This may explain why  $t_1$  might not be needed in the CTRW framework. Further real-world tests are needed to check the above hypotheses.

### 2.6.2 Parameter sensitivity

One example of parameter sensitivity is tested here for the tt-fADE (2-8). Sensitivity of the BTCs to variations of the four main parameters ( $D, \gamma, \beta, \lambda$ ) in the tt-fADE model is shown in Fig. 2-7.

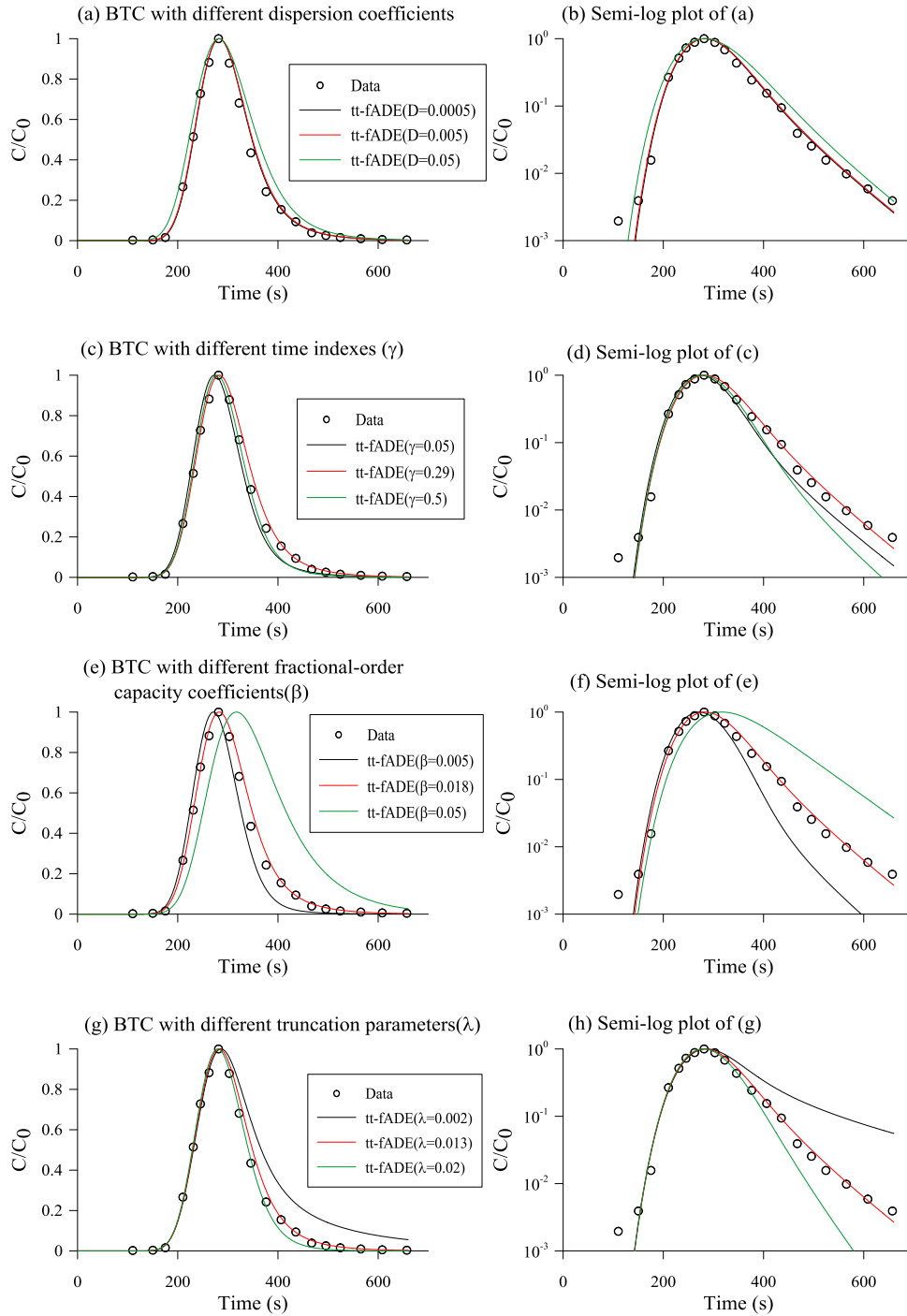


Figure 2-7. Sensitivity analysis for coefficients in the tt-fADE model.

First, the dispersion coefficient  $D$  has a subtle impact on the overall shape of BTCs. Decreasing  $D$  from  $0.005 \text{ cm}^2/\text{s}$  to  $0.0005 \text{ cm}^2/\text{s}$  results in similar BTCs after normalization (i.e., re-scaling), implying that trapping due to the immobile zones may account at least partially for the spatial expansion of solute plumes. When  $D$  increases from  $0.005 \text{ cm}^2/\text{s}$  to  $0.05 \text{ cm}^2/\text{s}$ , the BTC becomes wider and its shape slightly changes (Figs. 2-7a, b).

Second, the time index  $\gamma$  controls the power-law slope of the late-time BTC. For example, when  $\gamma$  increases from 0.29 to 0.50 (representing the decrease of probability for long retention times), the late-time BTC becomes steeper, approaching relatively fast to its Gaussian asymptote (Figs. 2-7c, d). When  $\gamma$  decreases from 0.29 to 0.05, the BTC's late-time tail becomes heavier (i.e., with a gentler slope), although the overall BTC looks narrower (likely due to the normalization of BTCs). The simulated BTC with the time index  $\gamma$  equal to 0.29 matches the observations better than the other  $\gamma$ .

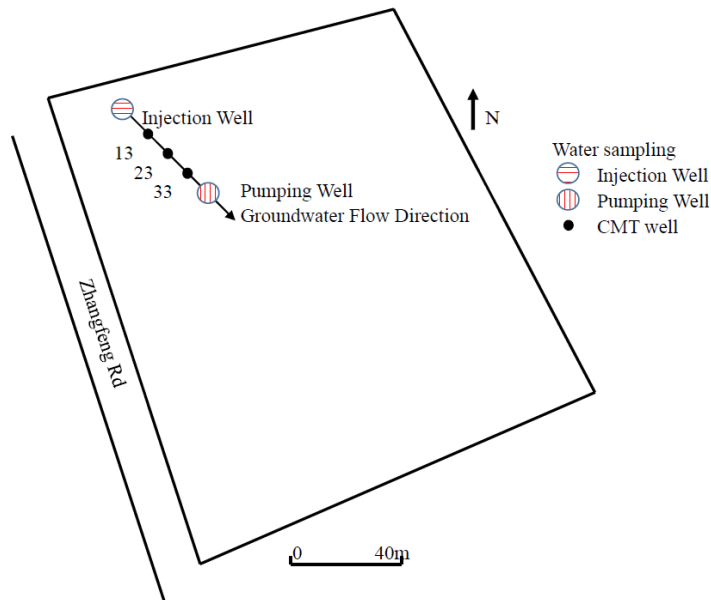
Third, the fractional-order capacity coefficient  $\beta$  shifts the BTC and expands the BTC's late-time tail. When  $\beta$  decreases (representing a decrease of the immobile zone volume or the immobile solute mass at equilibrium), the BTC becomes narrower and shifts to the left (representing a larger effective velocity). A faster drop is apparent in the late-time BTC tail with a smaller  $\beta$ . An opposite change of the BTC can be seen for an increasing  $\beta$  (Figs. 2-7e, f).

Fourth, the truncation parameter  $\lambda$  affects the speed for the late-time BTC to transfer from a heavy tailed, power-law slope to an exponential tail. A larger truncation parameter means an earlier transform from non-Fickian to Fickian transport (Figs. 2-7g, h). For the largest  $\lambda$  tested, the resultant BTC is the closest to the solution of the ADE model, as expected because the tt-fADE reduces to the ADE model for  $\lambda \rightarrow \infty$ .

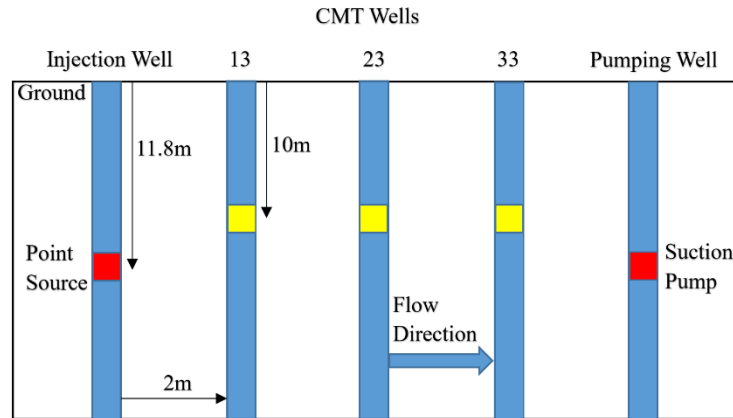
### 2.6.3 Application to field transport

A field trace transport test was conducted recently by Zheng et al. (2011), which provides field data to evaluate further the time nonlocal transport models and compare with the laboratory column experiment. The test site is located in the Zhangjiawan Village, Zhangjiawan Town, southeast of the Tongzhou District, Beijing, China, with the longitude of 116.72° and latitude 39.848°. This experimental site is located in the Chaobai River alluvial plain. The average annual precipitation in the vicinity is about 533 mm, and the evaporation is 1822 mm. It has a multi-layer aquifer structure. The aquifer is composed of gravelly coarse sand, coarse sand, fine sand, silty clay and clay layer in the test field and surrounding area. The hydraulic conductivity coefficient shows obvious heterogeneity, indicating that the aquifer develops a small-scale preferential flow channel network.

The subsurface network consisted of one injection well, one pumping well, and three monitoring wells with continuous multi-tubing (denoted as well 13, 23, and 33, respectively) (see Fig. 2-8 for the study site).



(a) Zhangjiawan test site location and distribution of wells



(b) Illustration for point source artificial hydraulic gradient tracing tests

Figure 2-8. Study site map.

All the five wells are along the same line of the general groundwater flow direction, and therefore a one-dimensional model can be used to approximate the overall transport. The injection well and the pumping well are separated by 8 meters, and the three observation wells have a uniform interval of 2 meters. Groundwater flows from the injection well to well 13, 23, 33, and to the pumping well.

Sodium bromide (NaBr), a commonly used conservative tracer, was injected into the injection well at a depth of 11.8 m, and groundwater samples were taken from the three observation wells (Well 13, 23, 33) located downstream at a depth of ~10 m. The concentration of the injected solution was 1288 mg/L. The injection rate was about 0.3 m<sup>3</sup>/h, and the injection duration was 6 hours. The peristaltic pump was used to collect the samples in a chronological order, and the sample concentration was measured using a MP523-06 bromide ion concentration meter.

The measured BTCs exhibit apparent late-time tailing (see Fig. 2-9), similar to that observed in the laboratory column transport. Applications show that the time nonlocal models

can capture part of the late-time BTC tail, but not the whole tail of BTC containing apparent noise. Due to the noise, it is also impossible to obtain a reliable RMSE. Although the apparent noise causes high uncertainty in model fitting, both the CTRW framework and the tt-fADE can capture a heavier late-time tail than the MRMT model with two sets of rate coefficients, and the measured BTCs do contain a high concentration at the very end of the sampling period (Fig. 2-9).

In addition, all the measured BTCs show apparent early time tail, which cannot be captured by the tt-fADE or the CTRW framework with the time index between 0 and 1. It is, however, not a surprise, since the early arrivals are most likely due to fast motion of tracer particles along preferential flow paths, while the delayed arrivals are caused by solute retention due to mass exchange between the mobile and relatively immobile zones. At the field site, high-permeable sand consists of the layers connecting the injection well and the three monitoring wells, likely forming the preferential channels. The time nonlocal transport models considered in this study were developed to capture solute retention, hence missing the early tail of the BTC. The spatiotemporal fADE may capture both the early and late time tails in the BTC (Benson et al., 2000; Schumer et al., 2003b), which will be explored in a future study.

It is also noteworthy that the flow velocity in real aquifers is several orders of magnitude smaller than that used in the laboratory experiments. Hence, the field transport is diffusion dominated, while the laboratory transport is advection dominated. This discrepancy might imply that the late-time BTC tail persists for groundwater flow with a broad range of Peclet numbers, which can be characterized by the time nonlocal models. However, for groundwater flow with a small Peclet number and potential preferential flow paths, the early time BTC tail may occur,

which cannot be efficiently captured by the time nonlocal transport models such as the tt-fADE or the CTRW framework with an index less than 1.

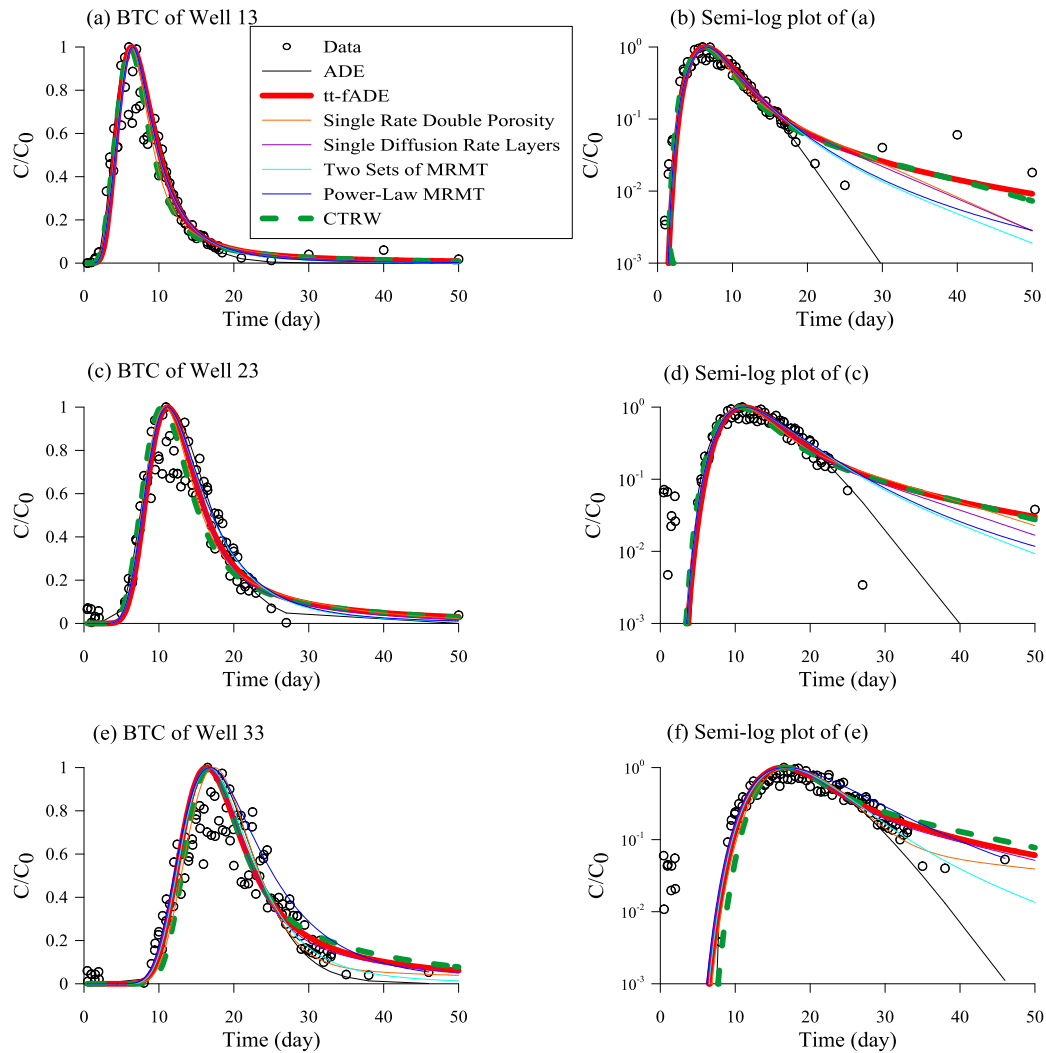


Figure 2-9. Field tracer test: comparison between the measured field data (symbols) and the modeled (lines) breakthrough curves using the ADE, the tt-fADE (red thick lines), the CTRW (green dashed lines), and the MRMT models.

## 2.7 Conclusion

This study compared three time-nonlocal transport models by combining theoretical analyses and applications for laboratory sand column transport experiments and field tracer tests. The models revisited by this study include the MRMT model with various specific forms, the tt-

fADE model, and the CTRW framework. Four major conclusions are obtained for these models, which can be used by practitioners to select the appropriate model and improve practical applications, and can improve our understanding of the nature of non-Fickian transport in heterogeneous media.

First, the sand column packed in the laboratory and soil in the field may contain multiple immobile domains with different mass transfer capabilities. This assumption and the laboratory measurements challenge the applicability of the classical ADE model with equilibrium adsorption (i.e., instantaneous sorption/desorption) and the single-rate mobile-immobile model in capturing the tracer BTCs with a late-time tail, which declines at a rate slower than exponential. The MRMT models with multiple rates do capture the BTC's late time tail typical for non-Fickian transport, as revealed before, but the MRMT solutions with power-law distributed mass-exchange rates cannot capture the nuance of observed transition from power-law to exponential decline of the late-time concentration. The increase of the number of unpredictable parameters (both the rate coefficient and the capacity coefficient) may create a challenge for the applicability of the MRMT model.

Second, the tt-fADE model and the CTRW framework are similar in functionality, but differ in detailed parameters. (1) Both the CTRW framework and the tt-fADE model can capture a complex BTC with late time tailing. Both the CTRW framework and the tt-fADE model assume an exponentially-truncated power-law memory function, to capture the gradual transition from power-law to exponential decline of late-time concentration in the observed BTCs. (2) The tt-fADE parameters can be linked to the CTRW framework parameters. For example, the power-law exponent  $\xi$  in the CTRW framework is functionally equivalent to the scale index  $\gamma$  in the tt-fADE model (as revealed before), and the cutoff time scale  $t_2$  in the CTRW framework is also

equivalent to the inverse of the truncation parameter  $\lambda$  in the tt-fADE (not shown specifically before). Hence the predictability obtained by the tt-fADE model can also improve the predictability of the CTRW framework, and vice-versa. (3) Compared to the tt-fADE model, the CTRW framework defines one additional parameter  $t_1$ , which represents the mean diffusive time, corresponding to the mean of the inverse of rate coefficients in the MRMT model. Model applications, however, showed that  $t_1$  in the CTRW framework is insensitive to model results, and may be neglected to alleviate model fitting burdens.

Third, in the tt-fADE model, the real BTC's peak velocity can be used to estimate the lower-end of the model velocity, increasing the predictability of the tt-fADE for real-world applications. Hence, the tt-fADE model may conveniently estimate the BTC late-time tailing under the conditions of the column experiment and field tracer tests.

Fourth, for tracer transport in the field, it is likely to view early arrivals due to the potential preferential flow paths. Super-diffusive jumps along preferential flow paths cannot be efficiently captured by a typical time-nonlocal transport model focusing on solute retention with a time index less than one. Fast motion (which can exhibit direction-dependent scaling rates) and delayed transport (which is dimensionless), although co-existing in some field sites, are driven by different mechanisms, and hence I recommend different physical components to capture these processes. This motivates the application of the spatiotemporal fADE (Benson et al., 2000; Schumer et al., 2003b), which will be re-visited in a future study.

## 2.8 Supplementary Materials

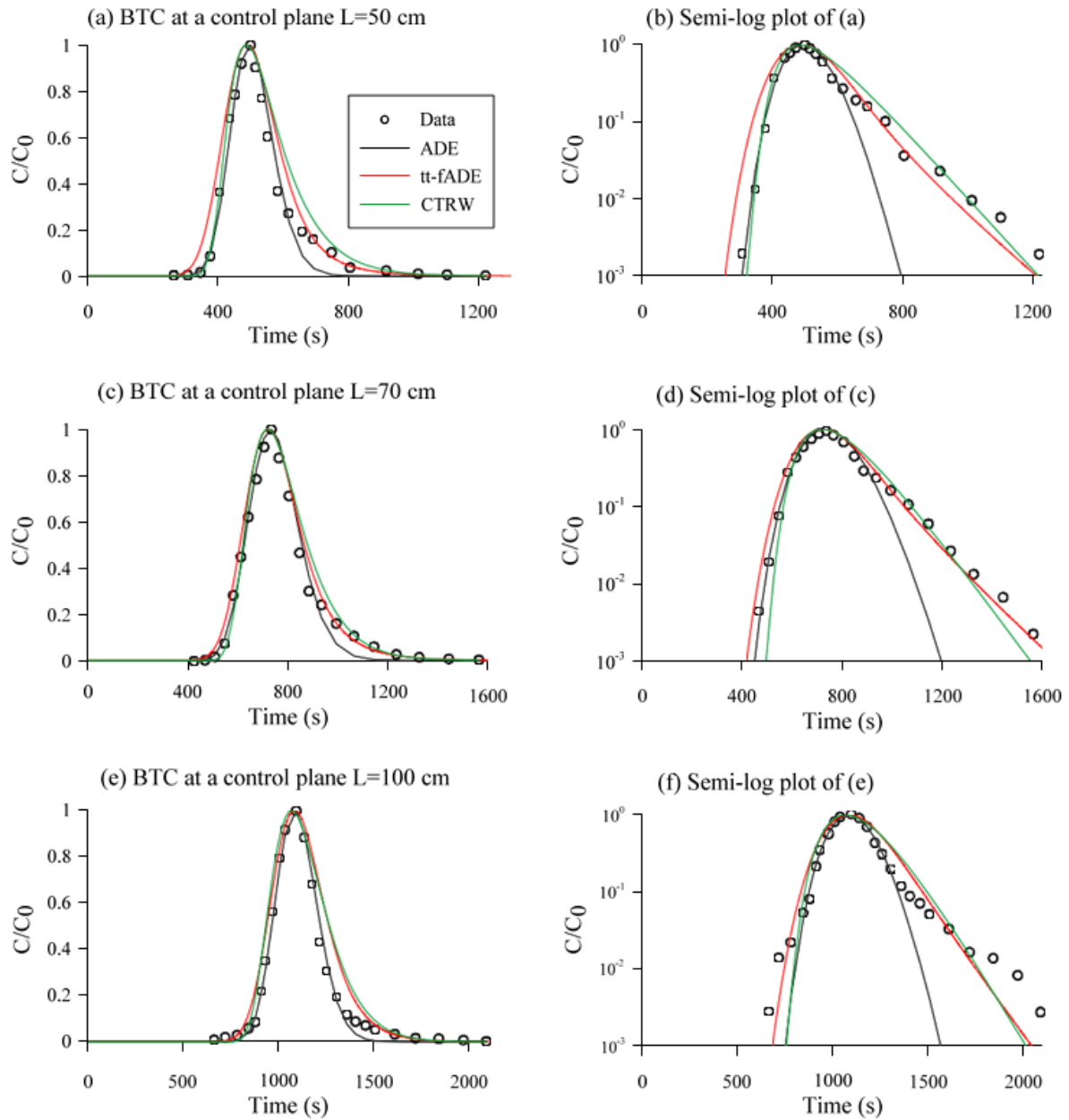


Figure 2-S1. Comparison between the measured (symbols) and modeled (lines) breakthrough curves using the ADE model (black line), the tt-fADE model (red line) and the CTRW model (green line) with the experimental water flow rate  $Q = 0.4$  mL/s.

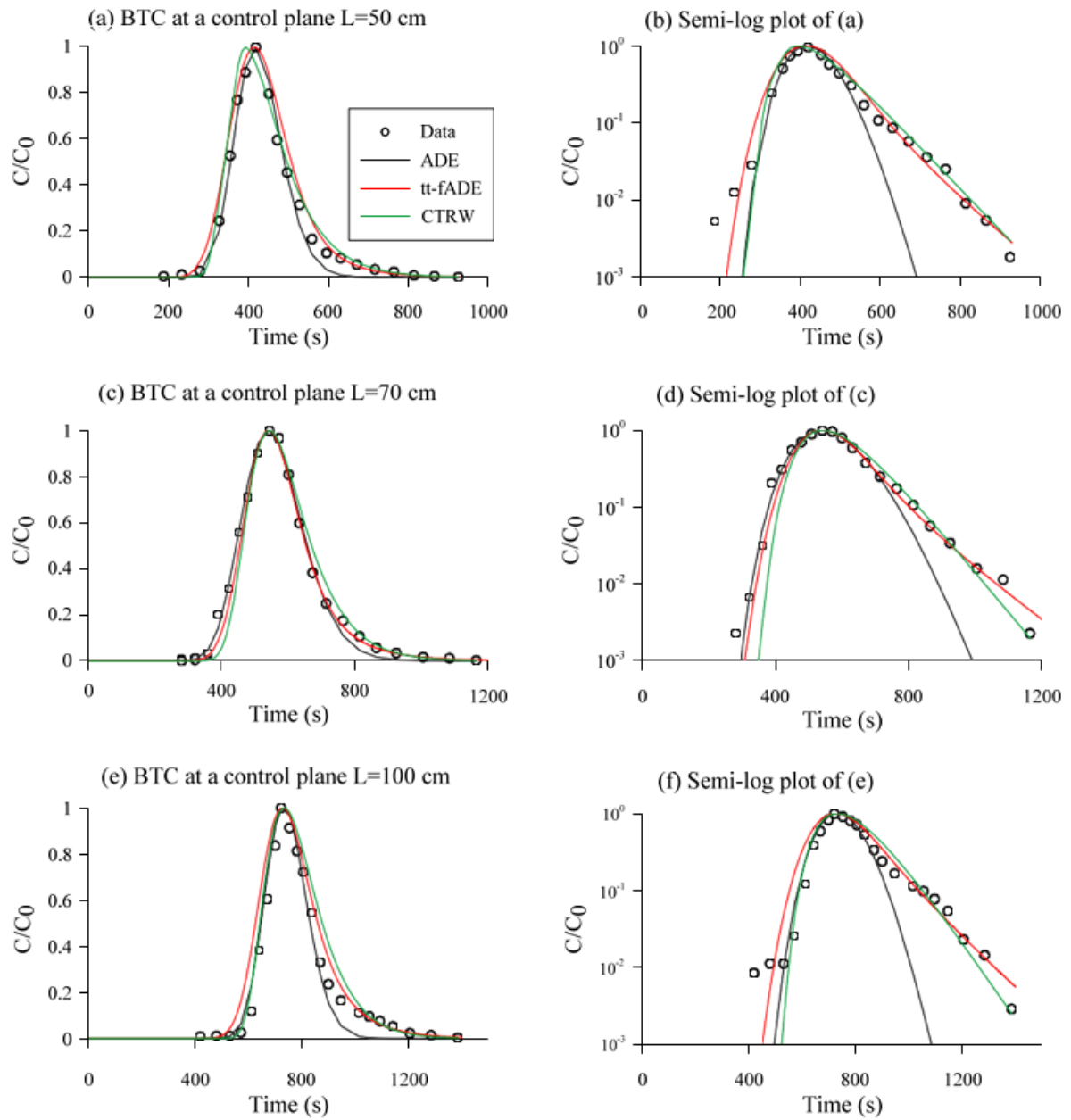


Figure 2-S2. Comparison between the measured (symbols) and modeled (lines) breakthrough curves using the ADE model (black line), the tt-fADE model (red line) and the CTRW model (green line) with the experimental water flow rate  $Q = 0.6$  mL/s.

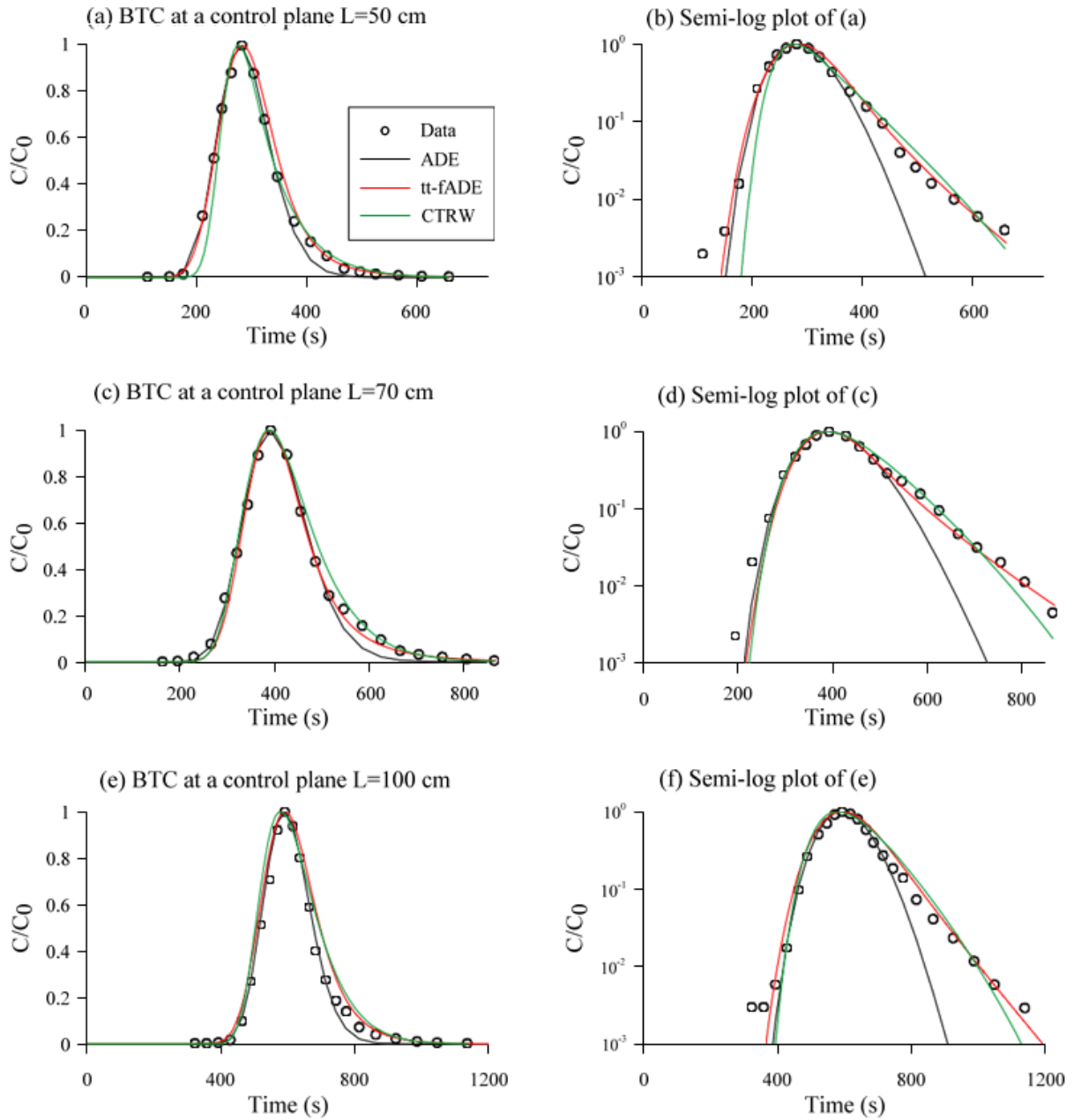


Figure 2-S3. Comparison between the measured (symbols) and modeled (lines) breakthrough curves using the ADE model (black line), the tt-fADE model (red line) and the CTRW model (green line) with the experimental water flow rate  $Q = 0.8$  mL/s.

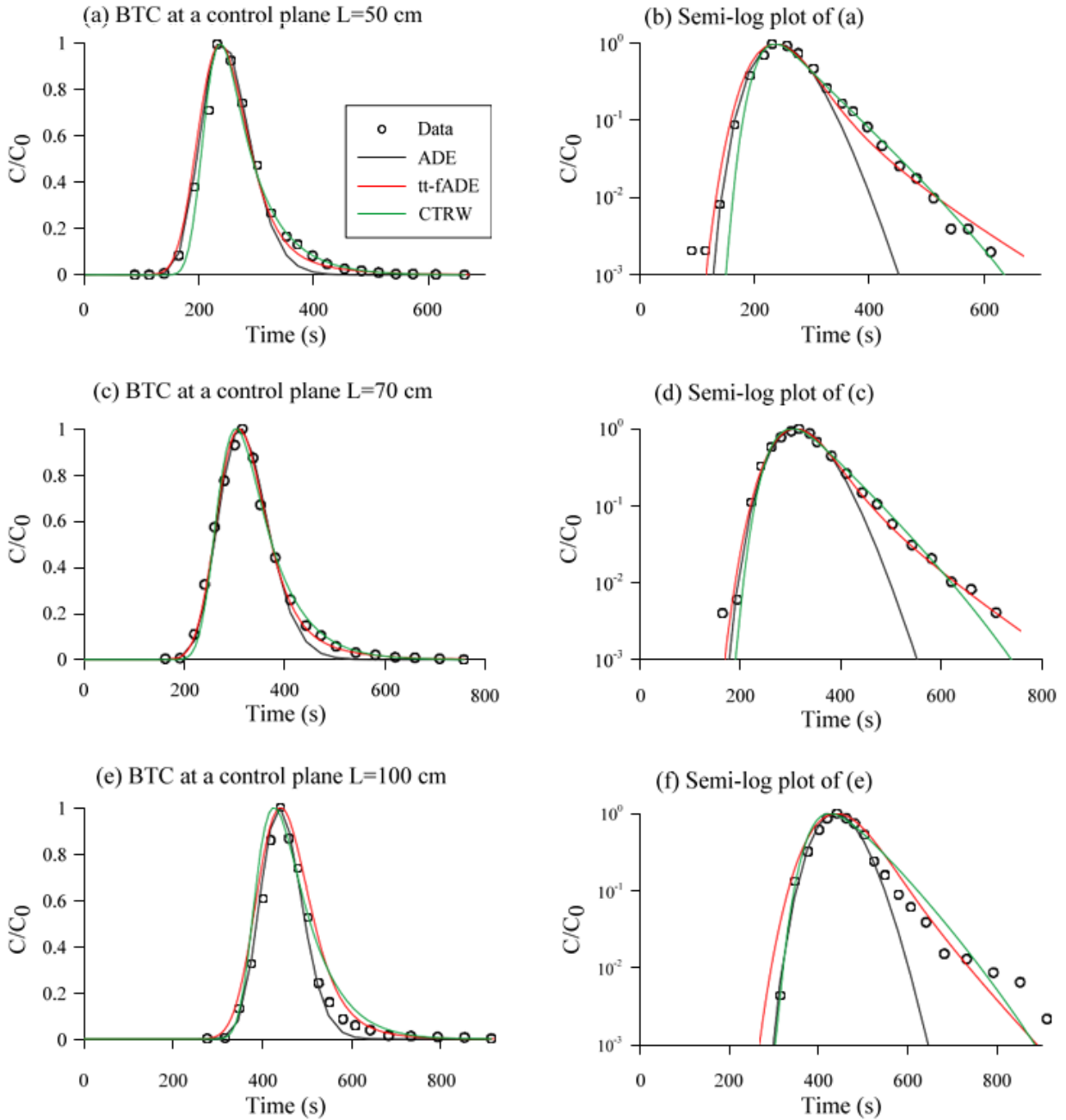


Figure 2-S4. Comparison between the measured (symbols) and modeled (lines) breakthrough curves using the ADE model (black line), the tt-fADE model (red line) and the CTRW model (green line) with the experimental water flow rate  $Q = 1.0$  mL/s.

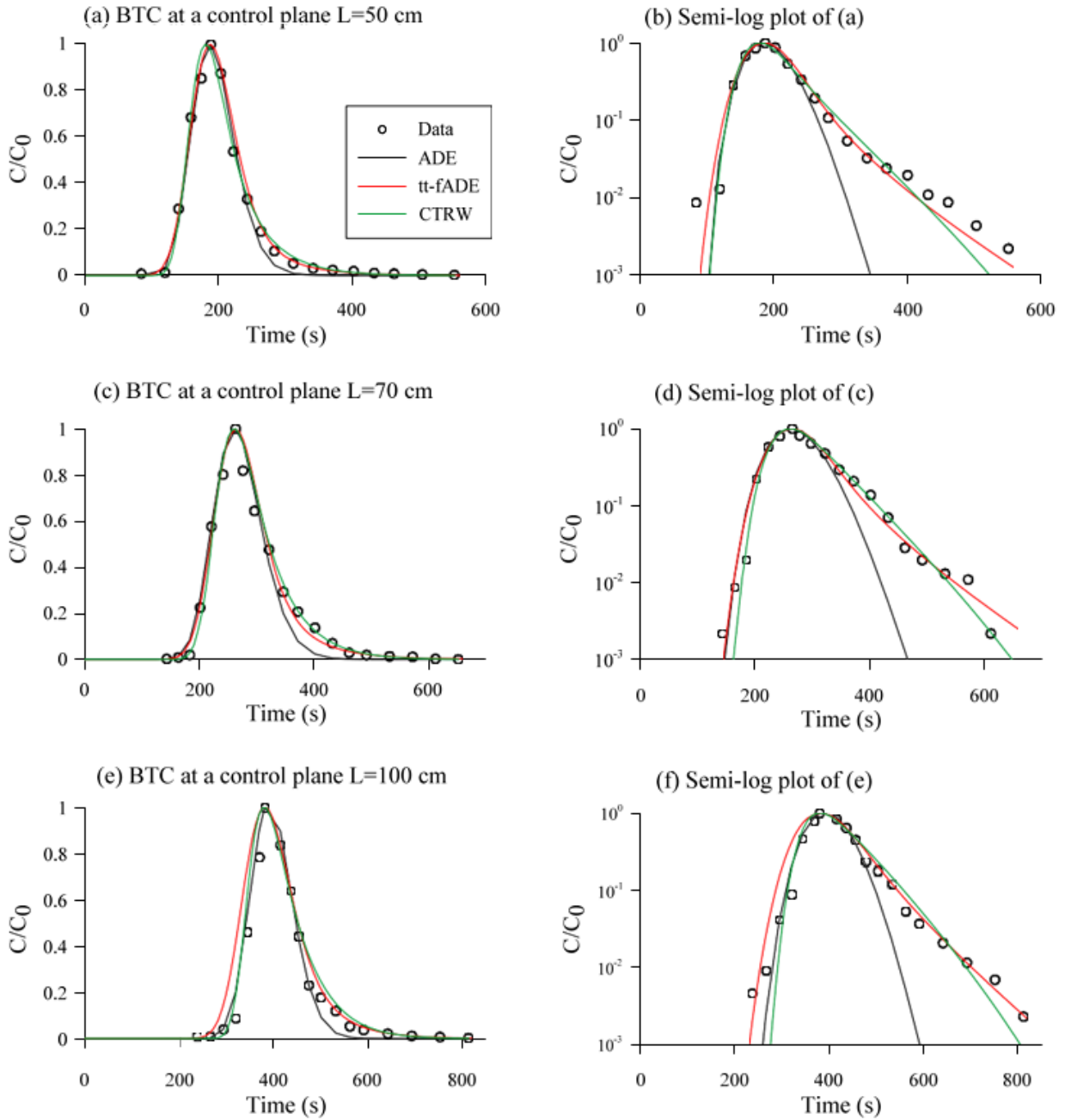


Figure 2-S5. Comparison between the measured (symbols) and modeled (lines) breakthrough curves using the ADE model (black line), the tt-fADE model (red line) and the CTRW model (green line) with the experimental water flow rate  $Q=1.2$  mL/s.

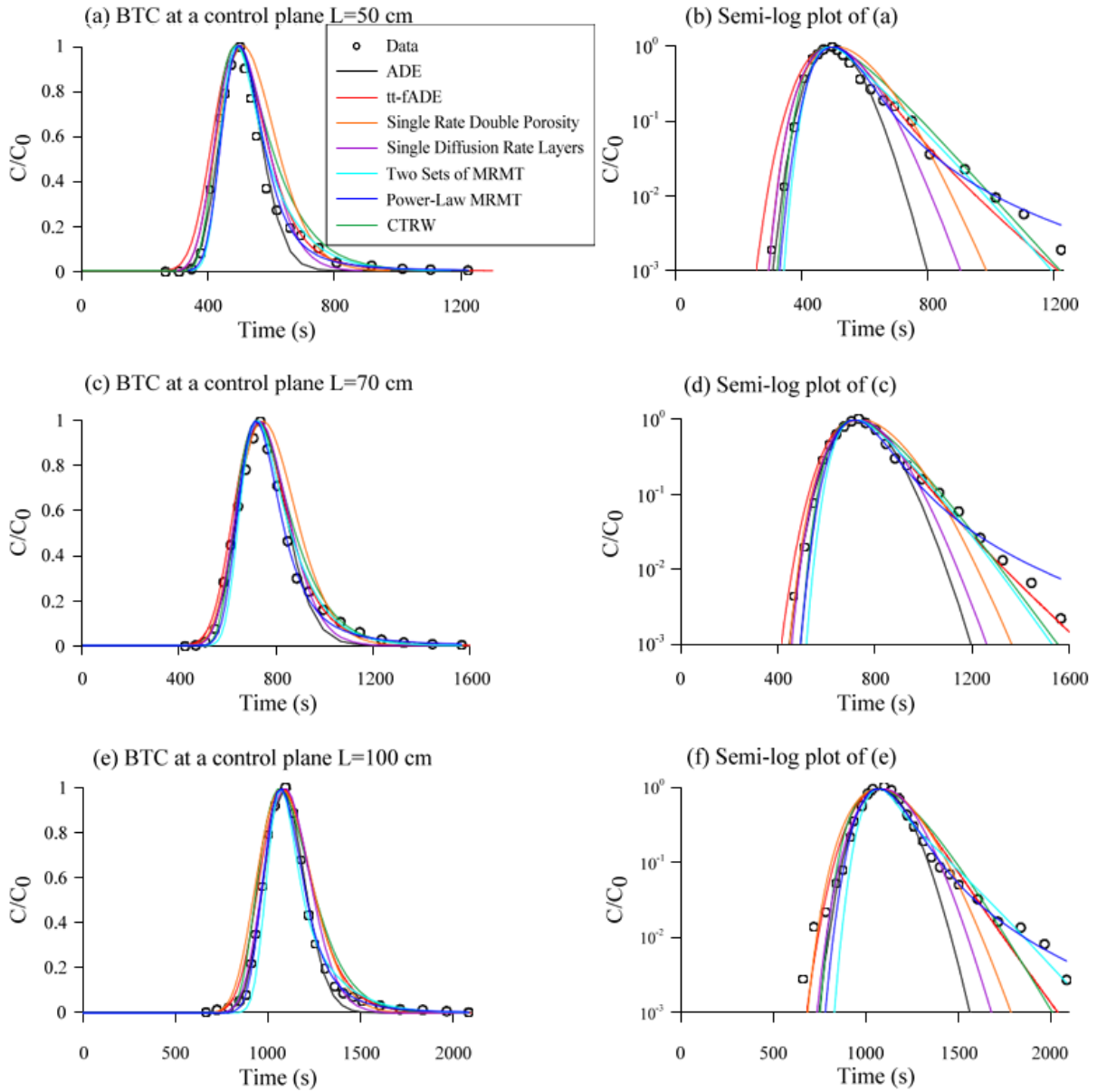


Figure 2-S6. Comparison between the measured (symbols) and the modeled (lines) breakthrough curves using the ADE, the tt-fADE, the MRMT, and the CTRW models with the water flow rate  $Q = 0.4$  mL/s.

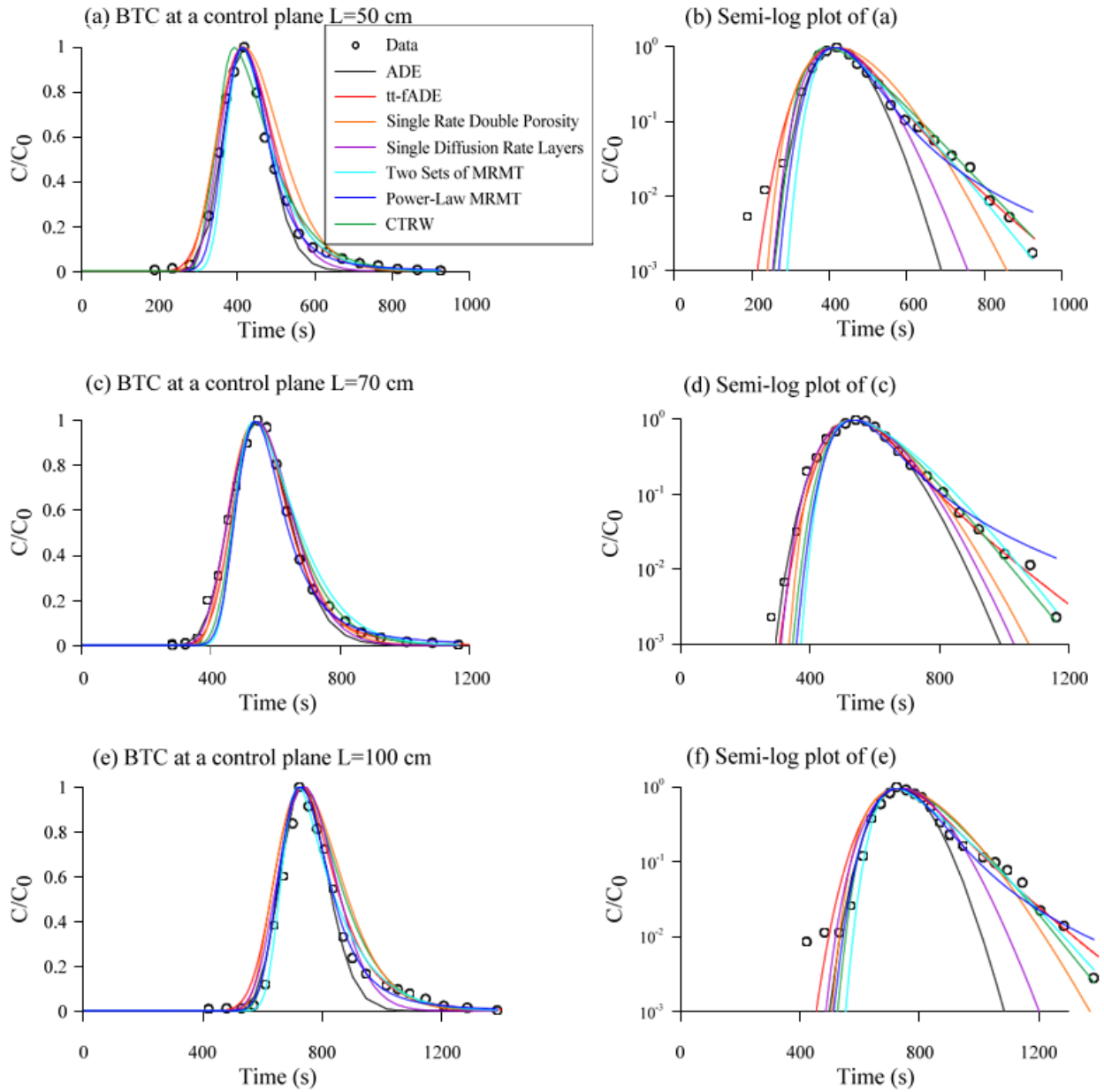


Figure 2-S7. Comparison between the measured (symbols) and the modeled (lines) breakthrough curves using the ADE, the tt-fADE, the MRMT, and the CTRW models with the water flow rate  $Q = 0.6$  mL/s.

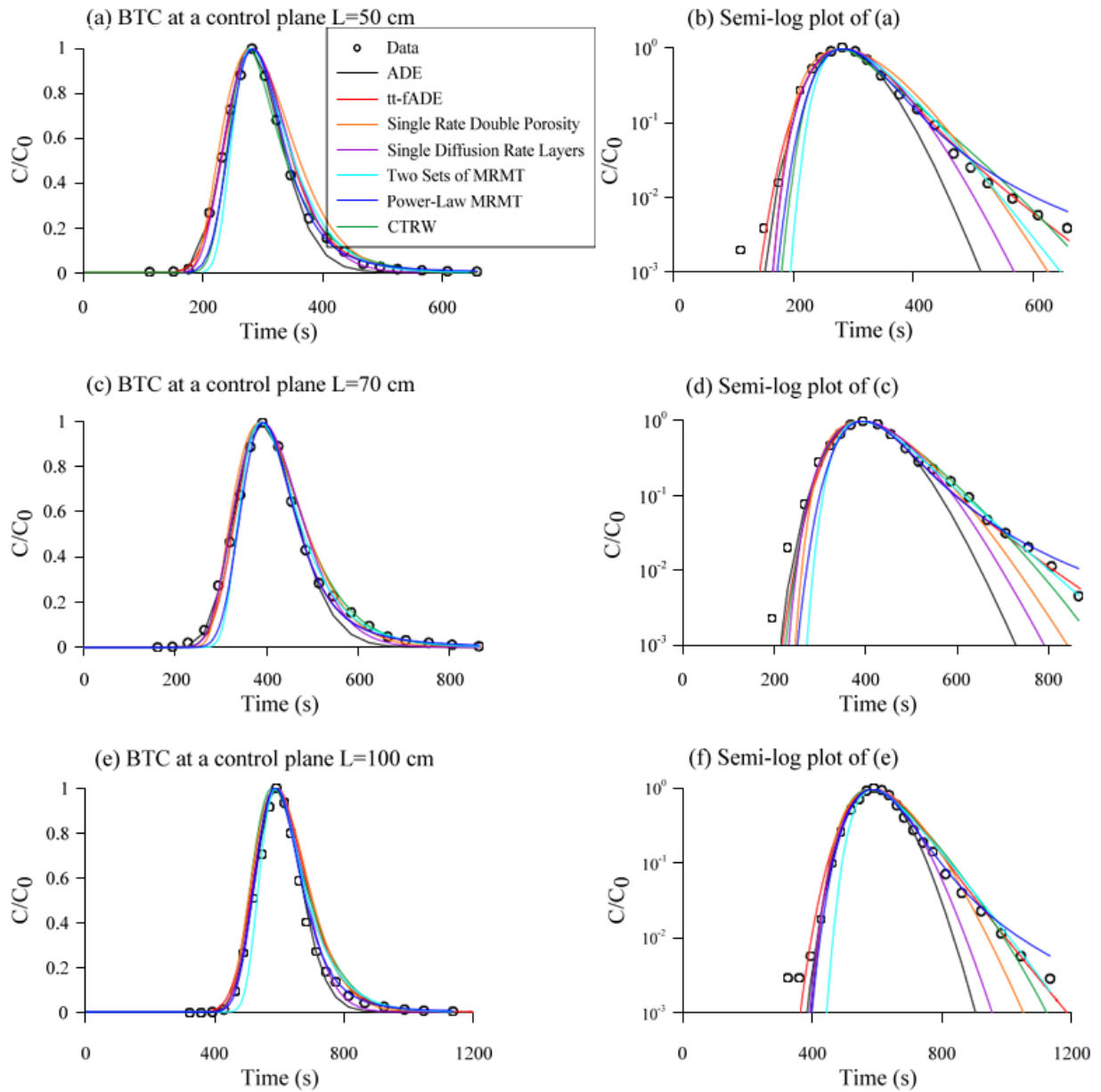


Figure 2-S8. Comparison between the measured (symbols) and the modeled (lines) breakthrough curves using the ADE, the tt-fADE, the MRMT, and the CTRW models with the water flow rate  $Q = 0.8$  mL/s.

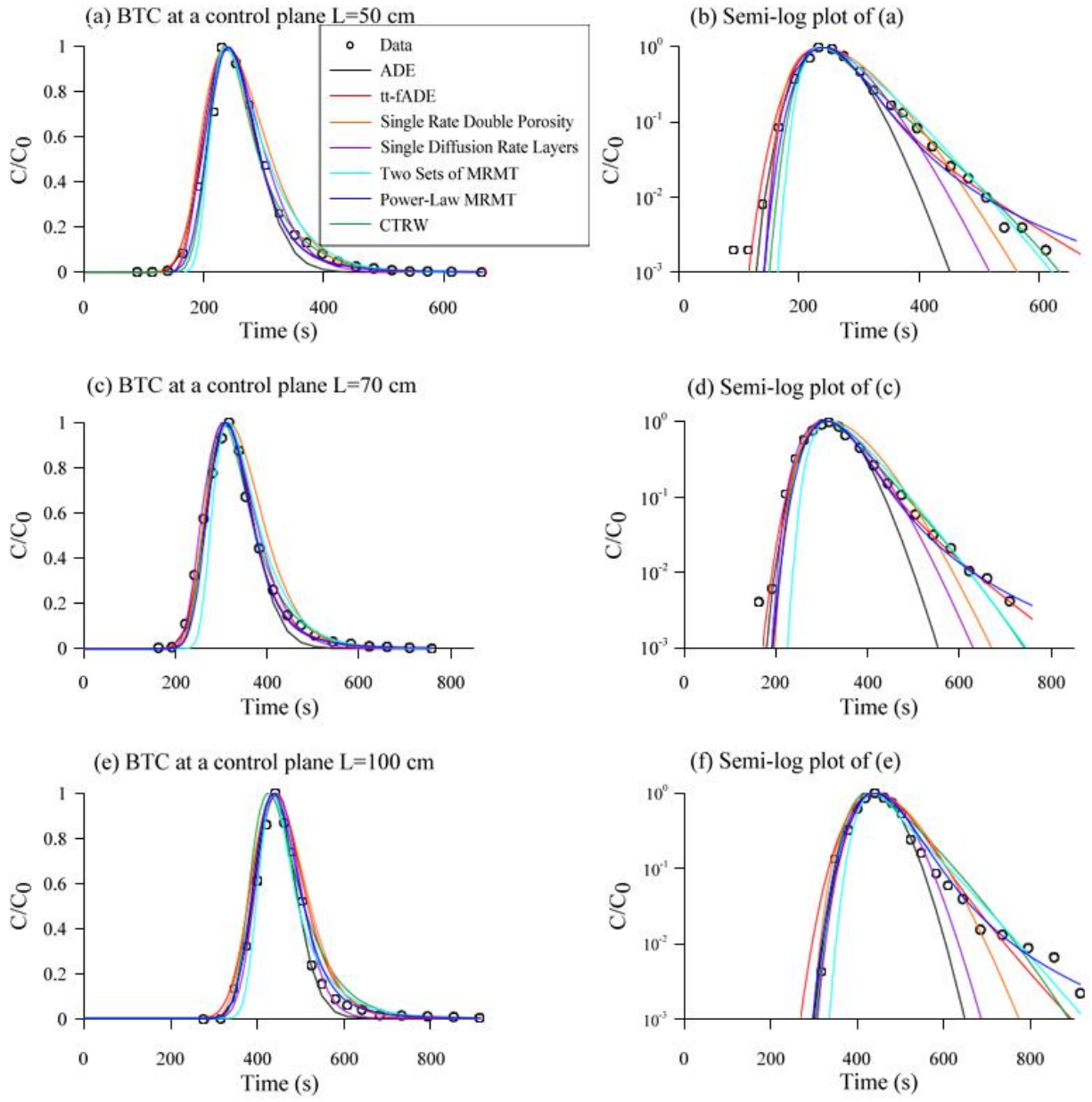


Figure 2-S9. Comparison between the measured (symbols) and the modeled (lines) breakthrough curves using the ADE, the tt-fADE, the MRMT, and the CTRW models with the water flow rate  $Q = 1.0$  mL/s.

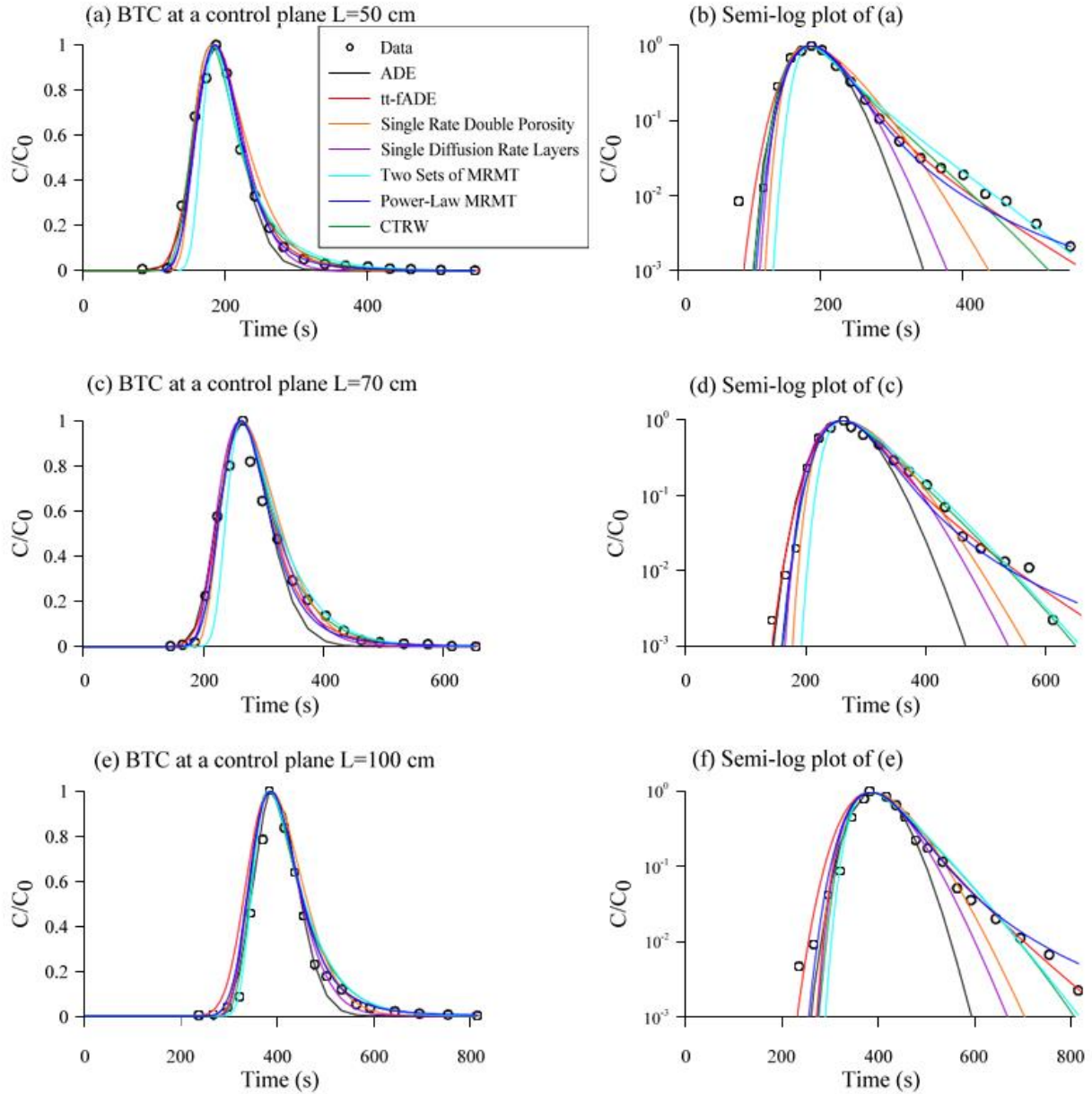


Figure 2-S10. Comparison between the measured (symbols) and the modeled (lines) breakthrough curves using the ADE, the tt-fADE, the MRMT, and the CTRW models with the water flow rate  $Q = 1.2$  mL/s.

## 2.9 Acknowledgments

This work was partially funded by the National Natural Science Foundation of China (under grants 41330632, 41628202, and 11572112), the University of Alabama, and the US Geological Survey. This paper does not necessarily reflect the views of the funding agencies.

## 2.10 References

- Anderson, M.P., 1984. Movement of contaminants in groundwater: groundwater transport--advection and dispersion. *Groundw. Contam.* 20, 37–45.
- Bakshevskaia, V.A., Pozdniakov, S.P., 2016. Simulation of Hydraulic Heterogeneity and Upscaling Permeability and Dispersivity in Sandy-Clay Formations. *Math. Geosci.* 48, 45–64. doi:10.1007/s11004-015-9590-1.
- Benson, D.A., Wheatcraft, S.W., and Meerschaert M.M., 2000. Application of a fractional advectiondispersion equation, *Water Resour. Res.*, 36(6), 1403-1412.
- Benson, D.A., Meerschaert, M.M., 2009. A simple and efficient random walk solution of multi-rate mobile/immobile mass transport equations. *Adv. Water Resour.* 32, 532–539. doi:10.1016/j.advwatres.2009.01.002.
- Berkowitz, B., Cortis, A., Dentz, M., Scher, H., 2006. Modeling Non-fickian transport in geological formations as a continuous time random walk. *Rev. Geophys.* 44. doi:10.1029/2005RG000178.
- Bianchi, M., Zheng, C., 2016. A lithofacies approach for modeling non-Fickian solute transport in a heterogeneous alluvial aquifer. *Water Resour. Res.* 52, 552–565. doi:10.1002/2015WR018186.
- Bromly, M., Hinz, C., 2004. Non-Fickian transport in homogeneous unsaturated repacked sand. *Water Resour. Res.* 40, 1–12. doi:10.1029/2003WR002579.
- Chang, C.-M., Yeh, H.-D., 2016. Investigation of flow and solute transport at the field scale through heterogeneous deformable porous media. *J. Hydrol.* 540, 142–147. doi:10.1016/j.jhydrol.2016.05.060.
- Coats, K., Smith, B., van Genuchten, M.T., Wierenga, P.J., 1964. Dead-End Pore Volume and Dispersion in Porous Media. *Soil Sci. Soc. Am. J.* 4, 73–84. doi:10.2118/647-PA.
- Cortis, A., Berkowitz, B., 2005. Computing “anomalous” contaminant transport in porous media: The CTRW MATLAB toolbox. *Ground Water* 43, 947–950. doi:10.1111/j.1745-6584.2005.00045.x.
- Cvetkovic, V., Dagan, G., 1994. Transport of kinetically sorbing solute by steady random velocity in heterogeneous porous formations. *J. Fluid Mech.* 265, 189. doi:10.1017/S0022112094000807.
- Cvetkovic, V., Fiori, A., Dagan, G., 2016. Tracer travel and residence time distributions in highly heterogeneous aquifers: Coupled effect of flow variability and mass transfer. *J. Hydrol.* doi:10.1016/j.jhydrol.2016.04.072.

- Dentz, M., 2003. Transport behavior of a passive solute in continuous time random walks and multirate mass transfer. *Water Resour. Res.* 39, 1–20. doi:10.1029/2001WR001163.
- Dentz, M., Cortis, A., Scher, H., Berkowitz, B., 2004. Time behavior of solute transport in heterogeneous media: Transition from anomalous to normal transport. *Adv. Water Resour.* 27, 155–173. doi:10.1016/j.advwatres.2003.11.002.
- Fiori, A., Zarlenga, A., Gotovac, H., Jankovic, I., Volpi, E., Cvetkovic, V., Dagan, G., 2015. Advective transport in heterogeneous aquifers: Are proxy models predictive? *Water Resour. Res.* 51, 9577–9594. doi:10.1002/2015WR017118.
- Fiori, A., Zarlenga, A., Gotovac, H., Jankovic, I., Volpi, E., Cvetkovic, V., Dagan, G., 2015. Advective transport in heterogeneous aquifers: Are proxy models predictive? *Water Resour. Res.* 51, 9577–9594. doi:10.1002/2015WR017118.
- Haggerty, R., 2009. STAMMT-L 3.0. A solute transport code for multirate mass transfer and reaction along flowlines.
- Haggerty, R., Gorelick, S.M., 1995. Multiple-rate mass transfer for modeling diffusion and surface reactions in media with pore-scale heterogeneity. *Water Resour. Res.* 31, 2383–2400. doi:10.1029/95WR01583.
- Haggerty, R., McKenna, S. a, Meigs, L.C., 2000. On the late-time behaviour of tracer breakthrough curves. *Water Resour. Res.* 36, 3467–3479.
- Huber, F., Enzmann, F., Wenka, A., Bouby, M., Dentz, M., Schäfer, T., 2012. Natural micro-scale heterogeneity induced solute and nanoparticle retardation in fractured crystalline rock. *J. Contam. Hydrol.* 133, 40–52. doi:10.1016/j.jconhyd.2012.03.004.
- Jury, W.A., Horton, R., 2004. *Soil Physics*. doi:10.2134/jeq1992.00472425002100040034x.
- Karadimitriou, N.K., Joekar-niasar, V., Babaei, M., Shore, C.A., 2016. Critical Role of the Immobile Zone in Non-Fickian Two-Phase Transport: A New Paradigm. *Environ. Sci. Technol.* 50, 4384–4392. doi:10.1021/acs.est.5b05947.
- Klafter, J., Silbey, R., 1980. Derivation of the continuous-time random-walk equation. *Phys. Rev. Lett.* 44, 55–58. doi:10.1103/PhysRevLett.44.55.
- Meerschaert, M.M., Scheffler, H.P., 2001. *Limit Distributions for Sums of Independent Random Vectors: Heavy Tails in Theory and Practice*. John Wiley & Sons, New York.
- Meerschaert, M.M., Zhang, Y., Baeumer, B., 2008. Tempered anomalous diffusion in heterogeneous systems. *Geophys. Res. Lett.* 35. doi:10.1029/2008GL034899.
- Montroll, E., Weiss, G., 1965. Random walks on lattices. II. *J. Math. Phys.* 6, 167. doi:10.1063/1.1704269.

- Naftaly, A., Dror, I., Berkowitz, B., 2016. Measurement and modeling of engineered nanoparticle transport and aging dynamics in a reactive porous medium. *Water Resour. Res.* doi:10.1002/2016WR018780.
- Nordin, C.F., Troutman, B.M., 1980. Longitudinal dispersion in rivers: The persistence of skewness in observed data. *Water Resour. Res.* 16, 123–128. doi:10.1029/WR016i001p00123.
- Pickens, J.F., Grisak, G.E., 1981. Scale-dependent dispersion in a stratified granular aquifer. *Water Resour. Res.* 17, 1191–1211. doi:10.1029/WR017i004p01191.
- Sardin, M., Schweich, D., Leij, F.J., van Genuchten, M.T., 1991. Modeling the Nonequilibrium Transport of Linearly Interacting Solutes in Porous Media: A Review. *Water Resour. Res.* 27, 2287–2307. doi:10.1029/91WR01034.
- Schumer, R., Benson, D.A., 2003a. Fractal mobile/immobile solute transport. *Water Resour. Res.* 39, 1–12. doi:10.1029/2003WR002141.
- Schumer, R., Benson, D.A., Meerschaert, M.M., and Baeumer, B., 2003b. Multiscaling fractional advection-dispersion equations and their solutions, *Water Resour. Res.*, 39(1), 1022, doi:10.1029/2001WR001229.
- Valocchi, A.J., 1985. Validity of the Local Equilibrium Assumption for Modeling Sorbing Solute Transport Through Homogeneous Soils. *Water Resour. Res.* 21, 808–820. doi:10.1029/WR021i006p00808.
- van Genuchten, M.T., Alves, W., 1982. Analytical solutions of the one-dimensional convective-dispersive solute transport equation. *Tech. Bull. - United States Dep. Agric.*
- van Genuchten, M.T., Wierenga, P.J., 1976. Mass Transfer Studies in Sorbing Porous Media I. Analytical Solutions I. *Soil Sci. Soc. Am. J.* 40, 473–480. doi:10.2136/sssaj1976.036159950040000400011x.
- Willmann, M., Carrera, J., Sánchez-Vila, X., 2008. Transport upscaling in heterogeneous aquifers: What physical parameters control memory functions? *Water Resour. Res.* 44, 1–13. doi:10.1029/2007WR006531.
- Zaramella, M., Marion, A., Lewandowski, J., Nützmann, G., 2016. Assessment of transient storage exchange and advection-dispersion mechanisms from concentration signatures along breakthrough curves. *J. Hydrol.* 538, 794–801. doi:10.1016/j.jhydrol.2016.05.004.
- Zhang, Y., Benson, D.A., Baeumer, B., 2007. Predicting the tails of breakthrough curves in regional-scale alluvial systems. *Ground Water* 45, 473–484. doi:10.1111/j.1745-6584.2007.00320.x.

Zhang, Y., Green, C.T., Baeumer, B., 2014. Linking aquifer spatial properties and non-Fickian transport in mobile-immobile like alluvial settings. *J. Hydrol.* 512, 315–331. doi:10.1016/j.jhydrol.2014.02.064.

Ziemys, A., Kojic, M., Milosevic, M., Ferrari, M., 2012. Interfacial effects on nanoconfined diffusive mass transport regimes. *Phys. Rev. Lett.* 108, 1–5. doi:10.1103/PhysRevLett.108.236102.

## CHAPTER 3:

### QUANTIFYING TRANSPORT OF ARSENIC IN BOTH NATURAL SOILS AND RELATIVELY HOMOGENEOUS POROUS MEDIA USING STOCHASTIC MODELS

#### 3.1 Abstract

The widespread distribution of arsenic in soils is a pollution source that jeopardizes human health, and the transport of Arsenic (As) under various conditions is not fully understood and quantified. This study proposes a tempered time fractional advection-dispersion equation (fADE), to model the rate-limited diffusion and sorption-desorption of As in soil. Applications show that the time fADE can effectively capture skewed breakthrough curves (BTCs) of As leaching from natural soils, which contain multiple stages of desorption that cannot be fully described by the single-rate mass transfer (SRMT) model. The time fADE model parameters change with soil properties, such as clay content and pH condition. For comparison purposes, a series of As injection column experiments packed with glass beads were conducted to generate BTCs under various hydrologic conditions. Applications show that the time fADE and the multi-rate mass transfer (MRMT) model perform better than the SRMT model in characterizing non-Fickian dynamics, especially for prolonged retention, in most runs of leaching and flushing experiments. Parameters in the MRMT model and the time fADE can be linked to simplify the fitting procedure. Such simplification and representation of experimental conditions demonstrate the promise and applicability of the time fADE model for capturing As transport in soil.

### 3.2 Introduction

Arsenic (As) is a toxic metalloid widely distributed in soils and sediments, which poses a worldwide threat for human health and the environment. Inorganic arsenic is naturally found at high levels in groundwater in various countries, such as Bangladesh, China, India, Japan, Mexico and the United States, among others (Mandal and Suzuki, 2002; Pecini et al., 2017; Thi Hoa Mai et al., 2014). Anthropogenic activities, such as mining and intensive agriculture, can accelerate the transport of arsenic to surface water, groundwater, and the food chain (Arco-Lázaro et al., 2016; Elwakeel and Al-Bogami, 2018; Gedik et al., 2015; Jiang et al., 2017; Pardo et al., 2014; Silveti et al., 2017). Water resource sustainability is significantly affected once arsenic enters aquatic ecosystems, jeopardizing human health due to its carcinogenic effects, adverse impacts on DNA replication, and substitution and binding in proteins that are vital to numerous physiological processes (Hossain, 2006; Karim, 2000; Smith et al., 2000, 1998; Sun et al., 2017), resulting in the 20<sup>th</sup> – 21<sup>st</sup> century calamity (Mohan and Pittman, 2007).

Adsorption/desorption is the major determinant of the mobility, toxicity and bioavailability of arsenic in soil (Feng et al., 2013). Adsorption to metal oxides forms inner-sphere complexes, which is the most important controlling factor of arsenic mobility in the environment (Al-Abed et al., 2007; Dickson et al., 2017). Although many methods have been proposed to remove As from liquid media, adsorption has been considered as a relatively simplistic and safer alternative (Gerard et al., 2016; Quintáns-Fondo et al., 2017). Release of arsenic from contaminated soils due to desorption is assumed to be a primary mechanism of remobilization for arsenic trapped in soils (Limousin et al., 2007; Nickson et al., 2000). Additionally, arsenic redox state and corresponding arsenic speciation and solubility are significantly controlled by pH, contributing to the degree of adsorption (stabilization or

retention) or release (mobility) of As in surface-water or groundwater (Masscheleyn et al., 1991). Chemical reactions including ligand exchange, oxidation-reduction, and precipitation may also affect the transport and transformation of arsenic in the environment (Banerjee et al., 2008; Dickson et al., 2017), and thus, the impact on arsenic dynamics can be mixed with adsorption/desorption. Reliable quantification of arsenic mobility, particularly the sorption-desorption process and other processes with similar impact (i.e. diffusional constraints) are of significant practical importance for contaminant transport prediction, appropriate remediation design, and accurate risk assessment, which are all major factors motivating this study.

The paper provides a review of quantitative methods used to model arsenic mobility in soils/sediments. The evaluation of previous modeling approaches helps to interpret the dynamics of arsenic in soils (Section 3.3), guiding the development of a generalized physical model (Section 3.4). Section 3.5 applies this new modeling approach and others to describe arsenic dynamics in soils/sediments for a leaching experiment documented in literature (Qi and Donahoe, 2011) and my laboratory flushing experiments using glass-bead columns. Section 3.6 presents model comparisons and extends implications and applications. Conclusions are drawn in Section 3.7.

### 3.3 Review of previous numerical modeling of arsenic transport in soils

Three types of models have been applied to quantify the mobility of As in soils, which are the equilibrium model, the single-rate mass transfer (SRMT) model, and the mixed equilibrium-kinetic model. The equilibrium models include the empirical distribution coefficient  $K_d$  model (De Brouwere et al., 2004; Nice et al., 2008), Langmuir and Freundlich isotherm models (Huber et al., 2012; Naftaly et al., 2016), their derivatives (Jeppu and Clement, 2012; Lin and Wu, 2001), and surface-complexation models (Goldberg, 1986; Goldberg et al., 2005). The

well-known MINTEQ geochemical code utilizes many of the above equilibrium models to solve geochemical equilibria using mass balance equations (Felmy et al., 1984; Peterson et al., 1987). Detailed evaluation of various sorption isotherm models can also be found in Limousin et al. (2007) and Selim (2013).

Second, the SRMT models have been used to analyze the fate and transport of As for various subsurface conditions. Fuller et al. (1993) found that the kinetics of As (V) (the thermodynamically stable oxidation state under oxidizing soil conditions; see Goldberg et al., 2005) sorption and desorption are consistent with diffusion as a rate-limiting process. Hence, the first-order kinetics of As, under particular conditions, can be approximated using a SRMT model. Ouvrard et al. (2002) developed a diffusive transport model with SRMT to describe sorption of As in natural manganese oxide sediment packed columns. Tufano et al. (2008) simulated the advective-dispersive transport of As under packed sand columns using a SRMT process embedded in the well-known software STAMMT-L (Haggerty and Gorelick, 1995).

Third, the mixed equilibrium-kinetic models have been applied to quantify the relatively long-term desorption of As observed in laboratory-scale experiments. Many column transport experiments have shown that the desorption of As (V) does not follow a single kinetic rate. Note that arsenate As (V) is the predominant form of arsenic in soil (Feng et al., 2013; Pansar-Kallio and Manninen, 1997) and it has a strong affinity for various minerals (Goldberg, 2002; Manning and Goldberg, 1997; Song et al., 2015). Under such dynamics, the measured desorption rate has been observed to be rapid initially (which can be interpreted as instantaneous equilibrium desorption following the linear isotherm model) and then decline slowly (i.e., a slow desorption following the first-order kinetics), resulting in extensive tailing in the breakthrough curves (BTCs) and, therefore, motivating the application of mixed equilibrium-kinetic models. Zhang

and Selim (2006) used a nonlinear equilibrium-kinetic multi-reaction transport model to describe the asymmetrical and retarded As (V) BTCs; and Qi and Donahoe (2011) combined equilibrium and nonequilibrium-kinetic models to quantify the time-dependent desorption rate of As. Zhang and Lv (2009) also proved numerically that the pore-scale heterogeneity of soils can result in time-dependent sorptive kinetics of solutes, using a lattice Boltzmann method.

To draw an intermediate conclusion, successful applications of the above three different models imply that both the magnitudes and desorption rates of As (denoted as  $\omega [T^{-1}]$ ) may change significantly with experimental conditions. If the reaction is relatively fast, the reversible sorption-desorption process can reach equilibrium during the experimental time and the equilibrium model is applicable. If the desorption process lasts longer than the experimental period, multiple mass-transfer coefficients might be needed to describe the time-dependent desorption rate of As.

Long-term (or variable) kinetics in sorption and/or desorption of As were also observed by many researchers after an initially rapid reaction, as documented by Qi and Donahoe (2009). Fuller et al. (1993) found that a period of rapid (<5 min) As (V) uptake from solution was followed by continued uptake for at least eight days, as As (V) moved to sorption sites on ferrihydrite surfaces within aggregates of colloidal particles. O'Reilly et al. (2001) found that >35% of the sorbed As can be released rapidly within 24 h, while taking ~5 months to 1 year to remove the remaining As from the system. Arai and Sparks (2002) observed slow sorption of As (V) at pH 7.8 for more than 1 year, while conversely demonstrating that As (V) can be sorbed rapidly (i.e., ~ 3 days) on aluminum oxide at pH 4.5 conditions. Zhang and Selim (2005) also found that the rate of As (V) retention was rapid initially, followed by slow retention for more than 1 month. How to efficiently model the variable As kinetics remains a historical challenge.

### 3.4 Stochastic models to simulate arsenic mobility in saturated soils

Novel stochastic models are needed to capture transport and fate of As in soils involving multiple stages and transfer rates. First, the long-term sorption or desorption process may sometimes include multiple stages, requiring a physical model containing more than two transfer rates. For example, Limousin et al. (2007) argued that the sorption process can contain three stages, including the fast desorption stage, the equilibrium or slow sorption stage, and the stage of enhanced adsorption. Qi and Donahoe (2009) found that As (V) is present on three different sites within soils after sequential leaching: equilibrium controlled (likely due to sorption on metal oxides and/or layer silicate minerals), kinetically controlled (likely due to sorption on residual herbicide particles in the soil), and irreversible sites (due likely to sorption to ferric hydroxide).

Second, the sorption-desorption process occurring at the water-soil interface has been found to be affected by various chemical, physical, biochemical, and hydrological properties. These properties include pH, competing anions (Arco-Lázaro et al., 2016), soil mineralogy (Cao et al., 2003; Ladeira and Ciminelli, 2004; Seco-Reigosa et al., 2013), redox potential (Couture et al., 2015; Masscheleyn et al., 1991), the water flow rate (Brusseau, 1992, 1993; Pang et al., 2002), and the soil particle size (Ouvrard et al., 2002). Due to the intrinsic heterogeneity of natural systems, the above factors may not be distributed homogeneously, which can lead to multiple sorption (or desorption) rates. The rate of mass exchange between mobile and immobile As particles therefore may exhibit a wide distribution for even one soil column. However, none of the previous models reviewed in section 3.3 can characterize such a broad distribution of mass exchange rate, motivating the development of a new physical model as described below.

To capture 1) the broad range of mass exchange rates, 2) the subtle quantitative relationship between As mobility and most of the controlling factors, and 3) complex transport dynamics of arsenic solutes after being released from sorbent phases in natural soils, I use the state-of-the-art fractional-order derivative model, which can describe complex transport behaviors (Zhang et al., 2015). I start from the general mobile-immobile model (Zhang et al., 2015):

$$\frac{1}{\theta_m} \frac{\partial C_{tot}}{\partial t} = \frac{\partial C_m}{\partial t} + \beta \frac{\partial C_m}{\partial t} * g(t) = -V \frac{\partial C_m}{\partial x} + D \frac{\partial^\alpha C_m}{\partial x^\alpha} - (C_{m,0} - \beta C_{im,0})g(t), \quad (3-1a)$$

$$C_{im}(x, t) = \int_0^t g(t-s) C_m(x, s) ds - \beta \int_0^t g(s) C_{im,0} ds, \quad (3-1b)$$

where  $C_m$ ,  $C_{im}$ , and  $C_{tot}$  [ $ML^{-3}$ ] denote the As concentration in the mobile, immobile, and total phases, respectively;  $\theta_m$  [dimensionless] represents the effective porosity in the mobile phase;  $\beta$  is the capacity coefficient;  $V$  [ $LT^{-1}$ ] and  $D$  [ $L^\alpha T^{-1}$ ] are the effective velocity and dispersion coefficient, respectively;  $\alpha$  [dimensionless] ( $1 < \alpha \leq 2$ ) is the space index; The initial conditions are:  $C_{m,0} = C_m(x, t=0)$  and  $C_{im,0} = C_{im}(x, t=0)$  [ $ML^{-3}$ ], which denote the initial concentration in the mobile and immobile phases, respectively; and  $g(t)$  denotes the memory function. The operator  $\partial^\alpha / \partial x^\alpha$  in (3-1a) denotes the standard Riemann-Liouville fractional derivative in space. Eq. (3-1a) describes the total concentration change due to the advection and (fractional) dispersion of mobile solutes with the source/sink terms, while Eq. (3-1b) shows that the immobile phase concentration is affected by both the previous mobile concentration as filtered by the memory function and the initial immobile source decaying in time. I used a flux type boundary condition at the inlet boundary and a zero-concentration gradient boundary condition at the outlet boundary. The model was solved numerically using the implicit, finite difference method.

I assume that the memory function  $g(t)$  follows the truncated power-law function defined by Meerschaert et al. (2008):

$$g(t) = \int_t^{\infty} e^{-\lambda r} \frac{\gamma r^{-\gamma-1}}{\Gamma(1-\gamma)} dr, \quad (3-2)$$

where  $\gamma$  [dimensionless] ( $0 < \gamma \leq 1$ ) is the time index,  $\lambda$  [ $T^{-1}$ ] is the truncation parameter, and the symbol  $\Gamma(\cdot)$  denotes the Gamma function. Inserting (3-2) into (3-1), I obtain the tempered time fractional advection-dispersion equation (fADE) model:

$$\frac{\partial C_m}{\partial t} + \beta \frac{\partial^{\gamma, \lambda} C_m}{\partial t^{\gamma, \lambda}} = -V \frac{\partial C_m}{\partial x} + D \frac{\partial^{\alpha} C_m}{\partial x^{\alpha}} - (C_{m,0} - \beta C_{im,0}) g(t), \quad (3-3a)$$

$$\frac{\partial C_{im}(x,t)}{\partial t} = \frac{\partial^{\gamma, \lambda} C_{im}(x,t)}{\partial t^{\gamma, \lambda}} - \beta g(t) C_{im,0}, \quad (3-3b)$$

where the operator  $\partial^{\gamma, \lambda} / \partial t^{\gamma, \lambda}$  denotes the tempered, Caputo-type of fractional derivative in time (Meerschaert et al., 2008), which is defined as  $\frac{\partial^{\gamma, \lambda}}{\partial t^{\gamma, \lambda}} P = e^{-\lambda t} \frac{\partial^{\gamma}}{\partial t^{\gamma}} (e^{\lambda t} P) - \lambda^{\gamma} P$ . Tempered anomalous subdiffusion/time fractional derivative assumes a specific memory function form (3-2) that is an exponentially truncated power-law function to describe waiting times for solute particles trapped in the immobile phases.

In the time fADE model (3-3), I assume that 1) arsenic contaminants can be initially located in the immobile phase (to represent the initial state of a leaching experiment) and/or the mobile phase (representing a flushing experiment which will be discussed in detail below), and 2) normal- to super-diffusive jumps along interconnected preferential flow paths. Eq. (3-3a) shows that the immobile particles can provide a source term (which represents desorbing As from solid soils and decays with time) for mobile mass, and the initial mobile mass continuing to decline due to transition (exchange) to the immobile state (phase). When the truncation

parameter  $\lambda \rightarrow 0$  and the space index  $\alpha = 2$ , (3-3) reduces to the fractal mobile/immobile model proposed by Schumer et al. (2003). When the contaminant is initially located in the mobile phase, model (3-3) reduces to the physical model proposed by Zhang et al. (2015).

To solve model (3-3), I extend the particle tracking method proposed by Zhang et al. (2015). All particles are released initially in the immobile domain, representing the sorbed, immobile As phase. The  $i$ -th particle can enter the mobile zone at a specific/random time  $\tau_i$ . Such a time is called the “birth age/birth time” of the  $i$ -th particle, which can be generated numerically using the following scheme:

$$\tau_i = \left[ \left| \cos\left(\frac{\pi\gamma}{2}\right) \beta \right|^{1/\gamma} dL_\gamma(\beta^* = +1, \sigma = 1, \mu = 0) \right], \quad (3-4)$$

where  $dL_\gamma(\beta^* = +1, \sigma = 1, \mu = 0)$  [dimensionless] denotes the stable random variable with the maximum skewness  $\beta^*$ , unit scale  $\sigma$ , and zero shift  $\mu$ .

It is noteworthy that the tempered stable density in model (3-3) is used to capture the truncated trapping time for As in soils. This is the major assumption used in this study to develop model (3-3). When the initially mobile As was absorbed by soils, the clock started to record the trapping time, whose distribution is assumed to follow the  $\gamma$ -stable density (Schumer et al., 2003). The  $\gamma$ -stable density is selected in this study to represent the residence time distribution density, since it was proved to be the universal density for hydrological transport, especially for the residence times of pollutants in soil and aquifers (Cvetkovic, 2011; Zhang et al., 2015). Before the leaching process started, each absorbed As particle already remained immobile for a random amount of time. The remaining residence time, therefore, should follow a truncated  $\gamma$ -stable density defined by the 2<sup>nd</sup> term in Eq. (3-3a). I test the above assumption in Sec. 3.5.1.

For comparison purposes, the following well-known MRMT model is also used

(Haggerty and Gorelick, 1995):

$$\frac{\partial C_m}{\partial t} + \sum_{j=1}^N \beta_j \frac{\partial C_{im}^j}{\partial t} = -V \frac{\partial C_m}{\partial x} + D \frac{\partial^2 C_m}{\partial x^2} \quad , \quad (3-5a)$$

$$\frac{\partial C_{im}^j(x,t)}{\partial t} = \omega_j [C_m(x,t) - C_{im}^j(x,t)] \quad , \quad (3-5b)$$

where  $j=1, 2, \dots, N$  denotes the  $j$ -th immobile zone;  $\beta_j$  [dimensionless] is the capacity coefficient for the  $j$ -th immobile zone; and  $\omega_j [T^{-1}]$  is the mass exchange rate between the mobile zone and the  $j$ -th immobile zone.

The time fADE model (3-3) can be practically convenient, since the time-nonlocal parameters in (3-3) do not depend on the exact location and/or concentration of each immobile zone, but rather are controlled by the residence time in the immobile domain (Zhang et al., 2014). On the contrary, the standard MRMT model (3-5) must fit each  $C_{im}^j(x, t=0) = f_j(x)$  (where  $j=1, 2, \dots, N$ ), increasing the total number of fitting parameters by  $2N$ . I will further investigate the discrepancy between these two models using real data in the next section.

### 3.5 Laboratory experiments and model applications

#### 3.5.1 Case 1: Leaching experiments through heterogeneous soils

Qi and Donahoe (2011) performed column leaching experiments on four arsenic-contaminated soil samples (collected from four different industrial sites after five decades of natural leaching), which were denoted as BH, FW, JA, and PA (see Table 3-1). All the measured BTCs showed rapid initial arsenic release, followed by prolonged concentration tailing whereby slopes can differ among soil samples (Fig. 3-1) due to different degrees of heterogeneity, and

unable to be effectively captured by the traditional equilibrium models (Qi and Donahoe, 2009, 2008).

Soil type	$L$ [cm]	$V$ [cm/day]	$D$ [cm <sup>2</sup> /day]	$\gamma$	$\beta$ [day <sup><math>\gamma</math>-1</sup> ]	$\lambda$ [day <sup>-1</sup> ]
	Measured	Measured	Fitted	Fitted	Fitted	Fitted
BH	40.64	100.9	0	0.08	9.5	$1 \times 10^{-6}$
FW	40.64	92.3	0	0.06	12.1	$1 \times 10^{-6}$
JA	40.64	89.7	0	0.30	5.5	$1 \times 10^{-6}$
PA	40.64	92.3	0	0.16	7.1	$1 \times 10^{-6}$

Table 3-1. Leaching experiment: Parameters for the time fADE model (3-3). In the legend,  $L$  denotes the travel distance (i.e., the length of the soil column);  $V$  is the flow velocity;  $D$  is the dispersion coefficient;  $\gamma$  is the time index;  $\beta$  is the fractional-order capacity coefficient; and  $\lambda$  is the truncation parameter.

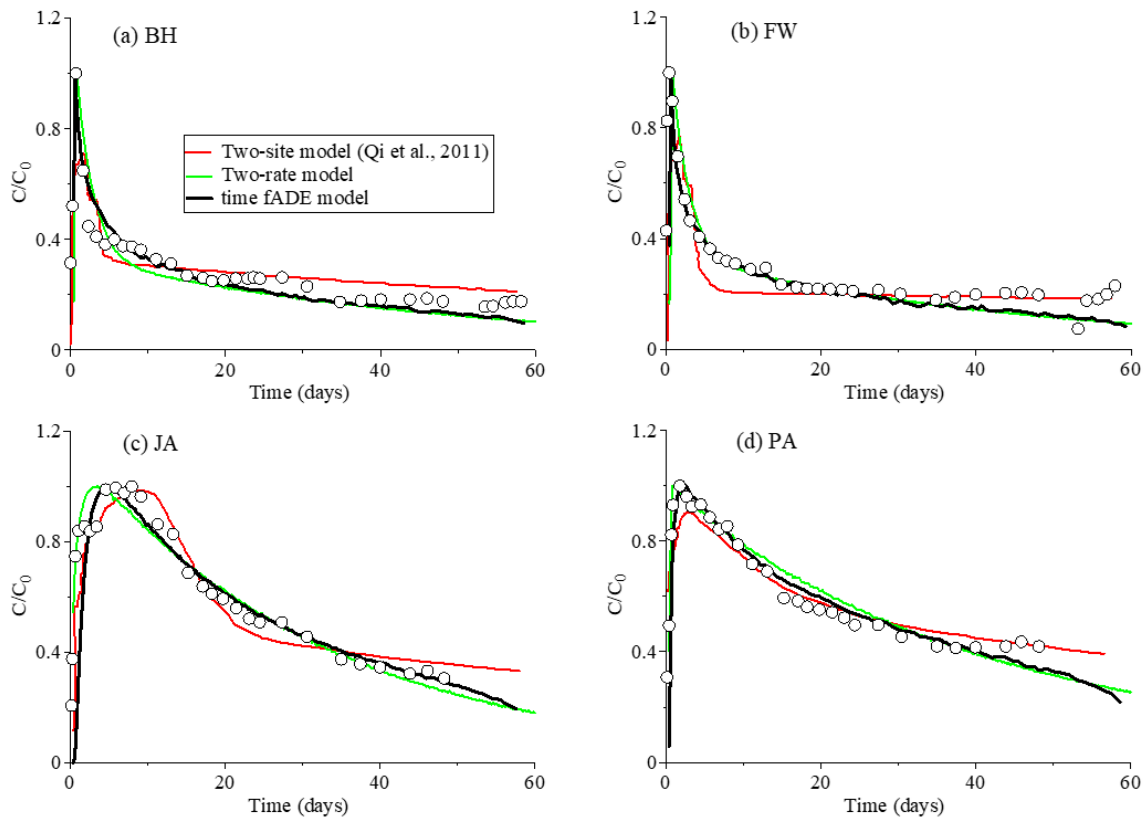


Figure 3-1. Leaching experiment: Comparison between measured (circles) and modeled (lines) arsenic breakthrough curves for four arsenic-contaminated soils (a) BH, (b) FW, (c) JA, (d) PA using the two-site model (red line), the MRMT model with two rates (green line), and the time fADE model (black line).

I first apply the time fADE model (3-3) to describe the measured arsenic BTCs. The best-fit results are shown in Fig. 3-1. The time fADE model (3-3) can capture the general trend of the measured BTCs, including both the fast peak and the strong tailing behavior. The best-fit parameters are shown in Table 3-1, where both the dispersion coefficient  $D$  and the truncation parameter  $\lambda$  approach zero. The negligible dispersion  $D$  is probably due to the high flow rate and the relatively short soil column (note that laboratory column transport experiments typically depict advection-dominated processes), compared to the field measured groundwater flow conditions (which are usually dispersion dominated). The relatively large fractional capacity coefficient  $\beta$  can also account for the strong variation in the transport rate of arsenic particles by assigning random trapping times for each arsenic particle. The small truncation parameter  $\lambda$  is required to capture the prolonged, power-law late-time tailing for all measured BTCs, indicating that the transport has not transformed from non-Fickian to Fickian behavior during the experimental period (<2 months). Therefore, although the sorption process in leaching should be described by a truncated distribution of the initially heavy-tailed residence times, the mean residence time in natural soils can be larger than the experimental period, and hence the truncation cannot be identified. Hence model (3-3) can be simplified to:

$$\frac{\partial C_m}{\partial t} + \beta \frac{\partial^\gamma C_m}{\partial t^\gamma} = -V \frac{\partial C_m}{\partial x} + \beta C_{im,0} \frac{t^{-\gamma}}{\Gamma(1-\gamma)} \quad , \quad (3-6a)$$

$$\frac{\partial C_{im}}{\partial t} + \beta \frac{\partial^\gamma C_{im}}{\partial t^\gamma} = -V \frac{\partial C_{im}}{\partial x} - C_{im,0} \frac{t^{-\gamma}}{\Gamma(1-\gamma)} \quad , \quad (3-6b)$$

$$\frac{\partial C_{tot}}{\partial t} + \beta \frac{\partial^\gamma C_{tot}}{\partial t^\gamma} = -V \frac{\partial C_{tot}}{\partial x} \quad , \quad C_{tot}(x, t = 0) = \theta_{im} C_{im,0} \quad . \quad (3-6c)$$

where  $\partial^\gamma / \partial t^\gamma$  is the standard (i.e., without truncation) Caputo-type fractional derivative to describe the power-law late time tailing behavior.

Using the simplified model (3-6), I only need to fit two model parameters – the time index  $\gamma$  and the fractional-order capacity coefficient  $\beta$ . My results further found that these two parameters are related to certain soil properties, such as pH level and clay content of the sample. The best-fit fractional capacity coefficient  $\beta$  is relatively large, indicating a large percentage of immobile mass in the soil samples, which also leads to a small dispersion coefficient (since the large capacity coefficient can describe a wide range of residence times for As particles, resulting in quite different transport velocities for As particles).

For comparison purposes, I also quantify the leaching experiments using the SRMT model, where  $N=1$  in model (3-5). Two examples are shown in Fig. 3-2.

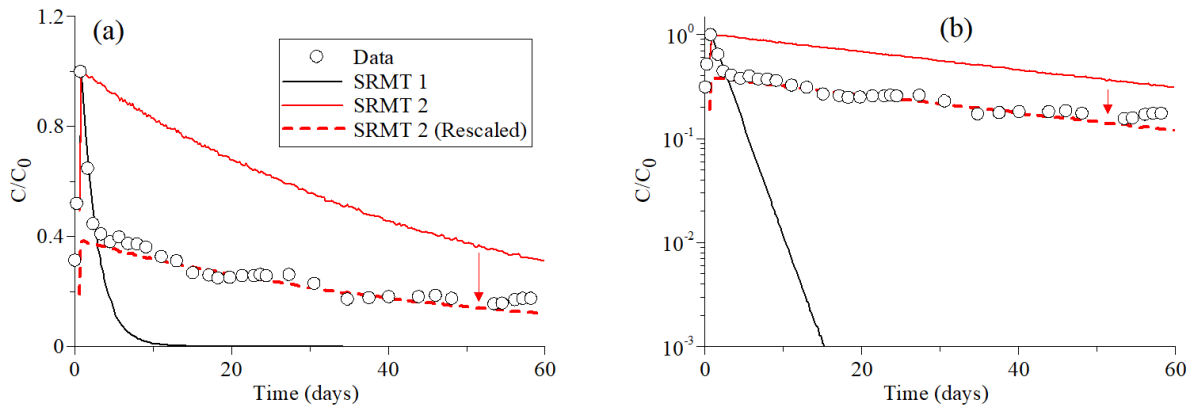


Figure 3-2. Leaching experiment: Comparison between the measured (circles) and modeled (lines) As breakthrough curves using the SRMT model. (b) is the semi-log plot of (a), to show the leading edge of the BTCs. The data are from the soil column BH in Qi and Donahoe (2011). In the model “SRMT1” (black line), the parameters are: capacity coefficient  $\beta = 0.5$ , and rate  $\omega = 0.5 \text{ day}^{-1}$ ; in the model “SRMT2” (red line),  $\beta = 0.5$ , and  $\omega = 0.02 \text{ day}^{-1}$ . The model “SRMT2 (Rescaled)” (red dashed line) denotes the rescaled result of SRMT2 to fit the late-time tail of the observed BTCs.

Example 1 has a relatively large rate coefficient  $\omega=0.5 \text{ day}^{-1}$ , representing a short mean residence time ( $1/\omega = 2$  days), generating a fast release of As. Example 2 has a much smaller  $\omega=0.02 \text{ day}^{-1}$ , representing a long mean residence time ( $1/\omega = 50$  days), generating a prolonged tailing at the late time, and the resultant slow decline of the BTC is similar to the data. None of

the SRMT models can capture both the early peak and the late-time tail of the BTC, indicating the presence of a multiple-rate mass transfer process, and therefore, motivating the application of the MRMT model.

I then fit the same BTCs using the standard MRMT model (3-5). Qi and Donahoe (2009) found that 20~50% As remained in the soils after leaching for 60 days. I select  $\beta_1$  and  $\beta_2$  to be 0.5, resulting in the immobile phase mass partition of 0.33 (i.e., 33% of the original total mass) when the immobile mass reaches equilibrium. Qi and Donahoe (2011) also found that the initial mass for As in the kinetic desorption stage should be much larger (1.2 to 46 times larger) than that in the equilibrium-controlled desorption stage. My best-fit results show that the initial mass for the slow mass exchange stage should be 9 times larger than that for the fast mass exchange stage. The fitting results are similar to those using the time fADE model (3-6), except for some subtle discrepancies described below (Fig. 3-1). For the JA soil column, the MRMT model (3-5) overestimates the arrival of As and the peak velocity; for the FW and PA soil columns, the MRMT model (3-5) slightly overestimates a portion of the decline rate of As. In most cases, the simplified time fADE model (3-6) fits the observed BTCs better than the MRMT model (3-5), and model (3-6) contains fewer parameters than model (3-5). It is also noteworthy that the best-fit dispersion coefficient for model (3-5) might be unrealistically large for the JA soil column (Table 3-2).

	$L$ [cm]	$V$ [cm/day]	$D$ [cm <sup>2</sup> /day]	$\beta_1$	$\omega_1$ [day <sup>-1</sup> ]	$\beta_2$	$\omega_2$ [day <sup>-1</sup> ]	$C_{im}^1 / C_{im}^2$
Source	Measured	Measured	Fitted	Fitted	Fitted	Fitted	Fitted	Fitted
BH	40.64	100.9	0.001	0.5	0.5	0.5	0.02	10%
FW	40.64	92.3	0.001	0.5	0.52	0.5	0.022	10%
JA	40.64	89.7	4000	0.5	0.05	0.5	0.03	10%
PA	40.64	92.3	0.001	0.5	0.05	0.5	0.02	10%

Table 3-2. Leaching experiment: Parameters for the MRMT model.  $\omega_j$  is the rate coefficient for the  $j$ -th immobile zone;  $\beta_j$  is the capacity coefficient for the  $j$ -th immobile zone; and  $C_{im}^1 / C_{im}^2$  denotes the initial mass ratio for particles located in the 1<sup>st</sup> and the 2<sup>nd</sup> immobile phases.

### 3.5.2 Case 2: Flushing experiment: As (V) transport through laboratory columns packed with ideal homogeneous glass beads

Two sets of laboratory column transport experiments were conducted, to provide first-hand data to quantify the time-dependent sorption-desorption of arsenic transport. Glass beads with a diameter varying from 0.8 to 1 mm filled the cylindrical borosilicate glass columns. The first set of experiments included a column with an inner diameter (*i.d.*) of 5.5 cm and a length (*L*) of 40 cm, wherein three steady-state water flux rates (*Q*) were used for flushing (4, 2, and 0.5 mL/min for the fast, moderate, and slow rates) with corresponding linear pore velocity of 0.44, 0.258, and 0.069 cm/min, respectively (see Fig. 3-3). The second set of experiments included a smaller column (*i.d.*=2.6 cm; *L*=20 cm) wherein three water flux rates (*Q*) were also used (2.5, 0.5, and 0.2 mL/min for the fast, moderate, and slow rates) with corresponding linear pore velocity of 1.67, 0.67, and 0.1 cm/min, respectively. All the other experimental apparatuses/conditions were kept the same, so that I could focus on the effect of travel distance and flow rate on the sorption-desorption process occurring at the water-soil interface. Also, all experiments were conducted in a climate-controlled laboratory at 22(±1) °C.

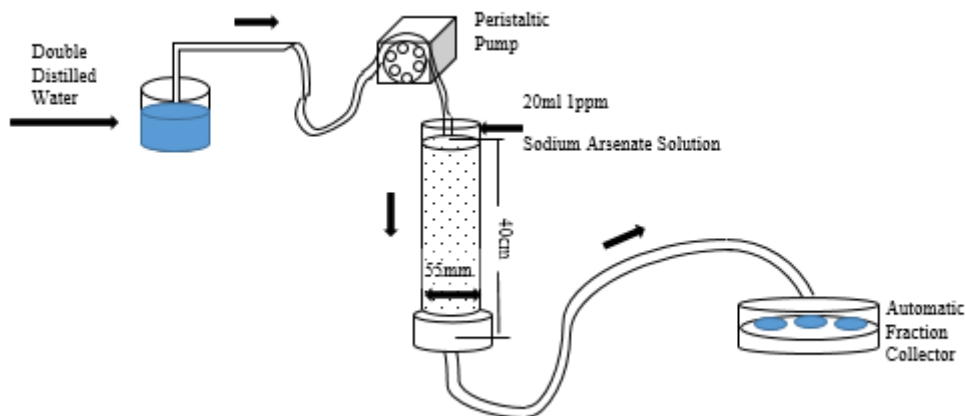


Figure 3-3. Case 2 (Flushing experiment): Schematic diagram showing the setup of the column transport flushing experiments (i.e., glass bead packings).

The glass-bead columns were first soaked in a 2 percent dilute nitric acid solution and then soaked in a 1 mole/L sodium hydroxide solution to remove any chemicals within the media. The columns were then flushed with tap water to displace any remaining acid or alkali in the column. Before each experiment, the column was flushed with double distilled water for at least 24 hours to remove any impurities in the glass beads. A multi-channels peristaltic pump (LongerPump BT 100-1L, Boonton, NJ) was calibrated before each use. The outflow ended in a dry 10 mL measuring cylinder. The operation was repeated several times, until the liquid in the measuring cylinder was in accordance with the set flow rate. A 20-ml 1 ppm sodium arsenate solution (As (V)) was injected at the top of the column. The injection rate (4 ml/min) was kept constant with the outflow rate at the bottom of the column under fully saturated conditions and monitored to ensure no air entered the column during injection. An automated fraction collector (BS-100A, 100 collection tubes, Max capacity 12 ml) was used to collect the leachate over time. The same experimental process was repeated for all the three different flow rates for each column system. A schematic diagram showing the setup of the first set of glass-bead column transport experiments is depicted in Fig. 3-3.

After all the arsenate was discharged, an inductively coupled plasma mass spectrometer (NexION 300X ICP-MS, Perkin Elmer) was used to measure the arsenate concentration from each tube (concentration vs. time). For each flow rate experiment, the aqueous leachate samples were collected from the end (bottom) of the column (i.e., discharged directly into the fraction collector) and analyzed for arsenate as described above, thus allowing for the BTCs to be generated (concentration vs. time). All measured BTCs showed rapid initial arsenic release combined with heavy late-time tailing behavior (see Fig. 3-4 and 3-5).

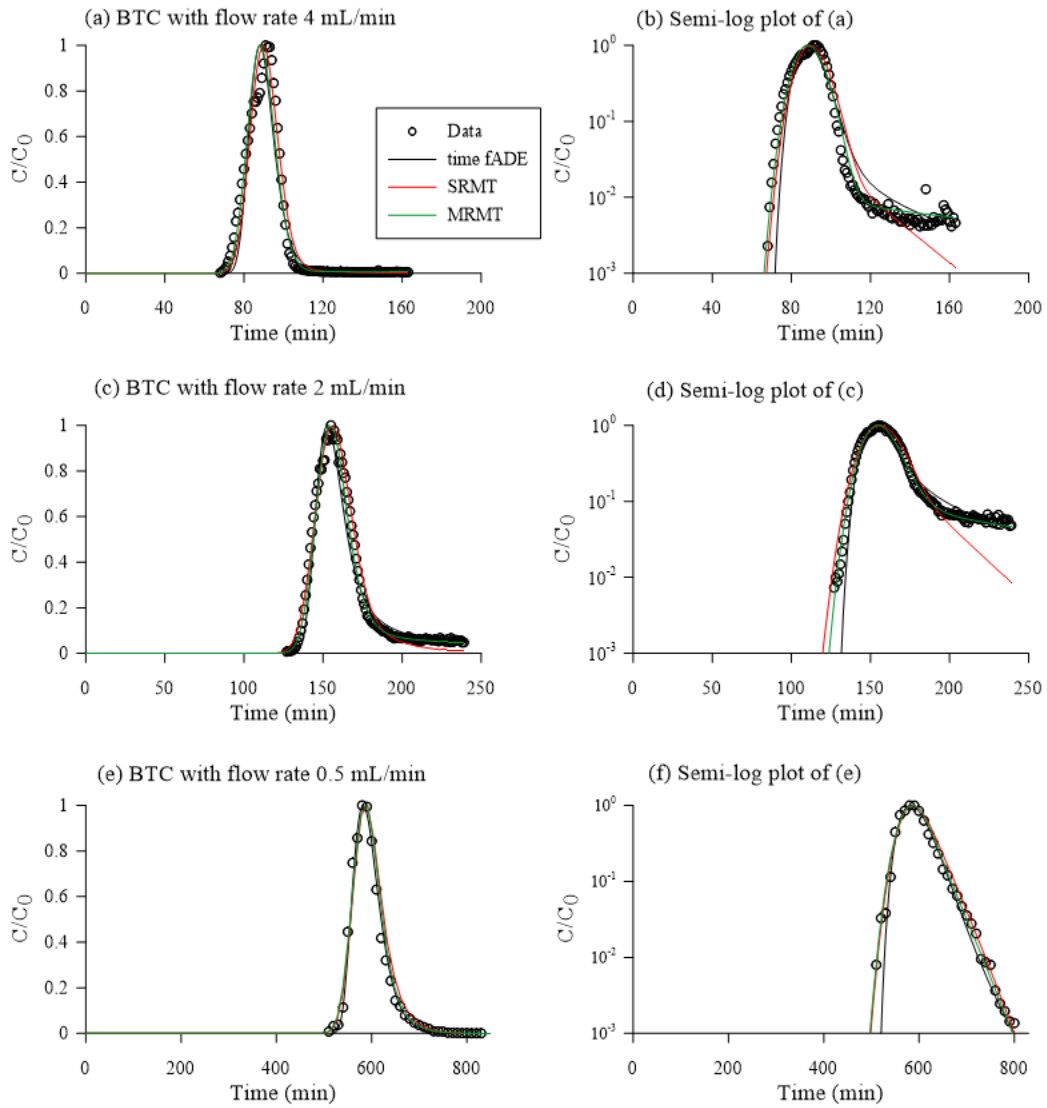


Figure 3-4. Case 2 (Flushing experiments): Comparison between the measured (circles) and modeled (lines) As BTCs using the time fADE model (black line), the SRMT model (red line) and the MRMT model (green line) with three different experimental water flow rates  $Q = 4$  mL/min, 2 mL/min, and 0.5 mL/min through the first column (40 cm ( $L$ )  $\times$  5.5 cm ( $i.d.$ )). The right plot is the semi-log plot of the left one, to show the leading edge of the BTCs and the slopes.

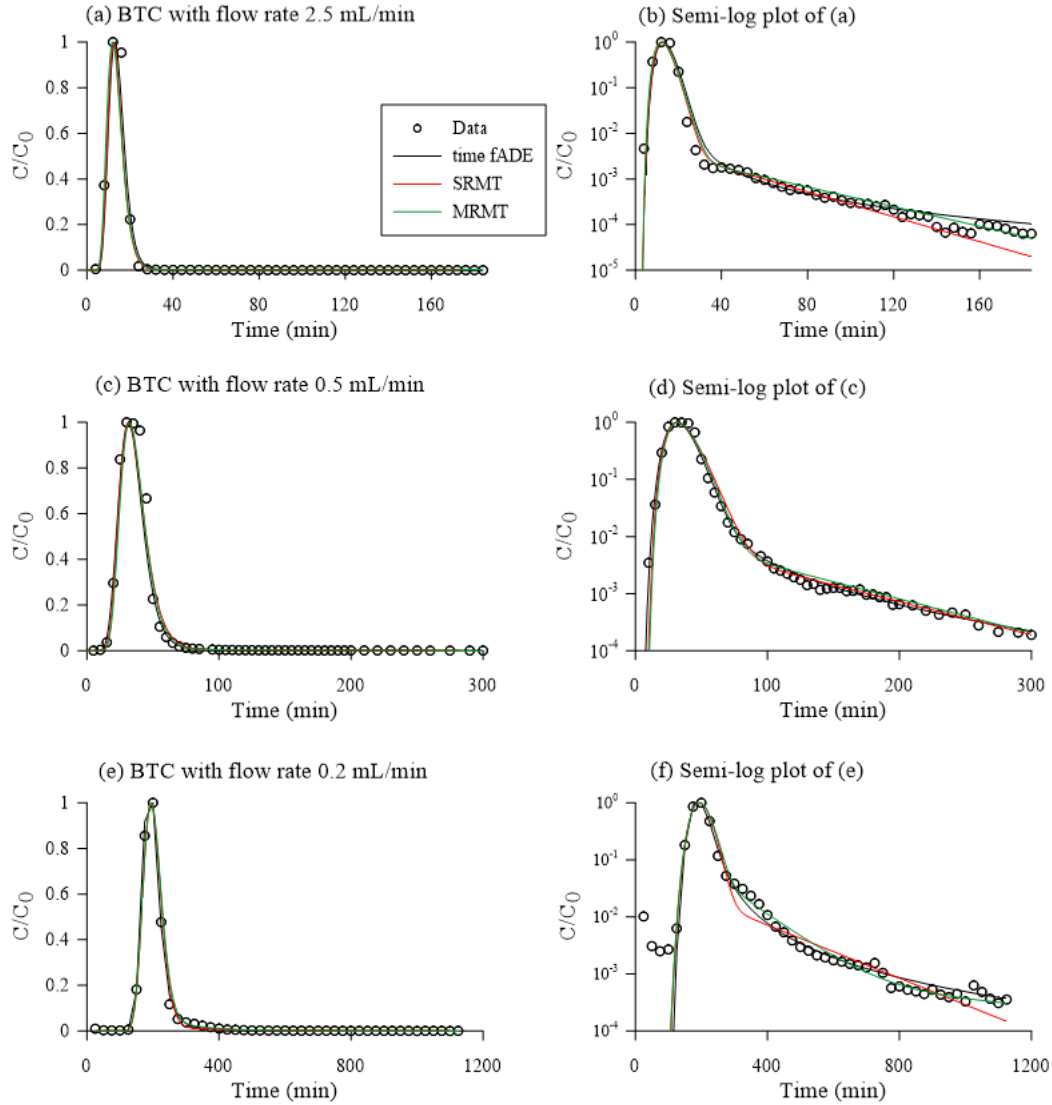


Figure 3-5. Case 2 (Flushing experiments): Comparison between the measured (circles) and modeled (lines) As BTCs using the time fADE model (black line), the SRMT model (red line) and the MRMT model (green line) with three different experimental water flow rates  $Q = 2.5$  mL/min, 0.5 mL/min, and 0.2 mL/min through the second column (20 cm ( $L$ )  $\times$  2.6 cm ( $i.d.$ )). The right plot is the semi-log plot of the left one, to show the leading edge of the BTCs and the slopes.

### 3.5.2.1 MRMT model

The MRMT model (3-5) was used to fit the generated arsenate BTCs. Since all the late-time tails of BTCs show two distinct slopes in the semi-log plot (Fig. 3-4 and 3-5) with a steep-sloped tail followed by a gentle-sloped tail, I use the MRMT model with two immobile domains

(i.e.,  $N=2$  in models (3-5)) to fit the BTC data. The best-fit results are shown in Fig. 3-4 and 3-5, with the best-fit parameters listed in Table 3-3.

Column scale	Flow rate [mL/min]	$L$ [cm]	$\alpha_L$ [cm]	$V$ [cm/min]	$\omega_1$ [min <sup>-1</sup> ]	$\beta_1$ [-]	$\omega_2$ [min <sup>-1</sup> ]	$\beta_2$ [-]
	Measured	Measured	Fitted	Fitted	Fitted	Fitted	Fitted	Fitted
40×5.5 cm	4	40	0.12	0.461	0.008	0.032	0.003	0.233
	2	40	0.08	0.265	0.007	0.078	0.007	0.455
	0.5	40	0.03	0.07	0.002	0.053	0.001	0.037
20×2.6 cm	2.5	20	0.85	1.42	0.02	0.047	0.0005	0.02
	0.5	20	0.8	0.53	0.007	0.096	0.0005	0.038
	0.2	20	0.2	0.1	0.0025	0.124	0.0002	0.054

Table 3-3. Case 2 - Fitted parameters for the MRMT model. In the legend,  $\alpha_L$  is the longitudinal dispersivity;  $\beta_j$  is the capacity coefficient for the  $j$ -th immobile zone; and  $\omega_j$  stands for the mass transfer rate between the mobile zone and the  $j$ -th immobile domain, where  $j=1, 2$  denotes the number of immobile zones.

The longitudinal dispersivity  $\alpha_L$  fitted above increases with an increasing flow rate in both columns (Table 3-3), and the same trend is found for the other models used in this study (discussed below) and shown in literature. For example, experimental studies have shown that dispersivity increases with an increasing velocity under a variety of conditions (Brusseau, 1993; Hu and Brusseau, 1994). For the relatively homogeneous glass-bead column experiments (i.e., with a relatively high flow velocity) conducted herein, mechanical dispersion is the major component of dispersion, and is consistent with the increasing trend with velocity. In addition, the velocity  $V$  in the MRMT model (Table 3-3) is close to the measured peak velocity.

The best-fit pair of mass-exchange coefficients,  $\omega_j$  and  $\beta_j$ , changes with a different trend with the flow rate (Table 3-3). The fastest flow rate corresponds to the largest mass-exchange rate and smallest capacity coefficient. The mass exchange rate for the first immobile domain is larger than the second domain ( $\omega_1 > \omega_2$ ), and the capacity coefficient for the first immobile domain is smaller than the second domain ( $\beta_1 < \beta_2$ ). Haggerty and Gorelick (1995) and Haggerty et al. (2000) found that the first few mass transfer rate coefficients in the multi-rate

series dominate, and that larger rate coefficients have very small weights (i.e., capacity coefficients). As shown by Fig. 3-4 and 3-5, the BTC tails for all three velocities initially have steep slopes, and are then followed by gentle slopes. This result is consistent with a large  $\omega_1$  and a small  $\omega_2$  describing the initial relative faster mass transfer and later time slow mass transfer dynamics, respectively. The MRMT model with two immobile domains is sufficient to capture the key characteristics of the BTCs. Comparing the three flow velocity cases varying from fast to slow flow, I observe a decrease in mass exchange rates for all immobile domains, and an increase in capacity coefficients for all immobile domains. A slower water flow rate will cause slow mass transfer rates between mobile and any number of immobile domains, and the immobile percentage will increase with decreasing flow rate, since particles will experience longer times at the solid-aqueous interface.

### 3.5.2.2 fADE model

For comparison purposes, I applied the time fADE model (3-3) to describe the arsenic transport behavior. The best-fit results using model (3-3) for the first and second columns (40 by 5.5 and 20 by 2.6 cm respectively) are shown in Fig. 3-4 and 3-5. The best-fit parameters for both column experiment data (BTCs) are shown in Table 3-4.

Column scale	Flow rate [mL/min]	$L$ [cm]	$V$ [cm/min]	$D$ [cm <sup>2</sup> /min]	$\gamma$	$\beta$ [min <sup>-1</sup> ]	$\lambda$ [min <sup>-1</sup> ]
40×5.5 cm	Measured	Measured	Fitted	Fitted	Fitted	Calculated	Calculated
	4	40	2.1	1	0.82	0.265	0.003
	2	40	1.7	1	0.87	0.533	0.007
20×2.6 cm	0.5	40	0.58	0.8	0.96	0.09	0.001
	2.5	20	2.4	0.8	0.83	0.067	0.0005
	0.5	20	0.8	0.1	0.88	0.135	0.0005
	0.2	20	0.125	0.001	0.95	0.178	0.0002

Table 3-4. Case 2 - Fitted parameters for the time fADE model for the two glass-bead column experiments.

The time fADE model (3-3) contains five parameters which are necessary in model fitting. However, two of them, which are the effective capacity coefficient  $\beta$  and the truncation parameter  $\lambda$ , can be obtained using the best-fit results in the above MRMT model to improve the model's applicability. As mentioned above, the time fADE model combines all immobile domains, so that the total number of unknown parameters can be minimized. The effective capacity coefficient in model (3-3), denoted as  $\beta$ , can be calculated by adding the two capacity coefficients used in the MRMT model, leading to  $\beta = \beta_1 + \beta_2$ . Most of the resultant  $\beta$  decrease corresponds directly with an increase in flow velocity. This trend is consistent with the assumption that a larger flow velocity tends to break up more grain clumps, leading to a smaller immobile domain percentage.

The truncation parameter  $\lambda$  is the inverse of the longest mean residence time, which is the second mass-exchange rate  $\omega_2$  obtained in the MRMT model. The best-fit truncation parameter  $\lambda$  decreases with a decrease in flow velocity. A smaller truncation parameter denotes a later transition from non-Fickian to Fickian transport condition. All truncation parameters used in the time fADE model are in the range of  $10^{-4}$  to  $10^{-3} \text{ min}^{-1}$ , which indicates a late transition. It should be noted that the experiments did not run until the model truncation time.

The three other parameters in model (3-3), which are the average plume velocity  $v$ , the dispersion coefficient  $D$ , and the fractional time index  $\gamma$ , need to be fitted using the measured arsenic BTC. The best-fit  $v$  is slightly larger than the measured one, likely due to the capacity coefficient  $\beta$  on the left-hand side of (3-3) that adds to the immobile component of arsenic dynamics (note that when  $\gamma = 1$  and  $\alpha = 2$ , model reduces to the standard advection-dispersion equation (ADE) with a retardation coefficient  $1 + \beta$ ).

The dispersion coefficient  $D$  has to be fitted from the measured BTC, due to the lack of direct estimation. The best-fit dispersion coefficient  $D$  (or dispersivity) increases with an increasing travel distance and scale of the experiment, for both columns with the same flow rate (such as 0.5 mL/min). This trend is consistent with the fitting results of the other models, following the well-known “scale effect” (Hauns et al., 2001; Khan and Jury, 1990; Vanderborght and Vereecken, 2007). The best-fit  $D$  (or dispersivity) also increases when the flow rate increases. The faster the water flows, the wider the plume becomes, resulting in a larger dispersion coefficient. A high flow rate with larger imposed pressure gradients may activate more inter-aggregate pores in the fine-textured glass beads. Future studies are needed to consider the pressure, the velocity threshold, diffusional vs. advection effects, and/or the forces that may activate greater pore accessibility in the soil.

The time index  $\gamma$  changes linearly with the slope of the late-time BTC tail in a log-log plot:

$$\gamma = 0.0234 * |k| + 0.7156, R^2 = 0.9995 \quad (3-7)$$

where  $|k|$  [dimensionless] represents the absolute value of the slope of the late time BTC tail in a log-log plot, and  $R^2$  stands for the coefficient of determination. The best-fit time index  $\gamma$  is found to increase with an increasing flow velocity for both column experiments (note that the slope  $k$  in formula (3-7) changes with the flow rate  $v$ ), since a higher flow velocity generates a steeper late time slope in the BTC (see Fig. 3-4 and 3-5). A larger time index  $\gamma$  also indicates a shorter mean residence time and smaller degree of medium heterogeneity. All the time indexes,  $\gamma$ , fitted for the laboratory column experiments are much larger than those fitted for the real soil samples (discussed in Sec. 3.6.2), demonstrating that real soil samples are more heterogeneous than the glass-bead columns re-packed in the laboratory.

In the five parameters discussed above, the time index  $\gamma$  and the fractional-order capacity coefficient  $\beta$  may be qualitatively related to certain soil properties. Numerous factors can affect soil structures, such as organic matter, plants, roots and residues, microbes, fertilizers, wetting and drying, surface area, exchangeable cations, inorganic cements, clay, mineral and mineral heterogeneity, inter- and intra-porosity, and different rounding/sorting degrees of soil particles. For example,  $\beta$  may be related to a specific or group of soil textures. Theoretically,  $\beta$  controls the immobile mass when the reaction reaches equilibrium. A larger  $\beta$  denotes more solutes remaining in the immobile phase, and therefore the late-time BTC will exhibit a heavier tail; see for example the BTC for BH and FW soil columns shown in Fig. 3-1. BH and FW soils are loamy soils, while the PA soil is a sandy soil and the JA soil is a well-sorted sand (Qi and Donahoe, 2011). Therefore,  $\beta$  tends to increase with an increase in the clay content/surface area of the soil. Sondal et al. (2016) also found that sorption of arsenate was greater and quicker by clayey soil as compared to sandy loam soil, which could be due to the difference in their pH, anion exchange capacity, organic matter, and Fe and Mn oxide content. Thus, a relatively lower amount of arsenate can be desorbed from clayey soil than from sandy loam soil (Sondal et al., 2016).

The time index  $\gamma$  may also decrease with an increase in pH. BH and FW soils have higher pH values due to higher calcium carbonate contents than the other soils (Qi and Donahoe, 2011), and they also have higher clay contents and different mineralogy, which may also influence the tailings of BTCs. With increased solution pH, the surface charge of soil particles becomes more negative through deprotonation and subsequent hydroxylation of the oxide surface. This change can decrease the soil arsenate sorption capacity (Qi and Donahoe, 2011), resulting in fast desorption of As, especially during early leaching times or stages (see Fig. 3-1).

Such a behavior can be characterized by a smaller  $\gamma$  in the time fADE model, representing more immobile solutes with small residence times and fast mobilization.

In addition, in the leaching experiment, the JA soil is characterized as a well-sorted sand and may contain less heterogeneity than the other three soils. The corresponding BTC is less skewed than the others (Fig. 3-1), and therefore the best-fit  $\gamma$  is larger (representing a less skewed stable density for the trapping time distribution) and the best-fit  $\beta$  is smaller (representing a less pronounced late-tailing behavior) than those for the other three soils.

### 3.5.2.3 SRMT model

For comparison purposes, I quantify the column transport experiments using the SRMT model (which is the simplified model (3-5) with  $N=1$ ) to determine whether a single diffusion rate model can describe non-Fickian transport for As (V). The fitting results are shown in Fig. 3-4 and 3-5, with the best-fit parameters listed in Table 3-5.

Column scale	Flow rate [mL/min]	$L$ [cm]	$\alpha_L$ [cm]	$V$ [cm/min]	$\beta_{tot}$	$\omega$ [min <sup>-1</sup> ]
40×5.5 cm	Measured	Measured	Fitted	Fitted	Fitted	Fitted
	4	40	0.12	0.45	0.01	0.0498
	2	40	0.1	0.258	0.03	0.0498
	0.5	40	0.035	0.069	0.03	0.0498
20×2.6 cm	2.5	20	0.9	1.6	0.04	0.0317
	0.5	20	1	0.55	0.04	0.0136
	0.2	20	0.2	0.1	0.05	0.0055

Table 3-5. Case 2 - Fitted parameters for the single rate, double porosity, first order mass transfer (SRMT) model. In the legend,  $\alpha_L$  is the longitudinal dispersivity;  $\beta_{tot}$  is the total capacity coefficient ( $\beta_{tot} = \phi_{im}/\phi_m$ ); and  $\omega$  stands for the mass transfer rate between mobile and immobile domains.

Model results show that the longitudinal dispersivity  $\alpha_L$  increases with an increasing flow rate, which is consistent with the result of other models discussed above. The total capacity coefficient  $\beta_{tot}$  decreases as the flow rate increases, likely due to the same reason mentioned

above. The best-fit velocity in the SRMT model is slightly smaller than that in the time fADE model (3-3), and is closer to the actual observed peak velocity, likely due to the relatively smaller capacity coefficient assumed by the SRMT compared to the fADE (3-3). The mass transfer rate remains constant for the first column (with a longer length of 40 cm and a larger diameter of 5.5 cm), and decreases with a decrease in flow rate for the second column (20 by 2.6 cm).

The SRMT model can capture the shape of the BTC for both the first column with the slowest flow rate (Fig. 3-4f) and the second column with a moderate flow rate (see Fig. 3-5d), but underestimates the heavy tailing (behavior) profile for all of the other BTCs. If the experimental time is longer, then the later time tailing of BTC in Fig. 3-4f and 3-5d can be observed, and whether the SRMT is still feasible for characterizing such systems remains to be shown.

## 3.6 Discussion

### 3.6.1 Model comparison

The MRMT model (3-5) with two sets of immobile domains (resulting in 6 parameters) can capture the general trend of the observed BTCs for both the leaching experiments (Fig. 3-1) and the flushing experiments (Fig. 3-4 and 3-5); however, the number of immobile domains is case-dependent, challenging the real-world applicability of the MRMT model. In addition, the two mass exchange rates imply two immobile phases. The first immobile phase has a relatively large rate coefficient, corresponding to the equilibrium-controlled desorption stage defined by Qi and Donahoe (2011); while the second phase, with a relatively small rate coefficient, corresponds to the kinetic-controlled desorption stage (Qi and Donahoe, 2011). The leaching

experiment and the MRMT model applications show that, the fast reaction does occur in the early stage (0~4 days) for some soil columns such as BH and FW (Table 3-2), while the slow mass exchange process from the second immobile phase can also contribute to the initial mobilization of arsenic particles sorbed on soil. The small mass exchange rate coefficient only represents a large average residence time for the second immobile domain, and does not imply that As species can only be desorbed and released after it has been disassociated from the first immobile phase. Some As solutes initially associated with the second immobile phase can be released before the mean residence time. The sorption-desorption process in each stage may start simultaneously, since the immobile phases are parallel (not series or perpendicular to each other, in which each immobile domain will release particles in a time sequence). The same situation was found in the applications shown in Sec. 3.5.2, where the MRMT model with two immobile phases was used for both series of column experiments. There is no practical way to measure the number of immobile phases, or the capacity coefficient and mass exchange rate for each immobile phase. Thus, artificially separating the prolonged BTC tailing into multiple, subsequent stages might not conform to the actual kinetics of the reaction.

The time fADE (3-3) can describe a broad range of mass exchange rates, which contains both the SRMT and MRMT models as end members. For example, in case 2, the time fADE model captures all of the observed arsenic dynamics after using one more parameter than the SRMT model (which failed to capture the heavy tailed BTCs), making it more convenient than the other models. The time fADE model combines all immobile phases into one overall immobile domain, significantly reducing the number of unknown parameters and does not require detailed information for each immobile domain. The root mean square errors (RMSE) were calculated for the above three models for Case 2 (Table 3-6). In general, the time fADE

model has fewer parameters but can better capture the characteristics of BTCs. I also calculated the Akaike information criterion (AIC) to estimate the relative quality of these statistical models, providing further information for model selection (Table 3-7). The AIC value quantifies the goodness of fit, and it also includes a penalty function increasing with the number of the estimated parameters. Results show that, although the MRMT model (with a smaller RMSE) fits better than the SRMT model, it has two more parameters, leading to a larger AIC that makes the MRMT a less favorable model choice. The penalty of more parameters discourages overfitting, since more parameters usually improve the fitting. The time fADE model with the fewest number of parameters has the minimum AIC in all three models tested here. The fitting parameters were chosen by visual inspection, which were laborious but necessary to make sure that 1) each model has the best-fit parameters to capture not only the plume peak, but also the overall trend of transport, and 2) all models can be applied in the same manner and then can be evaluated reliably. Due to the limited datasets, I could only identify the qualitative relationship between specific model parameters and some physical/chemical properties of the sand column (such as pH/soil clay content).

Column scale	Flow rate [mL/min]	time fADE	SRMT	MRMT
20×2.6 cm	2.5	0.0380	0.0562	0.0453
	0.5	0.0510	0.0564	0.0543
	0.2	0.0117	0.0378	0.0215

Table 3-6. Case 2 - The root mean square error (RMSE) for the time fADE, SRMT, and MRMT model.

Column scale	Flow rate [mL/min]	time fADE	SRMT	MRMT
20×2.6 cm	2.5	19.0804	19.5180	24.3805
	0.5	17.9003	19.3682	23.9377
	0.2	23.8027	24.7895	28.9857

Table 3-7. Case 2 - The Akaike information criterion (AIC) value for the time fADE, SRMT, and MRMT model.

The application of the time nonlocal transport models in this study has limitations with fitting parameters, since the predictability of most, if not all, time nonlocal transport models remains a historical challenge; see the recent debates/reviews about the applicability of stochastic models in hydrogeology (Cirpka and Valocchi, 2016; Fiori et al., 2016; Fogg and Zhang, 2016; Rajaram, 2016; Sanchez-Vila and Fernàndez-Garcia, 2016). This study used only limited datasets, which can only lead to qualitative and semi-quantitative relationship between transport parameters and medium properties. This implies that extensive laboratory, numerical, and stochastic analyses are needed to explore the reliable quantitative link between model parameters and the physical/chemical properties of the medium, even for the deceptively simple sand columns. In addition, the physical meaning of parameters in the time fADE model can be found in Zhang et al. (2014a). The tempered time fADE (3-3) explains in general the continuous-time random walk (CTRW) nature of arsenic in leaching: each arsenic particle starts with a random amount of time in waiting (since arsenic was immobile initially), followed by the potential mobile phase transition with a random advective/dispersive jump. The truncated, random waiting time is assumed to follow the single-side, tempered Lévy stable density, as suggested by Meerschaert et al. (2008) and Cvetkoic (2011).

### 3.6.2 Leaching versus flushing experiments

The leaching experiments generally show strong sub-diffusive dynamics for the transport of arsenic exhibiting extensive (heavy) late-time tailing in the BTCs. These experiments utilized real natural soils under low flow rate conditions closer to that of real-world groundwater flow rates. The arsenic solutes were initially located in the immobile phases (solid soil) for decades, and the leaching experiments in the laboratory represented a sorption-dominated process. Since the contaminated soil had been leached for five decades in the field prior to being used in the

laboratory leaching experiments, residence time for arsenic solutes had a truncated distribution (where the relatively short residence times were removed from the standard  $\gamma$ -stable density, resulting in the tempered  $\gamma$ -stable density with a relatively larger capacity coefficient  $\beta$  and a relatively smaller index  $\gamma$ ), motivating the use of the tempered time fractional derivative model (3-3). The resultant capacity coefficient in the time fADE model is relatively large, in order to capture the sorption-dominated dynamics. To remediate real-world contaminated soil, sorption may be regarded as the main factor affecting transport, and the corresponding nonlocal effect in chemical transport dynamics needs to be considered.

The flushing laboratory experiments represent retarded (reactive) transport of arsenic (due to sorption and/or retention processes) in a relatively homogeneous system, where arsenic solutes were initially mobile (i.e., aqueous phase). These series of experiments used two columns packed with the same glass beads using consistent packing procedures. The time index  $\gamma$  in the time fADE model does not change dramatically between the two sets of column experiments, for various flow rates under advection-dominated transport processes. The water flux ( $Q$ ) is much larger for the flushing experiments, and hence the arsenic solute might not have enough time to exhaustively transfer from the mobile state to the immobile state. Therefore, the random residence time for immobile arsenic solutes may also be described by a truncated  $\gamma$ -stable density (where the relatively large residence times were selectively truncated, leading to the tempered  $\gamma$ -stable density with a relatively smaller capacity coefficient  $\beta$  and a relatively larger index  $\gamma$ ). Compared with the leaching experiments, the flushing experiments within the relatively homogeneous media system had a much higher velocity, larger dispersion coefficient  $D$ , one order-of-magnitude larger time index  $\gamma$ , two orders-of-magnitude smaller capacity coefficient  $\beta$ , and 2~3 orders-of-magnitude larger truncation parameter  $\lambda$ , indicating that the glass beads

contain a significantly smaller degree of heterogeneity than natural soil (i.e. leaching experiments). Such similar discrepancies can be observed for the MRMT and SRMT models. It should be noted that for comparisons of advective and reactive transport, a conservative tracer should be considered in the flushing experiment, and, as such, will be performed in a future study, in addition to replicate flushing experiments for arsenic.

### 3.6.3 Extension of arsenic transport in large-scale soils

Anomalous diffusion may also be expected for dissolved As transport through larger-scale, structured soils. The experiments revisited by this study focus on laboratory-scale soil columns. For real soils, the co-existence of macro-pore and micro-pore (i.e., matrix) may significantly affect the transport dynamics of As, requiring a sophisticated model such as the full time fADE model (3-3) to capture the mixed super- and sub-diffusion effects.

In addition, under these more realistic conditions, if 1) the experimental time is long enough to observe the re-mobilization (or releasing) of most As solutes in the leaching experiment, 2) and the soil is relatively homogeneous, and/or 3) has specific pH that induce fast reaction (solute exchange), then a large truncation parameter  $\lambda$  may be needed in model (3), indicating an early transition from non-Fickian to Fickian transport behavior.

### 3.7 Conclusion

This study quantifies the dynamics of arsenic leaching in soils documented from literature and arsenic flushing in ideal columns packed with homogeneous glass bead packs conducted in our laboratory. The SRMT model, the standard MRMT model with two immobile domains, and the tempered time fADE model are applied and compared, leading to the following five major conclusions.

First, arsenic transport in soil is a multiple rate, sorption-desorption kinetic process, resulting in non-Fickian, sub-diffusive transport dynamics characterized by heavy-tailed late-time BTCs. The multiple rates of sorption-desorption are reflected by the variable elution concentration decline rates for the BTC at late times, which cannot be efficiently captured by the traditional equilibrium model or the mixed equilibrium-kinetic model, since the transport of arsenic in soil is a kinetic process where the sorption-desorption may not be able to reach equilibrium even in decades.

Second, both the leaching processes and the flushing processes of As (V) can be simulated using the tempered time fractional ADE, although the standard  $\gamma$ -stable density requires different truncation. For the diffusion-dominated leaching process with a slow flow rate, short residence times for arsenic particles are removed from the original  $\gamma$ -stable density; while for the advection-dominated flushing experiments with relatively large flow rates and long residence times should be truncated, resulting in relatively larger index coefficients and relatively smaller capacity coefficients. It is also noteworthy that the stable density is selected in this study to represent the residence time distribution density, as was determined by various researchers (Cvetkovic, 2011; Zhang et al., 2015) as the universal density for hydrological transport.

Third, the simplified tempered time fADE model is more convenient than the standard MRMT model in capturing the complex As transport through contaminated soils with multiple stages of sorption-desorption, since it contains less parameters and can capture the nuance of arsenic elution behavior observed in the BTCs of the leaching experiments. Both the time fADE model and the MRMT model with multiple pairs of immobile phases perform better than the SRMT model in capturing major characteristics of non-Fickian transport observed in the BTCs,

especially the late time tailing portion as the arsenic leaching (or flushing) involves multiple stages with different reaction rates. In addition, although the MRMT model can define multiple pairs of mass-transfer parameters (i.e., mass exchange rate and capacity coefficient) to characterize the multiple stages of As sorption-desorption, the real-world application of the MRMT model is not straightforward. In general, the first immobile domain is associated with the largest mass exchange rate and the smallest capacity coefficient, implying a fast release stage.

Fourth, the flushing experiment performed in this study provides useful information to expand the previous leaching experiments for understanding and interpreting As (V) dynamics in media with different degrees of heterogeneity. A weaker sub-diffusive effect on As transport is characterized by less pronounced (i.e., lighter) BTC late-time tailing observed for the flushing experiments (using glass beads) compared to the leaching experiments (using real soil). Under such logic and observations from the results of this study, it is my expectation that the As dynamics may exhibit super-diffusive behavior when large-scale, interconnected soil macropores provide preferential flow paths for dissolved arsenic species that represent more realistic conditions at the field scale.

Fifth, the fractional capacity coefficient and the truncation parameter in the time fADE model can be calculated using the results from the MRMT model, and they can also be related to soil properties and chemical conditions. An empirical relationship between the power law exponent and the time index  $\gamma$  was determined. The time index and the capacity coefficient in the time fADE model can be related to the pH level and the clay content of the system. A soil sample with high clay content will possess a larger capacity coefficient (more immobile phases), while a soil sample with a larger pH value will have a smaller time index (faster release of As during the

early stages of elution). Future studies are needed to quantify these relationships experimentally and theoretically for a better understanding of arsenic transport in soil.

### 3.8 Acknowledgments

This research was partially supported by the National Science Foundation (under Grant DMS-1460319), the University of Alabama, and the National Science Foundation of China (41628202 and 41101287). This paper does not necessarily reflect the view of the funding agencies.

### 3.9 References

- Al-Abed, S.R., Jegadeesan, G., Purandare, J., Allen, D., 2007. Arsenic release from iron rich mineral processing waste: Influence of pH and redox potential. *Chemosphere* 66, 775–782. doi:10.1016/j.chemosphere.2006.07.045.
- Arai, Y., Sparks, D.L., 2002. Residence time effects on arsenate surface speciation at the aluminum oxide-water interface. *Soil Sci.* 167, 303–314. doi:10.1097/00010694-200205000-00001.
- Arco-Lázaro, E., Agudo, I., Clemente, R., Bernal, M.P., 2016. Arsenic(V) adsorption-desorption in agricultural and mine soils: Effects of organic matter addition and phosphate competition. *Environ. Pollut.* 216, 71–79. doi:10.1016/j.envpol.2016.05.054.
- Banerjee, K., Amy, G.L., Prevost, M., Nour, S., Jekel, M., Gallagher, P.M., Blumenschein, C.D., 2008. Kinetic and thermodynamic aspects of adsorption of arsenic onto granular ferric hydroxide (GFH). *Water Res.* 42, 3371–3378. doi:10.1016/j.watres.2008.04.019.
- Brusseau, M.L., 1992. Nonequilibrium transport of organic chemicals: The impact of pore-water velocity. *J. Contam. Hydrol.* 9, 353–368. doi:10.1016/0169-7722(92)90003-W.
- Cao, X., Ma, L.Q., Shiralipour, A., 2003. Effects of compost and phosphate amendments on arsenic mobility in soils and arsenic uptake by the hyperaccumulator, *Pteris vittata* L. *Environ. Pollut.* 126, 157–167. doi:10.1016/S0269-7491(03)00208-2.
- Chakravarty, S., Dureja, V., Bhattacharyya, G., Maity, S., Bhattacharjee, S., 2002. Removal of arsenic from groundwater using low cost ferruginous manganese ore. *Water Res.* 36, 625–632. doi:10.1016/S0043-1354(01)00234-2.
- Cirpka, O.A., Valocchi, A.J., 2016. Debates—Stochastic subsurface hydrology from theory to practice: Does stochastic subsurface hydrology help solving practical problems of

- contaminant hydrogeology? *Water Resour. Res.* 52, 9218–9227.  
doi:10.1002/2016WR019087.
- Couture, R.M., Charlet, L., Markelova, E., Madé, B., Parsons, C.T., 2015. On-off mobilization of contaminants in soils during redox oscillations. *Environ. Sci. Technol.* 49, 3015–3023.  
doi:10.1021/es5061879.
- De Brouwere, K., Smolders, E., Merckx, R., 2004. Soil properties affecting solid-liquid distribution of As(V) in soils. *Eur. J. Soil Sci.* 55, 165–173. doi:10.1046/j.1365-2389.2003.00584.x.
- Dickson, D., Liu, G., Cai, Y., 2017. Adsorption kinetics and isotherms of arsenite and arsenate on hematite nanoparticles and aggregates. *J. Environ. Manage.* 186, 261–267.  
doi:10.1016/j.jenvman.2016.07.068.
- Elwakeel, K.Z., Al-Bogami, A.S., 2018. Influence of Mo(VI) immobilization and temperature on As(V) sorption onto magnetic separable poly p -phenylenediamine-thiourea-formaldehyde polymer. *J. Hazard. Mater.* 342, 335–346.  
doi:10.1016/j.jhazmat.2017.08.007.
- Felmy, A.R., Girvin, D.C., Jenne, E.A., 1984. MINTEQA--a Computer Program for Calculating Aqueous Geochemical Equilibria: February 1984. *Natl. Tech. Inf. Serv.*
- Feng, Q., Zhang, Zhiyong, Chen, Y., Liu, L., Zhang, Zhengjie, Chen, C., 2013. Adsorption and Desorption Characteristics of Arsenic on Soils: Kinetics, Equilibrium, and Effect of Fe(OH)<sub>3</sub> Colloid, H<sub>2</sub>SiO<sub>3</sub> Colloid and Phosphate. *Procedia Environ. Sci.* 18, 26–36.  
doi:10.1016/j.proenv.2013.04.005.
- Fiori, A., Cvetkovic, V., Dagan, G., Attinger, S., Bellin, A., Dietrich, P., Zech, A., Teutsch, G., 2016. Debates—Stochastic subsurface hydrology from theory to practice: The relevance of stochastic subsurface hydrology to practical problems of contaminant transport and remediation. What is characterization and stochastic theory good for? *Water Resour. Res.* 52, 9228–9234. doi:10.1002/2015WR017525.
- Fogg, G.E., Zhang, Y., 2016. Debates—Stochastic subsurface hydrology from theory to practice: A geologic perspective. *Water Resour. Res.* doi:10.1002/2016WR019699.
- Fuller J.A. AU3 - Waychunas, G.A. AU4 - Rea, B.A., C.C.A.-D., 1993. Surface chemistry of ferrihydrite: Part 2. Kinetics of arsenate adsorption and coprecipitation: RN - *Geochim. Cosmochim. Acta*, v. 57, p. 2271-2282. *Geochim. Cosmochim. Acta*.
- Gao, S., Goldberg, S., Herbel, M.J., Chalmers, A.T., Fujii, R., Tanji, K.K., 2006. Sorption processes affecting arsenic solubility in oxidized surface sediments from Tulare Lake Bed, California. *Chem. Geol.* 228, 33–43. doi:10.1016/j.chemgeo.2005.11.017.
- Gedik, K., Kongchum, M., Boran, M., Delaune, R.D., 2015. Adsorption and desorption of

- arsenate in Louisiana rice soils. *Arch. Agron. Soil Sci.* 62, 856–864.  
doi:10.1080/03650340.2015.1096015.
- Gerard, N., Santhana Krishnan, R., Ponnusamy, S.K., Cabana, H., Vaidyanathan, V.K., 2016. Adsorptive potential of dispersible chitosan coated iron-oxide nanocomposites toward the elimination of arsenic from aqueous solution. *Process Saf. Environ. Prot.* 104, 185–195.  
doi:10.1016/j.psep.2016.09.006.
- Goldberg, S., 2002. Competitive Adsorption of Arsenate and Arsenite on Oxides and Clay Minerals. *Soil Sci. Soc. Am. J.* 66, 413. doi:10.2136/sssaj2002.4130.
- Goldberg, S., 1986. Chemical modeling of arsenate adsorption on aluminum and iron oxide minerals. *Soil Sci. Soc. Am. J.* 50, 1154–1157.  
doi:10.2136/sssaj1985.03615995004900060009x.
- Goldberg, S., Lesch, S.M., Suarez, D.L., Basta, N.T., 2005. Predicting Arsenate Adsorption by Soils using Soil Chemical Parameters in the Constant Capacitance Model. *Soil Sci. Soc. Am. J.* 69, 1389. doi:10.2136/sssaj2004.0393.
- Haggerty, R., Gorelick, S.M., 1995. Multiple-rate mass transfer for modeling diffusion and surface reactions in media with pore-scale heterogeneity. *Water Resour. Res.* 31, 2383–2400. doi:10.1029/95WR01583.
- Hauns, M., Jeannin, P.Y., Atteia, O., 2001. Dispersion, retardation and scale effect in tracer breakthrough curves in karst conduits. *J. Hydrol.* 241, 177–193. doi:10.1016/S0022-1694(00)00366-8.
- Hossain, M., 2006. Arsenic contamination in Bangladesh—An overview. *Agric. Ecosyst. Environ.* 113, 1–16. doi:10.1016/j.agee.2005.08.034.
- Huber, F., Enzmann, F., Wenka, A., Bouby, M., Dentz, M., Schäfer, T., 2012. Natural micro-scale heterogeneity induced solute and nanoparticle retardation in fractured crystalline rock. *J. Contam. Hydrol.* 133, 40–52. doi:10.1016/j.jconhyd.2012.03.004.
- Jeppu, G.P., Clement, T.P., 2012. A modified Langmuir-Freundlich isotherm model for simulating pH-dependent adsorption effects. *J. Contam. Hydrol.* 129–130, 46–53.  
doi:10.1016/j.jconhyd.2011.12.001.
- Jiang, J., Dai, Z., Sun, R., Zhao, Z., Dong, Y., Hong, Z., Xu, R., 2017. Evaluation of ferrollysis in arsenate adsorption on the paddy soil derived from an Oxisol. *Chemosphere* 179, 232–241. doi:10.1016/j.chemosphere.2017.03.115.
- Karim, M.M., 2000. Arsenic in groundwater and health problems in Bangladesh. *Water Res.* 34, 304–310. doi:10.1016/S0043-1354(99)00128-1.
- Khan, A.U.H., Jury, W.A., 1990. A laboratory study of the dispersion scale effect in column

- outflow experiments. *J. Contam. Hydrol.* 5, 119–131. doi:10.1016/0169-7722(90)90001-W.
- Kundu, S., Gupta, A.K., 2005. Analysis and modeling of fixed bed column operations on As(V) removal by adsorption onto iron oxide-coated cement (IOCC). *J. Colloid Interface Sci.* 290, 52–60. doi:10.1016/j.jcis.2005.04.006.
- Ladeira, A.C.Q., Ciminelli, V.S.T., 2004. Adsorption and desorption of arsenic on an oxisol and its constituents. *Water Res.* 38, 2087–2094. doi:10.1016/j.watres.2004.02.002.
- Limousin, G., Gaudet, J.P., Charlet, L., Szenknect, S., Barthes, V., Krimissa, M., 2007. Sorption isotherms: a review on physical bases, modeling and measurement. *Appl. Geochemistry* 22, 249–275.
- Lin, T.F., Wu, J.K., 2001. Adsorption of arsenite and arsenate within activated alumina grains: Equilibrium and kinetics. *Water Res.* 35, 2049–2057. doi:10.1016/S0043-1354(00)00467-X.
- Mandal, B.K., Suzuki, K.T., 2002. Arsenic round the world: A review. *Talanta*. doi:10.1016/S0039-9140(02)00268-0.
- Manning, B.A., Goldberg, S., 1997. Adsorption and stability of arsenic(III) at the clay mineral-water interface. *Environ. Sci. Technol.* 31, 2005–2011. doi:10.1021/es9608104.
- Manning, B.A., Goldberg, S., 1996. Modeling Competitive Adsorption of Arsenate with Phosphate and Molybdate on Oxide Minerals. *Soil Sci. Soc. Am. J.* 60, 121. doi:10.2136/sssaj1996.03615995006000010020x.
- Masscheleyn, P.H., Delaune, R.D., Patrick, Jr., W.H., 1991. Effect of Redox Potential and pH on Arsenic Speciation and Solubility in a Contaminated Soil. *Environ. Sci. Technol.* 25, 1414–1419. doi:10.1021/es00020a008.
- Mohan, D., Pittman, C.U., 2007. Arsenic removal from water/wastewater using adsorbents-A critical review. *J. Hazard. Mater.* doi:10.1016/j.jhazmat.2007.01.006.
- Morel, F.M., Hering, J.G., 1993. Principles and applications of aquatic chemistry. John Wiley & Sons.
- Naftaly, A., Dror, I., Berkowitz, B., 2016. Measurement and modeling of engineered nanoparticle transport and aging dynamics in a reactive porous medium. *Water Resour. Res.* 1–20. doi:10.1002/2014WR015716.
- Nice, A.J., Lung, W.S., Riedel, G.F., 2008. Modeling arsenic in the Patuxent estuary. *Environ. Sci. Technol.* 42, 4804–4810. doi:10.1021/es702452e.
- Nickson, R.T., McArthur, J.M., Ravenscroft, P., Burgess, W.G., Ahmed, K.M., 2000. Mechanism

- of arsenic release to groundwater, Bangladesh and West Bengal. *Appl. Geochemistry* 15, 403–413. doi:10.1016/S0883-2927(99)00086-4.
- O'Reilly, S.E., Strawn, D.D.G., Sparks, D.L., 2001. Residence Time Effects on Arsenate Adsorption/Desorption Mechanisms on Goethite. *Soil Sci. Soc. Am. J.* 65, 67. doi:10.2136/sssaj2001.65167x.
- Ouvrard, S., Simonnot, M.O., de Donato, P., Sardin, M., 2002. Diffusion-controlled adsorption of arsenate on a natural manganese oxide. *Ind. Eng. Chem. Res.* 41, 6194–6199. doi:10.1021/ie020269m.
- Pang, L., Close, M., Schneider, D., Stanton, G., 2002. Effect of pore-water velocity on chemical nonequilibrium transport of Cd, Zn, and Pb in alluvial gravel columns. *J. Contam. Hydrol.* 57, 241–258. doi:10.1016/S0169-7722(01)00223-6.
- Pantsar-Kallio, M., Manninen, P.K.G., 1997. Speciation of mobile arsenic in soil samples as a function of pH. *Sci. Total Environ.* 204, 193–200. doi:10.1016/S0048-9697(97)00176-9.
- Pardo, T., Bernal, M.P., Clemente, R., 2014. Efficiency of soil organic and inorganic amendments on the remediation of a contaminated mine soil: I. Effects on trace elements and nutrients solubility and leaching risk. *Chemosphere* 107, 121–128. doi:10.1016/j.chemosphere.2014.03.023.
- Pecini, E.M., Springer, V., Brigante, M., Avena, M., 2017. Arsenate interaction with the surface of nanomagnetic particles. High adsorption or full release. *J. Environ. Chem. Eng.* 5, 4917–4922. doi:10.1016/j.jece.2017.09.020.
- Peterson, S.R., Hostetler, C.J., Deutsch, W.J., Cowan, C.E., 1987. MINTEQ user's manual. Pacific Northwest Lab. No. NUREG/CR-4808; PNL-6106.
- Qi, Y., Donahoe, R., 2009. Modeling arsenic desorption from herbicide-contaminated soils. *Environ. Toxicol. Chem.* 28, 1338–1345. doi:10.1897/08-487.1.
- Qi, Y., Donahoe, R.J., 2011. Modeling Arsenic Sorption in the Subsurface with a Dual-Site Model. *Ground Water* 49, 219–226. doi:10.1111/j.1745-6584.2010.00726.x.
- Qi, Y., Donahoe, R.J., 2008. The environmental fate of arsenic in surface soil contaminated by historical herbicide application. *Sci. Total Environ.* 405, 246–254. doi:10.1016/j.scitotenv.2008.06.043.
- Quintáns-Fondo, A., Fernández-Calviño, D., Nóvoa-Muñoz, J., Arias-Estévez, M., Fernández-Sanjurjo, M., Álvarez-Rodríguez, E., Núñez-Delgado, A., 2017. As(V) Sorption/Desorption on Different Waste Materials and Soil Samples. *Int. J. Environ. Res. Public Health* 14, 803. doi:10.3390/ijerph14070803.
- Rajaram, H., 2016. Debates—Stochastic subsurface hydrology from theory to practice:

- Introduction. *Water Resour. Res.* 52, 9215–9217. doi:10.1002/2016WR020066.
- Sanchez-Vila, X., Fernández-García, D., 2016. Debates—Stochastic subsurface hydrology from theory to practice: Why stochastic modeling has not yet permeated into practitioners? *Water Resour. Res.* 52, 9246–9258. doi:10.1002/2016WR019302.
- Schumer, R., Benson, D., Meerschaert, M., Baeumer, B., 2003. Fractal mobile/immobile solute transport. *Water Resour. Res.* 39.
- Seco-Reigosa, N., Bermúdez-Couso, A., Garrido-Rodríguez, B., Arias-Estévez, M., Fernández-Sanjurjo, M.J., Álvarez-Rodríguez, E., Núñez-Delgado, A., 2013. As (V) retention on soils and forest by-products and other waste materials. *Environ. Sci. Pollut. Res.* 20, 6574–6583.
- Selim, H.M., 2013. Transport and Retention of Heavy Metal in Soils. Competitive Sorption. *Adv. Agron.* 119, 275–308. doi:10.1016/B978-0-12-407247-3.00005-6.
- Silvetti, M., Garau, G., Demurtas, D., Marceddu, S., Deiana, S., Castaldi, P., 2017. Influence of lead in the sorption of arsenate by municipal solid waste composts: metal(loid) retention, desorption and phytotoxicity. *Bioresour. Technol.* 225, 90–98. doi:10.1016/j.biortech.2016.11.057.
- Smith, A.H., Lingas, E.O., Rahman, M., 2000. Contamination of drinking-water by arsenic in Bangladesh: a public health emergency: RN - Bull. W.H.O., v. 78, p. 1093-1103. *Bull. World Heal. Organ.* 78, 1093–1103. doi:10.1590/S0042-96862000000900005.
- Smith, E., Naidu, R., Alston, A.M., Donald, L.S., 1998. Arsenic in the Soil Environment: A Review. *Adv. Agron.* Volume 64, 149–195. doi:http://dx.doi.org/10.1016/S0065-2113(08)60504-0.
- Sondal, J., Singh, D., Sikka, R., 2016. Comparative evaluation of arsenate sorption–desorption in two soils of North India. *Environ. Earth Sci.* 75, 1–9. doi:10.1007/s12665-015-5018-y.
- Song, Y., Wang, S., Jia, Y., Yuan, Z., Wang, X., Gómez, M.A., 2015. Effects of nutrient and sulfate additions on As mobility in contaminated soils: A laboratory column study. *Chemosphere* 119, 902–909. doi:10.1016/j.chemosphere.2014.08.078.
- Sun, S., Ji, C., Wu, L., Chi, S., Qu, R., Li, Y., Lu, Y., Sun, C., Xue, Z., 2017. Facile one-pot construction of  $\alpha$ -Fe<sub>2</sub>O<sub>3</sub>/g-C<sub>3</sub>N<sub>4</sub> heterojunction for arsenic removal by synchronous visible light catalysis oxidation and adsorption. *Mater. Chem. Phys.* 194, 1–8. doi:10.1016/j.matchemphys.2017.03.023.
- Thi Hoa Mai, N., Postma, D., Thi Kim Trang, P., Jessen, S., Hung Viet, P., Larsen, F., 2014. Adsorption and desorption of arsenic to aquifer sediment on the Red River floodplain at Nam Du, Vietnam. *Geochim. Cosmochim. Acta* 142, 587–600. doi:10.1016/j.gca.2014.07.014.

- Tufano, K.J., Reyes, C., Saltikov, C.W., Fendorf, S., 2008. Reductive processes controlling arsenic retention: revealing the relative importance of iron and arsenic reduction. *Environ. Sci. Technol.* 42, 8283–8289.
- Vanderborght, J., Vereecken, H., 2007. Review of Dispersivities for Transport Modeling in Soils. *Vadose Zo. J.* 6, 29. doi:10.2136/vzj2006.0096.
- Zhang, H., Selim, H., 2006. Modeling the transport and retention of arsenic (V) in soils. *Soil Sci. Soc. Am. J.* 70, 1677–1687.
- Zhang, H., Selim, H.M., 2005. Kinetics of arsenate adsorption-desorption in soils. *Environ. Sci. Technol.* 39, 6101–6108. doi:10.1021/es050334u.
- Zhang, X., Lv, M., 2009. The nonlinear adsorptive kinetics of solute transport in soil does not change with pore-water velocity: Demonstration with pore-scale simulations. *J. Hydrol.* 371, 42–52. doi:10.1016/j.jhydrol.2009.03.017.
- Zhang, Yong, Green, C.T., Baeumer, B., 2014. Linking aquifer spatial properties and non-Fickian transport in mobile-immobile like alluvial settings. *J. Hydrol.* 512, 315–331. doi:10.1016/j.jhydrol.2014.02.064.
- Zhang, Y., Qian, J., Papelis, C., Sun, P., Yu, Z., 2014. Improved understanding of bimolecular reactions in deceptively simple homogeneous media: From laboratory experiments to Lagrangian quantification. *Water Resour. Res.* 50, 1704–1715. doi:10.1002/2012WR013085.

## CHAPTER 4:

### APPLICATION OF TEMPERED-STABLE TIME FRACTIONAL-DERIVATIVE MODEL TO UPSCALE SUBDIFFUSION FOR POLLUTANT TRANSPORT IN FIELD-SCALE DISCRETE FRACTURE NETWORKS

#### 4.1 Abstract

Fractional calculus provides efficient physical models to quantify non-Fickian dynamics broadly observed within the Earth system. The potential advantages of using fractional partial differential equations (fpDEs) for real-world problems are often limited by the current lack of understanding of how earth system properties influence the observed non-Fickian dynamics. This study explores non-Fickian dynamics for pollutant transport in field-scale discrete fracture networks (DFNs) by investigating how fracture and rock matrix properties influence the leading and tailing edges of pollutant breakthrough curves (BTCs). Fractured reservoirs exhibit erratic internal structures and multi-scale heterogeneity, resulting in complex non-Fickian dynamics. A Monte Carlo approach is used to simulate pollutant transport through DFNs with a systematic variation of system properties, and the resultant non-Fickian transport is upscaled using a tempered-stable fractional in time advection-dispersion equation. Numerical results serve as a basis for determining both qualitative and quantitative relationships between BTC characteristics and model parameters, in addition to the impacts of fracture density, orientation, and rock matrix permeability on non-Fickian dynamics. The observed impacts of medium heterogeneity on tracer transport at late times tend to enhance the applicability of fpDEs that may be parameterized using measurable fracture-matrix characteristics.

## 4.2 Introduction

Fractional calculus, defined by non-integer order derivatives and integrals, has been applied to problems involving non-Fickian or anomalous dynamics for almost three decades (Gorenflo and Mainardi, 1997; Metzler and Klafter, 2000). Despite their vast potential, both theoretical development and real-world applications of fractional partial differential equations (fPDEs) have commonly been constrained by the lack of understanding of how earth system properties influence non-Fickian transport dynamics, especially for the hydrologic sciences (Zhang et al., 2017b). This major challenge has historically reduced fPDEs to curve-fitting, mathematical exercises, instead of routine hydrological modeling tools (Fogg and Zhang, 2016). Intensive efforts are needed to link medium properties and the fPDE model parameters, and the commonly used Monte Carlo approach is particularly suitable for providing target dynamics for heterogeneous systems with well-controlled and definable properties.

Applications of fPDEs in the hydrologic sciences have a relatively shorter history, compared to the other stochastic hydrologic approaches such as the single or multiple rate mobile-immobile models used extensively in chemical engineering and hydrogeology (Coats et al., 1964; Haggerty et al., 2000). Anomalous transport has been observed in a variety of disordered systems in natural geological media, especially in heterogeneous porous media and fractured formations (Becker and Shapiro, 2003, 2000; Haggerty et al., 2000; Kang et al., 2015b; Klepikova et al., 2016). After Benson et al. (2000) first introduced the spatial fractional advection-dispersion equation (fADE) to capture super-diffusive transport in sand tanks and a relatively homogenous aquifer, the fADEs had been applied to model anomalous transport in saturated, heterogeneous porous media (Chang et al., 2005; Garrard et al., 2017; Green et al., 2014; Huang et al., 2006) and Earth surface such as natural rivers (Drummond et al., 2014; Schumer et al., 2009; Sun et al., 2015). Applications of fADEs for flow and transport in fractured

media are rather rare (Reeves et al., 2008; Zhang et al., 2010), although fractures are ubiquitous in geologic systems. More than 90% of natural aquifers are fractured.

Fractured media exhibit erratic heterogeneity and scale-dependent dynamics for flow and transport (Alle and Neuman, 2005; Berkowitz, 2002), challenging standard modeling tools and providing an ideal test case for fPDEs. Accurate and efficient simulation of contaminant transport within a fractured rock mass is practically important, since fractures play a large role in many natural and engineered processes, such as long-term disposal of high-level radioactive wastes in a geologic repository (Berkowitz, 2002; Selroos et al., 2002; Zhao et al., 2013, 2011). Fracture properties of natural rocks, such as fracture density, spatial location, length, aperture and orientation distributions, account for medium heterogeneity and result in non-Fickian contaminant transport (Gustafson and Fransson, 2006; Liu et al., 2016a; Mukhopadhyay and Cushman, 1998; Outters, 2003), where the feasibility of fADEs and the potential correlation between fracture properties and fADE parameters have not been fully understood( see pioneer work in (Reeves et al., 2008; Zhang et al., 2010)).

This study selected the fPDE to quantify pollutant transport through field-scale fractured rock. Due to the prohibitive computational burden in mapping each individual fracture in standard grid-based models (Zhang et al., 2010), different transport models have been developed to describe and predict complex transport behavior in fractured media at different scales (Cook, 2003; Cortis and Birkholzer, 2008; Haggerty et al., 1999; Zhang et al., 2006). For example, the fractured medium was treated as an equivalent continuum and the advection-dispersion equation (ADE) with ensemble averaged parameters was used to model contaminant transport (Alle and Neuman, 2005; Bear, 1972). However, the equivalent continuum assumption may only be valid for rocks with sufficiently high fracture densities that approximate an equivalent porous media

(Painter and Cvetkovic, 2005). This condition is rare in natural fractured rock, while sparsely fractured rock is more common and favored for geological disposal (Lei, 2016; Painter and Cvetkovic, 2005). Unlike the ADE which characterizes Fickian diffusion at local scales, non-Fickian transport behaviors and asymmetric plumes due to heterogeneity in fractures have been observed in both the laboratory experiments and field tests (Bakshevskaia and Pozdniakov, 2016; Cortis and Birkholzer, 2008; Klepikova et al., 2016). This provides my motivation to select a non-local fADE in this study, which can account for both spatial and temporal nonlocal processes (Kang et al., 2015a; Kelly et al., 2017; Yong et al., 2007; Zhang et al., 2007) in describing non-Fickian transport in fractured media.

The rest of the paper is organized as follows. In section 4.3, I present the Monte Carlo approach used to simulate multiple DFN flow and transport scenarios. The DFN is an efficient and conceptually robust numerical approach to simulate the dynamics of flow and transport in fractured media with definable fracture properties. It assumes that the rock mass is dissected by a network of discrete fractures and fluid flow and contaminant transport in a low-permeability rock mass is controlled by geometric and hydraulic properties of interconnected fractures of a network (CACaS et al., 1990; McClure and Horne, 2013). Results of the Monte Carlo simulations and applications of the fADE are then shown in section 4.4. In section 4.5, I explore the emergence of anomalous transport and its characterization to gain insight into the effective solute dynamics and major mechanisms behind the observed anomalous behavior. I focus on the impact of fracture density and orientation and rock matrix permeability on non-Fickian dynamics and the fADE parameters. Section 4.6 draws the main conclusions.

#### 4.3 Monte Carlo Simulations and the Fractional Advection-Dispersion Equation

The Monte Carlo approach utilized in this study contains three major steps. First, I generate multiple scenarios of stochastic fracture networks with varying properties using HydroGeoSphere (HGS) software (Therrien et al., 2010), which is a multi-dimensional control-volume finite element simulator designed to simulate the hydrologic cycle, including simulating flow and transport in fracture networks embedded in a porous medium with the discrete fracture (DF) approach. Second, groundwater flow through the generated DFNs is modeled, which is expected to lead to strongly non-Fickian dynamics for conservative tracer transport (see further discussion below), providing the synthetic data to evaluate the influence of the fractured media properties on non-Fickian dynamics. Third, pollutant transport characterized by breakthrough curves (BTCs) is then accounted for by a truncated power-law distribution memory function embodied in the fADE model. FracFit (Kelly et al., 2017), a robust parameter estimation tool using a weighted nonlinear least squares (WNLS) algorithm, is used to parameterize my fractional calculus model, which can capture salient features of anomalous transport, such as skewness and power law tails. Weights assigned by WNLS (Chakraborty et al., 2009) are proportional to the reciprocal of measured concentration. Therefore, areas of lower concentration (representing low probability regions) receive greater weight, which is essential for capturing early arrivals and late time tail characteristics.

#### 4.3.1 Generating the Random Discrete Fracture Networks

The model geometry, shown in Fig. 4-1, is  $50 \times 25 \text{ m}^2$  and represents a horizontally, two-dimensional (2-D) map view of the fractures with unit thickness and uniform blocks ( $100 \times 50$ ) along x and z axes. One hundred 2-D DFN realizations (for each scenario) are generated by superimposing two different sets of fractures onto the grid, with links between the fracture elements and matrix block elements, leading to realistic DFNs (Geiger et al., 2010; Long et al.,

1982). Each scenario represents the ensemble average of 100 total individual DFN flow and transport realizations. Fracture locations, orientations, lengths and hydraulic conductivities are generated from predefined distributions obtained in literature (Fiori and Becker, 2015; Haggerty et al., 1999):

- (1) Fracture location: distributed randomly over the entire domain with a random seed selected for each realization
- (2) Fracture orientation: two fracture sets follow mixed Gaussian distributions (each Gaussian distribution takes half weights and has its own mean and variance), with a mean and standard deviation of  $0^\circ \pm 10^\circ$  for the first set, and  $90^\circ \pm 10^\circ$  for the second set
- (3) Fracture length: log-normal distribution, with 10 length bins – the mean of the smallest length bin is 2.5 m (which is 1/10 of the minimum length of the x and z domain sizes), and the mean of the largest length bin is 25 m (which is the minimum length of the x and z domain sizes)
- (4) Fracture aperture: exponential distribution, with 10 aperture bins – the mean of the smallest aperture bin is 0.001 m, and the mean of the largest aperture bin is 0.0015 m.

Fracture permeability is calculated using the parallel plate law:  $k_f = \omega_f^2/12$  (CKeller et al., 1999; Klepikova et al., 2016; Klimczak et al., 2010; Zhao et al., 2014), which relates aperture  $\omega_f$  to permeability  $k_f$ . In my DFNs, fractures are open and act as flow conduits. Fracture permeability is dependent on aperture and varies from  $8.3 \times 10^{-8} \text{ m}^2$  to  $1.9 \times 10^{-7} \text{ m}^2$  given an exponential distribution. I test the matrix hydraulic conductivity of  $5 \times 10^{-8}$ ,  $10^{-7}$  and  $10^{-6} \text{ m/s}$ , with the corresponding permeability of  $5.5 \times 10^{-15}$ ,  $1.1 \times 10^{-14}$  and  $1.1 \times 10^{-13} \text{ m}^2$ , which are six to seven orders of magnitude smaller than the fracture permeability. The matrix permeability is assumed to be isotropic and in the range of an un-fractured, low-permeability rock like a real silt

medium ( $[1.15 \times 10^{-16}, 2.3 \times 10^{-12}] \text{ m}^2$ ). One realization of the DFN with 100 fractures is shown in Fig. 4-1. A horizontal fracture with the length of 10 m and aperture of 0.001 m is inserted in the middle of the left boundary to inject a conservative tracer. This zone provides a mobile source of pollutant, representing the real-world contamination where pollutant usually enters firstly the mobile region in aquifers before spreading downstream.

#### 4.3.2 Modeling Groundwater Flow and Pollutant Transport through the DFNs

Steady-state groundwater flow through the confined aquifer generated above is then solved by HGS. Parameters for the flow model, including the specific storage coefficient and porosity, are defined in Table 4-1. Boundary conditions are chosen so that the main flow direction is from left to right with a general hydraulic gradient of approximately 0.2. The high hydraulic gradient is selected for faster convergence and decreased simulation times in this work (so that I can observe the late-time behavior of solute transport, which is critical to identify the dynamics of sub-diffusive non-Fickian transport), and a future work will decrease the hydraulic gradient to 0.01~0.001 to represent real-world scenarios. The left and right boundaries are set to be constant head boundary conditions, and have values as 50 m and 40 m, respectively.

Pollutant transport through the saturated DFN is then solved by HGS using the same ILU-preconditioned ORTHOMIN solver as is used for the flow problem. Transport parameters are shown in Table 4-1. The longitudinal, transverse and the vertical transverse dispersivities assigned to both the un-fractured rock matrix and rock fractures are 0.01, 0.001, 0.001 m, respectively, where the longitudinal dispersivity is one order-of-magnitude smaller than the grid size and the horizontal dispersivity is one order-of-magnitude smaller than that along the longitudinal direction. Tortuosity is assumed to be 1, so that I can focus on the impact of other

measurable parameters (such as matrix permeability and porosity) on transport behaviors. A 10 s pulse of one conservative solute, representing for example sodium chloride, with a nominal concentration of  $1 \text{ kg/m}^3$  is injected in the fracture explicitly inserted at the middle of the left boundary. The free solution diffusion coefficient is  $1 \times 10^{-9} \text{ m}^2/\text{s}$  (which is on the same order of the diffusion coefficient for hydrogen in water). The matrix porosity (0.30) is selected after referring to literature (Edery et al., 2016; Callahan et al., 2000) where a value of 0.25~0.27 was assumed for the matrix porosity. I also tested a much smaller matrix porosity (0.05), and results (not shown here) revealed a tracer BTC (shifted toward younger times, likely due to a higher diffusion rate) with the overall trend similar to that with a porosity of 0.30.

The HGS transport time weighting factor is set to a fully implicit numerical scheme. The fully implicit time-weighting is less prone to exhibit oscillations than the central and explicit time-weighting.

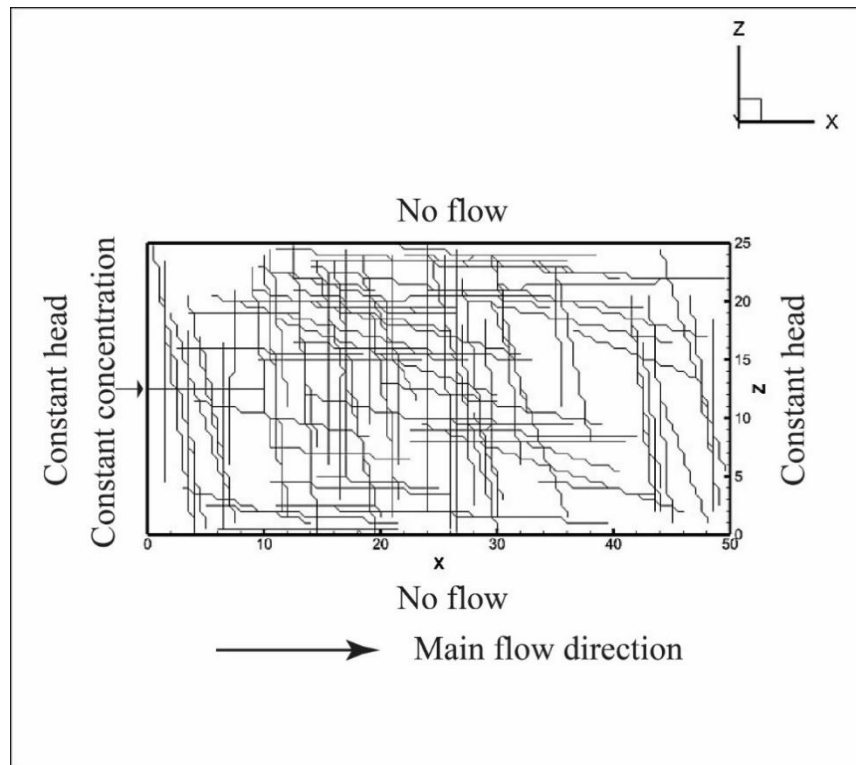


Figure 4-1. Map of the fractured domain, showing flow geometry and boundary conditions. Note that the discrete fractures are curved in the figure, after they are incorporated into the grid by HGS.

Parameter	Symbol	Value	Unit
<i>Matrix</i>			
Hydraulic conductivity	$K_{xx}=K_{yy}=K_{zz}$	$5 \times 10^{-8}, 10^{-7}, 10^{-6}$	$m\ s^{-1}$
Specific storage	$S_s$	$10^{-3}$	$m^{-1}$
Porosity	$\theta_s$	0.3	
Longitudinal dispersivity	$\alpha_L$	0.01	m
Transverse dispersivity	$\alpha_T$	0.001	m
Vertical_transverse dispersivity	$\alpha_V$	0.001	m
Tortuosity	$\tau$	1	
<i>Fractures</i>			
Conductivity (computed)	$K_f$	$(\rho g \omega_f^2)/(12\mu)^a$	$m\ s^{-1}$
Specific storage (computed)	$S_{sf}$	$\rho g \alpha_\omega^b = 4.3 \times 10^{-6}$	$m^{-1}$
Longitudinal dispersivity	$\alpha_{Lf}$	0.01	m
Transverse dispersivity	$\alpha_{Tf}$	0.001	m
Vertical_transverse dispersivity	$\alpha_{Vf}$	0.001	m
<i>Solute</i>			
free-solution diffusion coefficient	$D_{free}$	$10^{-9}$	$m^2/s$
<i>Initial conditions</i>			
Concentration	$C_{t=0}$	0	$kg/m^3$
<i>Boundary conditions</i>			
Inflow concentration	$C_{x=0}$	1	$kg/m^3$
<i>Simulation Settings</i>			
Tracer pulse	$T_{tracer}$	10	s

<sup>a</sup>  $\omega_f$  stands for aperture;  $\mu$  stands for fluid viscosity

<sup>b</sup>  $\alpha_\omega$  stands for fluid compressibility

Table 4-1. Model parameters, initial and boundary conditions used in the simulations

The governing equation for subsurface flow in porous media used in the HGS was a modified form of Richards' equation (Therrien and Sudicky, 1996):

$$-\nabla \cdot (\omega_m q) + \sum \Gamma_{ex} \pm Q = \omega_m \frac{\partial \theta_s}{\partial t} \quad (4-1)$$

where  $\omega_m$  [dimensionless] is the volumetric fraction of the total porosity occupied by the porous medium,  $\Gamma_{ex}$  [ $L^3L^{-3}T^{-1}$ ] represents the volumetric fluid exchange rate between the subsurface domain and discrete fractures,  $Q$  [ $L^3L^{-3}T^{-1}$ ] represents a source/sink term to the porous medium system, and  $\theta_s$  [dimensionless] is the saturated water content which is assumed equal to the porosity. The fluid flux  $q$  [ $LT^{-1}$ ] in (4-1) is given by Darcy's law:

$$q = -K \cdot k_r \nabla (\psi + z) \quad (4-2)$$

where  $K$  [ $LT^{-1}$ ] is hydraulic conductivity tensor,  $k_r$  [dimensionless] represents the relative permeability of the medium,  $\psi$  [ $L$ ] is the pressure head, and  $z$  [ $L$ ] is the elevation head.

A fracture is idealized as the space between two-dimensional parallel surfaces, with the tacit assumptions that the total head is uniform across the fracture width. The equation for saturated flow in a fracture of width/aperture  $\omega_f$  [ $L$ ] can be written by using the analogy of Richards Equation (4-1) for the porous matrix. The governing two-dimensional flow equation in a fracture has the form (Therrien et al., 2010):

$$-\overline{\nabla} \cdot (\omega_f q_f) - \omega_f \Gamma_f = \omega_f S_{sf} \frac{\partial \psi_f}{\partial t}, \quad (4-3)$$

where the fluid flux  $q_f$  [ $LT^{-1}$ ] is given by:

$$q_f = -K_f \cdot k_{rf} \overline{\nabla} (\psi_f + z_f), \quad (4-4)$$

where  $\overline{\nabla}$  is the two-dimensional gradient operator defined in the fracture plane,  $k_{rf}$  [dimensionless] is the permeability of the fracture,  $\psi_f$  and  $z_f$  [ $L$ ] are the pressure and the elevation

heads within the fracture, and  $S_{sf} [L^{-1}]$  is the specific storage coefficient for the fractures. The saturated hydraulic conductivity of a fracture  $K_f [LT^{-1}]$ , having a uniform aperture  $\omega_f$  given by:  $K_f = \rho g \omega_f^2 / 12 \mu$ . Because it is assumed that the fractures are non-deformable and fluid-filled, there is no contribution to the storage term from fracture compressibility. Thus, the specific storage coefficient for a fracture under saturated conditions is only related to the compressibility of water  $\alpha_w [LT^2M^{-1}]$ , according to:  $S_{sf} = \rho g \alpha_w$ .

Three-dimensional transport of solutes in a saturated porous matrix is described by the following ADE (Therrien et al., 2010):

$$-\nabla \cdot \omega_m (qC - \theta_s D \nabla C) + [\omega_m \theta_s R \lambda C] + \sum \Omega_{ex} \pm Q_c = \omega_m \left[ \frac{\partial(\theta_s RC)}{\partial t} + \theta_s R \lambda C \right], \quad (4-5)$$

where  $C$  is the solute concentration  $[ML^{-3}]$ ,  $R$  [dimensionless] is the retardation factor,  $\Omega_{ex} [ML^{-3}T^{-1}]$  represents the mass exchange rate of solutes per unit volume between the subsurface domain and discrete fractures, and  $\lambda$  is a first-order decay constant  $[L^{-1}]$ . Solute exchange with the outside of the simulation domain is represented by  $Q_c [ML^{-3}T^{-1}]$  which represents a source or a sink to the porous medium system.

The equation for solute transport in a saturated fracture is:

$$-\nabla \cdot (\omega_f q_f C_f - \omega_f \theta_f D_f \nabla C_f) + \omega_f [R_f \lambda_f C_f] - \omega_f \Omega_f = \omega_f \left[ \frac{\partial(\theta_f R_f C_f)}{\partial t} + \theta_f R_f \lambda_f C_f \right], \quad (4-6)$$

where  $C_f$  is the concentration in a fracture  $[ML^{-3}]$ ,  $\lambda_f$  is a first-order decay constant  $[L^{-1}]$ ,  $D_f$  is the hydrodynamic dispersion tensor of the fracture  $[L^2T^{-1}]$ , and  $R_f$  [dimensionless] represents retardation factor.

### 4.3.3 Applying the Fractional Advection-Dispersion Equations to Quantify Transport

If the solute is initially placed in the mobile zone (i.e., a fracture along the main flow direction), the corresponding fADE takes the form (Schumer et al., 2003):

$$\frac{\partial C_m}{\partial t} + \beta \frac{\partial^\gamma C_m}{\partial t^\gamma} = -\nabla \cdot [v C_m - D \nabla C_m] - \beta C_m(x, t=0) \frac{t^{-\gamma}}{\Gamma(1-\gamma)}, \quad (4-7a)$$

$$\frac{\partial C_{im}}{\partial t} + \beta \frac{\partial^\gamma C_{im}}{\partial t^\gamma} = -\nabla \cdot [v C_{im} - D \nabla C_{im}] + C_m(x, t=0) \frac{t^{-\gamma}}{\Gamma(1-\gamma)}, \quad (4-7b)$$

where  $C_m$  and  $C_{im}$  [ $ML^{-3}$ ] denote the solute concentration in the mobile and immobile phases, respectively;  $\gamma$  [dimensionless] ( $0 < \gamma \leq 1$ ) is the time index;  $\beta$  [ $T^{\gamma-1}$ ] is the fractional-order capacity coefficient;  $v$  [ $LT^{-1}$ ] and  $D$  [ $L^2T^{-1}$ ] are the effective velocity and dispersion coefficient, respectively; and  $\Gamma(\cdot)$  is the Gamma function.

Meerschaert et al. (2008) generalized the fADE (4-7) by introducing an exponentially truncated power-law function, which is an incomplete Gamma function, as the memory function:

$$g(t) = \int_t^\infty e^{-\lambda s} \frac{\gamma s^{-\gamma-1}}{\Gamma(1-\gamma)} ds, \quad (4-8)$$

where  $\lambda > 0$  [ $T^{-1}$ ] is the truncation parameter in time. This modification leads to the tempered time fADE (tt-fADE) (Meerschaert et al., 2008; Zhang et al., 2014):

$$\frac{\partial C_m}{\partial t} + \beta e^{-\lambda t} \frac{\partial^\gamma}{\partial t^\gamma} [e^{\lambda t} C_m] - \beta \lambda^\gamma C_m = -\nabla \cdot [v C_m - D \nabla C_m] - \beta C_m^0 \int_t^\infty e^{-\lambda \tau} \frac{\tau^{-\gamma-1}}{\Gamma(1-\gamma)} d\tau \quad (4-9a)$$

$$\frac{\partial C_{im}}{\partial t} + \beta e^{-\lambda t} \frac{\partial^\gamma}{\partial t^\gamma} [e^{\lambda t} C_{im}] - \beta \lambda^\gamma C_{im} = -\nabla \cdot [v C_{im} - D \nabla C_{im}] + C_m^0 \int_t^\infty e^{-\lambda \tau} \frac{\tau^{-\gamma-1}}{\Gamma(1-\gamma)} d\tau \quad (4-9b)$$

where  $C_m^0 = C_m(x, t=0)$  denotes the initial source located in the mobile phase or fractures. A few parameters in the tt-fADE (4-9a) and (4-9b) including the effective velocity  $v$  and the

dispersion coefficient  $D$ , may be determined by field experiments (i.e., monitoring wells) and laboratory experiments (transport through fractured media), while the other parameters should be approximated given the plumes observed in the field. The poor predictability of the fADE model motivated us to explore the relationship between DFN properties and model parameters in Section 4.5.

At the late time

$$t \ll 1/\lambda , \quad (4-10)$$

the tail of BTC for solutes in the mobile declines as a power law function:

$$C_m(x,t) \propto t^{-1-\gamma} , \quad (4-11)$$

The tail of the total-phase BTC also declines as a straight line in a log-log plot with a rate:

$$C(x,t) \propto t^{-\gamma} , \quad (4-12)$$

while at a much later time  $t \gg 1/\lambda$ , the slope of the mobile/total-phase BTC reaches infinity (i.e., the late-time BTC tail declines exponentially). Therefore, the value of  $\lambda$  controls the transition of the BTC late-time tail from a power-law function to exponential function (Zhang et al., 2014).

In the following sections, I try to link the time index  $\gamma$  to characteristics of the fractured porous media.

#### 4.4 Results of Monte Carlo Simulations

The ensemble average of BTCs for all 100 realizations for each DFN scenario are shown in Fig. 4-2, along with the best-fit solutions using the tt-fADE model (4-9). Three scenarios of DFN are considered by setting the total number of fractures to 20, 60 and 80, and holding mean fracture set orientations constant to  $0^\circ$  and  $90^\circ$ . An additional fourth scenario explores the impact

of fracture orientation on transport dynamics by changing mean fracture set orientation to  $-45^\circ$  and  $45^\circ$  for a 60 fracture DFN.

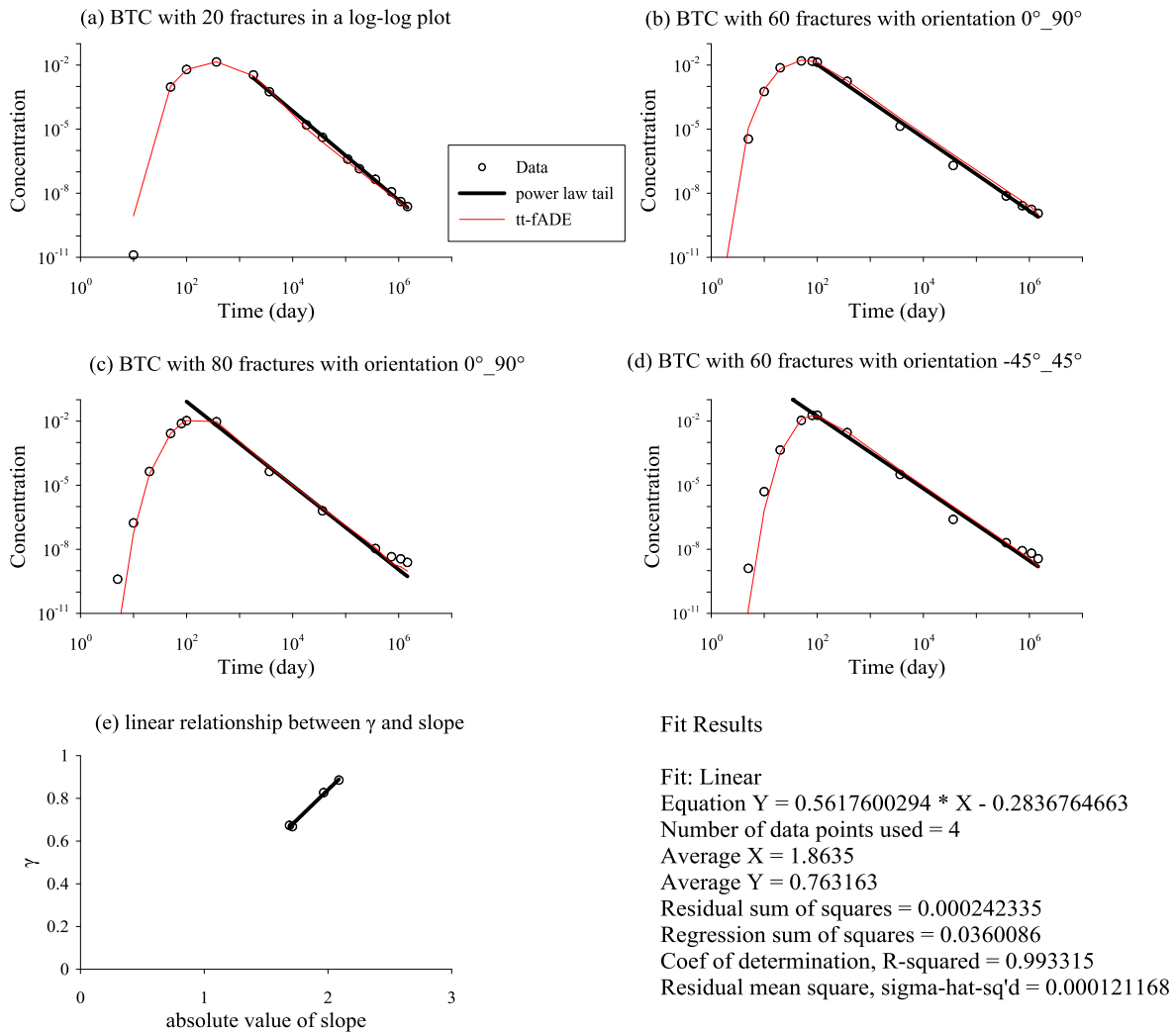


Figure 4-2. BTCs at the control plane  $x=50$  m for three different fracture densities (a), (b) and (c); (b) and (d) have the same fracture density with different orientations. The BTC data (i.e., symbols) are simulated by HGS. The red line is the solution of the tt-fADE model (4-9). The black line is a power law approximation to the late time decay in concentration. (e) shows the empirical linear relationship between the slope of the power-law decay in concentration and the time index  $\gamma$  in the tt-fADE model (4-9).

The best-fit parameters of the tt-fADE model (4-9) for all DFNs are listed in Table 4-2.

The effective velocity  $v$ , dispersion coefficient  $D$ , and fractional-order capacity coefficient  $\beta$  increase with an increasing fracture density. The other two parameters, including the time index  $\gamma$  and the truncation parameter  $\lambda$ , first decrease and then increase as the number of fractures

increases. This trend implies that the DFN domain containing 60 fractures might exhibit higher degree of heterogeneity and therefore translate from non-Fickian to Fickian transport at a much later time, compared to the DFN with 20 or 80 fractures. When the matrix hydraulic conductivity is set to be  $10^{-7}$  m/s, the BTCs are more sensitive to fracture density. For example, when the number of fractures is 20, the peak concentration appears at day 365, while the DFN with 60 (or 80) fractures has the peak BTC at day 50 (or day 100). The truncation parameter  $\lambda$  can be calculated by the reciprocal of the cutoff time representing the transition time from non-Fickian to Fickian transport, although in this study, the power-law portion of BTCs persists and the transition time cannot be identified directly.

Fracture numbers	$\nu$ [m/day]	$D$ [m <sup>2</sup> /day]	$\beta$ [day <sup><math>\gamma</math>-1</sup> ]	$\gamma$ [dimensionless]	$\lambda$ [day <sup>-1</sup> ]	$S_{BTC}$ [dimensionless]
20 (0°~90°)	0.46	9.40	2.17	0.885	3.29E-10	-2.088
60 (0°~90°)	10.53	40.36	5.46	0.667	3.76E-14	-1.712
80 (0°~90°)	12.11	93.84	27.66	0.827	1.75E-08	-1.965
60 (-45°~45°)	20.72	29.37	14.75	0.673	3.24E-08	-1.689

Table 4-2. Best-fit parameters for the tt-fADE model (4-9) for DFNs with different fracture densities and orientation scenarios. In the legend,  $\nu$  denotes the effective velocity,  $D$  is the dispersion coefficient,  $\gamma$  is the time/scale index,  $\beta$  is the fractional-order capacity coefficient,  $\lambda$  is the truncation parameter, and  $S_{BTC}$  stands for the late-time BTC slope in a log-log plot.

## 4.5 Discussion

### 4.5.1 Impact of Fracture Density on Non-Fickian Transport

The simulations indicate that fracture density dominates non-Fickian transport dynamics, and therefore significantly affects tt-fADE model parameters. For example, a denser DFN contains more connected flow paths, leading to faster plume movement (i.e., a larger effective velocity  $\nu$ ), greater plume spreading in space (corresponding to a larger dispersion coefficient  $D$ ), and more fracture/matrix interaction (i.e., tracer particles have a higher probability to enter the surrounding matrix, which correlates to a larger value of the capacity coefficient  $\beta$ ). In addition, the complex relationship between DFN density and other tt-fADE model parameters (time index

$\gamma$  and truncation parameter  $\lambda$ ) can be explained by the hypothesis that moderately dense DFNs (i.e., fracture scenario with 60 fractures) maximizes variations in matrix-fracture exchange rates, which leads to the heaviest late-time BTC tail (i.e., the smallest time index  $\gamma$ ) and the persistent power-law BTC (i.e., the smallest truncation parameter  $\lambda$ ). DFNs with a broader range of densities are needed in a future study to further investigate the above hypothesis.

The dominant impact of fracture density on pollutant transport may be due to two reasons. First, the number of fractures significantly affects the architecture of DFNs, including both the interconnectivity of fractures and the thickness of surrounding matrix. It is well-known that the interconnected fracture network forms the preferred flow paths in the formation (Neuman and Trends, 2005; Moreno and Tsang, 1991; Gerke, 2006). These pathways are “paths of least resistance”, where most of the flow and solute is concentrated (Klepikova et al., 2016; Mukhopadhyay and Cushman, 1998; Lei, 2016; Reeves et al., 2013), resulting in early arrivals. Matrix block size, which is typically characterized using fracture spacing, affects trapping time and influences late-time tailing in BTCs. Second, networks containing higher fracture densities may yield broader distribution of apertures (Neuman, 2008), resulting in a larger variation of advective velocities in the system. Flow in the fracture is constrained to the two-dimensional domain of the fracture aperture, where average flux at any location within a fracture is proportional to the cube of the aperture (Painter and Cvetkovic, 2005; Keller et al., 1999; Hirthe and Graf, 2015). Small variations in apertures (which is  $1 \times 10^3 \sim 1.5 \times 10^3 \mu m$  in this study), therefore, can cause a large, non-linear variations in advective velocity.

#### 4.5.2 Impact of Fracture Orientation on Non-Fickian Transport

Fracture orientation has a complex impact on pollutant transport behavior. The DFN with mean fracture set orientations of  $-45^\circ$  and  $45^\circ$  (where the overall flow direction is along  $0^\circ$ ) provides two major directions for pollutant particles to move, while the DFN with mean fracture set orientations of  $0^\circ$  and  $90^\circ$  offers horizontally dominant motion for pollutants. Hence, the former has a relatively larger effective velocity and less spatial spreading (i.e., a smaller dispersion coefficient). Mean fracture set orientations of  $-45^\circ$  and  $45^\circ$  also enhances the movement of solute particles into matrix blocks, resulting in greater immobile mass (and hence a larger capacity coefficient  $\beta$ ) than that for the cases with mean fracture set orientations of  $0^\circ$  and  $90^\circ$ . It is noteworthy, however, the BTC peak occurs at a time determined by both the effective velocity  $v$  and the capacity coefficient  $\beta$ . The larger for  $v$  and/or the smaller for  $\beta$ , the earlier for the BTC peak. Although the DFNs with mean fracture orientations of  $-45^\circ$  and  $45^\circ$  have a relatively larger  $v$ , the ensemble BTC peak appears later (at day 100) than that for the DFNs with mean fracture orientations of  $0^\circ$  and  $90^\circ$  (BTC peak occurs at day 50), because the DFNs with mean fracture orientations of  $-45^\circ$  and  $45^\circ$  have a much larger  $\beta$ , which acts as part of the retardation coefficient  $(1+\beta)$  when  $\gamma=1$ . The DFNs with mean fracture orientations of  $-45^\circ$  and  $45^\circ$  might also produce more tortuous pathways that lead to greater transverse dispersion than the DFNs with mean fracture orientations of  $0^\circ$  and  $90^\circ$  (Reeves et al., 2008). Finally, regardless of fracture orientation, late-time BTCs exhibit similar slopes, and therefore the similar time index  $\gamma$ , if the DFNs have the same density and a constant distribution of fracture length. The latter impact (caused by the fracture length distribution), however, cannot be reliably investigated in this study due to the field-scale DFNs (with a relatively small domain size). In a future study, I will increase the model domain size (to regional scale) and systematically explore the impact of fracture length distributions on non-Fickian dynamics.

The above analysis implies that the fracture density is more important than the fracture orientation in affecting the power-law late-time tailing of the BTC, while both properties can affect the plume mean displacement (captured mainly by the velocity in the tt-fADE model (4-9)), plume spreading (captured by the dispersion coefficient in model (4-9)), and fracture-matrix mass exchange ratio (captured by the capacity coefficient in (4-9)).

#### 4.5.3 Impact of Matrix Permeability on Late-Time BTC

Rock matrix permeability may affect the late-time behavior of chemical transport. To explore this potential impact, here I conduct additional Monte Carlo simulations using different matrix permeability: 1) increasing matrix permeability by 10 times (from  $1.1 \times 10^{-14} \text{ m}^2$  to  $1.1 \times 10^{-13} \text{ m}^2$ ) and 2) decreasing matrix permeability by 2 times (from  $1.1 \times 10^{-14} \text{ m}^2$  to  $5.5 \times 10^{-15} \text{ m}^2$ ). Results are shown in Fig. 4-3. I do not select the smaller value for matrix permeability, because preliminary numerical tests show that if matrix permeability is smaller than  $1.1 \times 10^{-15} \text{ m}^2$ , the numerical iteration (in the flow model) cannot converge.

The BTC declines faster at the late time with an increasing matrix permeability. This is because the matrix domain with higher permeability leads to shorter trapping times for chemical particles. Contrarily, the average velocity is smaller for rock matrix with smaller permeability, resulting in heavier late-time tailing in the BTC.

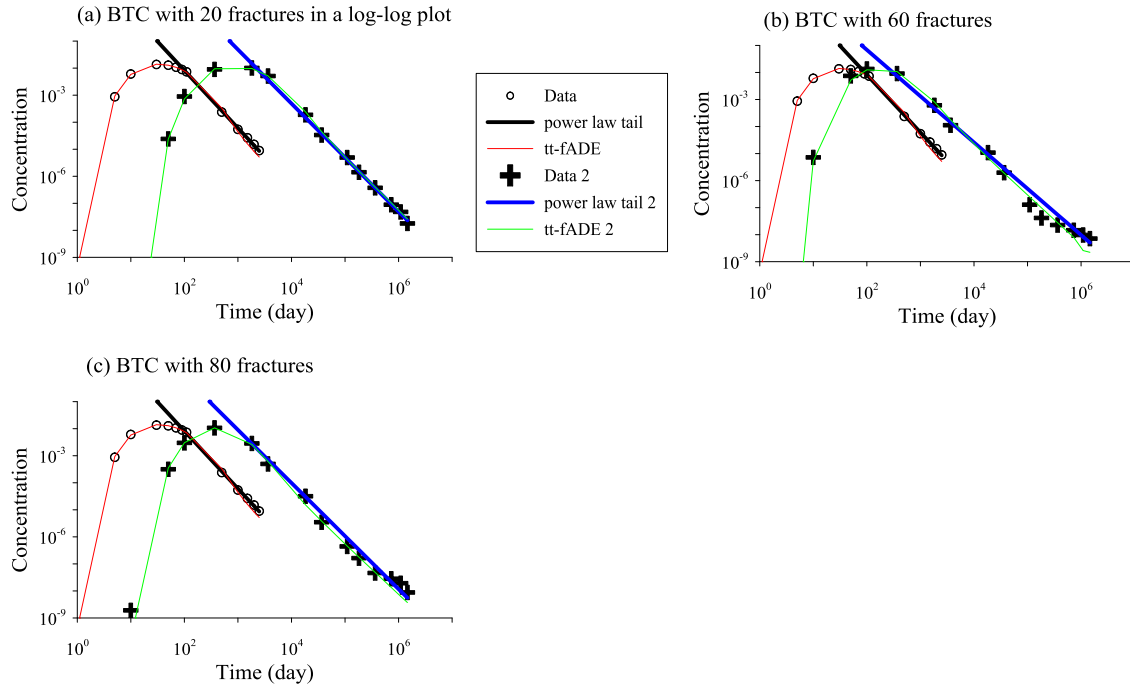


Figure 4-3. BTCs at the control plane  $x=50$  m for three different fracture densities (a), (b) and (c) with matrix permeability of  $1.1 \times 10^{-13} \text{ m}^2$  (red lines and circles) and  $5.5 \times 10^{-15} \text{ m}^2$  (green lines and crosses). The BTC data (i.e., symbols) are simulated by HGS. The red/green line is the solution of the tt-fADE model (4-9). The black/blue line is a power law approximation to the late time decay in concentration.

#### 4.5.4 How to Approximate the Time Index $\gamma$ Given the Limited Late-Time BTC?

Although the transport time considered by my Monte Carlo simulation is very long (~5000 years), I however could not observe the transition in the BTC from persistent non-Fickian to Fickian transport behaviors (in the Monte Carlo simulations performed in this study, the total modeling time cannot be longer than  $2 \times 10^6$  days, since the concentration at the outlet after  $2 \times 10^6$  days is so small that HGS generates negative BTCs). It is common that the measured BTC cannot last long enough to cover the whole power-law portion and/or its transition in the BTC at late times, due to the usually limited sampling period and/or the low concentration at the late time which might be below the detection limit. The time index  $\gamma$  cannot be directly estimated, when the power-law portion of the BTC at the late time cannot be identified.

One possible way to solve the above challenge is to approximate  $\gamma$  using the BTC's recession limb. In this study, the recession limb of each measured BTC exhibits a straight line in a log-log plot (Fig. 4-2), which indicates prolonged non-Fickian or anomalous transport. There is a linear relationship between the slope of the BTC recession limb (whose absolute value is denoted as  $|S_{BTC}|$ ) and the time index  $\gamma$  in the tt-fADE model (4-9):

$$\gamma = 0.5618 \times |S_{BTC}| - 0.2837, \quad (4-13)$$

where the corresponding coefficient of determination is 0.9933 (i.e., strong correlation). Since  $|S_{BTC}|$  can be measured easily, the above linear relationship might be practically useful.

#### 4.5.5 Subdiffusive Transport Shown by Plume Snapshots

I further explore the spatial distribution of chemical in the DFNs by depicting plume snapshots at different times for a single realization and the ensemble average of the Monte Carlo results (Fig. 4-4 and 4-5).

I choose the first time step ( $t = 1$  day) to show the early arrivals for the three different fracture densities with matrix permeability of  $1.1 \times 10^{-14} \text{ m}^2$ . All the three cases show chemical particles move along the preferential flow paths. With increasing fractures in the DFNs, the plume spreads to a wider area in the vertical direction with a more uniform moving front. For the 13<sup>th</sup> time step ( $t = 2000$  yrs), the snapshots exhibit apparent retention and sequestration (meaning that the surrounding low-permeable matrix traps chemical particles, especially near the source (Zhang et al., 2007; LaBolle and Fogg, 2001)) in the least dense fractured network. Competition between channeling and sequestration leads to persistent non-Fickian dynamics. Fast and slow moving chemical particles are counterbalanced, and the effective velocity becomes larger for the DFNs with more fractures.

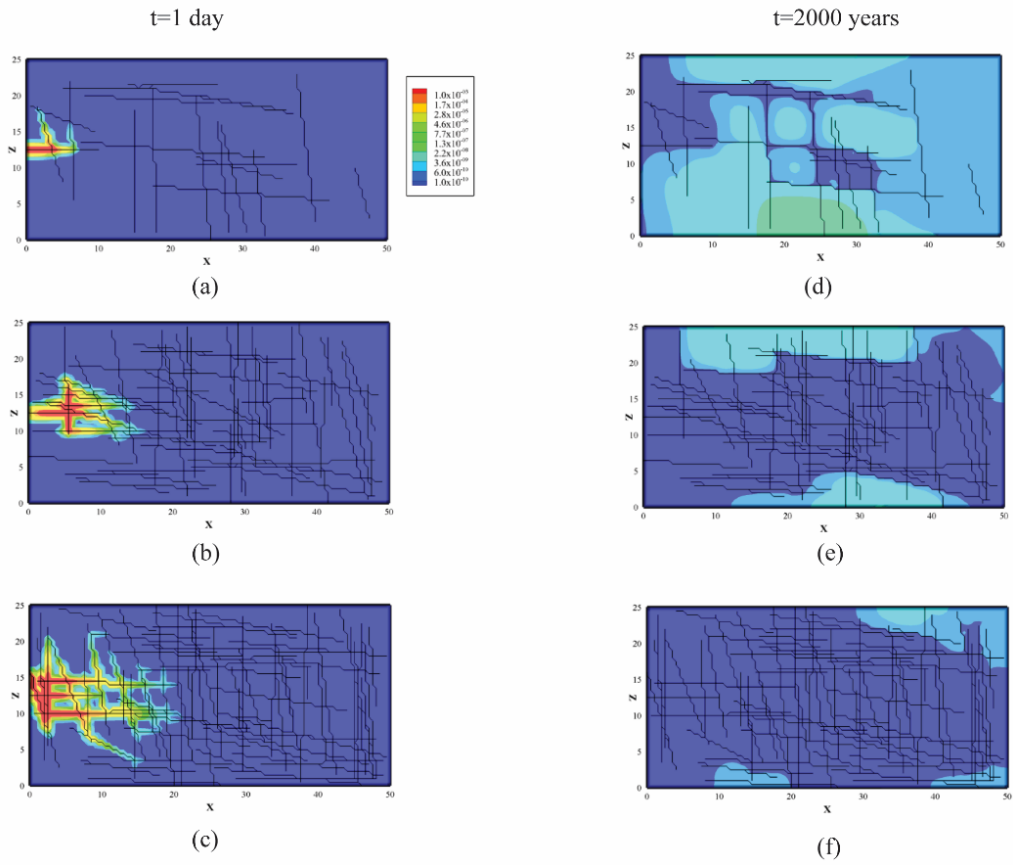


Figure 4-4. One realization of plume snapshots for the first time step ( $t = 1$  day) for the three different fracture densities: (a) the DFNs with 20 fractures, (b) 60 fractures, and (c) 80 fractures; the 13<sup>th</sup> time step ( $t = 2000$  years) for the three different fracture densities: (d) 20 fractures, (e) 60 fractures, and (f) 80 fractures.

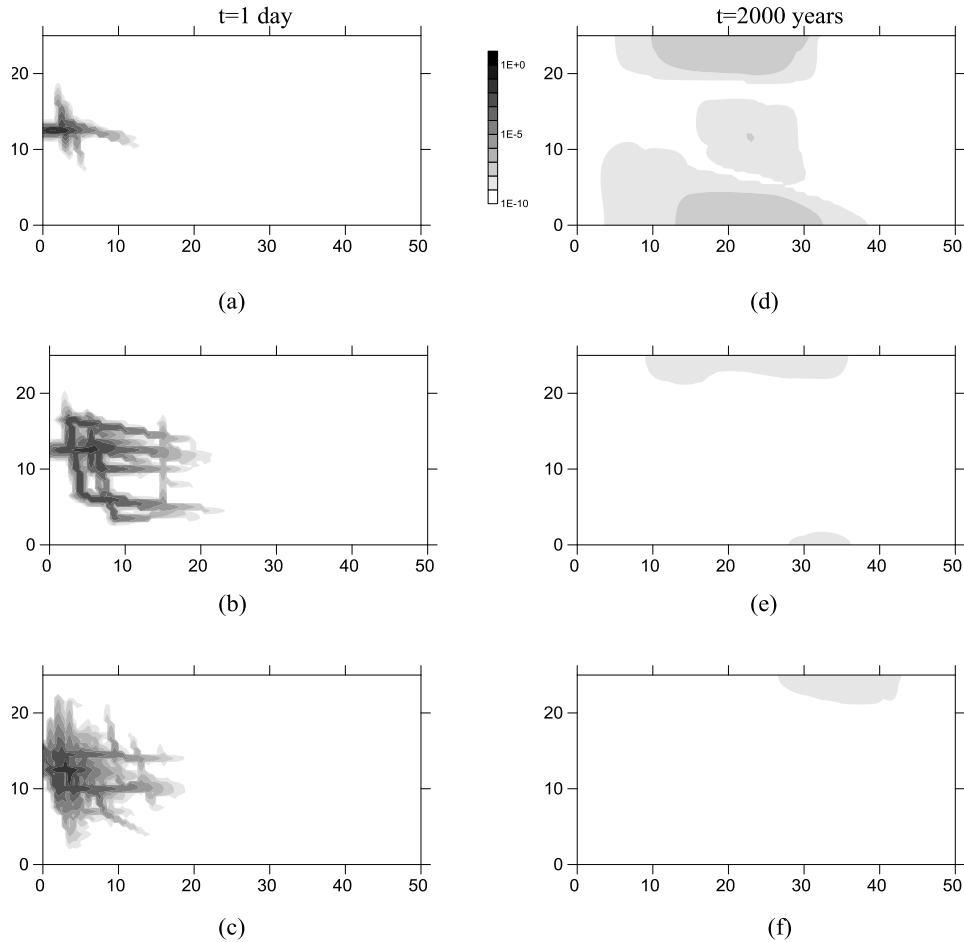


Figure 4-5. Monte Carlo results of plume snapshots for the first time step ( $t = 1$  day) for the three different fracture densities: (a) the DFNs with 20 fractures, (b) 60 fractures and (c) 80 fractures; the 13<sup>th</sup> time step ( $t = 2000$  years) for the three different fracture densities: (d) 20 fractures, (e) 60 fractures and (f) 80 fractures.

#### 4.6 Conclusions

This study aims at exploring the relationship between real-world aquifer properties and non-Fickian transport dynamics, so that the fractional partial differential equations built upon fractional calculus can be reliably applied with appropriate hydrogeologic interpretations. I use the Monte Carlo approach to generate field-scale DFNs where the fracture properties change systematically, and then simulate groundwater flow and pollutant transport through the complex DFNs. For a point source located initially in the mobile phase or fracture, the late-time behavior

for the BTCs simulated by the Monte Carlo approach is then explained by the tempered-stable time fractional advection dispersion equation. I build the relationship between medium heterogeneity and transport dynamics through the combination of numerical experiments and stochastic analysis. The following five primary conclusions are found.

First, the DFN density is the major factor affecting non-Fickian transport at the late time, since 1) the number of fractures significantly affects the internal structure of DFNs, and 2) DFNs containing a higher fracture density may yield broader distribution of apertures, resulting in a larger variation of advective velocities. A moderate dense DFN (filled with 60 fractures) results in the most heterogeneous domain and the heaviest late-time tail in the BTCs, implying that there might exist a potential threshold of fracture density for non-Fickian dynamics when both the domain size and the fracture length distribution remain unchanged.

Second, for the DFNs with the same density and different mean orientations, the late time tailing behavior is affected by the ratio of fractures along different directions. More longitudinal fractures aligned with the overall flow direction will lead to earlier arrivals, while more transverse fractures with flow deviating from the general flow direction will enhance chemical particles to interact with rock matrix, resulting in a higher immobile mass (a larger  $\beta$  in the tt-fADE) and a heavier late-time tailing. The BTC peak time is determined by both the effective velocity and capacity coefficient  $\beta$  (representing the immobile mass ratio). The time index and the slope of the late-time BTC, however, are similar for the DFNs with the similar density and different mean orientations, since the fracture density dominates the distribution of the mass-exchange rate between fracture and matrix (and therefore defines the index of the time fractional derivative in the tt-fADE model).

Third, rock matrix with higher permeability will lead to a relatively more homogeneous domain with a larger time index and a steeper slope in the late-time BTC, since the trapping times in rock matrix becomes relatively shorter.

Fourth, the DFN properties can be quantitatively linked to the slope of the recession limb of the BTC. Particularly, the time index  $\gamma$  in the tt-fADE model has a simple, linear empirical expression with the power-law slope of the BTC recession limb, which can help estimate the index  $\gamma$  in practical applications where the chemical transport time is usually not long enough to cover the full range of late-time transport behavior.

Fifth, plume snapshots show that all the three fracture densities built in this study exhibit early arrivals and sequestration effects. The denser DFNs can produce more early arrivals due to more preferential flow paths, while the sparse DFNs tend to show heavier sequestration near the source. Therefore, competition between the channeling effect (in relative high-permeable fractures or the mobile phase) and the trapping effect (in the surrounding rock matrix or immobile domains) results in complex prolonged non-Fickian characteristics in chemical transport. With predictable parameters, the fractional partial differential equations can be used as an efficient upscaling tool to address real-world contamination problems.

#### 4.7 Acknowledgments:

This work was funded partially by the National Natural Science Foundation of China under grants 41628202 and 41330632. This paper does not necessarily reflect the views of the funding agencies.

#### 4.8 References

Alle, Neuman, S.P., 2005. Trends, prospects and challenges in quantifying flow and transport through fractured rocks. *Hydrogeol. J.* doi:10.1007/s10040-004-0397-2.

- Bakshevskaia, V.A., Pozdniakov, S.P., 2016. Simulation of Hydraulic Heterogeneity and Upscaling Permeability and Dispersivity in Sandy-Clay Formations. *Math. Geosci.* 48, 45–64. doi:10.1007/s11004-015-9590-1.
- Bear, J., 1972. *Dynamics of fluids in porous media*, American Elsevier Publishing Company. New York.
- Becker, M.W., Shapiro, A.M., 2003. Interpreting tracer breakthrough tailing from different forced-gradient tracer experiment configurations in fractured bedrock. *Water Resour. Res.* 39. doi:10.1029/2001WR001190.
- Becker, M.W., Shapiro, A.M., 2000. Tracer transport in fractured crystalline rock: Evidence of nondiffusive breakthrough tailing. *Water Resour. Res.* 36, 1677. doi:10.1029/2000WR900080.
- Benson, D.A.D.A., Wheatcraft, S.W.S.W., Meerschaert, M.M.M., 2000. Application of a fractional advection-dispersion equation. *Water Resour. Res.* 36, 1403–1412. doi:10.1029/2000WR900031.
- Berkowitz, B., 2002. Characterizing flow and transport in fractured geological media: A review. *Adv. Water Resour.* 25, 861–884. doi:10.1016/S0309-1708(02)00042-8.
- CACaS, M.C., Ledoux, E., MARSiLY, G. De, Tillie, B., Calmels, P., Gaillard, B., Margritta, R., de Marsily, G., Tillie, B., Barbreau, A., Durand, E., Feuga, B., Peudecerf, P., 1990. Modeling Fracture Flow With a Stochastic Discrete Fracture Network: Calibration and Validation 2. The Transport Model. *Water Resour. Res.* 26, 491–500. doi:10.1029/WR026i003p00491.
- Chakraborty, P., Meerschaert, M.M., Lim, C.Y., 2009. Parameter estimation for fractional transport: A particle-tracking approach. *Water Resour. Res.* 45. doi:10.1029/2008WR007577.
- Chang, F.-X., Chen, J., Huang, W., 2005. Anomalous diffusion and fractional advection-diffusion equation. *Wuli Xuebao/Acta Phys. Sin.* 54, 1113–1117.
- CKeller, A.A., Roberts, P.V., Blunt, M.J., 1999. Effect of fracture aperture variations on the dispersion of contaminants. *Water Resour. Res.* 35, 55–63.
- Coats, K.K.H., Smith, B.B.D., van Genuchten, M.T., Wierenga, P.J., 1964. Dead-End Pore Volume and Dispersion in Porous Media. *Soil Sci. Soc. Am. J.* 4, 73–84. doi:10.2118/647-PA.
- Cook, P.G., 2003. *A guide to regional groundwater flow in fractured rock aquifers*. Aust. CSIRO 107.

- Cortis, A., Birkholzer, J., 2008. Continuous time random walk analysis of solute transport in fractured porous media. *Water Resour. Res.* 44, 1–11. doi:10.1029/2007WR006596.
- Drummond, J.D., Aubeneau, A.F., Packman, A.I., 2014. Stochastic modeling of fine particulate organic carbon dynamics in rivers. *Water Resour. Res.* 50, 4341–4356. doi:10.1002/2013WR014665.
- Fiori, A., Becker, M.W., 2015. Power law breakthrough curve tailing in a fracture: The role of advection. *J. Hydrol.* 525, 706–710. doi:10.1016/j.jhydrol.2015.04.029.
- Fogg, G.E., Zhang, Y., 2016. Debates—Stochastic subsurface hydrology from theory to practice: A geologic perspective. *Water Resour. Res.* doi:10.1002/2016WR019699.
- Garrard, R.M., Zhang, Y., Wei, S., Sun, H.G., Qian, J., 2017. Can a Time Fractional-Derivative Model Capture Scale-Dependent Dispersion in Saturated Soils? *Groundwater* 55, 857–870. doi:10.1111/gwat.12532.
- Geiger, S., Cortis, A., Birkholzer, J.T., 2010. Upscaling solute transport in naturally fractured porous media with the continuous time random walk method. *Water Resour. Res.* 46. doi:10.1029/2010WR009133.
- Gerke, H.H., 2006. Preferential flow descriptions for structured soils. *J. Plant Nutr. Soil Sci.* doi:10.1002/jpln.200521955.
- Gorenflo, R., Mainardi, F., 1997. Fractional Calculus, in: *Fractals and Fractional Calculus in Continuum Mechanics*. Springer Vienna, Vienna, pp. 223–276. doi:10.1007/978-3-7091-2664-6\_5.
- Green, C.T., Zhang, Y., Jurgens, B.C., Starn, J.J., Landon, M.K., 2014. Accuracy of travel time distribution (TTD) models as affected by TTD complexity, observation errors, and model and tracer selection. *Water Resour. Res.* 50, 6191–6213. doi:10.1002/2014WR015625.
- Gustafson, G., Fransson, Å., 2006. The use of the Pareto distribution for fracture transmissivity assessment. *Hydrogeol. J.* 14, 15–20. doi:10.1007/s10040-005-0440-y.
- Haggerty, R., McKenna, S. a, Meigs, L.C., 2000. On the late-time behaviour of tracer breakthrough curves. *Water Resour. Res.* 36, 3467–3479.
- Haggerty, R., McKenna, S.A., Meigs, L.C., 1999. Tracer Tests in a Fractured Dolomite 4 . Double Porosity , Multiple-Rate Mass Transfer Processes in Two-Well Convergent-Flow Tests.
- Hirthe, E.M., Graf, T., 2015. Fracture network optimization for simulating 2D variable-density flow and transport. *Adv. Water Resour.* 83, 364–375. doi:10.1016/j.advwatres.2015.07.001.

- Huang, G., Huang, Q., Zhan, H., 2006. Evidence of one-dimensional scale-dependent fractional advection-dispersion. *J. Contam. Hydrol.* 85, 53–71. doi:10.1016/j.jconhyd.2005.12.007.
- Kang, P.K., Dentz, M., Le Borgne, T., Juanes, R., 2015a. Anomalous transport on regular fracture networks: Impact of conductivity heterogeneity and mixing at fracture intersections. *Phys. Rev. E - Stat. Nonlinear, Soft Matter Phys.* 92, 1–15. doi:10.1103/PhysRevE.92.022148.
- Kang, P.K., Le Borgne, T., Dentz, M., Bour, O., Juanes, R., 2015b. Impact of velocity correlation and distribution on transport in fractured media: Field evidence and theoretical model. *Water Resour. Res.* 51, 940–959. doi:10.1002/2014WR015799.
- Kelly, J.F., Bolster, D., Meerschaert, M.M., Drummond, J.D. and Packman, A.I., 2017. FracFit: A robust parameter estimation tool for fractional calculus models. *Water Resour. Res.* 53, 2559–2567. doi:10.1002/2016WR019748.
- Klepikova, M.V., Le Borgne, T., Bour, O., Dentz, M., Hochreutener, R. and Lavenant, N., 2016. Heat as a tracer for understanding transport processes in fractured media: Theory and field assessment from multiscale thermal push-pull tracer tests. *Water Resour. Res.* 52, 5442–5457. doi:10.1002/2016WR018789.
- Klimczak, C., Schultz, R.A., Parashar, R., Reeves, D.M., 2010. Cubic law with aperture-length correlation: implications for network scale fluid flow. *Hydrogeol. J.* 18, 851–862. doi:10.1007/s10040-009-0572-6.
- LaBolle, E.M., Fogg, G.E., 2001. Role of Molecular Diffusion in Contaminant Migration and Recovery in an Alluvial Aquifer System. *Transp. Porous Media* 42, 155–179. doi:10.1023/A:1006772716244.
- Lei, Q., 2016. Characterisation and modelling of natural fracture networks: geometry, geomechanics and fluid flow (PhD thesis).
- Liu, R., Li, B., Jiang, Y., 2016. A fractal model based on a new governing equation of fluid flow in fractures for characterizing hydraulic properties of rock fracture networks. *Comput. Geotech.* 75, 57–68. doi:10.1016/j.compgeo.2016.01.025.
- Long Remer, S., Wilson, C.R. and Witherspoon, P.A., J.C.S., Long Remer, S., Wilson, C.R. and Witherspoon, P.A., J.C.S., 1982. Porous media equivalents for network of discontinuous fractures. *Water Resour. Res.* 18, 645–658. doi:10.1029/WR018i003p00645.
- McClure, M., Horne, R., 2013. *Discrete Fracture Network Modeling of Hydraulic Stimulation*, Springer. Springer.
- Meerschaert, M.M., Zhang, Y., Baeumer, B., 2008. Tempered anomalous diffusion in heterogeneous systems. *Geophys. Res. Lett.* 35, 1–5. doi:10.1029/2008GL034899.

- Metzler, R., Klafter, J., 2000. The random walk's guide to anomalous diffusion: a fractional dynamics approach. *Phys. Rep.* 339, 1–77. doi:10.1016/S0370-1573(00)00070-3.
- Moreno, L., Tsang, C.F., 1991. Multiple-Peak Response to Tracer Injection Tests in Single Fractures: A Numerical Study. *Water Resour. Res.* 27, 2143–2150. doi:10.1029/91WR00507.
- Mukhopadhyay, S., Cushman, J.H., 1998. Monte Carlo Simulation of Contaminant Transport: II. Morphological Disorder in Fracture Connectivity. *Transp. Porous Media* 31, 183–211. doi:10.1023/A:1006530216201.
- Outters, N., 2003. A generic study of discrete fracture network transport properties using FracMan/MAFIC. SKB.
- Painter, S., Cvetkovic, V., 2005. Upscaling discrete fracture network simulations: An alternative to continuum transport models. *Water Resour. Res.* 41, 1–10. doi:10.1029/2004WR003682.
- Reeves, D.M., Benson, D.A., Meerschaert, M.M., Scheffler, H.-P.P., 2008. Transport of conservative solutes in simulated fracture networks: 2. Ensemble solute transport and the correspondence to operator-stable limit distributions. *Water Resour. Res.* 44, 1–20. doi:10.1029/2008WR006858.
- Schumer, R., Benson, D., Meerschaert, M., Baeumer, B., 2003. Fractal mobile/immobile solute transport. *Water Resour. Res.* 39.
- Schumer, R., Meerschaert, M.M., Baeumer, B., 2009. Fractional advection-dispersion equations for modeling transport at the Earth surface. *J. Geophys. Res. Earth Surf.* 114, 1–15. doi:10.1029/2008JF001246.
- Selroos, J., Walker, D.D., Ström, A., Gylling, B., Follin, S., 2002. Comparison of alternative modelling approaches for groundwater flow in fractured rock. *J. Hydrol.* 257, 174–188. doi:10.1016/S0022-1694(01)00551-0.
- Sun, H.G., Chen, D., Zhang, Y., Chen, L., 2015. Understanding partial bed-load transport: Experiments and stochastic model analysis. *J. Hydrol.* 521, 196–204. doi:10.1016/j.jhydrol.2014.11.064.
- Therrien, R., McLaren, R.G., Sudicky, E.A. and Panday, S.M., Therrien, R., McLaren, R.G., Sudicky, E. a., Panday, S.M., 2010. HydroGeoSphere A Three-dimensional Numerical Model Describing Fully-integrated Subsurface and Surface Flow and Solute Transport. Groundw. Simulations Group, Univ. Waterloo, Waterloo, 429.
- Therrien, R and Sudicky, E., 1996. Three-dimensional analysis of variably-saturated flow and solute transport in discretely- fractured porous media. *J. Contam. Hydrol.* 23, 1–44.

doi:10.1016/0169-7722(95)00088-7.

- Yong, Z., Benson, D.A., Labolle, E.M., Reeves, D.M., 2007. Spatiotemporal Memory and Conditioning on Local Aquifer Properties. Report.
- Zhang, Y., Baeumer, B., Reeves, D.M., 2010. A tempered multiscaling stable model to simulate transport in regional-scale fractured media. *Geophys. Res. Lett.* 37, 1–5. doi:10.1029/2010GL043609.
- Zhang, Y., Benson, D.A., Baeumer, B., 2007. Predicting the tails of breakthrough curves in regional-scale alluvial systems. *Ground Water* 45, 473–484. doi:10.1111/j.1745-6584.2007.00320.x.
- Zhang, Y., Benson, D.A., Meerschaert, M.M., Labolle, E.M., Scheffler, H.P., 2006. Random walk approximation of fractional-order multiscaling anomalous diffusion. *Phys. Rev. E - Stat. Nonlinear, Soft Matter Phys.* 74, 1–10. doi:10.1103/PhysRevE.74.026706.
- Zhang, Y., Green, C.T., Baeumer, B., 2014. Linking aquifer spatial properties and non-Fickian transport in mobile-immobile like alluvial settings. *J. Hydrol.* 512, 315–331. doi:10.1016/j.jhydrol.2014.02.064.
- Zhang, Y., Sun, H.G., Stowell, H.H., Zayernouri, M., Hansen, S.E., 2017. A review of applications of fractional calculus in Earth system dynamics. *Chaos, Solitons and Fractals* 102, 29–46. doi:10.1016/j.chaos.2017.03.051.
- Zhao, Z., Jing, L., Neretnieks, I., Moreno, L., 2011. Numerical modeling of stress effects on solute transport in fractured rocks. *Comput. Geotech.* 38, 113–126. doi:10.1016/j.compgeo.2010.10.001.
- Zhao, Z., Li, B., Jiang, Y., 2014. Effects of fracture surface roughness on macroscopic fluid flow and solute transport in fracture networks. *Rock Mech. Rock Eng.* 47, 2279. doi:10.1007/s00603-013-0497-1.
- Zhao, Z., Rutqvist, J., Leung, C., Hokr, M., Liu, Q., Neretnieks, I., Hoch, A., Havlíček, J., Wang, Y., Wang, Z., Wu, Y., Zimmerman, R., 2013. Impact of stress on solute transport in a fracture network: A comparison study. *J. Rock Mech. Geotech. Eng.* 5, 110–123. doi:10.1016/j.jrmge.2013.01.002.

## CHAPTER 5:

### IDENTIFYING NON-DARCIAN FLOW AND NON-FICKIAN PRESSURE PROPAGATION IN FIELD-SCALE DISCRETE FRACTURE NETWORKS

#### 5.1 Abstract

Non-Darcian flow has been well documented for fractured media, while the potential non-Darcian flow and its driven factors in field-scale discrete fracture networks (DFNs) remain obscure. This study conducts Monte Carlo simulations of water flow through DFNs to identify non-Darcian flow and non-Fickian pressure propagation in field-scale DFNs, by adjusting fracture density, matrix hydraulic conductivity, and the general hydraulic gradient. Numerical simulations and analyses show that interactions of the fracture architecture with the hydraulic gradient affect non-Darcian flow in DFNs, by generating and adjusting complex pathways for water. The fracture density affects significantly the propagation of hydraulic head/pressure in the DFN, likely due to fracture connectivity and flow channeling. The non-Darcian flow pattern may not be directly correlated to the non-Fickian pressure propagation process in the regional-scale DFNs, because they refer to different states of water flow and their controlling factors may not be the same. Findings of this study improve our understanding of the nature of flow in DFNs.

#### 5.2 Introduction

Darcy's law proposed by Henry Darcy maintains that the specific discharge of water increases linearly with the gradient of hydraulic head along a 3.5-m-long saturated column filled with homogeneous sand (Darcy, 1865). This fundamental law has been used to quantify various

dynamics in natural media with different degrees of heterogeneity and scales for more than one century, such as disposal of radioactive waste, geothermal utilization by hot dry rock systems, oil and gas production from fractured reservoirs, and water production from fractured rock (Kohl et al., 1997; Şahin, 2018). However, subsurface fluid flow with non-Darcian characteristics, where the flow rate is nonlinearly related to the hydraulic gradient (also called “pressure drop”), has been detected in fractured media for decades, especially in the petroleum industry (Holditch and Morse, 1976) which noted that quantifying these effects has proved difficult (Miskimins et al., 2005). For example, non-Darcian flow has been observed in a variety of situations, such as a single confined vertical fracture toward a well (Wen et al., 2006), catalytic packed-bed reactors (Hunt and Tien, 1990), and fractured rock (Kohl et al., 1997).

This study aims at exploring the potential for non-Darcy flow in field-scale discrete fracture networks (DFNs). Fluid flow transition from Darcian to non-Darcian has been confirmed and broadly studied in the case of a single rock fracture (Liu et al., 2016), while such a transition in DFNs has not been fully studied. In addition, non-Darcy flow can occur over a broad spectrum of flow rates, including turbulent flow (for Reynolds number larger than 2000) and low rates in the initial regime (due to the competition between the interface friction and the pressure gradient). For example, previous studies found a nonlinear relationship between flow rate and pressure drop when either of these parameters becomes large (Cooke, 1973; Yeo and Ge, 2001). This study investigates the impact of flow velocity characteristics of subsurface flow through fracture networks on the evolution of non-Darcy dynamics. To address the above issues, I conducted flow simulations involving DFNs with systematic changes in geometric characteristics and applied hydraulic gradient. The impacts of fracture density and matrix permeability are also studied.

I also explored the possible impact of non-Darcy flow on the transient dynamics of water flow through DFNs, which has not been addressed in previous studies. Darcy or non-Darcy flow is usually defined using steady-state flows, where the asymptotic flow rate is used to build the relationship with the pressure drop. Water flow in natural aquifers is often transient, due to the change of input (such as short-term weather change) and/or output (i.e., pumping), and therefore the transient flow dynamics are practically important.

The rest of this work is organized as follows. Section 5.3 presents the Monte Carlo approach to simulation water flux and pressure propagation through multiple DFNs, which is one of the most efficient ways to investigate the impact of fracture properties on water flow behaviors. Results of the Monte Carlo simulations and evaluation using a standard dispersion equation (SDE) are presented in section 5.4. In section 5.5, I discuss the possible signal of non-Darcian flow and non-Fickian pressure propagation and their characterizations. The impacts of fracture density and rock matrix permeability on non-Darcian flow and non-Fickian pressure transfer are investigated. Conclusions are drawn in section 5.6.

### 5.3 Monte Carlo Simulation and Standard-Dispersion Equation

There are three major steps in the Monte Carlo simulation of water flow through saturated field-scale DFNs. First, I generate equally possible but different realizations of stochastic fracture networks for DFNs for each pre-assigned fracture density, using HydroGeoSphere (HGS) software (v.111, Aquanty Inc., Waterloo, ON, Canada) (Therrien et al., 2010). HGS is a multi-dimensional, control-volume, finite element simulator designed to quantify the hydrologic cycle, including groundwater flow and transport in fractured aquifers. Second, pressure drop and water flow through the generated DFNs under both steady state and

transient conditions are modeled using HGS, providing the synthetic data to evaluate the influence of the DFN property on water flow dynamics. Third, propagation of the hydraulic head/pressure is calculated by the Fick's law-based dispersion equation, which describes the Fickian type of transport and can be used to identify any anomalous dynamics embedded in transient flow in complex DFNs.

### 5.3.1 Random Discrete Fracture Network Generation

The two-dimensional DFN has a dimension of 50 m (discretized into 100 blocks) along the longitudinal direction ( $x$  axis) and 25 m (50 blocks) vertically ( $z$  axis). Three scenarios of DFNs, with each containing 100 realizations of DFNs, are built, which have their own unique time-dependent seed based on the current system time to generate random fractures. Each fracture network is composed of two superimposed sets of fractures, which are orthogonal to each other (orientations are  $0^\circ$  and  $90^\circ$ ) as observed commonly in realistic DFNs (Long et al., 1982). The ensemble average of the 100 flow and pressure propagation simulations is calculated for each scenario. A similar geometry was used previously to study subdiffusive transport in fractured formations by Lu et al. (2018), where details about the DFN models, such as fracture locations, orientation, length, and hydraulic conductivities distributions can be found. I extend the work of Lu et al. (2018) by investigating the relationship between pressure drop and flow rate, one of the fundamental problems in hydrologic sciences. I also test the influence of matrix hydraulic conductivity  $K$ , which increases from  $1 \times 10^{-8}$  to  $1 \times 10^{-7}$  m/s.

### 5.3.2 Modeling Groundwater Flow and Pressure Propagation in DFNs

Both the steady-state and transient groundwater flow through the confined aquifer generated above were solved by HGS. Parameters for the flow model are the same as those used

in Lu et al. (2018), which are chosen based on field experiments and literature values (Fiori and Becker, 2015; McKenna et al., 2001). The main flow direction is from left to right, with a general hydraulic gradient ( $J$ ) defined as the ratio of the hydraulic head difference to the DFN domain size ( $\Delta x = 50$  m). The left and right boundaries are then assigned as constant head boundaries, to propagate the general hydraulic gradient across the model domain.

### 5.3.3 Standard-Dispersion Equation to Quantify Pressure Propagation

Hydraulic head (or the propagation of the hydraulic pressure) is typically described by the well-known Boussinesq flow equation (Hornberger et al., 1970), which can be written in the following standard-diffusion equation form with constant parameter:

$$\frac{\partial p}{\partial t} = D \frac{\partial^2 p}{\partial x^2}, \quad (5-1)$$

where  $p(x,t)$  denotes the spatially and temporally varying pressure, and  $D$  represents the diffusion coefficient. Considering the initial condition:  $p(x,t=0)=0$  and the constant-pressure boundary conditions ( $p(x=0,t=0)=p_l$  for the inlet boundary), I obtain the following analytical solution for model (5-1):

$$p(x,t) = p_l \left[ 1 - \operatorname{erf} \left( \frac{x}{\sqrt{4Dt}} \right) \right], \quad (5-2)$$

where  $\operatorname{erf}(\cdot)$  represents the error function.

In the following two sections, I modeled the pressure propagation using the SDE (5-1) to investigate the mechanism behind the propagation of the pressure (head).

## 5.4 Results of Monte Carlo Simulations

The ensemble average of steady-state water flux across the outlet (right) boundary for all 100 realizations is plotted in Fig. 5-1 with the pre-assigned hydraulic gradient ( $J$ ). Curves in Fig. 5-1 show the best-fit linear trend line (black line) and the power-law trend line (blue line). Three scenarios of DFNs with different fracture densities are considered, which contain 20, 60 and 100 fractures, respectively.

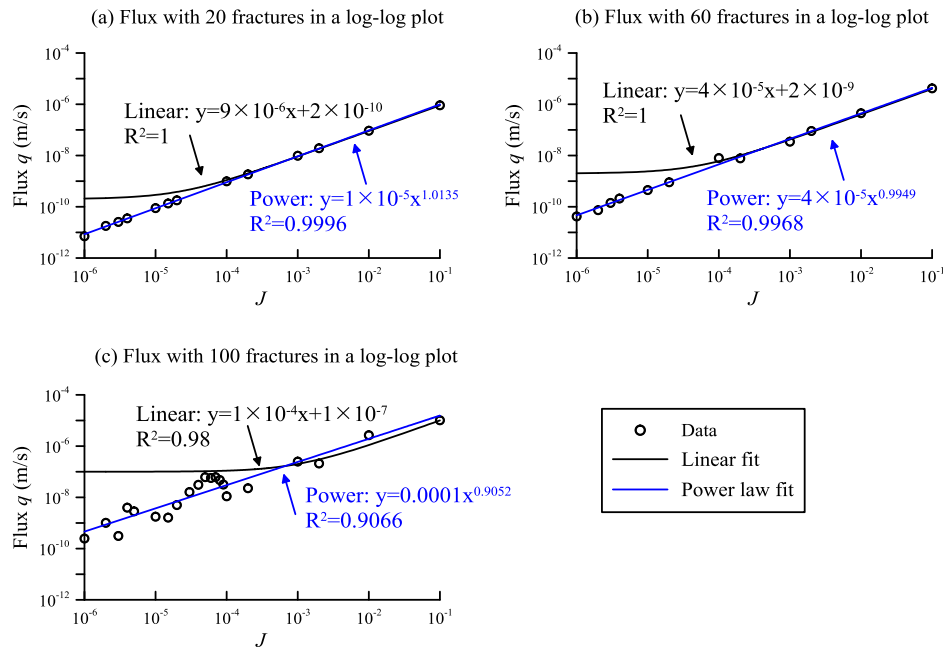


Figure 5-1. Ensemble average flux at the outlet boundary for the three DFN scenarios with a different number of fractures: 20 (a), 60 (b), and 100 (c). The symbols are steady-state flux data simulated by HGS, and the solid lines are the best-fit trend lines.

Results show that the DFN with 100 fractures contains the largest noise in the simulated flux (especially for a relatively small hydraulic gradient:  $1 \times 10^{-6} < J < 1 \times 10^{-3}$ ), and the relationship between hydraulic gradient and flux transfers from non-linear (power-law) to linear gradually (Fig. 5-1c). The noise in Fig. 5-1c might be an artificial oscillation due to the solver or the limited number of realizations, but the nonlinear region may be real since it also appears in all the other scenarios (Fig. 5-1a, b). With less fractures in the rock mass, the nonlinear portion

shortens (Fig. 5-1a, b). In all scenarios, the overall increasing trend of water flux due to an increasing hydraulic gradient can be captured by a power-law function (Fig. 5-1), satisfying the Izbash law (Munson et al., 2006).

The simulated transient flux at the outlet boundary is shown in Fig. 5-2 with the matrix hydraulic conductivity  $K = 1 \times 10^{-7}$  m/s. For illustration purposes, here I show the results with three hydraulic gradients:  $J = 1 \times 10^{-5}$ ,  $1 \times 10^{-4}$ , and  $1 \times 10^{-3}$ . To explore the impact of  $K$  on transient flux, I re-ran the above Monte Carlo simulations and obtain the transient flux for  $K = 1 \times 10^{-8}$  m/s (Fig. 5-3). The best-fit of transient flux using the SDE (5-1) is also shown in these figures.

Fig. 5-4 shows the distribution of hydraulic head, and Fig. 5-5 lists the probability density function (PDF) for the flux for grids at the outlet boundary.

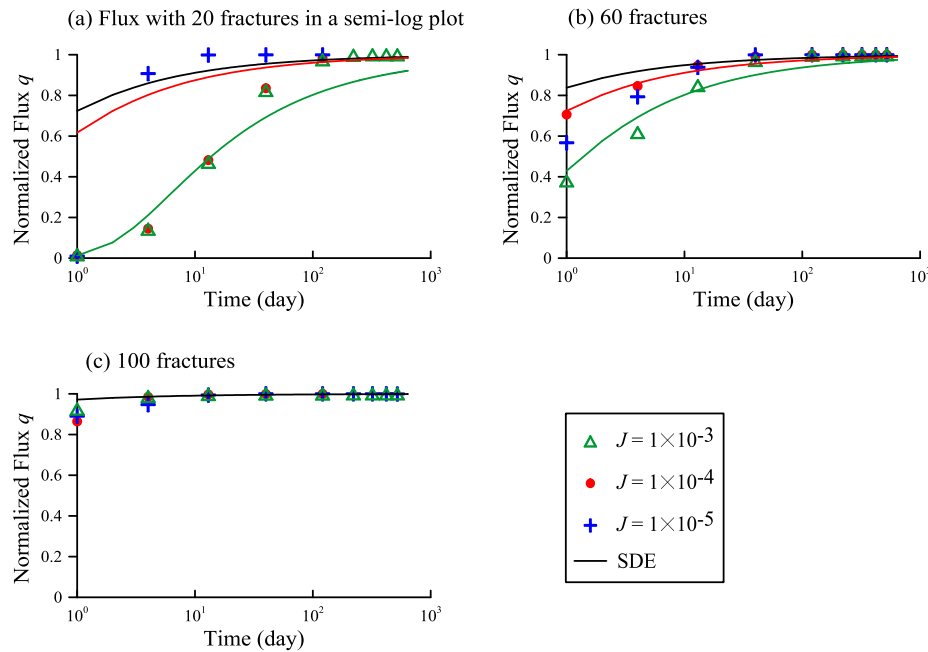


Figure 5-2. The normalized, ensemble average of transient flux for DFNs with the number of fractures being 20 (a), 60 (b) and 100 (c). The matrix conductivity is  $K = 1 \times 10^{-7}$  m/s. Solid lines are the best-fit solutions of the SDE (5-1). In (a),  $D = 2 \times 10^2$ ,  $5 \times 10^3$ , and  $1 \times 10^4$  m<sup>2</sup>/s for the green, red, and black lines, respectively. In (b),  $D = 2 \times 10^3$ ,  $1 \times 10^4$ , and  $3 \times 10^4$  m<sup>2</sup>/s for the green, red, and black lines, respectively. In (c),  $D = 1 \times 10^6$  m<sup>2</sup>/s.

## 5.5 Discussion

### 5.5.1 Fracture Density and Hydraulic Gradient Affect Non-Darcian Flow

The fracture density may affect Non-Darcian flow in field-scale fractured networks by generating complex flow paths for water, which can change with the magnitude of the general hydraulic gradient  $J$ . For a dense DFN (i.e., the DFN with 100 fractures, see Fig. 5-4c), the random distribution of multiple fractures causes a complex flow field consisting of multiple flow zones and surrounding dead ends, especially for a relatively small  $J$ . The resultant longitudinal ensemble flux may not be as large as that predicted by the Darcy's law (see the dots below the linear trend line shown in Fig. 5-1c). The overall hydraulic connectivity along the longitudinal direction can be enhanced with an increasing  $J$ , leading to a larger longitudinal flux. When the general hydraulic gradient reaches a threshold  $J_s$ , the overall flow paths reach stable (or reach the capacity of connection), and the corresponding longitudinal flux is now mainly controlled by  $J$ , resulting in Darcian flow.

For a sparse DFN (such as the one with 20 fractures shown in Fig. 5-4a), the flow channeling behavior is stronger than that in the dense DFN (similar to that observed in a fluvial setting with a small proportion of high-permeability ancient channels (Zhang et al., 2014)), and hence it requires a relatively smaller  $J_s$  to reach the connection capacity and the Darcian flow regime. Therefore, if  $J$  is less than  $J_s$ , both the DFN's internal architecture and the pressure gradient affect water flux, generating strong non-Darcian flow. When  $J$  is larger than  $J_s$ , Darcian flow dominates all DFNs. The denser for the DFN, the larger for the threshold  $J_s$ . For example, Monte Carlo simulations of this study show that  $J_s$  is equal to  $1 \times 10^{-4}$ ,  $2 \times 10^{-4}$ , and  $1 \times 10^{-3}$  for the DFN with 20, 60 and 100 fractures (see Fig. 5-1). The general hydraulic gradient  $J$  usually ranges between  $10^{-4}$  and  $10^{-1}$  in natural aquifers, and hence flow in the field-scale DFN most likely follows Darcy's law, especially for the DFN with sparse fractures.

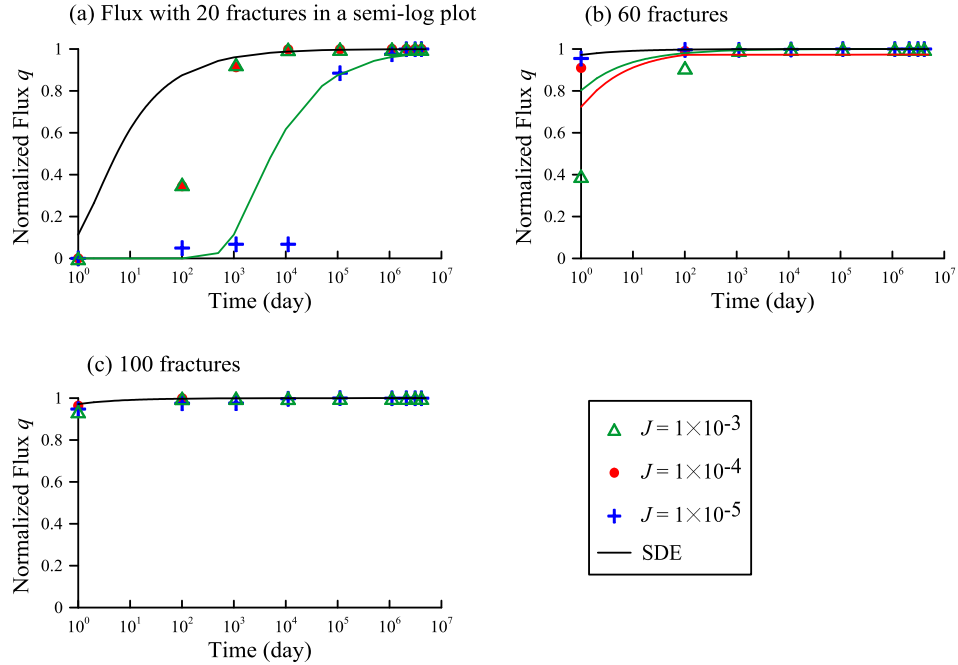


Figure 5-3. The same as Fig. 5-2, except that the hydraulic conductivity for the rock matrix is  $K = 1 \times 10^{-8}$  m/s. The solid lines are the best-fit solutions of the SDE (5-1). In (a),  $D = 5 \times 10^{-1}$  and  $5 \times 10^2$  m<sup>2</sup>/s for the green and black lines, respectively. In (b),  $D = 1 \times 10^6$  m<sup>2</sup>/s for the black line. In (c),  $D = 1 \times 10^6$  m<sup>2</sup>/s for the black line.

The channeling of flow can also be found in Fig. 5-5. Grid-based flux differs significantly between DFNs and shows a broad distribution. The dense DFN has a positive skewness for the PDF (Fig. 5-5c), while the sparse DFN has a relatively negative skewness for the PDF (Fig. 5-5a), implying a stronger channeling effect for the sparse DFN (where the large flux is embedded in a smaller number of fractures).

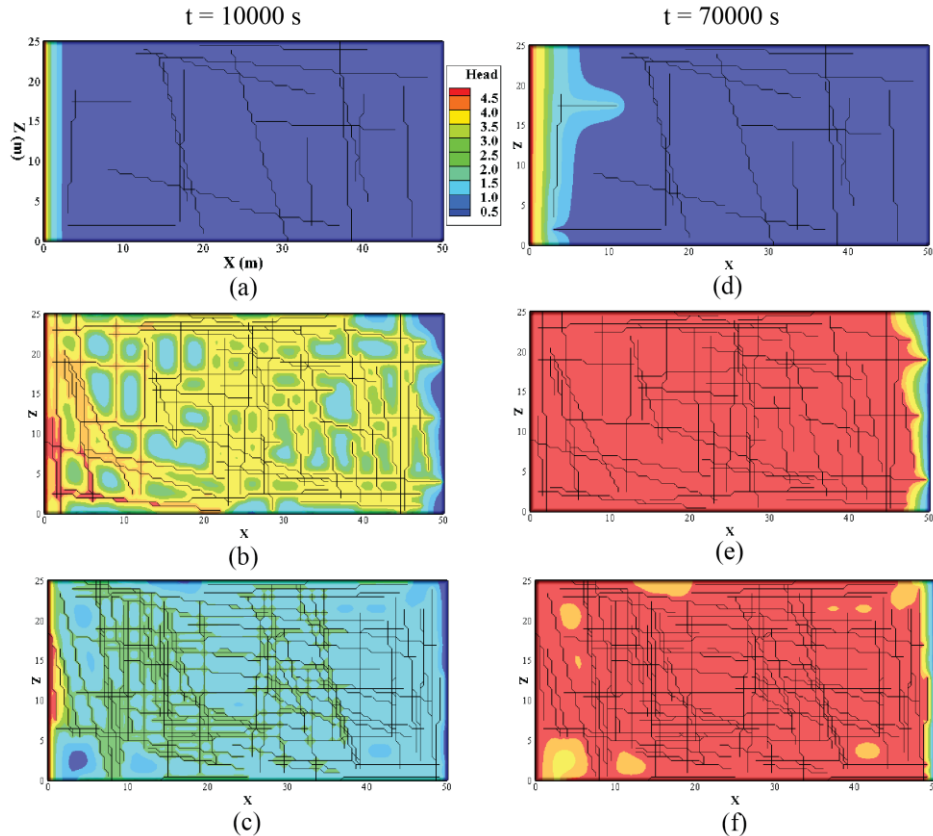


Figure 5-4. One realization of the hydraulic head distribution with the matrix hydraulic conductivity  $K = 1 \times 10^{-7}$  m/s and hydraulic gradient  $J = 0.1$  at an early time ( $t = 1 \times 10^4$  s) for the DFN with 20 (a), 60 (b), and 100 fractures (c). The right plot shows a late time ( $t = 7 \times 10^4$  s) hydraulic head for the DFN with 20 (d), 60 (e), and 100 fractures (f).

### 5.5.2 Impact of Fracture Density on Non-Fickian Pressure Propagation

The sparse DFN exhibits stronger non-Fickian pressure propagation, especially at the early time, due to the following three reasons. First, the sparse DFN has a relatively small effective hydraulic conductivity, resulting in an overall slow motion for water. It therefore takes a longer time for the transient flux in the sparse DFN to reach its asymptote, generating the transient flux with a delayed arriving limb at the early time (see Figs. 5-2 and 5-3). Second, the inlet boundary of the sparse DFN has a lower probability of direct connection with the fracture than the dense DFN, and hence water must pass through the low-permeable rock matrix before

reaching the preferential flow paths. Third, the sparse DFN has a stronger channeling impact, as mentioned above, and hence the major conduits consisting of the sparse and long fractures can transfer water (or pressure) quickly, when water reaches these water “conduits” (see Fig. 5-4). The transient flux can now increase quickly, as shown by the late-time symbols above the SDE curve in Fig. 5-2a. The delayed pressure propagation at the early time and the enhanced propagation at the middle to late times for the sparse DFN, therefore, transfer the hydraulic pressure quite differently from that predicted by a wave diffusive model like the SDE (5-1).

The delayed transfer of water at the early time is also observed for dense DFNs (Fig. 5-2c and Fig. 5-3c). Water needs to fill most of the discrete fractures, where some of them are not connected with the major flow paths. The time required to build the major flow paths may decrease with increasing fracture density, since more fractures in the domain can provide a higher probability for an interconnected network. I name this time the “initial regime”, where the propagation of pressure does not follow the Fick’s law. As shown by the above Monte Carlo simulations, the initial regime is shorter for a denser DFN.

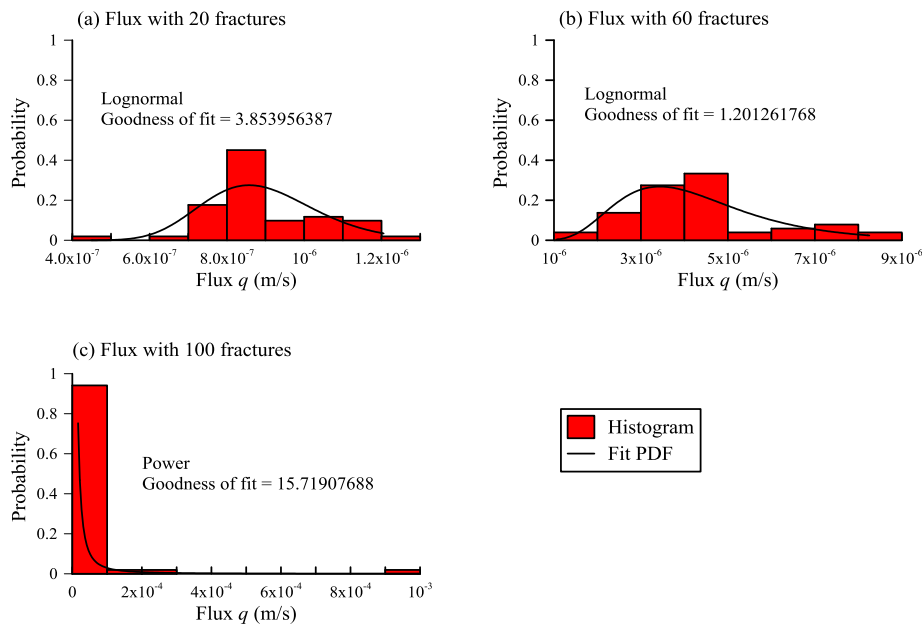


Figure 5-5. Histogram of the flux of 100 realizations for each node at the outlet boundary for the DFN with 20 (a), 60 (b), and 100 fractures (c). The matrix hydraulic conductivity  $K = 1 \times 10^{-7}$  m/s. The curve represents the best-fit probability distribution function.

### 5.5.3 Impact of Matrix Permeability on Transient Flow

Decrease of the rock matrix hydraulic conductivity tends to retard further the propagation of pressure for all DFNs tested in this study, implying that a larger permeability contrast between fractures and matrix leads to a stronger non-Fickian propagation of the hydraulic pressure. It is also noteworthy that for the sparse DFN (with 20 fractures), the inlet boundary for some realizations may not be directly connected with the major fractures, and hence the decrease of the matrix hydraulic conductivity causes significantly slow arrival of the transient flux (by comparing Figs. 5-2a and 5-3a). The delayed flow for the other DFNs is not so apparent, since their inlet boundary has a higher chance of fracture connection, as shown by Figs. 5-4b, c.

### 5.5.4 Non-Darcian Flow versus Non-Fickian Pressure Propagation

I do not find direct correlation between non-Darcian flow and non-Fickian pressure propagation in field-scale DFNs. Non-Darcian flow quantifies the steady-state flux, while non-Fickian pressure propagation focuses on the evolution dynamics of transient flux before reaching its steady-state asymptote. Hence, they need not to be directly connected. Indeed, the above Monte Carlo simulations showed that the dense DFN with strong non-Darcian flow tends to exhibit weak non-Fickian pressure propagation. My analysis also shows that the threshold hydraulic gradient  $J_s$  distinguishes Darcian and non-Darcian flow, while the initial regime related to fracture connectivity and architecture affects the early-time non-Fickian pressure propagation.

## 5.6 Conclusion

This study conducts Monte Carlo simulations to identify possible non-Darcian flow and non-Fickian pressure propagation in field-scale discrete fracture networks. Multiple scenarios of DFNs are generated with different fracture densities and matrix hydraulic conductivities. Flux needed for Darcian/non-Darcian flow analysis is calculated from the steady-state flow models using HGS, and the transient motion of water is modeled to reveal possible non-Fickian propagation of hydraulic pressure. Numerical simulations and result analysis lead to the following three main conclusions.

First, both the fracture network architecture and the general hydraulic gradient  $J$  affect the Darcian/non-Darcian flow in DFNs. The fracture density may affect flow dynamics by generating complex flow paths for water, and the gradient  $J$  can adjust the flow field and provide the criterion for Darcian/non-Darcian flow. Strong non-Darcian flow appears for  $J$  less than the threshold  $J_s$ , where this threshold increases with an increasing fracture density.

Second, fracture density affects significantly the propagation of hydraulic head or pressure in the DFN. A sparse DFN can cause both delayed motion of water at the early time (likely due to the small effective hydraulic conductivity and the poor fracture connectivity) and enhanced flow at the middle/late time (likely due to the enhanced flow channeling), resulting in strong non-Fickian pressure propagation.

Third, the non-Darcian flow pattern needs not to be directly related to the non-Fickian pressure propagation process in field-scale DFNs, because they refer to different states of water flow and their controlling factors may not be exactly the same.

## 5.7 Acknowledgements

This work was funded partially by the National Natural Science Foundation of China under grants 41628202, 41330632 and 11572112. This paper does not necessarily reflect the views of the funding agency.

## 5.8 References

- Cooke, C.E., 1973. CONDUCTIVITY OF FRACTURE PROPPANTS IN MULTIPLE LAYERS. *JPT, J. Pet. Technol.* 25, 1101–1107. doi:10.2118/4117-PA.
- Darcy, H.P.G., 1865. *Les Fontaines publiques de la ville de Dijon. Exposition et application des principes à suivre et des formules à employer dans les questions de distribution d'eau, etc.* V. Dalamont.
- Fiori, A., Becker, M.W., 2015. Power law breakthrough curve tailing in a fracture: The role of advection. *J. Hydrol.* 525, 706–710. doi:10.1016/j.jhydrol.2015.04.029.
- Holditch, S.A., Morse, R.A., 1976. EFFECTS OF NON-DARCY FLOW ON THE BEHAVIOR OF HYDRAULICALLY FRACTURED GAS WELLS. *JPT, J. Pet. Technol.* 28, 1169–1179. doi:10.2118/5586-PA.
- Hornberger, G.M., Ebert, J., Remson, I., 1970. Numerical Solution of the Boussinesq Equation for Aquifer- Stream Interaction. *Water Resour. Res.* 6, 601–608. doi:10.1029/WR006i002p00601.
- Hunt, M.L., Tien, C.L., 1990. Non-darcian flow, heat and mass transfer in catalytic packed-bed reactors. *Chem. Eng. Sci.* 45, 55–63. doi:10.1016/0009-2509(90)87080-C.
- Kohl, T., Evans, K.F., Hopkirk, R.J., Jung, R., Rybach, L., 1997. Observation and simulation of non-Darcian flow transients in fractured rock. *Water Resour. Res.* 33, 407–418. doi:http://dx.doi.org/10.1029/96WR03495; doi:10.1029/9.
- Liu, R., Li, B., Jiang, Y., 2016. Critical hydraulic gradient for nonlinear flow through rock fracture networks: The roles of aperture, surface roughness, and number of intersections. *Adv. Water Resour.* 88, 53–65. doi:10.1016/j.advwatres.2015.12.002.
- Long Remer, S., Wilson, C.R. and Witherspoon, P.A., J.C.S., Long Remer, S., Wilson, C.R. and Witherspoon, P.A., J.C.S., 1982. Porous media equivalents for network of discontinuous fractures. *Water Resour. Res.* 18, 645–658. doi:10.1029/WR018i003p00645.
- Lu, B., Zhang, Y., Reeves, D., Sun, H., Zheng, C., 2018. Application of Tempered-Stable Time Fractional-Derivative Model to Upscale Subdiffusion for Pollutant Transport in Field-

- Scale Discrete Fracture Networks. *Mathematics* 6, 5. doi:10.3390/math6010005.
- McKenna, S.A., Meigs, L.C., Haggerty, R., 2001. Tracer tests in a fractured dolomite: 3. Double-porosity, multiple-rate mass transfer processes in convergent flow tracer tests.
- Miskimins, J.L., Lopez-Hernandez, H.D., Barree, R.D., 2005. Non-darcy flow in hydraulic fractures: Does it really matter?, in: *Proceedings - SPE Annual Technical Conference and Exhibition*. Society of Petroleum Engineers, pp. 2709–2716. doi:10.2118/96389-MS.
- Munson, B.R., Young, D.F., Okiishi, T.H., 2006. *Fundamentals of Fluid Mechanics*, John Wiley & Sons. Inc., USA.
- Şahin, A.U., 2018. A Particle Swarm Optimization Assessment for the Determination of Non-Darcian Flow Parameters in a Confined Aquifer. *Water Resour. Manag.* 32, 751–767.
- Therrien, R., McLaren, R.G., Sudicky, E.A. and Panday, S.M., Therrien, R., McLaren, R.G., Sudicky, E. a., Panday, S.M., 2010. *HydroGeoSphere A Three-dimensional Numerical Model Describing Fully-integrated Subsurface and Surface Flow and Solute Transport*. Groundw. Simulations Group, Univ. Waterloo, Waterloo, 429.
- Wen, Z., Huang, G., Zhan, H., 2006. Non-Darcian flow in a single confined vertical fracture toward a well. *J. Hydrol.* 330, 698–708. doi:10.1016/j.jhydrol.2006.05.001.
- Yeo, I.W., Ge, S., 2001. Solute dispersion in rock fractures by non-Darcian flow. *Geophys. Res. Lett.* 28, 3983–3986. doi:10.1029/2001GL013274.
- Zhang, Y., Green, C.T., Baeumer, B., 2014. Linking aquifer spatial properties and non-Fickian transport in mobile-immobile like alluvial settings. *J. Hydrol.* 512, 315–331. doi:10.1016/j.jhydrol.2014.02.064.

CHAPTER 6:  
QUANTIFYING FATE AND TRANSPORT OF NITRATE IN SATURATED SOIL SYSTEMS  
USING FRACTIONAL-DERIVATIVE MODEL

6.1 Abstract

Natural soil systems usually exhibit complex properties such as fractal geometry, resulting in complex dynamics for the movement of solutes and colloids in soils, such as the well-documented non-Fickian or anomalous diffusion for contaminant transport in saturated soils. The development of robust methods to model anomalous diffusion for reactive contaminants at all relevant scales remains an historical challenge. This study aims to develop and validate a novel fractional-derivative, advection-dispersion-reaction equation (fADRE) with first order decay to quantify nitrate contaminants transport in various soil systems. As an essential nutrient for crop growth, nitrogen in various forms (i.e. fertilizers) is typically applied to agricultural plots but a certain fraction or excess that is converted to nitrate or nitrite will serve as a critical pollutant to surface-water and groundwater. Applications show that the fADRE model can consider both hydrological and biogeochemical processes describing the fate and transport of nitrate in saturated soil. The model is tested and validated using the results from three independent studies including: 1) nitrate transport in natural soil columns collected from the North China Plain agricultural pollution zone, 2) nitrate leaching from aridisols and entisols soil columns, and 3) two bacteria (*Escherichia coli* and *Klebsiella* sp.) transport through saturated soil columns. The qualitative relationship between model parameters and the target

system properties (including soil physical properties, experimental conditions, and nitrate/bacteria physical and chemical properties) is also explored in detail, as well as the impact of chemical reactions on nitrate transport and fate dynamics. Results show that the fADRE can be a reliable mathematical model to quantify non-Fickian and reactive transport of chemicals in various soil systems, and it can also be used to describe other biological degradation and decay processes in soil and groundwater. Hence, the mathematical model proposed by this study may help provide valuable insight on the quantification of various biogeochemical dynamics in complex soil systems, but needs to be tested in real-world applications in the future.

## 6.2 Introduction

Soils play a critical role in the ecosystem by 1) providing the medium for plant growth, habitat for organisms and storage zones for carbon and other gases, and 2) acting as a filter, buffer, and transformation system between atmosphere, biosphere, hydrosphere, and lithosphere (Blum, 2005; Totsche et al., 2010). Natural soil systems usually exhibit physical, chemical, and/or biological heterogeneity at all relevant scales (Young and Crawford, 2004; Pouyat et al., 2010; Pepper and Brusseau, 2019, among many others), which can significantly affect the dynamics of mass, momentum, and energy moving in soil (Pachepsky et al., 2010). For example, interconnected macropores (such as root channels, earthworm burrows, and interconnected cracks) build complex pore networks in soils and form preferential flow paths which exhibit multi-scaling structure (Tarquis et al., 2009, 2006) and enhance water flow, resulting in super-diffusive non-Fickian transport for dissolved contaminants (Beven and Germann, 2013, 1982; Zhang et al., 2017a). Meanwhile, micropores and clay minerals in soil and/or other soil matrix regions tend to delay chemical transport, causing the well-documented retention or sub-diffusion for contaminants (Brusseau, 1993; Chen et al., 2012; Tick et al., 2007; van Genuchten and

Wagenet, 2010; Zhang et al., 2017b). For these reasons, significant challenges still exist to effectively describe non-Fickian or anomalous transport of contaminants at various scales when using a multitude of approaches such as traditional Fickian diffusion based transport models (Novák and Hlaváčiková, 2019; Vanderborght and Vereecken, 2007; Zhang et al., 2009). This historical challenge in soil and groundwater transport is the primary motivation for this study.

One of the common pollutants found in soils impacted by agricultural or other human activities and identified worldwide is nutrient in the form of nitrogen-nitrate (N-NO<sub>3</sub><sup>-</sup>). Nitrogen contamination (in the form of nitrate, NO<sub>3</sub><sup>-</sup>, or nitrite, NO<sub>2</sub><sup>-</sup>) in soil mainly comes from nitrogen-enriched fertilizers and animal manure used as crop nutrients (Almasri and Kaluarachchi, 2007a; Carey and Lloyd, 1985; Oyarzun and Oyarzun, 2007). Nitrogen exceeding plant demand and soil denitrification capacity can leach to deep vadose zone or groundwater mostly as nitrate (Almasri and Kaluarachchi, 2007b; Shamruk et al., 2001). For example, in the North China Plain, the human impact on soil and groundwater has increased in depth since 1960s, resulting in great changes in soil and groundwater chemical properties over time. According to the China Geological Survey, the average concentration of NO<sub>3</sub><sup>-</sup> in saturated soils at Shijiazhuang, Hebei Province, increased continuously from 2.35 mg/L in 1959 to 56.2 mg/L in 2005 (Cheng et al., 2017), exceeding the maximum contaminant level set by U. S. Environmental Protection Agency (10 mg/L, nitrate as nitrogen (NO<sub>3</sub>-N)). The overabundance of nitrate in soil and water can cause various adverse ecological effects. For example, ingestion of NO<sub>3</sub><sup>-</sup> is carcinogenic and might be associated with hypertension (Malberg et al., 1978), increased infant mortality (Super et al., 1981), central nervous system birth defects (Dorsch et al., 1984), stomach cancer (Hill et al., 1973), and non-Hodgkin's lymphoma (Weisenburger, 1991). Mathematical models reliably

describing fate and transport of nitrogen can help to manage and remediate nitrogen contamination in saturated soil systems.

Many efforts have been made to explore the fate and transport of nitrate in soil and groundwater. For example, Han et al. (2015) found that nitrate could accumulate and be transported for a long time due to retention in soil matrix. Rahmati et al. (2015) found that nitrate transport in saturated soil was affected by the water flow pattern. Atekwana and Geyer (2018) found that nitrate behaved remarkably different in time despite seasonal hydrological variations, and heterogeneous denitrification and precipitation dilution attenuated nitrate spatially in saturated soil. Menció et al. (2015) evaluated nitrate pollution in various aquifers and found the positive linear relationship between nitrate and some ions. Murgulet and Tick (2016, 2013, 2009) conducted a series of groundwater studies to assess the extent and source of nitrate contamination and applied models to understand fate and transport of nitrate. These studies showed that the dynamics of  $\text{NO}_3^-$  in saturated soils can be affected by various physical and biogeochemical processes, which cannot be measured at all relevant scales or mapped exhaustively using the classical transport models. Nitrate transport in saturated soils can also be affected by a complex interplay of various factors, such as flow conditions, nitrogen sources, climate, microbial ecology, soil toxic conditions, plant uptake, geology, the land surface area contributing to the well, and residence time of contaminants in the soil system (Mekala et al., 2017). Therefore, reliable simulation of nitrate dynamics in saturated soil was proved to be difficult, yet imperative.

This study aims at developing a stochastic, fractional-derivative model (FDM) to simulate reactive transport of nitrate in saturated soil systems with various degrees of heterogeneity. The FDM, built upon fractional calculus methods, is selected because previous

studies showed that it can effectively capture non-Fickian diffusion in various natural systems (Metzler and Klafter, 2004, 2000). Particularly, the spatial FDM with a maximum skewness for fractional dispersion describes the fast displacement of mobile chemicals along preferential flow paths, while the temporal FDM captures delayed motion or retention of chemicals due to mass exchange between flow zones and relatively immobile zones in the soil system (Zhang et al., 2017b). Therefore, by combining spatial and temporal fractional derivatives in the transport model, one can model super-diffusion, sub-diffusion, and their broad mixture for pollutants transported in saturated soils. In addition, chemical reactions such as sorption and denitrification can be added into the FDM to quantify reactive transport for nitrate.

The rest of the work is organized as follows. In Section 6.3, a brief literature review is provided for nitrate transport, showing the major dynamics revealed by various studies. In Section 6.4, a review of previous numerical modeling of nitrate transport and transformation through saturated soils is presented. Based on deficiencies of such modeling approaches for highly-skewed breakthrough transport, a stochastic FDM is proposed to simulate anomalous and reactive transport behavior of nitrate in heterogeneous soil systems, with a numerical solution of this new model approach. In Section 6.5, I apply the proposed model to the observed non-Fickian breakthrough curves (BTCs) for the nitrate transport behavior documented in literature (various studies). Section 6.6 discusses the relationship between model parameters and porous media properties and the influence of reaction on transport dynamics. The FDM is also compared with previous models, to identify the appropriate model with the minimum number of parameters to effectively quantify nitrate transport and transformation. The model is also extended to capture bacteria transport, to check its capability for generalization and/or to simulate colloidal transport behavior in saturated porous media. Conclusions are presented in Section 6.7.

### 6.3 Nitrate dynamics revealed by laboratory experiments documented in literature

Here I review two well-documented laboratory transport experiments for nitrate. In the first experiment, soil samples were taken from the Beijing Tongzhou field site in the North China Plain, a major agricultural area where over-fertilization is common, and nitrate underwent transformation processes through anaerobic processes (environment) (Zheng et al., 2012; Ju et al., 2006). The second experiment observed the transport dynamics of nitrate in undisturbed calcareous soils with various internal structures (Mahmood-Ul-Hassan et al., 2010). By analyzing these two experiments, I can gain insight into the impacts of soil structures, transformation processes, particle properties, and reactions on solute fate and transport, aiding the development of mathematical models in the next section.

#### 6.3.1 Review of laboratory experiment 1: saturated soil from a test site in Beijing, China

Laboratory transport experiments through fine soils conducted by Zheng et al. (2012) provide data to evaluate nitrate transport/fate dynamics under well controlled conditions. The soil used for the column was collected from alluvial deposits located in southeastern Beijing, China, from longitude of 116.72° E and latitude of 39.848° N.

Zheng et al. (2012) conducted three experiments. The first experiment was to explore the sorption-desorption kinetics of nitrate in saturated soils in the absence of microbial degradation (all soils and solutions were sterilized prior). Samples of nitrate concentrations were tested at the same time interval to study the effect of nitrate-soil sorption. Two experimental scenarios were conducted for comparative purposes: one was to add deionized water in the soil, and the other was to put nitrate solution into the centrifuge tube directly. The sorption-desorption results showed basically no differences. Since the test soils were collected from a previously

agriculturally-dominated region, the soil had high levels of residual  $\text{NO}_3\text{-N}$  already. The main components of the soil are quartz, calcite, plagioclase and chlorite, which contain high iron and aluminum ions. The second set of experiments were conducted within untreated soils (i.e. unsterilized) to determine the kinetics of nitrate denitrification. Results showed that with insufficient carbon sources (i.e. low carbon-content as the soil samples from the field), the nitrate denitrification reaction generally follows the first-order rate kinetics behavior (Zheng et al., 2012). The initial nitrate concentration had no effect on the denitrification intensity (reaction rate). The pH and carbon source are important factors affecting denitrification processes. Finally, laboratory soil column experiments were conducted to analyze both nitrate transport and transformation processes through saturated soil. Two experimental scenarios were used to check the feasibility of the fractional-order stochastic model which is proposed in the next section (Section 6.5).

In order to test fine-grain impacts on nitrate transport, the review study used silty-clay soil samples collected from the Beijing Tongzhou test site. Soil samples were pretreated by air drying, crushing, and passing through a 1 mm pore size nylon sieve to remove sand and debris. The soil was then packed into a stainless-steel column with an inner diameter of 3.5 cm and height of 20 cm. In the first experiment, a solution of  $\text{KNO}_3$  ( $\text{NO}_3^-$  concentration of 100 mg/L) was pumped through the saturated silty-clay packed column at 0.1 mL/min (Darcy velocity) until 100 mL of solution was pumped through and then immediately followed by pumping deionized water through the system. In the second experiment, all the conditions were kept the same with the exception that  $\text{NO}_3^-$  concentration was reduced to 50 mg/L to evaluate the influence of initial concentration difference on the nitrate transport behavior. After normalizing the concentration and time (nondimensional time), it was observed that transport behavior of the two different

experiments were similar, except for the fact that the first experiment had a slightly earlier initial penetration time (when the concentration of transported ion in the outflow liquid starts to change) and complete penetration time (when the ion concentration in the outflow liquid does not change), implying that  $\text{NO}_3^-$  in higher concentration solution moves slightly faster through a similar medium. Under the high initial concentration condition, both nitrite and ammonium concentration were significantly higher than those of low initial concentration condition, which indicated the accumulation of nitrite and the increase of ammonium ions. Since nitrite reductase was inhibited under high concentration of nitrate, nitrite could not be effectively reduced and resulting in net accumulation. However, high concentration of nitrate can promote the reduction of nitrate to ammonium, leading to an increase in ammonium. The results were consistent with the findings of Kelso et al. (1997). Compared with denitrification, other biological reactions only account for a small proportion of the whole process. Denitrification was the main reaction in nitrate removal under the conditions of these experiments. In Section 6.5, these two experiments will be used to check the feasibility of the mathematical model developed in Section 6.4.

### 6.3.2 Review of laboratory experiment 2: nitrate leaching in aridisols and entisols

To further investigate the kinetics of nitrate, a review of results from leaching experiments is presented (Mahmood-Ul-Hassan et al., 2010). Undisturbed columns packed with calcareous soils of different clay contents and structures were used in laboratory leaching studies. Mahmood-Ul-Hassan et al. (2010) used four different soil samples from a highly developed agricultural system: Shahdara (sandy loam, massive to weak coarse sub-angular blocky), Sultanpur (very fine sandy loam, weak coarse sub-angular blocky), Lyallpur (silt loam, weak coarse and medium sub-angular blocky), and Pacca (silty clay, moderate medium and fine sub-angular blocky), which were located between longitudes  $73.17^\circ$ - $73.75^\circ$  E and latitudes  $31.17^\circ$ -

31.5° N. The experimental leaching data was simulated (fitted) using two deterministic models: the standard advection-dispersion equation (ADE) model with retardation and the two-region mobile-immobile (MIM) model (discussed further in Section 6.5.2). Physical and chemical characteristics of the soils showed that the cation exchange capacity and clay contents of the four soils decreased in the following order: Pacca > Lyallpur > Shahdara > Sultanpur. Under a similar scenario and conditions, I apply the new FDM to these experimental data to investigate the influence of different ions, reaction dynamics, and various structures on the fate and transport of nitrate in saturated soils.

## 6.4 Methodology development

### 6.4.1 Stochastic model to simulate nitrate reaction and transport in saturated soils

Various numerical models have been developed to simulate reaction and transport of nitrate in saturated or partially saturated soils. For example, Kinzelbach et al. (1991) presented a multi-species transport model incorporating microbial denitrification as the major process of nitrate elimination. MacQuarrie and Sudicky (2001) developed a numerical model to describe reactive transport containing multiple species of carbon and nitrogen in three-dimensional saturated soil, and formulated the reaction system as a fully kinetic chemistry problem.

Chowdary et al. (2004) proposed a model to assess mass evolution of nitrate in water percolating out of the flooded rice fields, where all the N-transformations (except plant uptake and leaching) were assumed to follow first-order kinetics. Lee et al. (2006) developed a kinetic model to study nitrification-denitrification reactions in saturated soil. Binley et al. (2018) added both the single-rate nitrate uptake and the first-order nitrification terms into the classical ADE model to simulate nitrate transport through a deep, regional-scale vadose zone. Similarly, Akbariyeh et al. (2018) added a sequential first-order decay chain into the ADE to simulate  $\text{NO}_3\text{-N}$  transport in vadose

zone with detailed soil heterogeneity. Most of these models, however, are data intensive and unpredictable in the field, since the classical transport models (such as the ADE) require information such as physical and chemical heterogeneity, dominating nitrate dynamics, which is difficult to measure exhaustively (Kinzelbach et al., 1991).

The challenge mentioned above motivates me to develop a parsimonious, upscaling mathematical model which does not rely on detailed mapping of the medium's physical and chemical properties. The proposed model should account for 1) non-Fickian transport for nitrate, and 2) reaction processes including sorption/desorption and denitrification/nitrification, which are the dominant chemical reactions affecting nitrate kinetics in saturated soils (Almasri and Kaluarachchi, 2007b; Shamruk et al., 2001). I propose the following spatiotemporal fractional advection-dispersion-reaction equation (fADRE) model with sorption and denitrification transformations to simulate fate and transport of nitrate in saturated soils:

$$\frac{\partial C(x,t)}{\partial t} + \beta {}^{TC}D_t^{\gamma,\lambda} C(x,t) = -v \frac{\partial C(x,t)}{\partial x} + D {}^{RL}D_x^\alpha C(x,t) - KC(x,t), \quad (6-1)$$

where  $C [ML^{-3}]$  represents the nitrate concentration;  $\beta [T^{\gamma-1}]$  is the fractional capacity coefficient; the operator  ${}^{TC}D_t^{\gamma,\lambda} C(x,t)$  denotes the truncated Caputo fractional derivative in time;  $\gamma$  [dimensionless] is the time index ( $0 < \gamma \leq 1$ );  $\lambda [T^{-1}]$  is the truncation parameter in time defining the transition time from non-Fickian to Fickian transport;  $v [LT^{-1}]$  is the mean velocity;  $D [L^2T^{-1}]$  is the fractional dispersion coefficient; the operator  ${}^{RL}D_x^\alpha C(x,t)$  denotes the Riemann-Liouville fractional derivative in space;  $\alpha$  [dimensionless] is the space index ( $1 < \alpha \leq 2$ ); and  $K [T^{-\alpha}]$  is the first-order rate constant for reactions.

There are seven parameters ( $\beta, \gamma, \lambda, v, D, \alpha, K$ ) in model (6-1). The truncation parameter  $\lambda$  can be omitted when the nitrate BTC does not exhibit any slope variation (i.e., truncation from

power-law decline to exponential decline in nitrate concentration), or the experimental time is too short to observe the truncation. When  $\gamma = 1$  (i.e., without retention) and  $\alpha = 2$  (representing Fickian diffusion), Eq. (6-1) reduces to the standard advection-dispersion-reaction equation (ADRE).

Eq. (6-1) uses the spatial and temporal fractional-derivative terms to capture super-diffusion (along preferential flow paths) and sub-diffusion (due to nitrate retention); therefore, no detailed soil heterogeneity information is required when capturing non-Fickian transport for nitrate. In addition, Eq. (6-1) assumes the first-order decay to account for nitrate chemical reactions. Studies of nitrate mass change in low-permeability soil (such as Experiment 1 mentioned in Section 6.3.1) showed that denitrification is the most important factor of nitrate attenuation, followed by nitrate adsorption. Nitrate transport experiments done by Zheng et al. (2012) also showed nitrate sorption and denitrification followed the first-order reaction kinetics. Reddy et al. (2010) also found that under anaerobic conditions, the nitrate reduction process followed the first-order kinetics. Hence, the first-order decay is selected for nitrate reactions in model (6-1).

Compared with the classical models (i.e., MIM model), the fADRE model (6-1) has the least parameters when effectively quantifying major N-transformation and non-Fickian transport. Physical meanings and relationship of model parameters with soil properties, experimental conditions (see discussion in Section 6.6.1), and solute's properties (Section 6.6.3) will be discussed below.

#### 6.4.2 Numerical solver and validation

To capture nitrate transport in soil columns (described in Section 6.3), I define the following boundary and initial conditions:

$$\left. \frac{\partial C(x,t)}{\partial x} \right|_{x=x_l} = 0, \quad (6-2a)$$

$$\left. \frac{\partial C(x,t)}{\partial x} \right|_{x=x_r} = 0, \quad (6-2b)$$

$$C(x, t = 0) = C_0 \delta(x - x_0), \quad (6-2c)$$

where  $x_l$  and  $x_r$  [L] denote the left (i.e., inlet or upstream) and right (i.e., outlet or downstream) boundary position, respectively;  $C_0$  is the initial concentration of nitrate; and  $\delta(\cdot)$  is the Dirac delta function. The boundary condition (6-2a) is a zero-value, second type boundary defining a fully reflective boundary at the inlet (because advection is from upstream to downstream, the nitrate particles cannot exit the inlet via advection or dispersion). The boundary condition (6-2b) represents the commonly used exit boundary by hydrologists where the nitrate concentration is continuous across the outlet boundary (Danckwerts, 1953; Schwartz et al., 1999) (in this case, the nitrate particles can only exit the downstream boundary via advection). The initial condition (6-2c) denotes an instantaneous point source located at  $x_0$ , as used in the laboratory column transport experiments for nitrate (Section 6.3.1).

I then solve the fADRE (6-1) with the boundary/initial conditions (6-2) numerically using the implicit finite difference scheme. The space and time domains are discretized first, with  $x_l \leq x_i \leq x_r$  and  $0 < t_i \leq T$ , where  $x_i$  represents the spatial position and  $t_i$  stands for the temporal point. The numerical scheme to approximate the Riemann-Liouville space fractional derivative in model (6-1) is (Zhang et al., 2009):

$${}^{RL}D_x^\beta c(x_l, t_{k+1}) = \frac{(-1)^n}{\Gamma(n-\alpha)} \frac{d^n}{dx^n} \int_x^b (\xi - x_l)^{n-\beta-1} f(\xi) d\xi \approx \frac{1}{h^\beta} \sum_{j=0}^{l+1} g_j c(x_{l-j+1}, t_{k+1}), \quad (6-3)$$

where  $n - 1 < \beta < n$ ,  $g_j$  denotes the Grünwald weight with  $g_0 = 1$ ,  $g_j = -\frac{\beta-j+1}{j}g_{j-1}$ ,  $j = 1, 2, 3 \dots$ , and  $h$  is the space step size.

In addition, the numerical scheme for the tempered Caputo fractional derivative is (Cao et al., 2014):

$$\begin{aligned} {}^T C_0 D_t^{\alpha, \lambda} c(x, t_{k+1}) &= \frac{e^{-\lambda t_{k+1}}}{\Gamma(1-\alpha)} \int_0^{t_{k+1}} \frac{e^{\lambda \xi} c'(x, \xi) d\xi}{(t_{k+1} - \xi)^\alpha} \\ &\approx \frac{e^{-\lambda t_{k+1}}}{\Gamma(1-\alpha)} \sum_{j=0}^k \left( \frac{e^{\lambda t_{j+1}} c(x, t_{j+1}) - e^{\lambda t_j} c(x, t_j)}{\tau} \right) \int_{j\tau}^{(j+1)\tau} \frac{d\xi}{(t_{k+1} - \xi)^\alpha} \\ &= \frac{e^{-\lambda t_{k+1} \tau^{-\alpha}}}{\Gamma(2-\alpha)} \sum_{j=0}^k \left( e^{\lambda t_{k-j+1}} c(x, t_{k-j+1}) - e^{\lambda t_{k-j}} c(x, t_{k-j}) \right) [(j+1)^{1-\alpha} - j^{1-\alpha}], \end{aligned} \quad (6-4)$$

where  $0 < \alpha \leq 1$ , and  $\tau$  is the time step size.

Inserting Eq. (6-3) and Eq. (6-4) into the fADRE (6-1), I get the following numerical scheme for the control equation (6-1):

For  $t_{k+1} = t_1$  (i.e.,  $k=0$ ):

$$\begin{aligned} &\left( \frac{\tau^{-\alpha}}{\Gamma(2-\alpha)} - \frac{D}{h^\beta} g_1 - \frac{V}{h} + 1 - \gamma \lambda^\alpha \right) c(x_l, t_1) + \left( \frac{V}{h} - \frac{1}{h^\beta} g_0 \right) c(x_{l+1}, t_1) \\ &+ \frac{1}{h^\beta} \sum_{j=2}^{l+1} g_j c(x_{l-j+1}, t_1) = \frac{e^{-\lambda t_1 \tau^{-\alpha}}}{\Gamma(2-\alpha)} e^{\lambda t_0} c(x_l, t_0) \end{aligned}, \quad (6-5)$$

For  $t_{k+1} = t_2$  (i.e.,  $k=1$ ):

$$\begin{aligned} &\left( \frac{\tau^{-\alpha}}{\Gamma(2-\alpha)} - \frac{D}{h^\beta} g_1 - \frac{V}{h} + 1 - \gamma \lambda^\alpha \right) c(x_l, t_2) + \left( \frac{V}{h} - \frac{1}{h^\beta} g_0 \right) c(x_{l+1}, t_2) \\ &+ \frac{1}{h^\beta} \sum_{j=2}^{l+1} g_j c(x_{l-j+1}, t_2) = -\frac{e^{-\lambda t_2 \tau^{-\alpha}}}{\Gamma(2-\alpha)} [e^{\lambda t_1} c(x_l, t_1)(2^{1-\alpha} - 2) - e^{\lambda t_0} c(x_l, t_0)(2^{1-\alpha} - 1)] \end{aligned}, \quad (6-6)$$

For  $t_{k+1}$  with  $k \geq 2$ :

$$\begin{aligned}
& \left( \frac{\tau^{-\alpha}}{\Gamma(2-\alpha)} - \frac{D}{h^\beta} g_1 - \frac{V}{h} + 1 - \gamma\lambda^\alpha \right) c(x_l, t_{k+1}) + \left( \frac{V}{h} - \frac{1}{h^\beta} g_0 \right) c(x_{l+1}, t_{k+1}) \\
& + \frac{1}{h^\beta} \sum_{j=2}^{l+1} g_j c(x_{l-j+1}, t_{k+1}) = - \frac{e^{-\lambda t_{k+1} \tau^{-\alpha}}}{\Gamma(2-\alpha)} e^{\lambda t_k} c(x_l, t_k) (2^{1-\alpha} - 2) \\
& - \frac{e^{-\lambda t_{k+1} \tau^{-\alpha}}}{\Gamma(2-\alpha)} \sum_{j=1}^{k-1} e^{-\lambda t_{k-j}} c(x_l, t_{k-j}) [(j+2)^{1-\alpha} - 2(j+1)^{1-\alpha} + j^{1-\alpha}] \\
& + \frac{e^{-\lambda t_{k+1} \tau^{-\alpha}}}{\Gamma(2-\alpha)} e^{-\lambda t_0} c(x_l, t_0) [(k+1)^{1-\alpha} - k^{1-\alpha}]
\end{aligned} \tag{6-7}$$

To validate the above solver, I construct an exact solution for a special case of Eq. (6-1):

$$\frac{\partial C(x,t)}{\partial t} + A {}^R C_0^{0.8, \lambda} D_t C(x, t) = D {}^R L_0^{1.6} D_x C(x, t) - KC(x, t), \tag{6-8a}$$

$$C(x, 0) = 0, \tag{6-8b}$$

$$C(0, t) = 0, \quad C(1, t) = 0, \tag{6-8c}$$

where  $D = \frac{x^{1.6} \Gamma(1.4)}{\Gamma(3)}$ ,  $A = \frac{x^{0.8} \Gamma(2.2)}{4}$ ,  $K = (\lambda + 0.5 - 2/t)$ ,  $x \in [0, 1]$ , and  $t \in [0, 100]$ . The exact

solution for problem (6-8) is:

$$C_{exact}(x, t) = x^2 t^2 e^{-\lambda t}, \tag{6-9}$$

Fig. 6-1 shows the distribution of numerical error in space with different numbers of time nodes, demonstrating a convergent trend.

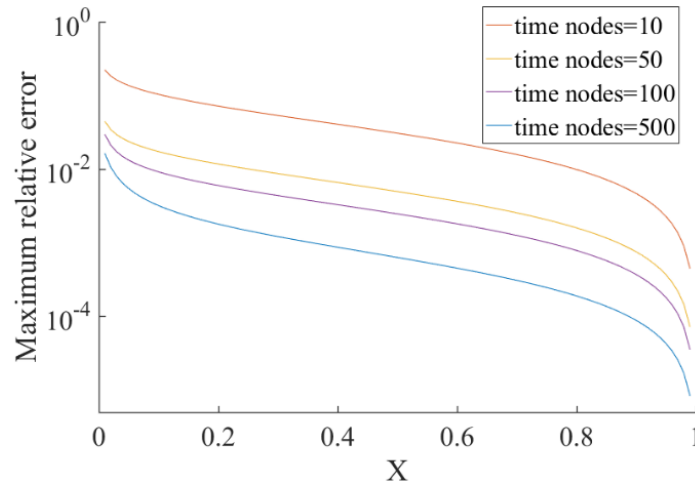


Figure 6-1. Distribution of numerical error in space with different numbers of time nodes. The maximum relative error ( $|C(x, t) - C_{exact}(x, t)|/C_{exact}(x, t)$ ) of Eq. (6-4) is shown, with the space nodes 100 and the truncation parameter 0.1 at time 100.

## 6.5 Applications

### 6.5.1 Results of model application for laboratory experiment 1

The measured and best-fit BTCs for experiment 1 (Zheng et al., 2012) using the fADRE (6-1) and the classical ADRE model are shown in Fig. 6-2. The model results are obtained by manual calibration based on careful visual inspections. The ADRE underestimates the early-time BTCs due to fast movement of dissolved nitrate along the preferential flow paths. It also overestimates the decline rate of the late-time BTC, which was controlled by retention processes. Contrarily, the fADRE model can capture the early arrivals using the spatial fractional diffusive term and the late time BTC tail using the temporal fractional-derivative term. The best-fit parameters for both models are listed in Table 6-1. I also calculated the Root Mean Squared Logarithmic Error (RMSLE) to evaluate the prediction errors. The fADRE model has much smaller RMSLE values, compared to the ADRE model, indicating a better fit of the data, especially in the early and late tailing parts of the BTC.

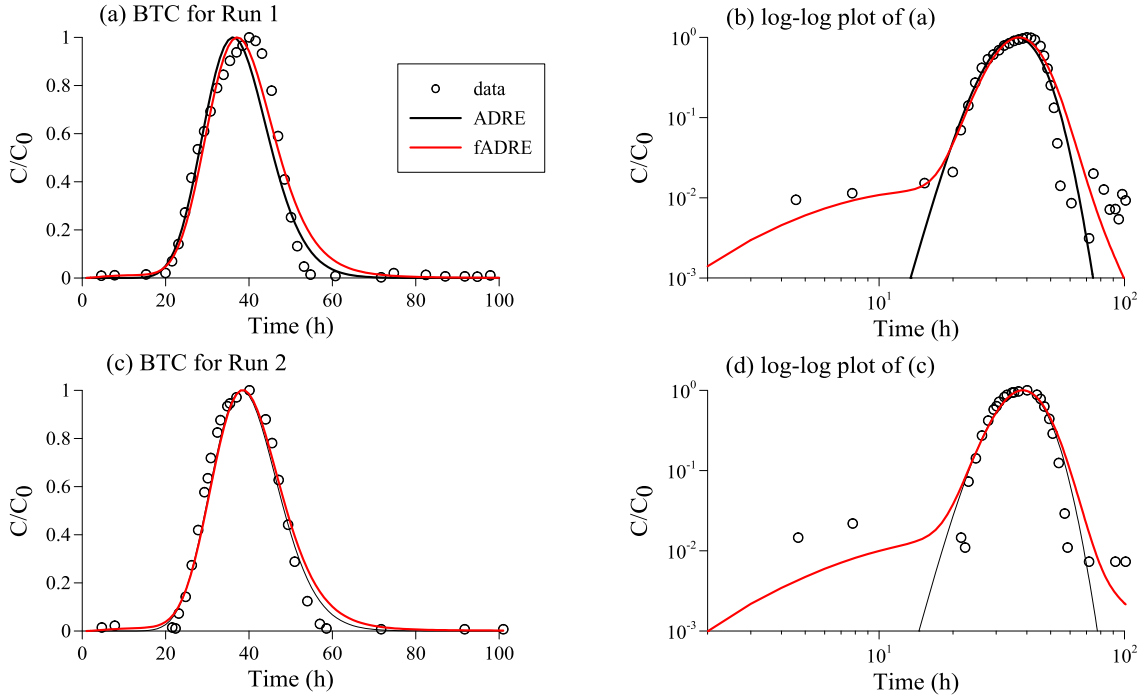


Figure 6-2. Experiment 1: Comparison between the measured (symbols) and modeled (lines) breakthrough curves (BTCs) using the ADRE (black line) and the fADRE (6-1) (red line). Log-log plots at the right column emphasize the early and late time BTC tails.

Model	Experimental Runs	$v$ (cm/min)	$D$ (cm <sup>2</sup> /min)	$\beta$ (min <sup><math>\gamma-1</math></sup> )	$\gamma$	$\lambda$ (min <sup>-1</sup> )	$\alpha$	$K$ (min <sup>-<math>\alpha</math></sup> )	RMSLE
fADRE	1	0.8	0.01	2	0.96	0.04	1.97	0.6	0.4273
	2	0.8	0.01	2	0.99	0	1.93	0.6	0.4030
ADRE	1	0.25	0.01	n/a	n/a	n/a	2	0.3	1.7480
	2	0.23	0.01	n/a	n/a	n/a	2	0.3	1.7256

Table 6-1. Experiment 1: Best-fit parameters for the advection–dispersion–reaction equation (ADRE) and the fADRE model (6-1) for nitrate transport in the soil columns (Zheng et al., 2012). In the legend:  $v$  is the effective velocity;  $D$  is the dispersion coefficient;  $\beta$  is the fractional capacity coefficient;  $\gamma$  is the time index;  $\lambda$  is the truncation parameter;  $\alpha$  is the space index;  $K$  is the first-order rate constant; RMSLE (Root Mean Squared Logarithmic Error) is the standard deviation of the logarithmic residual to measure the prediction errors.

### 6.5.2 Results of model application for laboratory experiment 2

BTCs of  $\text{NO}_3^-$  leaching from four different soil samples showed long tails, implying that the nutrient initially entering the matrix pores moved back slowly into the flow paths during flushing (Mahmood-Ul-Hassan et al., 2010). Mahmood-Ul-Hassan et al. (2010) divided the four

soils into two groups: the first is the massive soil (Shahdara and Sultanpur) featuring low clay content, more homogeneous structure, and more symmetric BTCs; and the second is the structured soil (Pacca and Lyallpur) with higher clay content, more heterogeneous structure, and skewed BTCs. They used two models: the ADE with retardation and the following two-region MIM model:

$$\frac{\partial C_m}{\partial t} + \beta \frac{\partial C_{im}}{\partial t} = -v \frac{\partial C_m}{\partial x} + D_m \frac{\partial^2 C_m}{\partial x^2}, \quad (6-10)$$

to fit the BTCs. The three models' results (the ADE, MIM and fADRE models) are shown in Fig. 6-3.

This application leads to three conclusions. *First*, the ADE model is bell shaped and misses the tailings completely even with retardation, since the mass exchange between matrix and the interconnected pores is more complicated than an instantaneous linear retardation mechanism. *Second*, the MIM model (6-10) is slightly better than the ADE model in capturing the heavy tailing characteristics since it adds an immobile zone interacting with the mobile phase. It still overestimates the decline rate in the late time, since the real heterogeneous porous medium can have a random, unpredictable number of immobile zones which have their own individual properties and mass exchange rates with the mobile zone. A single deterministic mass exchange rate is not enough to describe the variable interaction between mobile and various immobile zones.

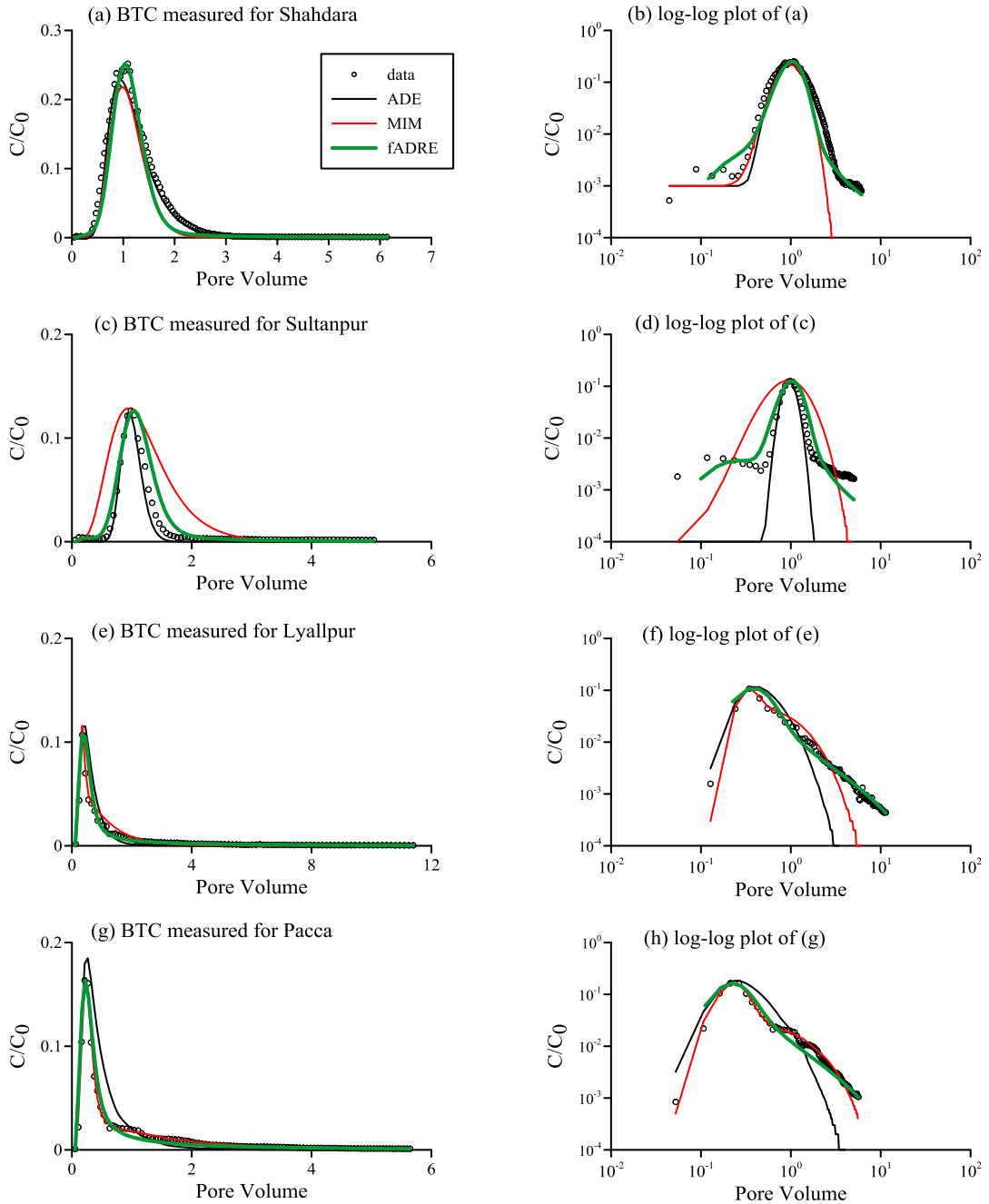


Figure 6-3. Experiment 2: The measured (symbols) and modeled (lines) BTCs for nitrate using the ADE (black line) (Mahmood-Ul-Hassan et al., 2010), the MIM model (6-10) (Mahmood-Ul-Hassan et al., 2010) and the fADRE model (6-1) (green line). Log-log plots at the right column emphasize the early and late time BTC tails.

Third, the fADRE model (6-1) fits the data best, especially for the early arrival and late time tailing behaviors. The fADRE model treats each particle's motion as a random process

which fits the actual situation that heterogeneous porous media are unpredictable in reality. It uses a truncated power law memory function to filter the residence time for each nitrate particle trapped in the immobile zones. In that way, this model does not need to map each individual mass exchange rate for each immobile zone, and it can describe the whole broad range of mobile-immobile interactions with a minimum number of parameters. Besides, the space fractional derivative accounts for the early arrivals from super-diffusive particles jumping fast in the preferential flow paths. Overall, our fractional calculus-based model fits well the data without redundant parameters. The best-fit parameters of the fADRE model (6-1) for nitrate transport through four soils are listed in Table 6-2. The RMSLE value is hard to calculate due to the noises of the data. The fADRE model (6-1) fits the tail parts best by visual inspection.

Nutrient	Soil	$v$ (cm/h)	$D$ (cm <sup>2</sup> /h)	$\beta$ (h <sup><math>\gamma</math>-1</sup> )	$\gamma$	$\lambda$ (h <sup>-1</sup> )	$\alpha$	$K$ (h <sup>-<math>\alpha</math>)</sup>
Nitrogen	Shahdara	0.9	0.004	0.4	0.98	0	1.9	0.8
	Sultanpur	1	0.0001	1	0.96	0	1.5	1.25
	Lyallpur	13	0.01	1	0.8	0.01	2	4
	Pacca	10	0.01	1	0.77	0.01	2	3

Table 6-2. Experiment 2: Best-fit parameters of the fADRE model (6-1) for nitrate transport through four soil columns from a high input cropping system. The meaning of each parameter is the same as that shown in Table 6-1.

## 6.6 Discussion

### 6.6.1 Variation of model parameters among experiments

The fractional-derivative models usually have poor predictability for model parameters. Here I explore the potential qualitative connection between the parameters in the fADRE model (6-1) and soil column properties and the experimental conditions. A quantitative relationship between model parameters and medium properties may require multi-year of effort in laboratory/field experiments and stochastic model analysis, which is beyond the major focus of

this study. However, qualitative conclusions drawn from this study may shed light on future quantitative analysis.

#### 6.6.1.1 Model parameters for laboratory experiment 1

In laboratory experiment 1 (Zheng et al., 2012), the best-fit parameters change between Run 1 and Run 2 (Table 6-1). Specifically, the time index increases from 0.96 to 0.99 (from Run 1 to Run 2), indicating a faster reaction/larger decline rate at the late time in Run 2. Since the nitrate concentration in Run 2 is half of Run 1, the concentration in the outflow drops quicker. The truncation parameter decreases from 0.04 to 0  $\text{min}^{-1}$ , implying a delayed transition from non-Fickian transport to Fickian transport in Run 2. I observed from the experimental data that nitrate with a higher concentration moves slightly faster. The space index decreases from 1.97 to 1.93, implying that the early BTC tail is heavier in Run 2. When the initial nitrate concentration decreases to 50% in the same soil in Run 2, the heavier early arrival and lighter late time tailing behaviors are observed from the BTCs, implying less particles trapped in the immobile/matrix zone for lower concentration outflow, and more particles in the preferential flow paths. All the other parameters remain the same, which may be due to the fixed medium's properties since the same medium is used for both experiments. The same experimental procedure may ensure similar best fit velocity and dispersion coefficient in the experiments, and the fixed internal structure of the medium ensures that the capacity coefficient and the transformation rate of the nitrate are constant.

Parameters can be divided into two groups. The first group, which includes velocity, dispersion coefficient, capacity coefficient, and reaction rate constant, is mainly controlled by the medium's structure and properties. The second group, which includes time and space index, and

truncation parameters, is more likely be related to the experimental conditions, such as the initial concentration, which further affect the anomalous transport pattern shown in the BTCs. Curve-fitting exercise for Experiment 1 shows that, on one hand, if the same soil column is used, one can keep the first group parameters as constants and then only adjust the parameters in the second group according to the observed transport characteristics, which can significantly simplify the fitting procedure. On the other hand, if the same procedure is conducted for different experimental runs of nitrate transport in different soil columns, parameters in the second group may remain stable, and parameters belonging to the first group need to be adjusted based on the heterogeneity characteristics of the soil column and the resultant BTCs.

For the same experimental run (i.e., Run 1 or 2), the best-fit velocity and transformation rate of the classical ADRE model are smaller than those of the fADRE model (6-1). Since the ADRE model does not distinguish mobile and immobile phases, the overall effective velocity is smaller than the fADRE (6-1) (or in other words, the fADRE needs a larger velocity to capture solute retention). The fADRE model has a larger transformation rate in the mobile zone than the ADRE model. The smaller effective velocity in the ADRE model results in a longer residence time for nitrate in the saturated soil system, which leads to a smaller reaction rate  $K$ .

#### 6.6.1.2 Model parameters for laboratory experiment 2

The BTCs of the massive soils (i.e., Shahdara and Sultanpur), which are less heterogeneous, were more symmetrical compared to those of the structured soils (Pacca and Lyallpur). Different skewness or tailing behaviors of the BTCs imply different parameter values in the fADRE model (6-1) (listed in Table 6-2) when capturing nitrate transport in soils with different internal structures.

First, the best-fit velocity  $v$  for the massive soils is apparently smaller than that for the structured soils, likely due to fewer preferential flow paths, through which a majority of nitrate particles can travel rapidly bypassing the soil matrix (Radulovich et al., 2010), leading to an accelerated breakthrough at the outlet (Buchter et al., 2010; Gaber et al., 2010).

Second, the dispersion coefficient  $D$  is one to two orders of magnitude smaller in the massive soils, due to the less heterogeneous soil structure and the much smaller velocity. Nutrients flowing through relatively homogeneous soils tend to experience less deviation in advective transport, with a smaller variation in the local velocities.

Third, the capacity coefficient  $\beta$  in the massive soils is smaller due to their relatively homogeneous structure (for example, less storage zones), leading to a larger decline rate for nitrate concentration at the late time; hence, the time index  $\gamma$  in the massive soils is also larger.

Fourth, no truncation in solute residence time was needed for the massive soils (i.e.,  $\lambda = 0$ ), since the experimental time was not long enough to capture the transition of slope of the late-time BTCs (Fig. 6-3).

Fifth, a smaller space index  $\alpha$  for the massive soils represents heavier early-time arrivals and a smaller transformation rate for nitrate, probably due to the smaller velocity through the soil column. Notably, the larger space index for the structured soils does not necessarily mean that there must be less early arrivals for nitrate at the very beginning. The velocity is so large for the structured soils that the relatively coarse resolution of the sampling frequency cannot reliably identify the fast, early-time arrivals (i.e., super-diffusion).

## 6.6.2 Impacts of reaction on nitrate dynamics

Numerical tests show that the fADRE model (6-1) solution is sensitive to the reaction rate coefficient  $K$ . After normalizing the BTCs, I find that the decrease of the rate  $K$  (from  $1.0 \text{ min}^{-1}$  to  $0.2 \text{ min}^{-1}$ ) leads to a heavier BTC tail with a slower decline rate at the late time. The plume becomes wider and shifts to the right (in time) with a later breakthrough time and lighter early arrivals (Fig. 6-4a and 6-4b). The most significant feature of the large reaction rate ( $K = 1 \text{ min}^{-1}$ ) is the double peak phenomenon (Fig. 6-4c). The reason might be that with a large denitrification reaction rate, even a small number of denitrifying bacteria can consume a certain amount of fast-moving nutrients at the early time, causing the first (small) decline in the BTC. The bacteria then continue consuming the remaining nutrients releasing from the storage zones later, generating the even faster second decline in the BTC at the late time. With a smaller reaction rate ( $K = 0.2$  or  $0.6 \text{ min}^{-1}$ ), the BTC is single-peaked, likely due to the period (such as 24~48 hours) required for the denitrifying bacteria to be fully cultivated, and hence they are more likely to consume the nutrients releasing from the immobile or stagnant zones at the late time with only one decline limb.

Zheng et al. (2012) also found that the denitrifying bacteria in soil columns have higher activity and a higher denitrification rate after a period of cultivation, and denitrification is stronger at the later time. In 0~1 day, the nitrate concentration did not change much, showing that adsorption-desorption and microbial cultivation mainly happened in this stage; while the concentration of nitrate decreased sharply in 2~10 days, implying strong denitrification reaction; and in 10~13 days, the change of nitrate concentration tended to be slow, showing that the denitrification reaction became gentle. Therefore, the whole process can be roughly divided into four stages: adsorption-desorption stage, microbial cultivation stage, denitrification reaction stage, and the end of denitrification stage. Zheng et al. (2012) simulated the whole process using

the classical ADRE model with two phases: the first phase from 0~26 h with  $K_1 = 0.907 d^{-1}$ , and the second phase from 26~65 h with a larger  $K_2 = 1.296 d^{-1}$ . The denitrification rate increased by 43%. However, our fADRE model (6-1) only requires one constant reaction coefficient  $K$  to model the whole process, eliminating significantly the number of fitting parameters.

Without normalization, I find that the larger the reaction rate, the smaller the peak concentration with more nutrients being consumed and less solutes left in the outflow (Fig. 6-4d). This behavior is expected, supporting the model results.

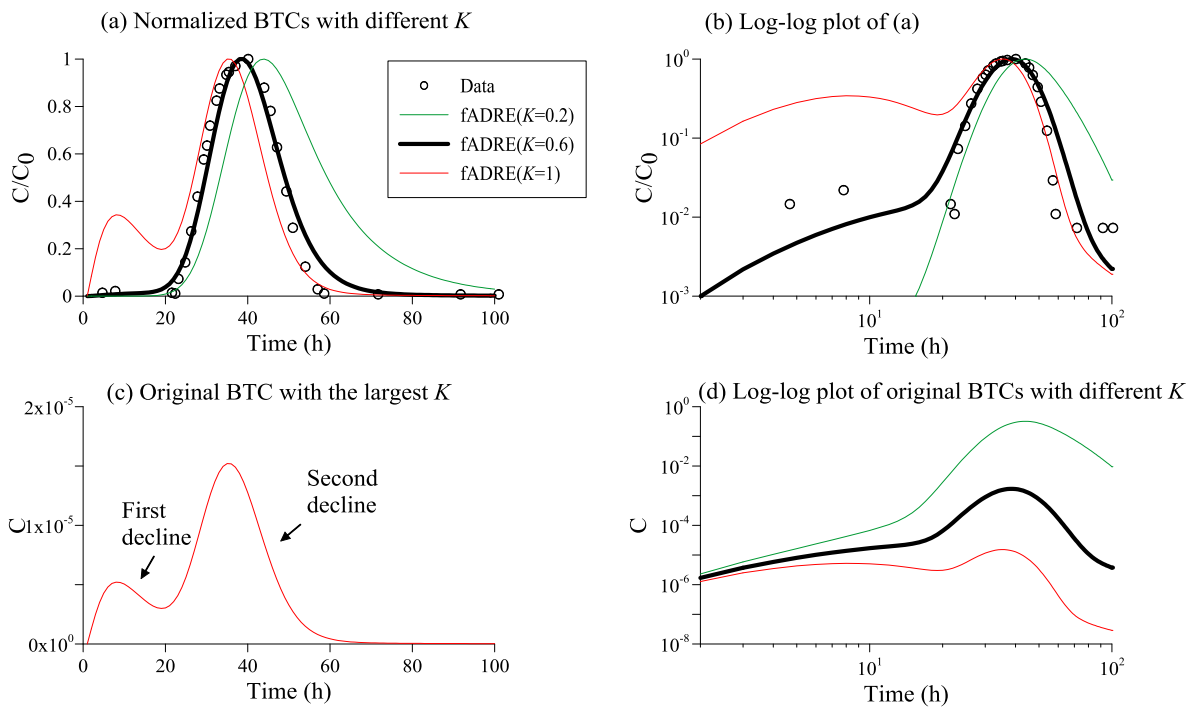


Figure 6-4. Sensitivity analysis for the reaction rate coefficient  $K$  in the fADRE model (6-1). (a) is the normalized BTCs of Run 1 for Experiment 1 with three different  $K$  ( $\text{min}^{-1}$ ) values. (b) is the log-log plot of (a) to show the leading front and late time tail. (c) is the modeled BTC in (a) with the largest reaction coefficient  $K = 1 \text{ min}^{-1}$ , which contains two peaks. (d) is the log-log plot of the BTCs (shown in (a) with three different  $K$ ) to show the decreasing peak concentration (without normalization).

### 6.6.3 Model generalization: bacteria transport

To test the model's generalization, i.e., whether it can be used for other first-order decay (or growth) reactions, such as the growth of bacteria, biological degradation, decay of radioactive isotopes, etc., I validate and apply the model (6-1) using data from BTCs of two bacteria: *Escherichia coli* (*E. coli*) and *Klebsiella* sp. in three saturated soils under saturated flow conditions done by Bai et al. (2016) (Fig. 6-5). Bai et al. (2016) also used the MIM model (6-10) to quantify the microbial transport in three different soil columns: the homogeneous sand column 1, the heterogeneous sand column 2, and the heterogeneous calcareous gravel column 3, which have different size distributions.

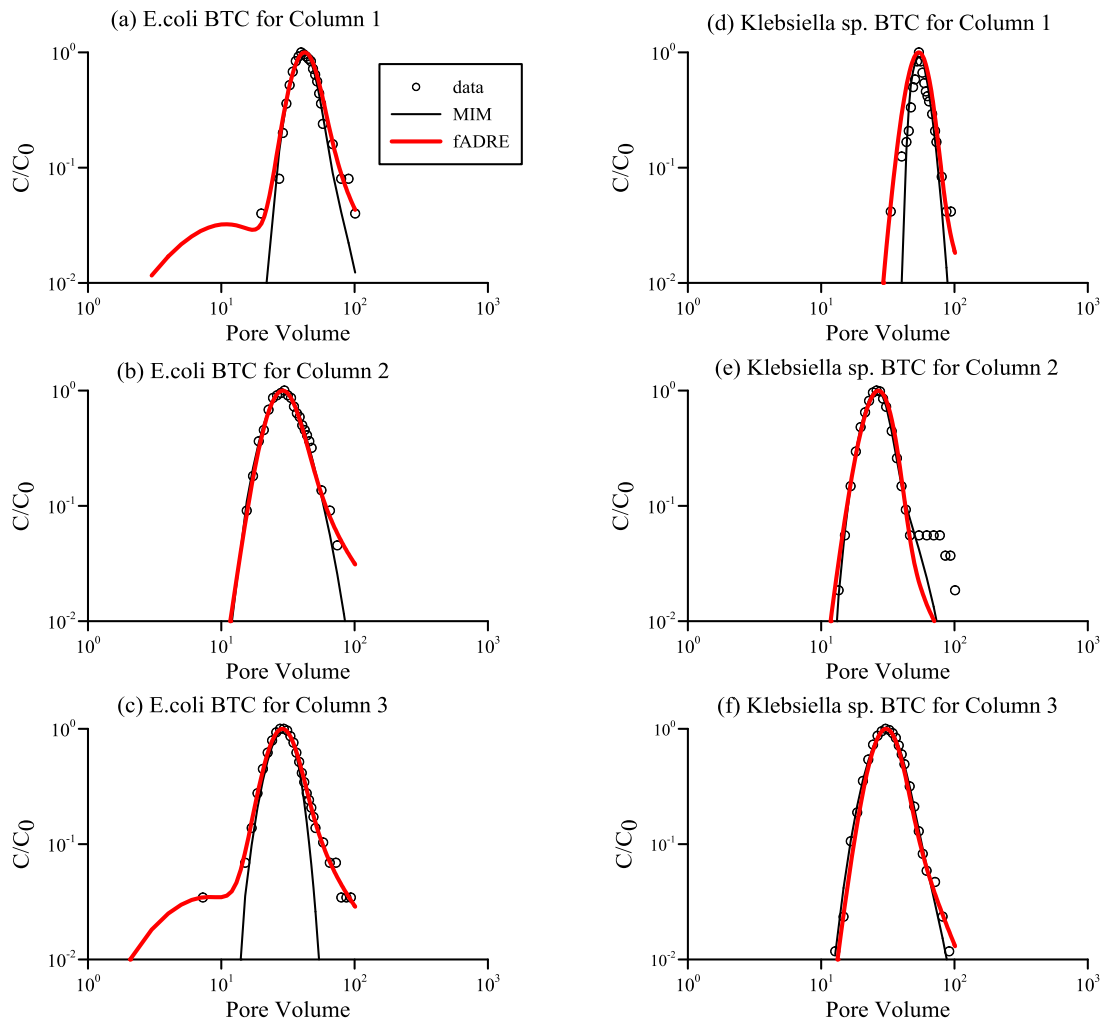


Figure 6-5. Comparison between the measured (symbols) and modeled (lines) BTCs for the two bacteria (*E. coli* and *Klebsiella* sp.) through three different soil columns (column 1, 2, 3) using the MIM model (black line) (Bai et al., 2016) and the fADRE model (red line) in log-log plots to show the early and late time tails.

Compared to the MIM model (6-10), the fADRE model (6-1) fits the early arrival and late time tailing behaviors in the BTCs much better (Fig. 6-5). Comparing the three soil columns, I found that the non-Fickian characteristics become more obvious from column 1 to column 3. This is because the increased degree of medium heterogeneity from column 1 to 3. The gravel, packed in column 3, has intra-granular porosity inside particles and inter-granular porosity between particles (Bai et al., 2016). The grain size distribution becomes wider with a larger median grain size from columns 1 to 3. A more heterogeneous medium with stronger preferential flow paths leads to a more non-Fickian BTC. Column 3, filled with gravel, has the widest range of particle size distribution, which needs the fADRE model (6-1) to capture the broad range of retention times in all immobile domains. In addition, *E. coli* is a motile strain, while *Klebsiella* sp. is non-motile (Bai et al., 2016). This means that *E. coli* can swim into regions with different physical properties and then return to the mobile zone, resulting in a more skewed concentration profile whose reliable quantification requires a sophisticated stochastic model such as the fADRE (6-1). The best-fit parameters of the fADRE model for the two bacteria are listed in Table 6-3. The RMSLE of the BTCs simulated by the MIM model (6-10) and fADRE model (6-1) are also calculated and listed in Table 6-4. The fADRE model has a slightly smaller RMSLE than the MIM model, indicating better fitting with the BTCs, especially in early and late time tailing parts.

Bacterium	Column	$v$ (cm/min)	$D$ (cm <sup>2</sup> /min)	$\beta$ (min <sup><math>\gamma</math>-1</sup> )	$\gamma$	$\lambda$ (min <sup>-1</sup> )	$\alpha$	$K$ (min <sup>-<math>\alpha</math>)</sup>
<i>E. coli</i>	1	0.55	0.001	1.2	0.915	0	1.9	0.6
	2	0.9	0.001	1.2	0.895	0	1.9	0.55
	3	0.83	0.001	1.2	0.895	0	1.85	0.9

<i>Klebsiella</i> sp.	1	0.3	0.001	1	0.975	0	2	0.9
	2	0.67	0.001	1	0.97	0	2	1.5
	3	0.55	0.01	0.8	0.92	0.01	2	1

Table 6-3. The best-fit parameters of the fADRE model (6-1) for two bacteria (*E. coli* and *Klebsiella* sp.) through three saturated soil columns (1-3). The meaning of each parameter is the same as that shown in Table 6-1.

Bacterium	Column	RMSLE	
		MIM	fADRE
<i>E. coli</i>	1	0.3327	0.0962
	2	0.0835	0.0504
	3	2.1206	0.0368
<i>Klebsiella</i> sp.	1	1.0506	0.2139
	2	0.4686	0.3714
	3	0.0987	0.0695

Table 6-4. The RMSLE of the BTCs fitted by the MIM (6-10) and fADRE model (6-1) for two bacteria (*E. coli* and *Klebsiella* sp.) moving through three saturated soil columns (1-3) (Figure 6-5).

The particle size distribution of sand packed in the column might be connected to the model parameters. If the column sand has a wider size distribution (i.e., relatively stronger medium heterogeneity or higher variation for the resultant flow field), the best-fit time and space indexes in the fADRE model (6-1) tend to slightly decrease, representing stronger non-Fickian transport. Measurements by Bai et al. (2016) showed that the average total porosity increases from columns 1 to 3. For a randomly structured medium, larger pores are often associated with larger particles. However, the relationship between the pore size and the particle size in most non-randomly structured soils is much more complex. Large pores can be related to both large particles and small particles, such as large interaggregate pores produced by clay aggregation (Nimmo, 2004). To be specific, the pore size distribution of sand filling columns 1 and 2 has a single peak (column 1 peaks at 55  $\mu\text{m}$ , and column 2 at 108  $\mu\text{m}$ ), while the pore size distribution of column 3 has three peaks: small pores with diameter ranging from 0.005 to 5  $\mu\text{m}$  with a peak at 0.035  $\mu\text{m}$ ; larger pores ranging from 5 to 365  $\mu\text{m}$  with the first peak at 15  $\mu\text{m}$  and the second

peak at 200  $\mu\text{m}$  (Bai et al., 2016). The large pores in column 3 can form complex pore networks and provide preferential flow paths for dissolved bacteria. The peak of small pores in the gravel medium in column 3 (0.035  $\mu\text{m}$ ) is far less than the peak of the sand medium in column 1 (55  $\mu\text{m}$ ) and column 2 (108  $\mu\text{m}$ ). These extremely small pores increase the number of immobile/storage zones in the saturated sand, leading to stronger non-Fickian transport. The best-fit velocity increases from column 1 to column 2, and then decreases from columns 2 to 3. In column 1, more surface areas contacted between the colloids/bacteria and the matrix in a more uniform flow with less preferential flow paths will lead to a higher probability of bacteria entrapment (Lamy et al., 2013) and further smaller velocity. Column 2 is composed of coarser sand with larger pore sizes, compared with column 1; while column 3 is coarser than column 2 with abundant extremely small pores, leading to a smaller velocity than column 2.

The bacteria's physical and chemical properties might also be connected qualitatively to the model parameters. *First*, compared to the non-motile bacterial strain (i.e., *Klebsiella* sp.), the motile strain (*E. coli*) moves with a larger velocity  $v$  in the same porous medium, since bacteria swimming can enhance their transport (De Kerchove and Elimelech, 2008). *Second*, the median cell size (as the equivalent spherical diameter) is  $\sim 1.11 \mu\text{m}$  for *E. coli* and  $\sim 1.58 \mu\text{m}$  for *Klebsiella* sp., and *E. coli* also has a higher hydrophobicity and mobility than *Klebsiella* sp. (Bai et al., 2016). The smaller size, higher hydrophobicity and higher mobility make *E. coli* be retained/attached stronger in the porous media (since *E. coli* can access more small pores/dead ends/stagnation zones) than *Klebsiella* sp., resulting in a larger capacity coefficient  $\beta$  (representing the mass ratio between immobile and mobile masses) and a smaller time index  $\gamma$  for *E. coli* in the fADRE model (6-1) (see Table 6-3). Shapiro et al. (2003) also reported that motile bacteria have a greater attachment rate in comparison with their non-motile mutants in the

coated and clean beads column study. *Klebsiella* sp's time index  $\gamma$  depends more on the porous medium's properties (i.e., a more heterogeneous structure leads to a smaller time index), while *E. coli*'s time index can be relatively stable from column 2 to column 3 (which is a constant:  $\gamma = 0.895$ ), since it has the ability to move by itself to counteract the impact of the porous medium's heterogeneity to a certain degree (in other words, porous medium structure has less impact on *E. coli*). Third, *E. coli* has a smaller truncation parameter  $\lambda$  in time, meaning a later transition from non-Fickian to Fickian transport. Fourth, a smaller space index  $\alpha$  for *E. coli* is due to its smaller cell size, ability to swim, and the larger velocity through porous media. Fifth, *E. coli*'s slower transformation rate  $K$  might be caused by its higher hydrophobicity and more retention in immobile domains. In general, all these parameters imply a stronger non-Fickian transport process for *E. coli* than *Klebsiella* sp.

## 6.7 Conclusion

Natural soils usually exhibit multi-scale heterogeneity, especially the interconnected pore networks (which enhance preferential flow paths) and low-permeability zones (causing strong retention impact), which can generate various non-Fickian transport for contaminants. Those disparate transport behaviors, which may occur simultaneously, cannot be efficiently captured by the classical Fickian-diffusion based transport models. To reliably quantify the fate and transport of nitrate in complex, saturated soil systems, this study proposes a spatiotemporal fractional advection-dispersion-reaction equation or fADRE model. Two well-documented laboratory experiments focusing on nitrate dynamics in saturated soil columns were adopted to check the feasibility of the stochastic model. One bacteria transport experiment was also applied to test the generality of the mathematical model. Widely used classical transport models, including the ADRE and the two-region MIM model, were selected for model comparison. The model

development, application, comparison and generalization lead to four major conclusions, which can improve our understanding of the characterizations and mechanisms of nitrate migration in soil, and the impact of reactions on kinetics of non-Fickian transport in complex soil systems.

First, nitrate transport in low-permeability, saturated soil is affected by reaction and mixed super- and sub-diffusion, a complex process that can be captured by the fADRE model (6-1). The soil column filled with the low-permeability soil exhibits strong heterogeneity which can lead to both early arrivals and late time tailing behaviors for nitrate transport, challenging the applicability of the classic ADRE and the MIM model (6-10). The stochastic fADRE model (6-1), contrarily, can describe the whole range of the reaction rate in the soil system with a minimum number of parameters.

Second, model solution is sensitive to the reaction term in the fADRE (6-1), which is convenient to capture the nutrient transformation process. A relatively large reaction rate will lead to multiple peaks in the BTC, due likely to the function of denitrifying bacteria and non-Fickian transport dynamics of nitrate.

Third, the parameters of the fADRE model may be related qualitatively to the physical properties of the soil (including clay content, pore size distribution, and soil internal structure), the experimental conditions (including the initial solute concentration) and the solute/bacteria's chemical properties (sorption and motility). Hence, those relationships can improve the predictability and applicability of the model qualitatively and guide the future effort in linking quantitatively the model parameters and the system properties.

Fourth, our model can not only describe nitrate transformations through saturated soils, but also other first-order reactions, such as the growth of bacteria in complex soil systems. It may also be used to capture biological degradation and decay of radioactive isotopes, using the first-

order decline term in the model. Hence, the mathematical model proposed in this study may shed lights on the quantification of various biogeochemical dynamics in complex soil systems, which needs to be tested in real-world applications in the future.

## 6.8 Acknowledgments

The work was supported by the National Natural Science Foundation of China with Grant Nos. 41628202 and 41330632. This paper does not necessarily reflect the view of the funding agency.

## 6.9 References

- Akbariyeh, S., Bartelt-Hunt, S., Snow, D., Li, X., Tang, Z., Li, Y., 2018. Three-dimensional modeling of nitrate-N transport in vadose zone: Roles of soil heterogeneity and groundwater flux. *J. Contam. Hydrol.* 211, 15–25. doi:10.1016/j.jconhyd.2018.02.005.
- Almasri, M.N., Kaluarachchi, J.J., 2007a. Modeling nitrate contamination of groundwater in agricultural watersheds. *J. Hydrol.* 343, 211–229. doi:10.1016/j.jhydrol.2007.06.016.
- Almasri, M.N., Kaluarachchi, J.J., 2007b. Modeling nitrate contamination of groundwater in agricultural watersheds. *J. Hydrol.* 343, 211–229. doi:10.1016/j.jhydrol.2007.06.016.
- Atekwana, E.A., Geyer, C.J., 2018. Spatial and temporal variations in the geochemistry of shallow groundwater contaminated with nitrate at a residential site. *Environ. Sci. Pollut. Res.* 25, 27155–27172. doi:10.1007/s11356-018-2714-7.
- Bai, H., Cochet, N., Drelich, A., Pauss, A., Lamy, E., 2016. Comparison of transport between two bacteria in saturated porous media with distinct pore size distribution. *RSC Adv.* 6, 14602–14614. doi:10.1039/C5RA21695H.
- Beven, K., Germann, P., 2013. Macropores and water flow in soils revisited. *Water Resour. Res.* 49, 3071–3092. doi:10.1002/wrcr.20156.
- Beven, K., Germann, P., 1982. Macropores and water flow in soils. *Water Resour. Res.* 18, 1311–1325. doi:10.1029/WR018i005p01311.
- Binley, A., Shao, M., Jia, X., Turkeltaub, T., Zhu, Y., 2018. Recharge and Nitrate Transport Through the Deep Vadose Zone of the Loess Plateau: A Regional-Scale Model Investigation. *Water Resour. Res.* 54, 4332–4346. doi:10.1029/2017wr022190.

- Blum, W.E.H., 2005. Functions of soil for society and the environment. *Rev. Environ. Sci. Biotechnol.* doi:10.1007/s11157-005-2236-x.
- Brusseau, M.L., 1993. The influence of solute size, pore water velocity, and intraparticle porosity on solute dispersion and transport in soil. *Water Resour. Res.* 29, 1071–1080. doi:10.1029/92WR02595.
- Buchter, B., Hinz, C., Flury, M., Flühler, H., 2010. Heterogeneous Flow and Solute Transport in an Unsaturated Stony Soil Monolith. *Soil Sci. Soc. Am. J.* 59, 14. doi:10.2136/sssaj1995.03615995005900010002x.
- C. Zheng, M. C. Hill, G. Cao, R. Ma, 2012. MT3DMS: Model Use, Calibration, and Validation. *Trans. ASABE* 55, 1549–1559. doi:10.13031/2013.42263.
- Cao, J., Li, C., Chen, Y., 2014. On tempered and substantial fractional calculus, in: MESA 2014 - 10th IEEE/ASME International Conference on Mechatronic and Embedded Systems and Applications, Conference Proceedings. IEEE, pp. 1–6. doi:10.1109/MESA.2014.6935561.
- Carey, M.A., Lloyd, J.W., 1985. Modelling non-point sources of nitrate pollution of groundwater in the Great Ouse Chalk, U.K. *J. Hydrol.* 78, 83–106. doi:10.1016/0022-1694(85)90155-6.
- Chen, W., Sun, H., Zhu, J., Zhang, Y., Meerschaert, M.M., 2012. A fractal Richards' equation to capture the non-Boltzmann scaling of water transport in unsaturated media. *Adv. Water Resour.* 52, 292–295. doi:10.1016/j.advwatres.2012.11.005.
- Cheng, Z., Zhang, Y., Su, C., Chen, Z., 2017. Chemical and isotopic response to intensive groundwater abstraction and its implications on aquifer sustainability in Shijiazhuang, China. *J. Earth Sci.* 28, 523–534. doi:10.1007/s12583-017-0729-5.
- Chowdary, V.M., Rao, N.H., Sarma, P.B.S., 2004. A coupled soil water and nitrogen balance model for flooded rice fields in India. *Agric. Ecosyst. Environ.* 103, 425–441. doi:10.1016/j.agee.2003.12.001.
- Danckwerts, P. V., 1953. Continuous flow systems. Distribution of residence times. *Chem. Eng. Sci.* doi:10.1016/0009-2509(53)80001-1.
- De Kerchove, A.J., Elimelech, M., 2008. Bacterial swimming motility enhances cell deposition and surface coverage. *Environ. Sci. Technol.* 42, 4371–4377. doi:10.1021/es703028u.
- Dorsch, M.M., Scragg, R.K., McMichael, A.J., Baghurst, P.A., Dyer, K.F., 1984. Congenital malformations and maternal drinking water supply in rural South Australia: a case-control study. *Am. J. Epidemiol.* 119, 473–86. doi:10.1093/oxfordjournals.aje.a113764.

- Gaber, H.M., Inskip, W.P., Wraith, J.M., Comfort, S.D., 2010. Nonequilibrium Transport of Atrazine through Large Intact Soil Cores. *Soil Sci. Soc. Am. J.* 59, 60. doi:10.2136/sssaj1995.03615995005900010009x.
- Han, D., Cao, G., McCallum, J., Song, X., 2015. Residence times of groundwater and nitrate transport in coastal aquifer systems: Daweijia area, northeastern China. *Sci. Total Environ.* 538, 539–554. doi:10.1016/j.scitotenv.2015.08.036.
- Hill, M.J., Hawksworth, G., Tattersall, G., 1973. Bacteria, nitrosamines and cancer of the stomach. *Br. J. Cancer* 28, 562–567. doi:10.1038/bjc.1973.186.
- Ju, X.T., Kou, C.L., Zhang, F.S., Christie, P., 2006. Nitrogen balance and groundwater nitrate contamination: Comparison among three intensive cropping systems on the North China Plain. *Environ. Pollut.* 143, 117–125. doi:10.1016/j.envpol.2005.11.005.
- Kelso, B.H.L., Smith, R. V., Laughlin, R.J., Lennox, S.D., 1997. Dissimilatory nitrate reduction in anaerobic sediments leading to river nitrite accumulation. *Appl. Environ. Microbiol.* 63, 4679–4685.
- Kinzelbach, W., Schäfer, W., Herzer, J., 1991. Numerical modeling of natural and enhanced denitrification processes in aquifers. *Water Resour. Res.* 27, 1123–1135. doi:10.1029/91WR00474.
- Lamy, E., Lassabatere, L., Bechet, B., Andrieu, H., 2013. Effect of a nonwoven geotextile on solute and colloid transport in porous media under both saturated and unsaturated conditions. *Geotext. Geomembranes* 36, 55–65. doi:10.1016/j.geotextmem.2012.10.009.
- Lee, M.S., Lee, K.K., Hyun, Y., Clement, T.P., Hamilton, D., 2006. Nitrogen transformation and transport modeling in groundwater aquifers. *Ecol. Modell.* 192, 143–159. doi:10.1016/j.ecolmodel.2005.07.013.
- MacQuarrie, K.T.B., Sudicky, E.A., 2001. Multicomponent simulation of wastewater-derived nitrogen and carbon in shallow unconfined aquifers - I. Model formulation and performance. *J. Contam. Hydrol.* doi:10.1016/S0169-7722(00)00137-6.
- Mahmood-Ul-Hassan, M., Rashid, M., Akhtar, M.S., Rafique, E., 2010. Nitrate and phosphate leaching from aridisols and entisols: Laboratory studies and field observations. *Soil Sediment Contam.* 19, 261–276. doi:10.1080/15320381003695207.
- Malberg, J.W., Savage, E.P., Osteryoung, J., 1978. Nitrates in drinking water and the early onset of hypertension. *Environ. Pollut.* 15, 155–160. doi:10.1016/0013-9327(78)90103-9.
- Mas-Pla, J., Regàs, O., Brusi, D., Menció, A., Otero, N., Zamorano, M., Folch, A., Puig, R., Bach, J., Domènech, C., Boy-Roura, M., 2015. Nitrate pollution of groundwater; all right. . . , but nothing else? *Sci. Total Environ.* 539, 241–251. doi:10.1016/j.scitotenv.2015.08.151.

- Mekala, C., Gaonkar, O., Nambi, I.M., 2017. Understanding nitrogen and carbon biogeoformations and transport dynamics in saturated soil columns. *Geoderma* 285, 185–194. doi:10.1016/j.geoderma.2016.10.004.
- Metzler, R., Klafter, J., 2004. The restaurant at the end of the random walk: recent developments in the description of anomalous transport by fractional dynamics. *J. Phys. A. Math. Gen.* 37, R161–R208. doi:10.1088/0305-4470/37/31/R01.
- Metzler, R., Klafter, J., 2000. The random walk's guide to anomalous diffusion: a fractional dynamics approach. *Phys. Rep.* 339, 1–77. doi:10.1016/S0370-1573(00)00070-3.
- Murgulet, D., Tick, G.R., 2016. Effect of variable-density groundwater flow on nitrate flux to coastal waters. *Hydrol. Process.* 30, 302–319. doi:10.1002/hyp.10580.
- Murgulet, D., Tick, G.R., 2013. Understanding the sources and fate of nitrate in a highly developed aquifer system. *J. Contam. Hydrol.* 155, 69–81. doi:10.1016/j.jconhyd.2013.09.004.
- Murgulet, D., Tick, G.R., 2009. Assessing the extent and sources of nitrate contamination in the aquifer system of southern Baldwin County, Alabama. *Environ. Geol.* 58, 1051–1065. doi:10.1007/s00254-008-1585-5.
- Nimmo, J.R., 2004. Porosity and pore size distribution. *Encycl. Soils Environ.* doi:10.1081/E-ESS-120042734.
- Novák, V., Hlaváčiková, H., 2019. Redistribution of water in homogeneous soil, in: *Theory and Applications of Transport in Porous Media*. Springer, Cham, pp. 165–170. doi:10.1007/978-3-030-01806-1\_11.
- Oyarzun, J., Oyarzun, R., 2007. Massive Volcanism in the Altiplano-Puna Volcanic Plateau and Formation of the Huge Atacama Desert Nitrate Deposits: A Case for Thermal and Electric Fixation of Atmospheric Nitrogen. *Int. Geol. Rev.* 49, 962–968. doi:10.2747/0020-6814.49.10.962.
- Pachepsky, Y., Benson, D., Rawls, W., 2010. Simulating Scale-Dependent Solute Transport in Soils with the Fractional Advective–Dispersive Equation. *Soil Sci. Soc. Am. J.* 64, 1234. doi:10.2136/sssaj2000.6441234x.
- Pepper, I., Brusseau, M.L., 2019. Physical-Chemical Characteristics of Soils and the Subsurface. *Environ. Pollut. Sci.* 9–22. doi:10.1016/B978-0-12-814719-1.00002-1.
- Pouyat, R. V., Yesilonis, I.D., Groffman, P.M., Szlavecz, K., Schwarz, K., 2010. Chemical, Physical, and Biological Characteristics of Urban Soils. *Urban Ecosyst. Ecol.* 0129, 119–152. doi:10.2134/agronmonogr55.c7.

- Radulovich, R., Baveye, P., Sollins, P., Solórzano, E., 2010. Bypass Water Flow through Unsaturated Microaggregated Tropical Soils. *Soil Sci. Soc. Am. J.* 56, 721. doi:10.2136/sssaj1992.03615995005600030008x.
- Rahmati, O., Samani, A.N., Mahmoodi, N., Mahdavi, M., 2015. Assessment of the Contribution of N-Fertilizers to Nitrate Pollution of Groundwater in Western Iran (Case Study: Ghorveh–Dehgelan Aquifer). *Water Qual. Expo. Heal.* 7, 143–151. doi:10.1007/s12403-014-0135-5.
- Reddy, K.R., Patrick, W.H., Phillips, R.E., 2010. The Role of Nitrate Diffusion in Determining the Order and Rate of Denitrification in Flooded Soil: I. Experimental Results1. *Soil Sci. Soc. Am. J.* 42, 268. doi:10.2136/sssaj1978.03615995004200020012x.
- Schwartz, R.C., McInnes, K.J., Juo, A.S.R., Wilding, L.P., Reddell, D.L., 1999. Boundary effects on solute transport in finite soil columns. *Water Resour. Res.* 35, 671–681. doi:10.1029/1998WR900080.
- Shamrukh, M., Corapcioglu, M.Y., Hassona, F.A.A., 2001. Modeling the effect of chemical fertilizers on ground water quality in the Nile Valley aquifer, Egypt. *Ground Water* 39, 59–67. doi:10.1111/j.1745-6584.2001.tb00351.x.
- Shapiro, A.M., Harvey, R.W., Metge, D.W., Collins, S.A., Becker, M.W., 2003. Effect of cell physicochemical characteristics and motility on bacterial transport in groundwater. *J. Contam. Hydrol.* 69, 195–213. doi:10.1016/j.jconhyd.2003.08.001.
- Super, M., Heese, H. de V., MacKenzie, D., Dempster, W.S., du Plessis, J., Ferreira, J.J., 1981. An epidemiological study of well-water nitrates in a group of south west african/namibian infants. *Water Res.* 15, 1265–1270. doi:10.1016/0043-1354(81)90103-2.
- Tarquis, A.M., Heck, R.J., Andina, D., Alvarez, A., Antón, J.M., 2009. Pore network complexity and thresholding of 3D soil images. *Ecol. Complex.* 6, 230–239. doi:10.1016/j.ecocom.2009.05.010.
- Tarquis, A.M., McInnes, K.J., Key, J.R., Saa, A., García, M.R., Díaz, M.C., 2006. Multiscaling analysis in a structured clay soil using 2D images. *J. Hydrol.* 322, 236–246. doi:10.1016/j.jhydrol.2005.03.005.
- Tick, G.R., McColl, C.M., Yolcubal, I., Brusseau, M.L., 2007. Gas-phase diffusive tracer test for the in-situ measurement of tortuosity in the vadose zone. *Water. Air. Soil Pollut.* 184, 355–362. doi:10.1007/s11270-007-9403-3.
- Totsche, K.U., Rennert, T., Gerzabek, M.H., Kögel-Knabner, I., Smalla, K., Spiteller, M., Vogel, H.J., 2010. Biogeochemical interfaces in soil: The interdisciplinary challenge for soil science. *J. Plant Nutr. Soil Sci.* doi:10.1002/jpln.200900105.
- van Genuchten, M.T., Wagenet, R.J., 2010. Two-Site/Two-Region Models for Pesticide

- Transport and Degradation: Theoretical Development and Analytical Solutions. *Soil Sci. Soc. Am. J.* 53, 1303. doi:10.2136/sssaj1989.03615995005300050001x.
- Vanderborght, J., Vereecken, H., 2007. Review of Dispersivities for Transport Modeling in Soils. *Vadose Zo. J.* 6, 29. doi:10.2136/vzj2006.0096.
- Weisenburger, D.D., 1991. Potential health consequences of ground-water contamination by nitrates in Nebraska. *Nitrate Contam.* 78, 309–315. doi:10.1007/978-3-642-76040-2\_23.
- Young, I.M., Crawford, J.W., 2004. Interactions and self-organization in the soil-microbe complex. *Science* (80-. ). doi:10.1126/science.1097394.
- Zhang, Y., Benson, D.A., Reeves, D.M., 2009. Time and space nonlocalities underlying fractional-derivative models: Distinction and literature review of field applications. *Adv. Water Resour.* 32, 561–581. doi:10.1016/j.advwatres.2009.01.008.
- Zhang, Y., Sun, H.G., Lu, B., Garrard, R., Neupauer, R.M., 2017a. Identify source location and release time for pollutants undergoing super-diffusion and decay: Parameter analysis and model evaluation. *Adv. Water Resour.* 107, 517–524. doi:10.1016/j.advwatres.2017.05.017.
- Zhang, Y., Sun, H.G., Stowell, H.H., Zayernouri, M., Hansen, S.E., 2017b. A review of applications of fractional calculus in Earth system dynamics. *Chaos, Solitons and Fractals* 102, 29–46. doi:10.1016/j.chaos.2017.03.051.

## CHAPTER 7: CONCLUSIONS

In this dissertation, I applied a wide variety of time nonlocal transport models, including t-fADE, MRMT, SRMT, and CTRW, with laboratory sand column experiments and field tracer tests to investigate the mechanisms in contaminant fate and transport through heterogeneous porous and fractured media at various scales, and the associated non-Darcian flow and non-Fickian pressure propagation in field-scale discrete fracture networks. I demonstrated that the tempered spatial/temporal fractional advection dispersion equation can capture a wide range of solute particle velocities ranging from sub-diffusion to super diffusion, as well as chemical reactions, with the least fitting effort and the best fitting results. Physical meanings of model parameters and the intrinsic correlation with media properties and experimental conditions are also investigated. These efforts lead to the identification of qualitative and quantitative relationships between model parameters and media or BTCs' characteristics, as well as the impacts of matrix heterogeneity on non-Fickian dynamics.

In Chapter 2, three time-nonlocal transport models (the MRMT model with various specific forms, the tt-fADE model, and the CTRW framework) are compared by combining theoretical analyses and applications for laboratory sand column transport experiments and field tracer tests. The sand column packed in the laboratory and soil in the field may contain multiple immobile domains with different mass transfer capabilities. The MRMT models with multiple rates can capture the BTC's late time tail typical for non-Fickian transport, but the MRMT

solutions with power-law distributed mass-exchange rates cannot capture the nuance of the observed transition from power-law to exponential decline of the late-time concentration. The increase of the number of unpredictable parameters (both the rate coefficient and the capacity coefficient) creates a challenge for the applicability of the MRMT model. The tt-fADE model and the CTRW framework are similar in functionality, but differ in detailed parameters in the following three ways. (1) Both the CTRW framework and the tt-fADE model can capture a complex BTC with late time tailing. Both the CTRW framework and the tt-fADE model assume an exponentially-truncated power-law memory function, to capture the gradual transition from power-law to exponential decline of late-time concentration in the observed BTCs. (2) The tt-fADE parameters can be linked to the CTRW framework parameters. Hence the predictability obtained by the tt-fADE model can also improve the predictability of the CTRW framework, and vice-versa. (3) Compared to the tt-fADE model, the CTRW framework defines one additional parameter  $t_l$ , which represents the mean diffusive time, corresponding to the mean of the inverse of rate coefficients in the MRMT model. Model applications, however, showed that  $t_l$  in the CTRW framework is insensitive to model results, and may be neglected to alleviate model fitting burdens. In the tt-fADE model, the real BTC's peak velocity can be used to estimate the lower-end of the model velocity, increasing the predictability of the tt-fADE for real-world applications. Hence, the tt-fADE model with less parameters may conveniently and accurately estimate the BTC late-time tailing under the conditions of the column experiments and field tracer tests. For tracer transport in the field, early arrivals are likely due to preferential flow paths. Super-diffusive jumps along preferential flow paths cannot be efficiently captured by a typical time-nonlocal transport model focusing on solute retention with a time index less than one. Fast motion and delayed transport, which can co-exist in some aquifers, are driven by

different mechanisms, and hence I recommend using different physical components to capture these processes, such as those embedded in the spatiotemporal fADE.

In Chapter 3, I quantify the dynamics of arsenic leaching in soils documented from literature and arsenic flushing in ideal columns packed with homogeneous glass bead packs conducted in our laboratory. The SRMT model, the standard MRMT model with two immobile domains, and the tempered time fADE model are applied and compared. Arsenic transport in soil is a multiple rate, sorption-desorption kinetic process, resulting in non-Fickian, sub-diffusive transport dynamics characterized by the heavy-tailed late-time BTCs. The multiple rates of sorption-desorption are reflected by the variable elution concentration decline rates for the BTC at late times, which cannot be efficiently captured by the traditional equilibrium model or the mixed equilibrium-kinetic model. Both the leaching and the flushing processes of As (V) can be simulated using the tempered time fractional advection-dispersion equation, with different truncation in the standard  $\gamma$ -stable density function. The simplified tempered time fADE model is more convenient than the standard MRMT model in capturing the complex As transport through contaminated soils with multiple stages of sorption-desorption, with less parameters. Both the time fADE model and the MRMT model with multiple pairs of immobile phases perform better than the SRMT model in capturing major characteristics of non-Fickian transport observed in the BTCs, especially the late time tailing portion as the arsenic leaching (or flushing) involves multiple stages with different reaction rates. In addition, although the MRMT model can define multiple pairs of mass-transfer parameters (i.e., mass exchange rate and capacity coefficient) to characterize the multiple stages of As sorption-desorption, the real-world application of the MRMT model is not straightforward. The flushing experiment performed in this study provides useful information to expand the previous leaching experiments for understanding and

interpreting As (V) dynamics in natural media with different degrees of heterogeneity. A weaker sub-diffusive effect on As (V) transport is characterized by the less pronounced (i.e., lighter) BTC late-time tail observed for the flushing experiments (using glass beads) compared to the leaching experiments (using real soil). According to this study, I expect that the As (V) dynamics may exhibit super-diffusive behavior, when large-scale, interconnected soil macro-pores provide preferential flow paths for dissolved arsenic species, in more realistic conditions at the field scale. The fractional capacity coefficient and the truncation parameter in the time fADE model can be calculated using the results from the MRMT model, and they can also be related to soil properties and chemical conditions. An empirical relationship between the power law exponent and the time index  $\gamma$  was determined. The time index and the capacity coefficient in the time fADE model can be related to the pH level and the clay content of the system. A soil sample with high clay content tend to possess a larger capacity coefficient (more immobile phases), while a soil sample with a larger pH value can be characterized by a smaller time index (faster release of As during the early stages of elution) in the time fADE model.

In Chapter 4, I explore the relationship between discret fracture networks' (DFNs) properties and non-Fickian transport dynamics. The DFN density is the major factor affecting non-Fickian transport at the late time. A moderate dense DFN results in the most heterogenous domain and the heaviest late-time tail in the BTCs, implying that there might exist a potential threshold of fracture density for non-Fickian dynamics when both the domain size and the fracture length distribution remain unchanged. For the DFNs with the same density and different mean orientations, the late time tailing behavior is affected by the ratio of fractures along different directions. More longitudinal fractures aligned with the overall flow direction will lead to an increase in earlier arrivals, while more transverse fractures, with flow deviating from the

general flow direction, will enhance chemical particles to interact with the rock matrix, resulting in a greater immobile mass and a heavier late-time tailing. The BTC peak time is determined by both the effective velocity and capacity coefficient. The time index and the slope of the late-time BTC, however, are similar for the DFNs with the similar density and different mean orientations. A rock matrix with higher permeability will lead to a relatively more homogeneous domain with a larger time index and a steeper slope in the late-time BTC. The DFN properties can be quantitatively linked to the slope of the recession limb of the BTC. The time index  $\gamma$  in the tt-fADE model has a simple, linear empirical expression with the power-law slope of the BTC recession limb, which can help estimate the index  $\gamma$  in practical applications where the chemical transport time is usually not long enough to cover the full range of late-time transport behavior. Plume snapshots show that all the three fracture densities built in this study exhibit early arrivals and sequestration effects. The denser DFNs can produce more early arrivals, due to more preferential flow paths, while the sparse DFNs tend to show heavier sequestration near the source. Therefore, competition between the channeling effect (in relative high-permeable fractures or the mobile phase) and the trapping effect (in the surrounding rock matrix or immobile domains) results in complex, prolonged non-Fickian characteristics in chemical transport. With predictable parameters, the fractional partial differential equations can be used as an efficient upscaling tool to address real-world contaminant transport.

In Chapter 5, I conducted Monte Carlo simulations to identify possible non-Darcian flow and non-Fickian pressure propagation in field-scale DFNs. Multiple scenarios of DFNs are generated with different fracture densities and matrix hydraulic conductivities. I concluded that both the fracture network architecture and the general hydraulic gradient  $J$  affect the non-Darcian flow in DFNs. The fracture density affects flow dynamics by generating complex flow paths for

water, and the gradient  $J$  can adjust the flow field and provide the criterion for Darcian versus non-Darcian flow. Strong non-Darcian flow appears for  $J$  less than the threshold  $J_s$ , where this threshold increases with an increasing fracture density. Fracture density affects significantly the propagation of hydraulic head/pressure in the DFNs. A sparse DFN can cause both delayed motion of water at the early time (likely due to the small effective hydraulic conductivity and the poor fracture connectivity) and enhanced flow at the middle/late time (likely due to the enhanced flow channeling), resulting in strong non-Fickian pressure propagation. The non-Darcian flow pattern does not relate to or drive the non-Fickian pressure propagation process directly, because they refer to different states of water flow and their controlling factors may not be the same.

In Chapter 6, I developed and validated a novel fractional-derivative, advection-dispersion-reaction equation (fADRE) with first order decay to quantify nitrate contaminants transport in various soil systems. Widely used classical transport models, including the ADRE and the two-region MIM model, were selected for model comparison. Applications show that the fADRE model can consider both hydrological and biogeochemical processes describing the fate and transport of nitrate in saturated soil. The model is tested and validated using the results from three independent studies including: 1) nitrate transport in natural soil columns collected from the North China Plain agricultural pollution zone, 2) nitrate leaching from aridisols and entisols soil columns, and 3) two bacteria (*Escherichia coli* and *Klebsiella* sp.) transport through saturated soil columns. Model solution is sensitive to the reaction term in the fADRE, which is convenient to capture the nutrient transformation process. A relatively large reaction rate will lead to multiple peaks in the BTC, due likely to the function of denitrifying bacteria and non-Fickian transport dynamics of nitrate. The parameters of the fADRE model can be related qualitatively to the physical properties of the soil (including clay content, pore size distribution,

and soil internal structure), the experimental conditions (including the initial solute concentration) and the solute/bacteria's chemical properties (sorption and motility). Hence, those relationships can improve the predictability and applicability of the model qualitatively and guide the future effort in linking quantitatively the model parameters and the system properties. This model can not only describe nitrate transformations through saturated soils, but also other first-order reactions, such as the growth of bacteria in complex soil systems. It may also be used to capture biological degradation and decay of radioactive isotopes, using the first-order decline term in the model.

In Chapter 2 and 3, I quantify the flow and transport processes in porous media; in Chapter 4 and 5, I extent the fractional-derivstive models to fractured porous media; and in Chapter 6, a reaction term is added to model the reactive contaminants fate and transport in groundwater. Fractures widely exsit in most rocks and aquifers as major conduits or barriers for fluid flow (Berre et al., 2018). Fractures are present in soil (Council, 2001) and glaciers (Fountain and Walder, 1998), and in porous materials such as wood (Smith et al., 2003; Watanabe, 1998). The fractured media also arouse huge interest in inductry, since most natural water or oil reservoirs are fractured and the major portion of the fluids is stored in the porous matrix (Bogdanov et al., 2003). The fluid tends to flow through the fracture network. Hence, a study of the interaction between the porous matrix and the fractures is necessary to better predict the reservoir performance. Formation properties can be measured by cutting a core and measuring in the laboratory (Ning et al., 1993). However, adequate representations of porous and fractured media are challenging in reservoir simulation. In standard porous media, an effective value might be reached with the increasing of the domain size. The corresponding domain is a representative elementary volume (REV) (Bear, 1972). For fractured media, existence of such an

REV is not clear (Berre et al., 2018). The parameters of the traditional models are difficult to define and measure. With the tempered-stable time fractional-derivative model, I can upscale subdiffusion for pollutant transport in field-scale DFNs, and determine both qualitative and quantitative relationships between BTC characteristics and model parameters, in addition to evaluate the impacts of fracture density, orientation, and rock matrix permeability on non-Fickian dynamics. The observed impacts of medium heterogeneity on tracer transport at late time can enhance the applicability of fPDEs since the measurable fracture–matrix characteristics can guide the determination of major model parameters. Most contaminants in groundwater are reactive. With the development of a fractional-derivative model with reaction, it can not only describe nitrate transformations through saturated soils, but also other first-order reactions, such as the growth of bacteria in complex soil systems. It may also be used to capture biological degradation and decay of radioactive isotopes, using the first-order decline term in the model. Hence, the mathematical model proposed in this study may shed lights on the quantification of various biogeochemical dynamics in complex soil systems, which can be applied with real-world datasets.

## Reference

- Ahmed, E., Elgazzar, A.S., 2007. On fractional order differential equations model for nonlocal epidemics. *Phys. A Stat. Mech. its Appl.* 379, 607–614. doi:10.1016/j.physa.2007.01.010.
- Anderson, M.P., 1984. Movement of contaminants in groundwater: groundwater transport--advection and dispersion. *Groundw. Contam.* 20, 37–45.
- Bear, J., 1972. *Dynamics of fluids in porous media*, American Elsevier Publishing Company. New York.
- Bear, J., Bachmat, Y., 1990. Introduction to modeling of transport phenomena in porous media. *Introd. to Model. Transp. Phenom. porous media*.
- Berkowitz, B., Cortis, A., Dentz, M., Scher, H., 2006. Modeling Non-fickian transport in geological formations as a continuous time random walk. *Rev. Geophys.* 44. doi:10.1029/2005RG000178.
- Berre, I., Doster, F., Keilegavlen, E., 2018. Flow in Fractured Porous Media: A Review of Conceptual Models and Discretization Approaches. *Transp. Porous Media* 1–22. doi:10.1007/s11242-018-1171-6.
- Bogdanov, I.I., Mourzenko, V. V., Thovert, J.F., Adler, P.M., 2003. Effective permeability of fractured porous media in steady state flow. *Water Resour. Res.* 39. doi:10.1029/2001WR000756.
- Council, N.R., 1997. *Innovations in ground water and soil cleanup: from concept to commercialization*, National Academies Press. National Academies Press, Washington, D.C. doi:10.17226/5781.
- Council, N.R., 1994. *Alternatives for ground water cleanup*, National Academies Press. doi:10.2113/gseegeosci.iii.3.464.
- Council, N.R., 2001. *Conceptual models of flow and transport in the fractured vadose zone*, National Academies Press. doi:10.2136/vzj2002.2000.
- Debnath, L., Bhatta, D.D., 2004. Solutions to few linear fractional inhomogeneous partial differential equations in fluid mechanics. *Fract. Calc. Appl. Anal.* 7, 21–36.
- Fountain, A.G., Walder, J.S., 1998. Water flow through temperate glaciers. *Rev. Geophys.* 36, 299–328. doi:10.1029/97RG03579.

- Fried, J.J., 1975. Groundwater pollution, in: Elsevier. p. 330. doi:10.1016/b978-0-408-01409-0.50011-8.
- Haggerty, R., Gorelick, S.M., 1995. Multiple-rate mass transfer for modeling diffusion and surface reactions in media with pore-scale heterogeneity. *Water Resour. Res.* 31, 2383–2400. doi:10.1029/95WR01583.
- Haggerty, R., McKenna, S. a, Meigs, L.C., 2000. On the late-time behaviour of tracer breakthrough curves. *Water Resour. Res.* 36, 3467–3479.
- Luchko, Y., Gorenflo, R., 1999. An operational method for solving fractional differential equations with the Caputo derivatives. *Acta Math. Vietnam.* 24, 207–233.
- Meerschaert, M.M., Zhang, Y., Baeumer, B., 2008. Tempered anomalous diffusion in heterogeneous systems. *Geophys. Res. Lett.* 35, 1–5. doi:10.1029/2008GL034899.
- Ning, X., Fan, J., Holditch, S.A., Lee, W.J., 1993. Measurement of matrix and fracture properties in naturally fractured cores, in: *Rocky Mountain Regional Meeting/Low Permeability Reservoirs Symposium and Exhibition*. Society of Petroleum Engineers, pp. 555–570. doi:10.2118/25898-MS.
- Oldham, K.B., 2010. Fractional differential equations in electrochemistry. *Adv. Eng. Softw.* 41, 9–12. doi:10.1016/j.advengsoft.2008.12.012.
- Podlubny, I., 2001. Geometric and physical interpretation of fractional integration and fractional differentiation. *arXiv Prepr. math/0110241* 1–20.
- Russell, M.E., Coglazier, W., English, M., 1991. *Hazardous Waste Remediation: The task ahead*. Univ. Tennessee, Waste Manag. Res. Educ. Inst.
- Smith, I., Landis, E., Gong, M., 2003. *Fracture and Fatigue in Wood*.
- Taylor, G.I., 1922. Diffusion by continuous movements. *Proc. london Math. Soc.* 2, 196–212. doi:https://doi.org/10.1112/plms/s2-20.1.196.
- Turut, V., Güzel, N., 2013. On solving Partial Differential Equations of Fractional Order by Using the Variational Iteration Method and Multivariate Padé Approximations. *Eur. J. Pure Appl. Math.* 6, 147–171.
- Watanabe, U., 1998. Liquid penetration of precompressed wood VI: Anatomical characterization of pit fractures. *J. Wood Sci.* 44, 158–162. doi:10.1007/BF00526263.
- Zhang, Y., Benson, D.A., Reeves, D.M., 2009. Time and space nonlocalities underlying fractional-derivative models: Distinction and literature review of field applications. *Adv. Water Resour.* 32, 561–581. doi:10.1016/j.advwatres.2009.01.008.

Zhang, Y., Sun, H.G., Stowell, H.H., Zayernouri, M., Hansen, S.E., 2017. A review of applications of fractional calculus in Earth system dynamics. *Chaos, Solitons and Fractals* 102, 29–46. doi:10.1016/j.chaos.2017.03.051.